



# 5

## Detection of Regions of Interest

In CAD, one of the roles of image processing is to detect the region of interest (ROI) in the given application;

then perform characterization and classification of the regions.



## Examples of ROIs:

- Cells in cervical-smear test images  
(Papanicolaou or Pap-smear test).
- Calcifications in mammograms.
- Tumors and masses in mammograms.
- The pectoral muscle in mammograms.
- The breast outline or skin-air boundary in mammograms.
- The fibroglandular disc in mammograms.
- The air-way tree in lungs.
- The arterial tree in lungs.
- The arterial tree of the left ventricle;  
constricted parts of the same due to plaque development.



Segmentation is the process that divides an image into its constituent parts, objects, or ROIs.

Segmentation is an essential step before the description, recognition, or classification of an image or its constituents.

Two major approaches to image segmentation are based on the detection of the following characteristics:

- **Discontinuity** — Abrupt changes in gray level (corresponding to edges) are detected.
- **Similarity** — Homogeneous parts are detected, based on gray-level thresholding, region growing, and region splitting/merging.



Applications do exist where entire images need to be analyzed for global changes in patterns.

Images with multicomponent ROIs:

analysis may commence with the detection of single units of the pattern of interest;

several such units present in a given image may need to be analyzed, separately and together, in order to reach a decision.

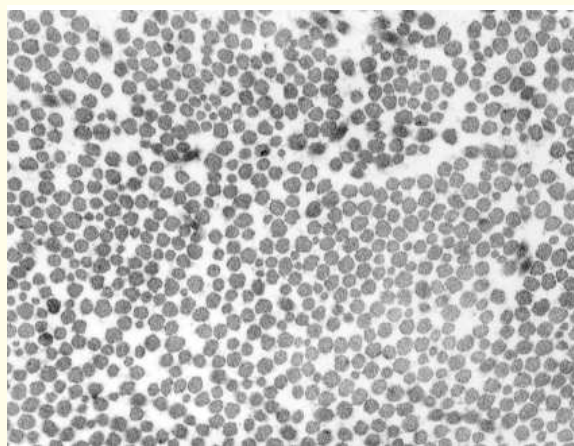


## 5.1 Thresholding and Binarization

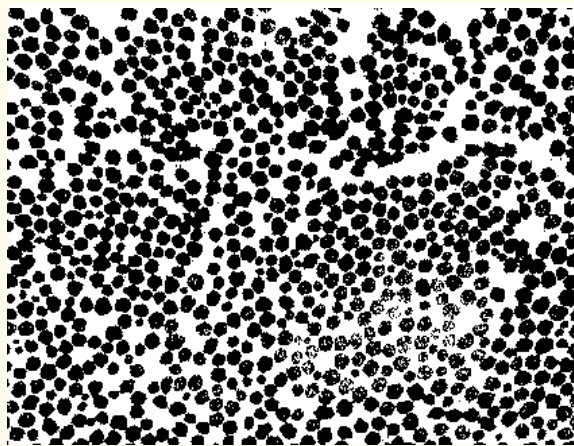
If the gray levels of the objects of interest in an image are known from prior knowledge, or can be determined from its histogram,

the image may be thresholded to detect the features of interest and reject other details.

$$g(m, n) = \begin{cases} 0 & \text{if } f(m, n) \leq L_1 \\ 255 & \text{if } f(m, n) > L_1 \end{cases}. \quad (5.1)$$

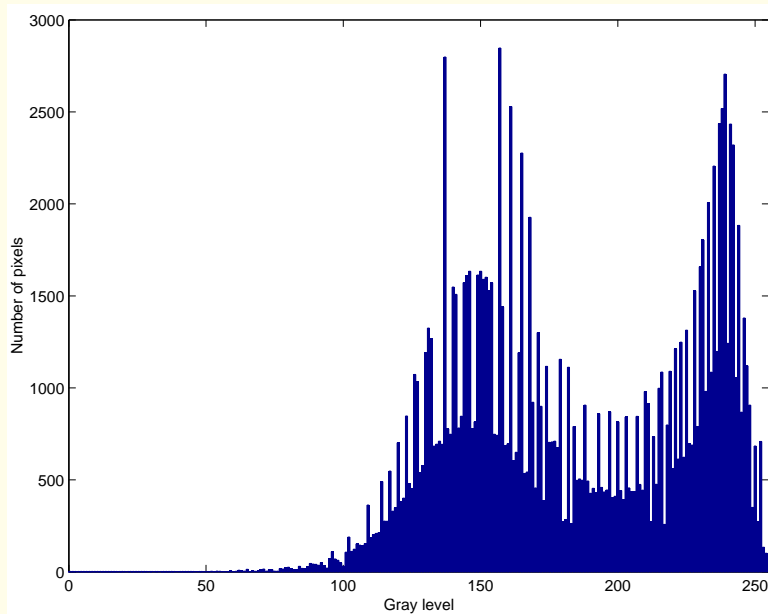


(a)

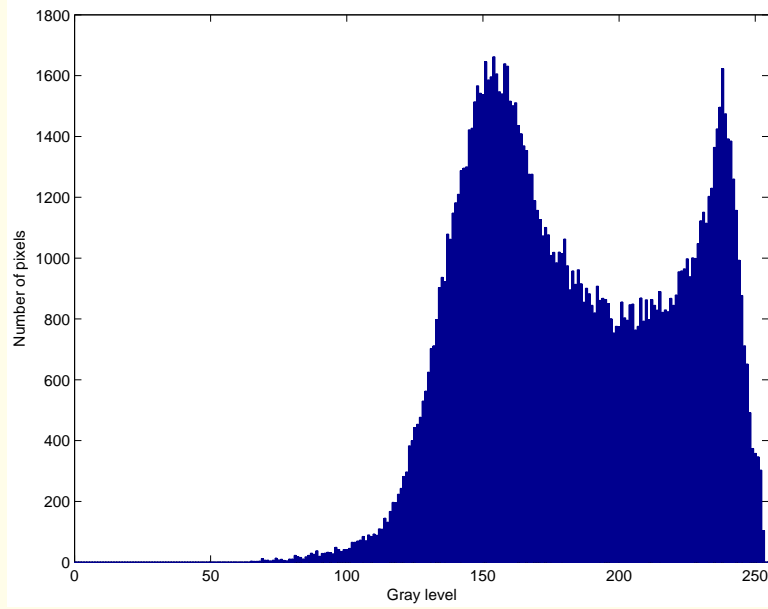


(b)

Figure 5.1: (a) TEM image of collagen fibers in a scar-tissue sample from a rabbit ligament at a magnification of approximately  $\times 30,000$ . Image courtesy of C.B. Frank, Department of Surgery, University of Calgary. See Figure 2.12 for the histogram of the image. (b) Image in (a) thresholded at the gray level of 180.



(a)



(b)

(a) Histogram of the image of the collagen fibers.

(b) Histogram of the image after the application of the  $3 \times 3$  mean filter and rounding the results to integers.



## 5.2 Detection of Isolated Points and Lines

Useful in noise removal and the analysis of particles.

$$\begin{bmatrix} -1 & -1 & -1 \\ -1 & 8 & -1 \\ -1 & -1 & -1 \end{bmatrix}. \quad (5.2)$$



Straight lines or line segments oriented at  $0^\circ$ ,  $45^\circ$ ,  $90^\circ$ , and  $135^\circ$  may be detected by using the following  $3 \times 3$  convolution masks:

$$\begin{bmatrix} -1 & -1 & -1 \\ 2 & 2 & 2 \\ -1 & -1 & -1 \end{bmatrix}, \quad \begin{bmatrix} -1 & -1 & 2 \\ -1 & 2 & -1 \\ 2 & -1 & -1 \end{bmatrix},$$

$$\begin{bmatrix} -1 & 2 & -1 \\ -1 & 2 & -1 \\ -1 & 2 & -1 \end{bmatrix}, \quad \begin{bmatrix} 2 & -1 & -1 \\ -1 & 2 & -1 \\ -1 & -1 & 2 \end{bmatrix}. \quad (5.3)$$

A line may be said to exist in the direction for which the corresponding mask provides the largest response.



## 5.3 Edge Detection

### 5.3.1 *Convolution mask operators for edge detection*

An edge is characterized by a large change in the gray level from one side to the other, in a particular direction dependent upon the orientation of the edge.

Gradients or derivatives measure the rate of change, and could serve as the basis for methods for edge detection.



First derivatives (differences) in  $x$  and  $y$ :

$$f'_{yb}(m, n) \approx f(m, n) - f(m - 1, n),$$

$$f'_{xb}(m, n) \approx f(m, n) - f(m, n - 1), \quad (5.4)$$

subscript  $b$  indicates a backward-difference operation.

Causality is usually not a matter of concern in image processing:

$$f'_{yf}(m, n) \approx f(m + 1, n) - f(m, n),$$

$$f'_{xf}(m, n) \approx f(m, n + 1) - f(m, n), \quad (5.5)$$

subscript  $f$  indicates a forward-difference operation.



A limitation of the operators as above:  
they are based upon the values of only two pixels;  
susceptible to noise or spurious pixel values.

To design robust operators and reduce the sensitivity to noise:  
incorporate averaging over multiple measurements.

Averaging the backward and forward derivatives:

$$f'_{ya}(m, n) \approx 0.5 [f(m + 1, n) - f(m - 1, n)],$$

$$f'_{xa}(m, n) \approx 0.5 [f(m, n + 1) - f(m, n - 1)], \quad (5.6)$$

subscript *a* indicates the inclusion of averaging.



It is desirable to express operators in terms of odd-sized masks that may be centered upon the pixel being processed.

Prewitt operators:

$$G_x : \begin{bmatrix} -1 & 0 & 1 \\ -1 & 0 & 1 \\ -1 & 0 & 1 \end{bmatrix}. \quad (5.7)$$

$$G_y : \begin{bmatrix} -1 & -1 & -1 \\ 0 & 0 & 0 \\ 1 & 1 & 1 \end{bmatrix}. \quad (5.8)$$

Three differences used, across pairs of pixels in three rows or columns around the pixel being processed; normalize if needed.



Vectorial form of the gradient:

$$\mathbf{G}_f(m, n) = G_{fx}(m, n) + j G_{fy}(m, n),$$

$$\|\mathbf{G}_f(m, n)\| = \sqrt{G_{fx}^2(m, n) + G_{fy}^2(m, n)},$$

$$\angle \mathbf{G}_f(m, n) = \tan^{-1} \left( \frac{G_{fy}(m, n)}{G_{fx}(m, n)} \right), \quad (5.9)$$

$$G_{fx}(m, n) = (f * G_x)(m, n), \quad (5.10)$$

$$G_{fy}(m, n) = (f * G_y)(m, n). \quad (5.11)$$



Sobel operators:

$$G_x : \begin{bmatrix} -1 & 0 & 1 \\ -2 & 0 & 2 \\ -1 & 0 & 1 \end{bmatrix}, \quad (5.12)$$

$$G_y : \begin{bmatrix} -1 & -2 & -1 \\ 0 & 0 & 0 \\ 1 & 2 & 1 \end{bmatrix}. \quad (5.13)$$



Edges oriented at  $45^\circ$  and  $135^\circ$  may be detected by using rotated versions of the masks as above.

The Prewitt operators for the detection of diagonal edges are

$$G_{45^\circ} : \begin{bmatrix} 0 & -1 & -1 \\ 1 & 0 & -1 \\ 1 & 1 & 0 \end{bmatrix}, \quad (5.14)$$

$$G_{135^\circ} : \begin{bmatrix} -1 & -1 & 0 \\ -1 & 0 & 1 \\ 0 & 1 & 1 \end{bmatrix}. \quad (5.15)$$

Similar masks may be derived for the Sobel operator.



The positive and negative signs of the elements in the masks above may be interchanged to obtain operators that detect gradients in the opposite directions.

(Not necessary if directions are considered in the range  $0^\circ - 180^\circ$  only, or if only magnitudes of the gradients are required.)

The sum of all of the weights in the masks above is zero:

derivative or gradient operation;  
zero output values in areas of constant gray level;  
loss of intensity information.



Roberts operator:  $2 \times 2$  neighborhoods; cross-differences.

$$\begin{bmatrix} -1 & 0 \\ 0 & 1 \end{bmatrix} \text{ and } \begin{bmatrix} 0 & -1 \\ 1 & 0 \end{bmatrix}. \quad (5.16)$$

The masks are positioned with the upper-left element placed on the pixel being processed.



The absolute values of the results of the two operators are added to obtain the net gradient:

$$g(m, n) = |f(m + 1, n + 1) - f(m, n)| \quad (5.17)$$

$$+ |f(m + 1, n) - f(m, n + 1)|,$$

with the indices in matrix-indexing notation.

Advantage: forward-looking operator,  
the result may be written in the same array as the input image.

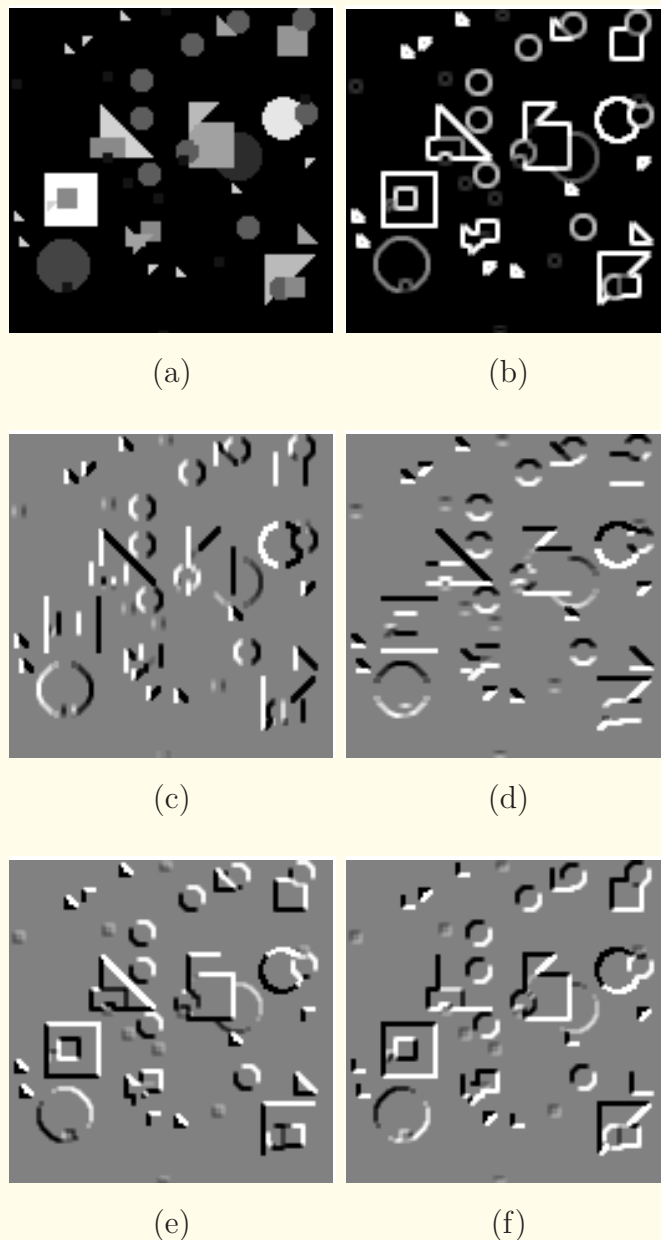
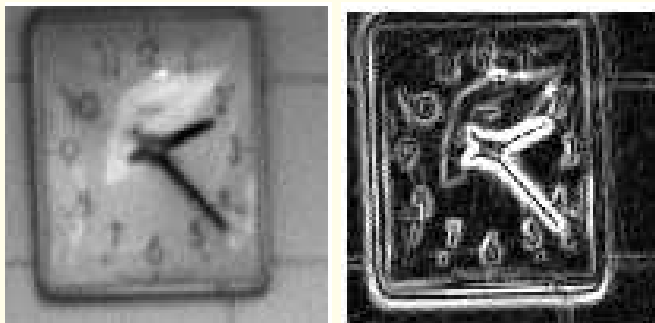
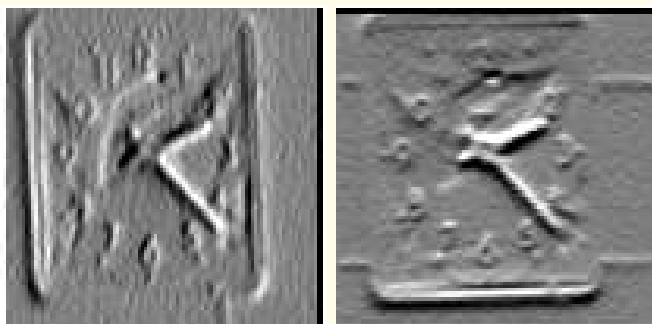


Figure 5.2: (a) Shapes test image. (b) Gradient magnitude, display range [0, 400] out of [0, 765]. (c) Horizontal derivative, display range [-200, 200] out of [-765, 765]. (d) Vertical derivative, display range [-200, 200] out of [-765, 765]. (e)  $45^\circ$  derivative, display range [-200, 200] out of [-765, 765]. (f)  $135^\circ$  derivative, display range [-200, 200] out of [-765, 765].



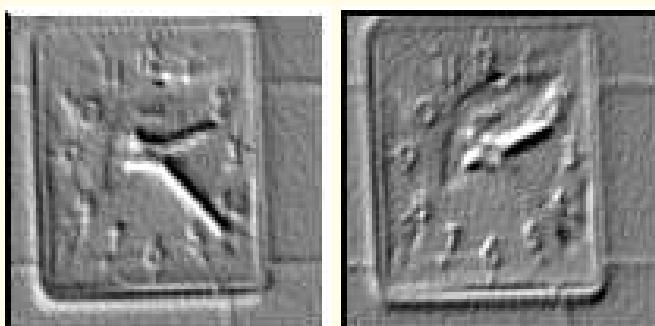
(a)

(b)



(c)

(d)



(e)

(f)

Figure 5.3: (a) Clock test image. (b) Gradient magnitude, display range [0, 100] out of [0, 545]. (c) Horizontal derivative, display range [-100, 100] out of [-538, 519]. (d) Vertical derivative, display range [-100, 100] out of [-446, 545]. (e)  $45^\circ$  derivative, display range [-100, 100] out of [-514, 440]. (f)  $135^\circ$  derivative, display range [-100, 100] out of [-431, 535].

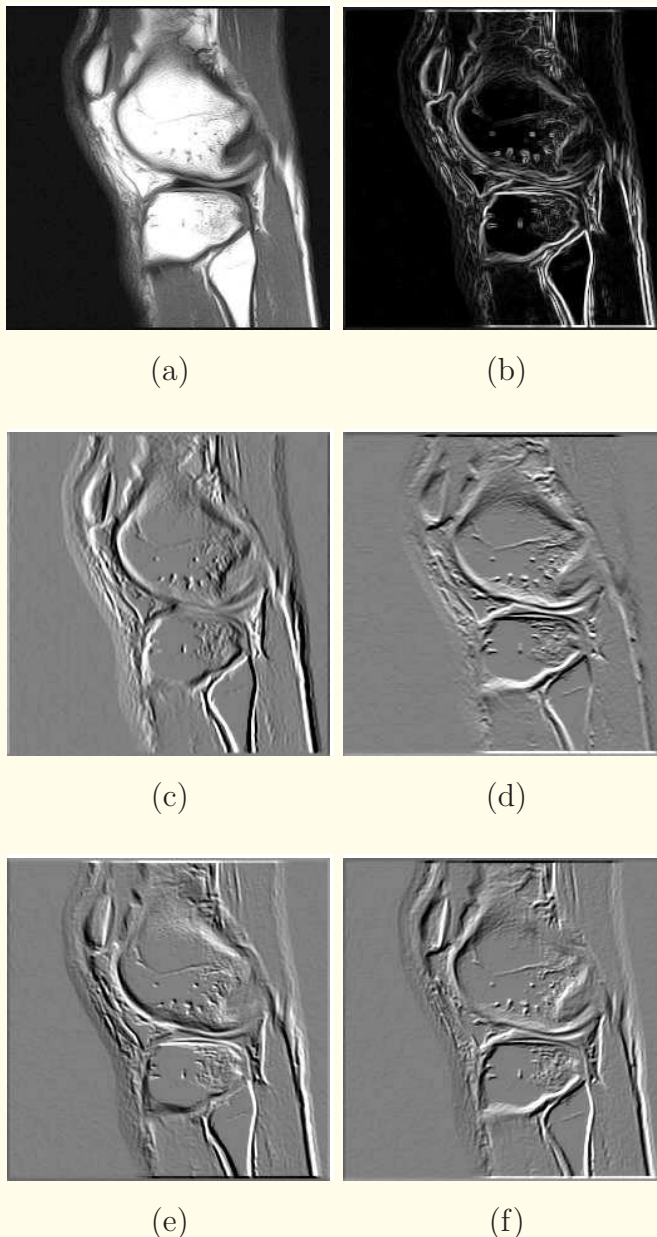
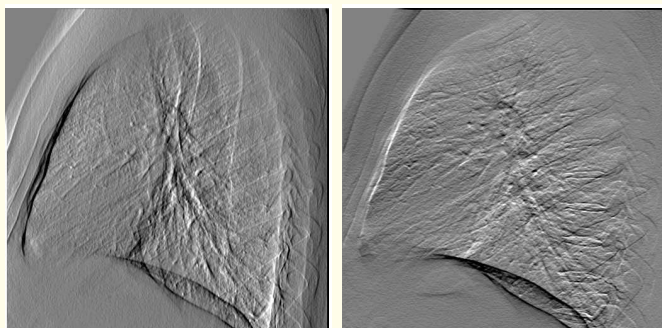


Figure 5.4: (a) Knee MR image. (b) Gradient magnitude, display range [0, 400] out of [0, 698]. (c) Horizontal derivative, display range [-200, 200] out of [-596, 496]. (d) Vertical derivative, display range [-200, 200] out of [-617, 698]. (e)  $45^\circ$  derivative, display range [-200, 200] out of [-562, 503]. (f)  $135^\circ$  derivative, display range [-200, 200] out of [-432, 528].



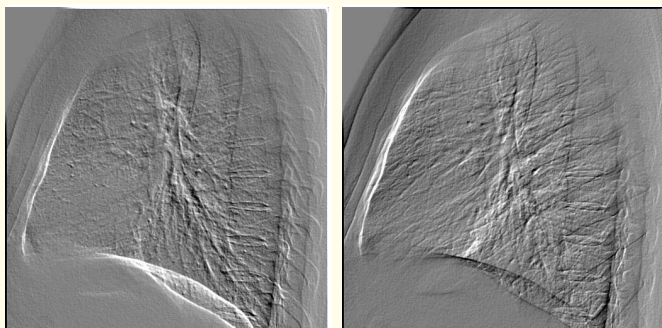
(a)

(b)



(c)

(d)



(e)

(f)

Figure 5.5: (a) Part of a chest X-ray image. (b) Gradient magnitude, display range [0, 50] out of [0, 699]. (c) Horizontal derivative, display range [−50, 50] out of [−286, 573]. (d) Vertical derivative, display range [−50, 50] out of [−699, 661]. (e)  $45^\circ$  derivative, display range [−50, 50] out of [−452, 466]. (f)  $135^\circ$  derivative, display range [−50, 50] out of [−466, 442].



### 5.3.2 *The Laplacian of Gaussian*

**Laplacian:** second-order gradient operator;

double-edged outputs with positive/negative values at edges;

omnidirectional — sensitive to edges in all directions;

not possible to derive the angle of an edge from the result;

sensitive to noise — no averaging included in the operator;

gain increases quadratically with frequency, causing significant amplification of high-frequency noise components;

not directly useful in edge detection.

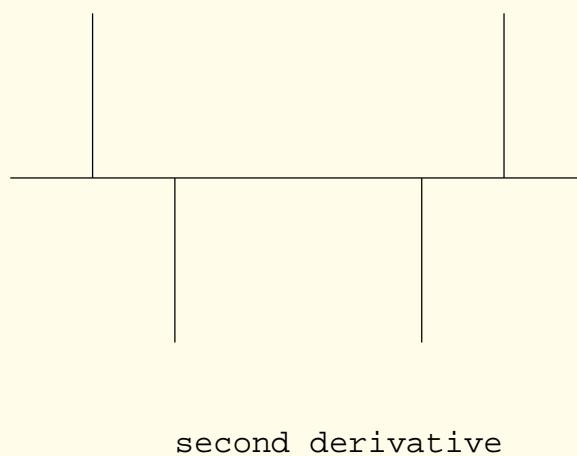
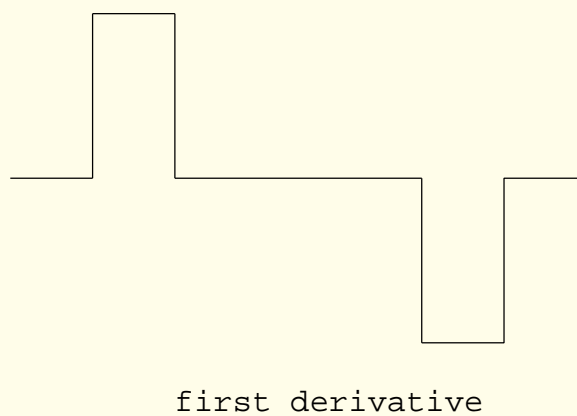
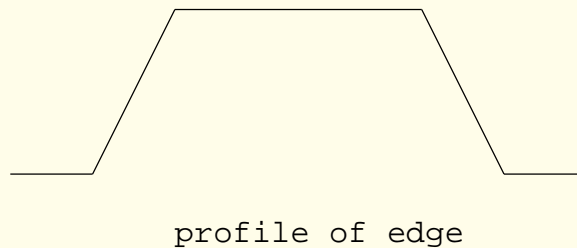


Figure 5.6: Top to bottom: A profile of a blurred object showing two edges, the first derivative, and the second derivative (see also Figure 4.26).



The double-edged output of the Laplacian indicates an important property of the operator:

the result possesses a *zero crossing* in between the positive and negative outputs across an edge;

even when the edge in the original image is significantly blurred.

Useful in the development of robust edge detectors.



Noise sensitivity reduced by including a smoothing operator.

A scalable smoothing operator could be defined in terms of a 2D Gaussian function,

with the variance controlling the spatial extent of smoothing.

Combining the Laplacian and the Gaussian, we obtain the popular **Laplacian-of-Gaussian** or LoG operator.



Consider the Gaussian specified by the function

$$g(x, y) = -\exp\left(-\frac{x^2 + y^2}{2 \sigma^2}\right). \quad (5.18)$$

The usual normalizing scale factor has been left out.

$$\begin{aligned} \frac{\partial^2 g}{\partial x^2} &= -\frac{x^2 - \sigma^2}{\sigma^4} \exp\left(-\frac{x^2 + y^2}{2 \sigma^2}\right), \\ \frac{\partial^2 g}{\partial y^2} &= -\frac{y^2 - \sigma^2}{\sigma^4} \exp\left(-\frac{x^2 + y^2}{2 \sigma^2}\right). \end{aligned} \quad (5.19)$$



$$\nabla^2 g(x, y) = \text{LoG}(r) = -\frac{r^2 - 2\sigma^2}{\sigma^4} \exp\left(-\frac{r^2}{2\sigma^2}\right), \quad (5.20)$$

where  $r = \sqrt{x^2 + y^2}$ .

LoG function: isotropic, has positive and negative values.

Due to its shape, referred to as the Mexican hat or sombrero.

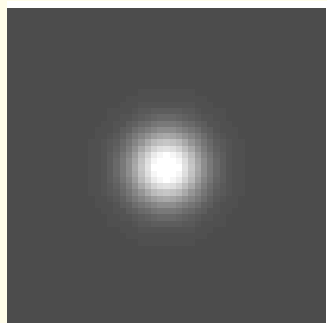


Whereas the Gaussian is a lowpass filter (also a 2D Gaussian in the frequency domain), the LoG is a bandpass filter.

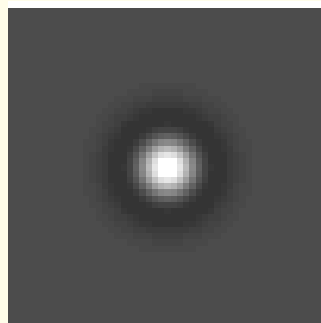
Width of filter controlled by the parameter  $\sigma$  of the Gaussian.

Approximation to the LoG provided by taking the difference between two Gaussians of appropriate variances:

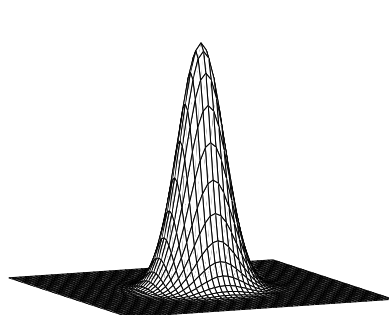
**difference-of-Gaussians** or DoG operator.



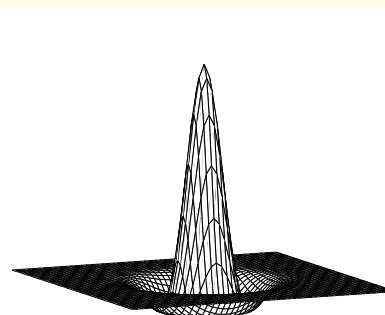
(a)



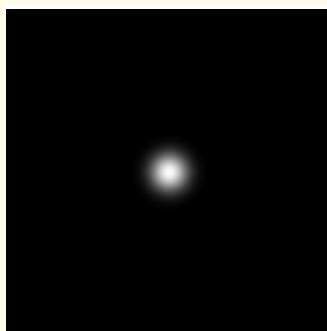
(b)



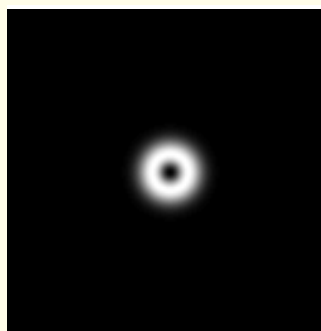
(c)



(d)

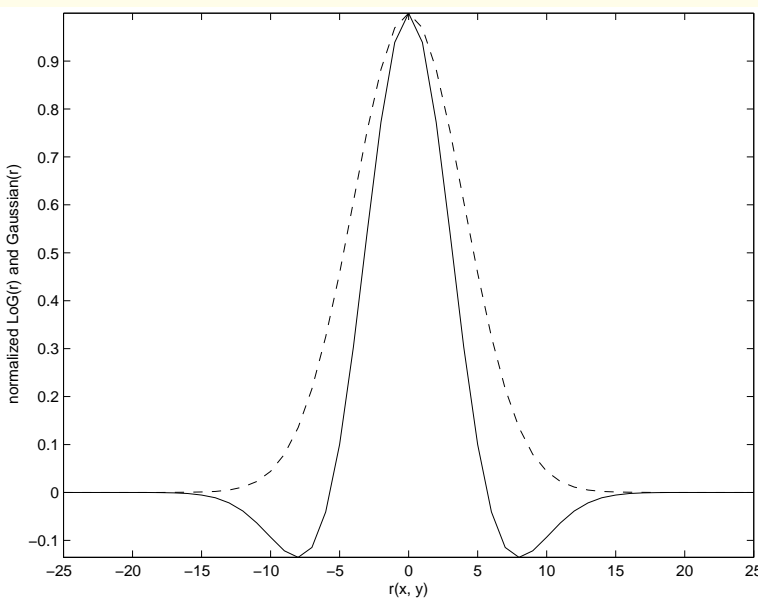


(e)

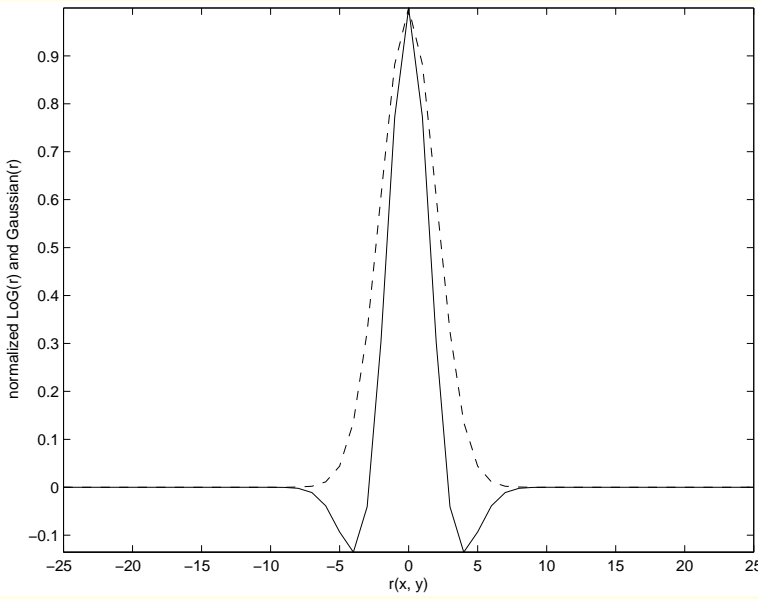


(f)

Figure 5.7: The Laplacian of Gaussian in (b) image format and (d) as a mesh plot. The related Gaussian functions are shown in (a) and (c). The size of the arrays is  $51 \times 51$  pixels; standard deviation  $\sigma = 4$  pixels. The Fourier magnitude spectra of the functions are shown in (e) and (f).

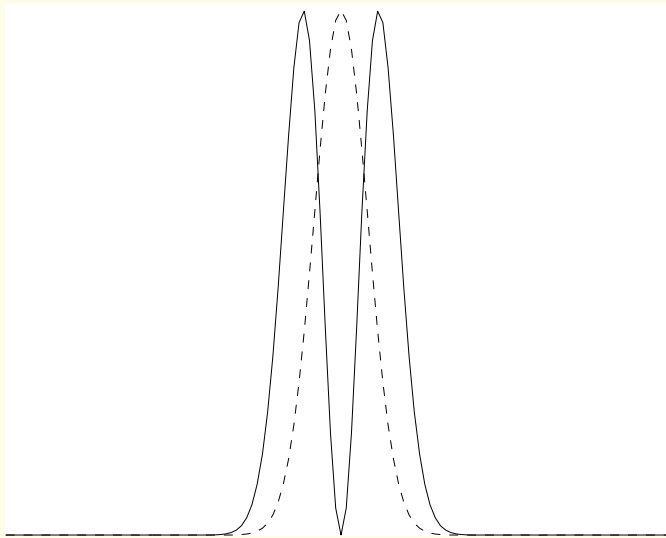


(a)

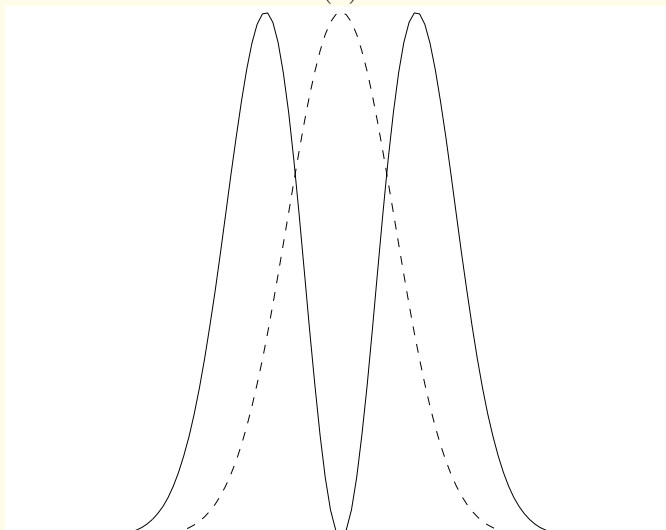


(b)

Figure 5.8: Profiles of the Laplacian of Gaussian (solid line) and the related Gaussian (dashed line) in Figure 5.7. The functions have been normalized to a maximum value of unity. The unit of  $r$  is pixels. (a)  $\sigma = 4$  pixels. (b)  $\sigma = 2$  pixels.



(a)



(b)

Figure 5.9: Profiles of the Fourier magnitude spectra of the Laplacian of Gaussian (solid line) and the related Gaussian (dashed line) in Figure 5.7. Both functions have been normalized to have a maximum value equal to unity. (a)  $\sigma = 4$  pixels. (b)  $\sigma = 2$  pixels. The zero-frequency point is at the center of the horizontal axis.

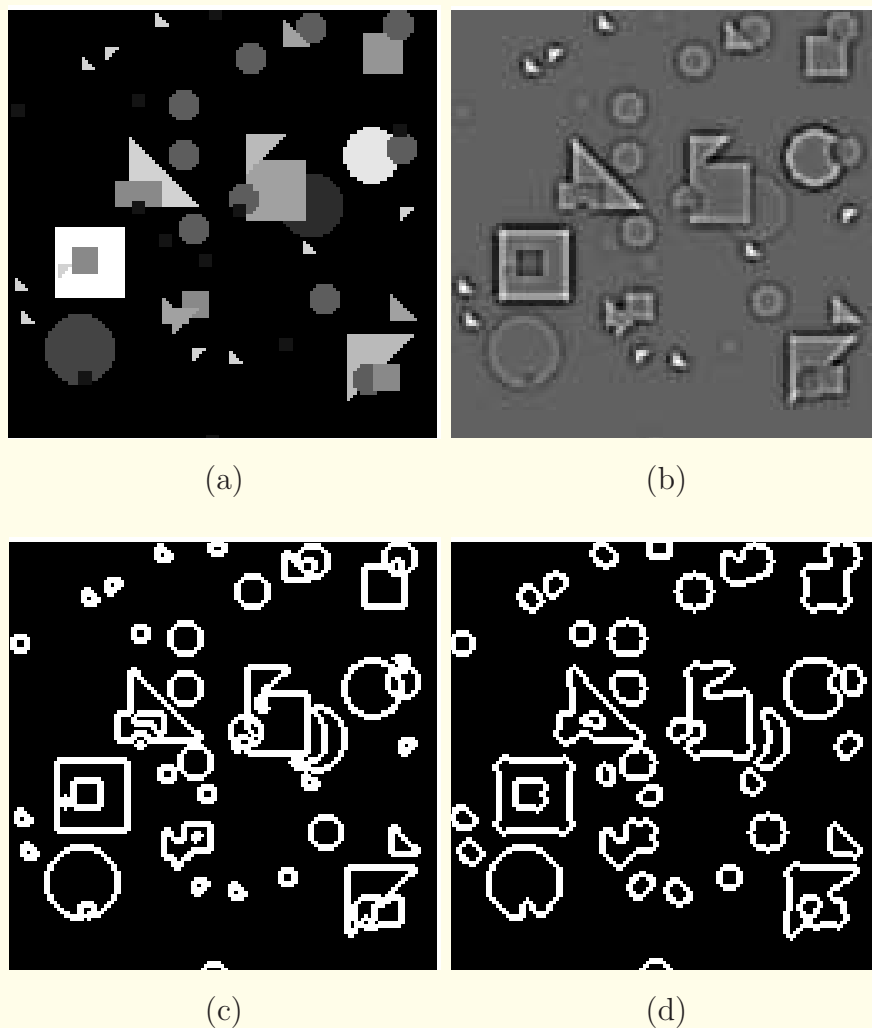


Figure 5.10: (a) The Shapes test image. (b) The LoG of the image in (a) with  $\sigma = 1$  pixel. (c) Locations of the zero-crossings in the LoG in (b). (d) Locations of the zero-crossings in the LoG with  $\sigma = 2$  pixels.

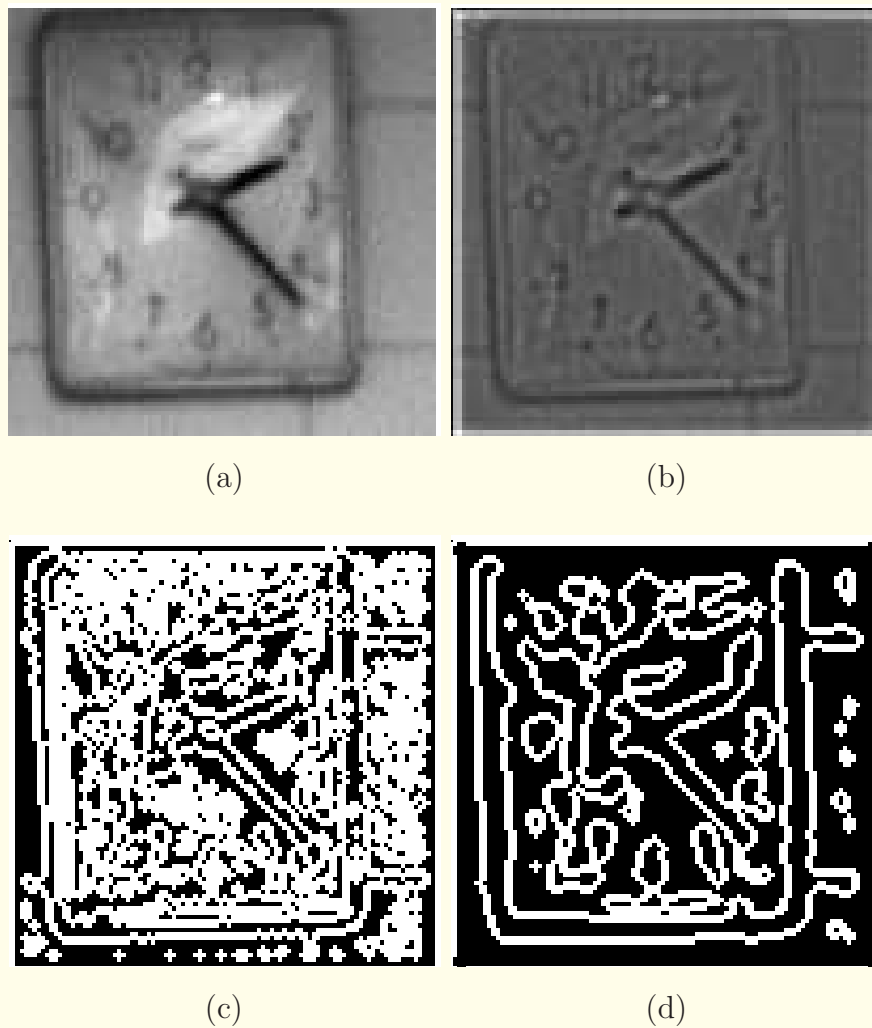


Figure 5.11: (a) The clock test image. (b) The LoG of the image in (a) with  $\sigma = 1$  pixel. (c) Locations of the zero-crossings in the LoG in (b). (d) Locations of the zero-crossings in the LoG with  $\sigma = 2$  pixels.

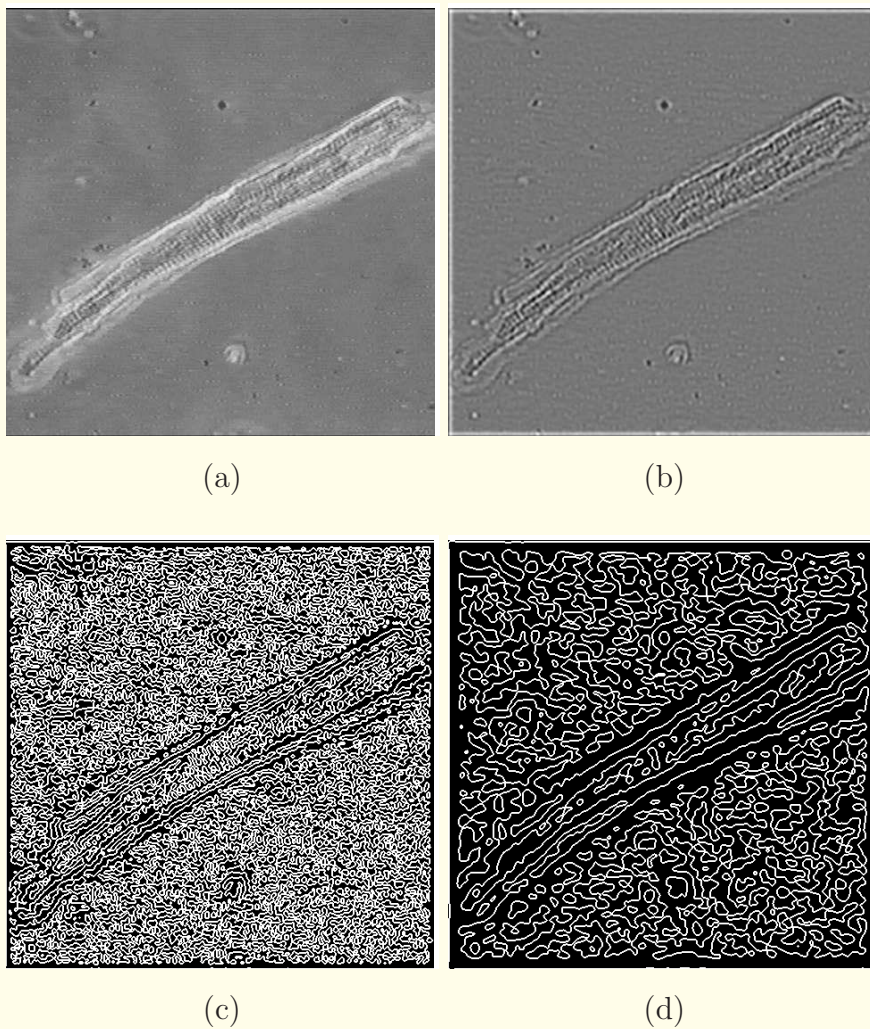


Figure 5.12: (a) Image of a myocyte. (b) The LoG of the image in (a) with  $\sigma = 2$  pixels. (c) Locations of the zero-crossings in the LoG in (b). (d) Locations of the zero-crossings in the LoG with  $\sigma = 4$  pixels.

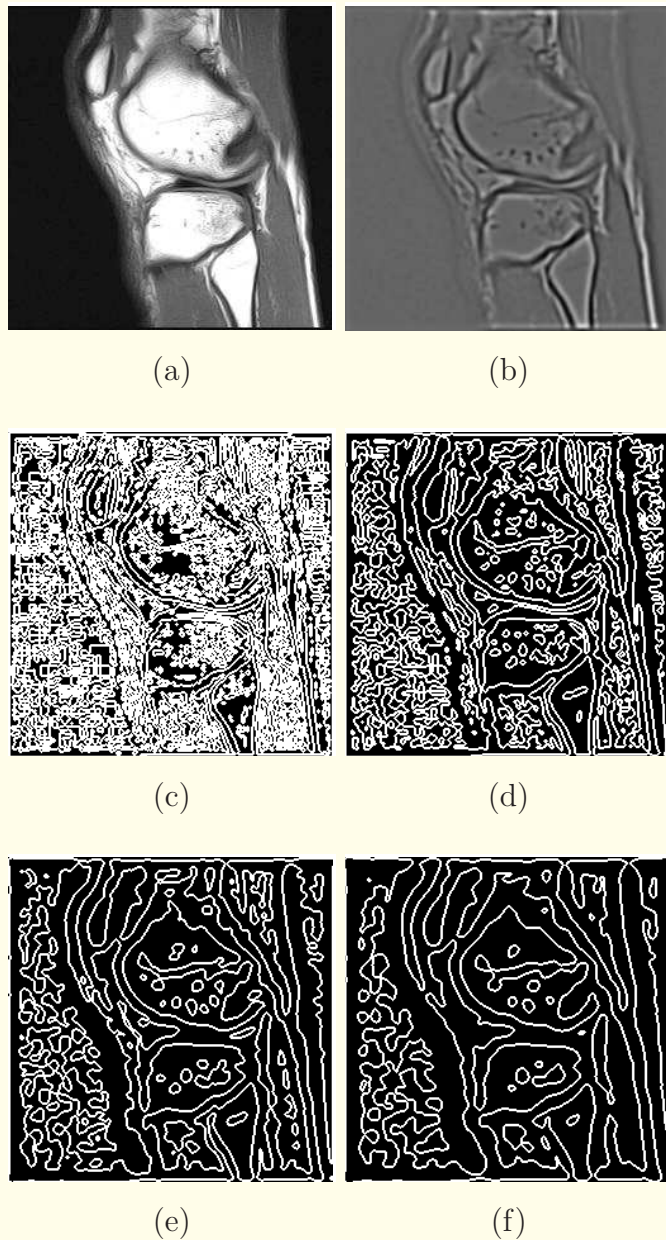


Figure 5.13: (a) MR image of a knee. (b) The LoG of the image in (a) with  $\sigma = 2$  pixels. (c) – (f) Locations of the zero-crossings in the LoG with  $\sigma = 1, 2, 3$ , and  $4$  pixels.

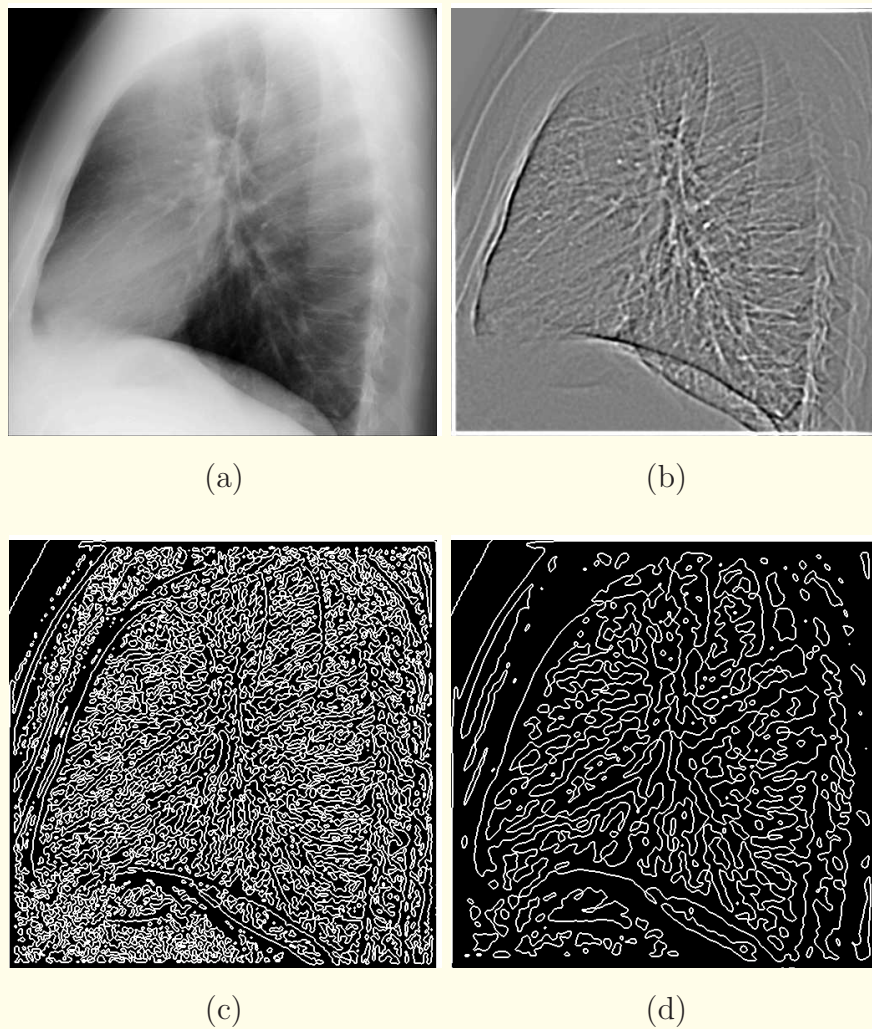


Figure 5.14: (a) Part of a chest X-ray image. (b) The LoG of the image in (a) with  $\sigma = 2$  pixels; display range  $[-150, 150]$  out of  $[-231, 956]$ . (c) Locations of the zero-crossings in the LoG in (b). (d) Locations of the zero-crossings in the LoG with  $\sigma = 4$  pixels.



### 5.3.3 *Scale-space methods for multiscale edge detection*

Marr and Hildreth suggested that physical phenomena may be detected simultaneously over several channels

— tuned to different spatial sizes or *scales* —

with an approach known as the spatial coincidence.



An intensity change that is due to a single physical phenomenon is indicated by zero-crossing segments present in independent channels over a certain range of scales,

having the same position and orientation in each channel.

The use of techniques based on zero-crossings generated from filters of different scales could be more effective than the conventional (single-scale) methods for edge detection;



## Zero-crossings and scale-space:

The multichannel model for the HVS and the Marr-Hildreth spatial coincidence assumption led to methods for

multiscale analysis performed with filters of different scales.

Bank of LoG filters with several values of  $\sigma$ :

$$\{\nabla^2 g(x, y; \sigma)\} \text{ with } \sigma > 0.$$



Witkin introduced the concept of scale-space:

$\Psi(x, y; \sigma)$  of an image  $f(x, y)$  defined as the set of all zero-crossings of its LoG:

$$\{\Psi(x, y; \sigma)\} = \{(x, y; \sigma) \mid \zeta(x, y; \sigma) = 0,$$

$$\left(\frac{\partial \zeta}{\partial x}\right)^2 + \left(\frac{\partial \zeta}{\partial y}\right)^2 \neq 0, \quad \sigma > 0, \quad (5.21)$$

$$\zeta(x, y; \sigma) = \{\nabla^2 g(x, y; \sigma) * f(x, y)\}. \quad (5.22)$$



As the scale  $\sigma$  varies from 0 to  $\infty$ , the set  $\{\Psi(x, y; \sigma)\}$  forms continuous surfaces in the  $(x, y; \sigma)$  scale-space.

Liu et al.: discrete scale-space approach used to construct a representation of a given image in terms of a **stability map**:

a measure of pattern boundary persistence over a range of scale of the filters.

A set of zero-crossing maps is generated by convolving the image with the set of isotropic functions  $\nabla^2 g(x, y; \sigma_i)$ ,  $1 \leq i \leq N$ .

$N = 8$  sampled  $\sigma_i$  values ranging from 1 to 8 pixels.



Instead of directly matching all the zero-crossing locations at a point  $(x, y)$  over the zero-crossing maps, Liu et al. proposed a criterion  $C(\sigma_i)$  to define a neighborhood in which the matching procedure is performed:

$$C(\sigma_i) = \{(x', y')\} \mid x - \lambda\sigma_i \leq x' \leq x + \lambda\sigma_i, \quad (5.23)$$

$$y - \lambda\sigma_i \leq y' \leq y + \lambda\sigma_i, \quad \lambda \leq 1,$$

$(x', y')$  are the actual locations of the zero-crossings,  
 $(x, y)$  is the pixel location at which the filters are being applied,  
and  $\lambda$  is a constant to be determined experimentally  
( $\lambda = 1$  was used by Liu et al.).



If a zero-crossing  $\psi(x, y; \sigma_i)$  is found in the neighborhood defined by  $C(\sigma_i)$ , an arbitrary constant  $\kappa$  is assigned to a function  $S_i(x, y)$ :

$$S_i(x, y) = \begin{cases} \kappa & \text{if } \psi(x, y; \sigma_i) \in C(\sigma_i) \\ 0 & \text{otherwise,} \end{cases} \quad (5.24)$$

where the subscript  $i$  corresponds to the  $i^{th}$  scale  $\sigma_i$ .



Applying Equations 5.24 and 5.24 to the set of zero-crossings detected, a set of adjusted zero-crossing maps is obtained:

$$\{S_1(x, y), S_2(x, y), \dots, S_N(x, y)\},$$

$N$  is the number of scales.

The adjusted zero-crossing maps are used to construct the zero-crossing stability map  $\chi(x, y)$  as

$$\chi(x, y) = \sum_{i=1}^N S_i(x, y). \quad (5.25)$$

The values of  $\chi(x, y)$  are, in principle, a measure of boundary stability through the filter scales.



According to the spatial-coincidence assumption, a true boundary should be high in contrast and have relatively large  $\chi$  values at the corresponding locations.

Furthermore, there should be no other edges within a given neighborhood.

Thus, if in a neighborhood of  $\chi(x, y)$ , nonzero stability map values exist only along the orientation of a local segment of the stability map that crosses  $(x, y)$ , then  $\chi(x, y)$  may be considered to signify a stable edge pixel at  $(x, y)$ .



Liu et al. proposed a relative stability index  $\mu(x, y)$  computed from the stability map where  $\chi(x, y) \neq 0$ , as follows.

In a neighborhood of  $\chi(x, y)$ , if  $m$  nonzero values are found,  $\chi(x, y)$  is relabeled as  $l_0$ , and the rest of  $\chi(x_k, y_k)$  are relabeled as  $l_k$ ,  $k = 1, \dots, m - 1$ ; see Figure 5.15.

In order to avoid using elements in the neighborhood that belong to the same edge, those  $\chi(x', y')$  having the same orientation as that of  $l_0$  are not included in the computation of  $\mu(x, y)$ .



Based upon these requirements, the relative stability index  $\mu(x, y)$  is defined as

$$\mu(x, y) = \frac{l_0}{\sum_{k=0}^{m-1} \rho_k l_k}, \quad (5.26)$$

$$\rho_k = \exp(-d_k^2), \quad d_k = \sqrt{(x - x_k)^2 + (y - y_k)^2},$$

and  $(x_k, y_k)$  are the locations of  $l_k$ .

It should be noted that  $0 < \mu(x, y) \leq 1$ , and that the value of  $\mu(x, y)$  is governed by the geometrical distribution of the neighboring stability index values.

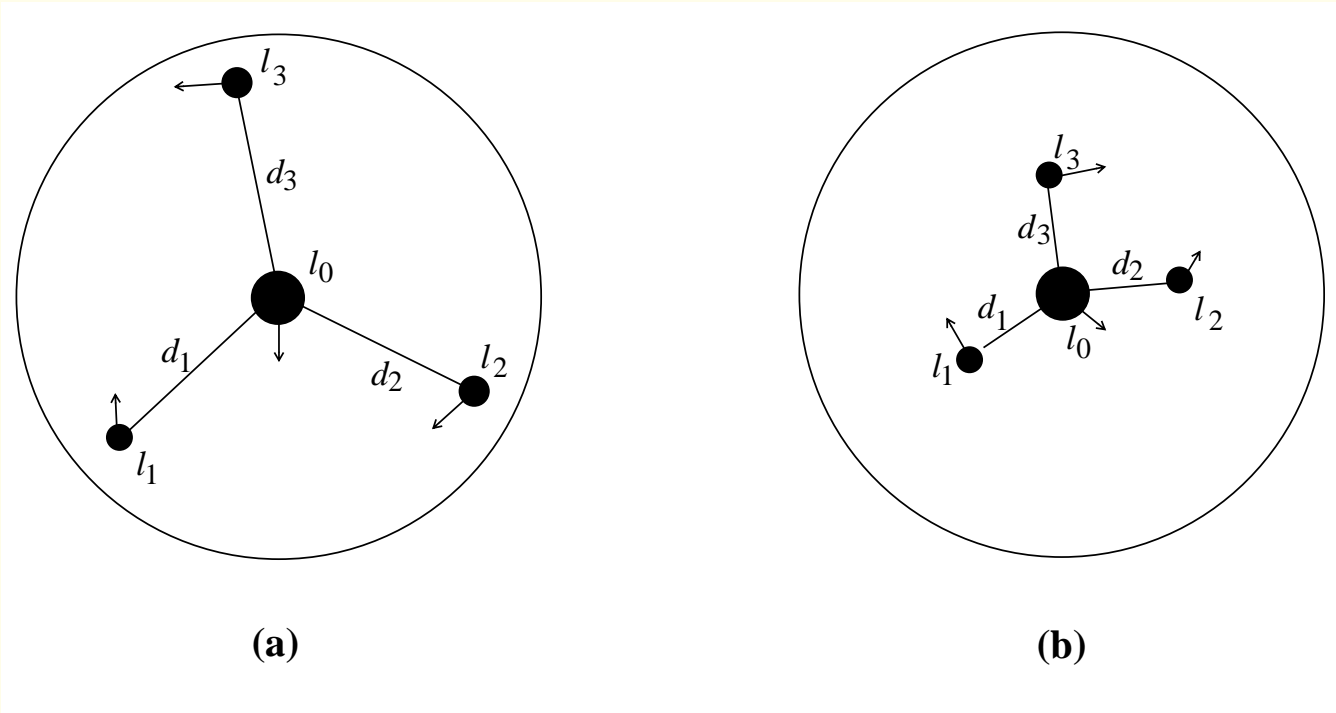


Figure 5.15: A case where three zero-crossings  $\{l_1, l_2, l_3\}$  are found in a neighborhood of a zero-crossing  $l_0$ .  $d_i$  indicates the distance from  $l_i$  to  $l_0$ . The arrows indicate the directions of the zero-crossings. (a) The neighboring zero-crossings are far apart from  $l_0$ , imposing a low penalty to the zero-crossing associated with  $l_0$ . (b) The neighboring zero-crossings are close to  $l_0$ , imposing a high penalty to the zero-crossing associated with  $l_0$ . Reproduced with permission from Z.-Q. Liu, R.M. Rangayyan, and C.B. Frank, “Statistical analysis of collagen alignment in ligaments by scale-space analysis”, *IEEE Transactions on Biomedical Engineering*, 38(6):580–588, 1991. © IEEE.



## Stability of zero-crossings:

In image analysis based upon zero-crossings, it is desirable to be able to distinguish real zero-crossings from false ones.

Clark proposed that zero-crossings may be classified as real

if  $\xi(x, y) < 0$  and

false if  $\xi(x, y) > 0$ ,

where  $\xi(x, y) = \nabla[\nabla^2 p(x, y)] \bullet \nabla p(x, y)$ ,

where  $\bullet$  denotes the dot product.



$p(x, y)$  is a smoothed version of the given image,

such as  $p(x, y) = g(x, y; \sigma) * f(x, y)$ ,

$$\nabla p(x, y) = \left[ \frac{\partial p}{\partial x}, \frac{\partial p}{\partial y} \right]^T ,$$

$$\nabla[\nabla^2 p(x, y)] = \left[ \frac{\partial^3 p}{\partial x^3} + \frac{\partial^3 p}{\partial x \partial y^2}, \quad \frac{\partial^3 p}{\partial x^2 \partial y} + \frac{\partial^3 p}{\partial y^3} \right]^T .$$

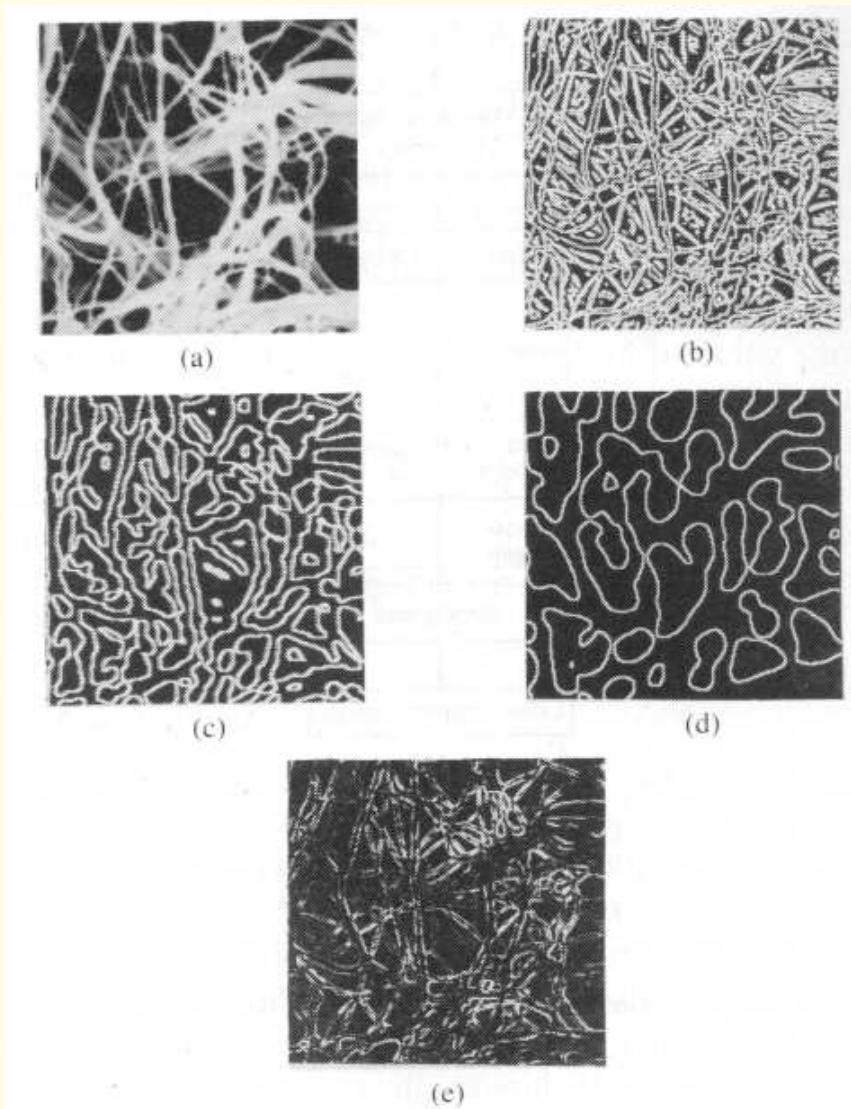


Figure 5.16: (a) SEM image of a ligament scar-tissue sample. (b) – (d) Zero-crossing locations detected using the LoG operator with  $\sigma = 1, 4$ , and  $8$  pixels, respectively. (e) The stability map, depicting the major edges present in the image. Reproduced with permission from Z.-Q. Liu, R.M. Rangayyan, and C.B. Frank, “Statistical analysis of collagen alignment in ligaments by scale-space analysis”, *IEEE Transactions on Biomedical Engineering*, 38(6):580–588, 1991. © IEEE.



### 5.3.4 Canny's method for edge detection

Canny proposed an approach for edge detection based upon three criteria for good edge detection, multidirectional derivatives, multiscale analysis, and optimization procedures.

The three criteria relate to

- low probabilities of false edge detection and missing real edges, represented in the form of an SNR;
- good localization, represented by the RMS distance of the detected edge from the true edge; and
- the production of a single output for a single edge, represented by the distance between the adjacent maxima in the output.



A basic filter was approximated by the first derivative of a Gaussian.

Multiscale analysis and directional filters were incorporated to facilitate efficient detection of edges at all orientations and scales, including adaptive thresholding with hysteresis.

Canny's method selectively evaluates a directional derivative across each edge;

avoids derivatives at other angles that would not contribute to edge detection but increase the effects of noise.



### 5.3.5 Fourier-domain methods for edge detection

Highpass filters may be applied in the Fourier-domain to extract the edges in the given image.

However, the inclusion of all of the high-frequency components present in the image could lead to noisy results.

Reduction of high-frequency noise: use bandpass filters.

Edges are often weak or blurred in images: enhancement of the corresponding frequency components would be desirable.



This argument leads us to the LoG filter: a combination of

the Laplacian, a high-frequency-emphasis filter with its gain quadratically proportional to frequency,

and a Gaussian lowpass filter.



### 5.3.6 *Edge linking*

Results of most methods for edge detection are discontinuous:

need to be processed further to link disjoint segments and obtain complete representations of the boundaries of ROIs.

Two principal properties that may be used to establish the similarity of edge pixels from gradient images:



- The strength of the gradient —  
a point  $(x', y')$  in a neighborhood of  $(x, y)$  is similar in gradient magnitude to the point  $(x, y)$  if

$$\|\mathbf{G}(x, y) - \mathbf{G}(x', y')\| \leq T, \quad (5.27)$$

where  $\mathbf{G}(x, y)$  is the gradient vector of the given image  $f(x, y)$  at  $(x, y)$  and  $T$  is a threshold.



- The direction of the gradient —  
a point  $(x', y')$  in a neighborhood of  $(x, y)$  is similar in gradient direction to the point  $(x, y)$  if

$$|\alpha(x, y) - \alpha(x', y')| \leq A, \quad (5.28)$$

$$\alpha(x, y) = \angle \mathbf{G}(x, y) = \tan^{-1} \left\{ \frac{\partial f(x, y)/\partial y}{\partial f(x, y)/\partial x} \right\},$$

where  $A$  is a threshold.

$3 \times 3$  or  $5 \times 5$  neighborhoods may be used for checking pixels for similarity in their gradients as above.

Further processing steps may include linking of edge segments separated by small breaks and deleting isolated short segments.



## 5.4 Segmentation and Region Growing

Dividing an image into regions that could correspond to structural units, objects of interest, or ROIs is an important prerequisite for most techniques for image analysis.

Four main categories of image segmentation techniques:

- thresholding techniques,
- boundary-based methods,
- region-based methods, and
- hybrid techniques that combine boundary and region criteria.



## Thresholding methods:

Based upon the assumption that all pixels whose values lie within a certain range belong to the same class.

The threshold may be determined based upon the valleys in the histogram of the image.

Because thresholding algorithms are solely based upon pixel values and neglect all of the spatial information in the image, their accuracy of segmentation is limited;

furthermore, thresholding algorithms do not cope well with noise or blurring at object boundaries.



## Boundary-based techniques:

Use the property that, usually, pixel values change rapidly at the boundaries between regions.

The methods start by detecting intensity discontinuities lying at the boundaries between objects and their backgrounds, typically through a gradient operation.

High values of the output provide candidate pixels for region boundaries, which must then be processed to produce closed curves representing the boundaries between regions.



## Region-based methods:

Rely on the postulate that neighboring pixels within a region have similar values.

*Region splitting and merging:* subdivide the given image into a set of arbitrary, disjoint regions, and then merge and/or split the regions in an attempt to satisfy some prespecified conditions.

*Region growing:* group similar pixels into regions.

Different homogeneity criteria will lead to regions with different characteristics.



### 5.4.1 *Optimal thresholding*

Suppose it is known *a priori* that the image consists of only two principal brightness levels with prior probabilities  $P_1$  and  $P_2$ .

Consider the situation where natural variations or noise modify the two gray levels to distributions represented by Gaussian PDFs  $p_1(x)$  and  $p_2(x)$ ;  $x$  represents the gray level.



The PDF of the image gray levels is then

$$p(x) = P_1 p_1(x) + P_2 p_2(x) \quad (5.29)$$

$$= \frac{P_1}{\sqrt{2\pi}\sigma_1} \exp\left[-\frac{(x - \mu_1)^2}{2\sigma_1^2}\right] + \frac{P_2}{\sqrt{2\pi}\sigma_2} \exp\left[-\frac{(x - \mu_2)^2}{2\sigma_2^2}\right],$$

where  $\mu_1$  and  $\mu_2$  are the means of the two regions, and

$\sigma_1$  and  $\sigma_2$  are their standard deviations.



Let  $\mu_1 < \mu_2$ .

Suppose that the dark regions in the image correspond to the background, and the bright regions to the objects of interest.

All pixels below a threshold  $T$ : belong to the background;

all pixels above  $T$ : belong to the object of interest.

The probability of erroneous classification is then

$$P_e(T) = P_1 \int_T^{\infty} p_1(x) dx + P_2 \int_{-\infty}^T p_2(x) dx. \quad (5.30)$$



To find the optimal threshold, we may differentiate  $P_e(T)$  with respect to  $T$  and equate the result to zero, which leads to

$$P_1 p_1(T) = P_2 p_2(T). \quad (5.31)$$



Applying this result to the Gaussian PDFs gives (after taking logarithms and some simplification) the quadratic equation

$$AT^2 + BT + C = 0, \quad (5.32)$$

where

$$A = \sigma_1^2 - \sigma_2^2,$$

$$B = 2(\mu_1\sigma_2^2 - \mu_2\sigma_1^2),$$

$$C = \sigma_1^2\mu_2^2 - \sigma_2^2\mu_1^2 + 2\sigma_1^2\sigma_2^2 \ln \left( \frac{\sigma_2 P_1}{\sigma_1 P_2} \right). \quad (5.33)$$



If  $\sigma_1^2 = \sigma_2^2 = \sigma^2$ , a single threshold may be used, given by

$$T = \frac{\mu_1 + \mu_2}{2} + \frac{\sigma^2}{\mu_1 - \mu_2} \ln \left( \frac{P_2}{P_1} \right). \quad (5.34)$$

If the two prior probabilities are equal ( $P_1 = P_2$ ),

or if the variance is zero ( $\sigma = 0$ ),

the optimal threshold is equal to the average of the two means.



## Thresholding using boundary characteristics:

The number of pixels covered by the objects of interest to be segmented from an image is almost always a small fraction of the total number of pixels in the image:

gray-level histogram of image likely to be almost unimodal.

Histogram may be made closer to bimodal if only the pixels on or near boundaries of object regions are considered.



The selection and characterization of the edge or boundary pixels may be achieved by using gradient and Laplacian operators as

$$b(x, y) = \begin{cases} 0 & \text{if } \nabla_f(x, y) < T, \\ L_+ & \text{if } \nabla_f(x, y) \geq T \text{ and } \nabla_f^2(x, y) \geq 0, \\ L_- & \text{if } \nabla_f(x, y) \geq T \text{ and } \nabla_f^2(x, y) < 0, \end{cases} \quad (5.35)$$

where  $T$  is a threshold;  $\nabla_f(x, y)$  is a gradient and

$\nabla_f^2(x, y)$  is the Laplacian of the given image  $f(x, y)$ ;

and  $0, L_+, L_-$  represent three distinct gray levels.



In the resulting image:

the pixels that are not on an edge are set to zero,

the pixels on the darker sides of edges are set to  $L_+$ ,

and the pixels on the lighter sides of edges are set to  $L_-$ .

This information may be used not only to detect objects and edges, but also to identify the leading and trailing edges of objects (with reference to the scanning direction).



### 5.4.2 *Region-oriented segmentation of images*

Let  $R$  represent the region spanning the entire given image.

Segmentation may be viewed as a process that partitions  $R$  into

$n$  subregions  $R_1, R_2, \dots, R_n$  such that:

- $\bigcup_{i=1}^n R_i = R$ ; the union of all of the regions detected spans the entire image (every pixel must belong to a region);
- $R_i$  is a connected region,  $i = 1, 2, \dots, n$ ;
- $R_i \cap R_j = \emptyset \forall i, j, i \neq j$  (that is, the regions are disjoint);



- $\mathcal{P}(R_i) = \text{TRUE}$ , for  $i = 1, 2, \dots, n$  (for example, all pixels within a region have the same intensity);
- $\mathcal{P}(R_i \cup R_j) = \text{FALSE} \quad \forall i, j, i \neq j$  (for example, the intensities of the pixels in different regions are different);

$\mathcal{P}(R_i)$  is a logical predicate defined over the points in  $R_i$ ;

$\emptyset$  is the null set.



A simple algorithm for region growing by pixel aggregation based upon the similarity of a local property is as follows:

- Start with a *seed* pixel (or a set of seed pixels).
- Append to each pixel in the region those of its 4-connected or 8-connected neighbors that have properties (gray level, color) that are similar to those of the seed.
- Stop when the region cannot be grown any further.

The results of an algorithm as above depend upon the procedure used to select the seed pixels and the measures of similarity or inclusion criteria used.

The results may also depend upon the method used to traverse the image; that is, the sequence in which neighboring pixels are checked for inclusion.



### 5.4.3 *Splitting and merging of regions*

Divide the given image arbitrarily into a set of disjoint regions;

split and/or merge the regions using conditions or predicates  $\mathcal{P}$ .

A general split/merge procedure is as follows:

Assuming the image to be square, subdivide the entire image  $R$  successively into smaller and smaller quadrant regions such that, for any region  $R_i$ ,  $\mathcal{P}(R_i) = \text{TRUE}$ .



In other words:

if  $\mathcal{P}(R) = \text{FALSE}$ , divide the image into quadrants;

if  $\mathcal{P}$  is *FALSE* for any quadrant, subdivide that quadrant into subquadrants.

Iterate the procedure until no further changes are made, or a stopping criterion is reached.

The splitting technique may be represented as a quadtree.

Difficulties could exist in selecting an appropriate predicate  $\mathcal{P}$ .



Because the splitting procedure could result in adjacent regions that are similar, a merging step would be required:

Merge two adjacent regions  $R_i$  and  $R_k$

if  $\mathcal{P}(R_i \cup R_k) = \text{TRUE}$ .

Iterate until no further merging is possible.



#### 5.4.4 *Region growing using an additive tolerance*

A commonly used region-growing scheme is pixel aggregation.

The method compares the properties of spatially connected neighboring pixels with those of the seed pixel;

the properties used are determined by homogeneity criteria.

For intensity-based image segmentation, the simplest property is the pixel gray level.



The term “additive tolerance level” stands for the permitted absolute gray-level difference between the neighboring pixels and the seed pixel:

a neighboring pixel  $f(m, n)$  is appended to the region if its absolute gray-level difference with respect to the seed pixel is within the additive tolerance level  $T$ :

$$|f(m, n) - \text{seed}| \leq T. \quad (5.36)$$



|   | 1   | 2   | 3   | 4   | 5   |
|---|-----|-----|-----|-----|-----|
| 1 | 100 | 101 | 101 | 100 | 101 |
| 2 | 100 | 127 | 126 | 128 | 100 |
| 3 | 100 | 124 | 128 | 127 | 100 |
| 4 | 100 | 124 | 125 | 126 | 101 |
| 5 | 101 | 100 | 100 | 101 | 102 |

(a)

|   | 1   | 2    | 3   | 4   | 5   |
|---|-----|------|-----|-----|-----|
| 1 | 100 | 101  | 101 | 100 | 101 |
| 2 | 100 | seed | 126 | 128 | 100 |
| 3 | 100 | 124  | 128 | 127 | 100 |
| 4 | 100 | 124  | 125 | 126 | 101 |
| 5 | 101 | 100  | 100 | 101 | 102 |

(b)

|   | 1   | 2   | 3    | 4   | 5   |
|---|-----|-----|------|-----|-----|
| 1 | 100 | 101 | 101  | 100 | 101 |
| 2 | 100 | 127 | 126  | 128 | 100 |
| 3 | 100 | 124 | seed | 127 | 100 |
| 4 | 100 | 124 | 125  | 126 | 101 |
| 5 | 101 | 100 | 100  | 101 | 102 |

(c)

|   | 1   | 2   | 3    | 4   | 5   |
|---|-----|-----|------|-----|-----|
| 1 | 100 | 101 | 101  | 100 | 101 |
| 2 | 100 | 127 | 126  | 128 | 100 |
| 3 | 100 | 124 | seed | 127 | 100 |
| 4 | 100 | 124 | 125  | 126 | 101 |
| 5 | 101 | 100 | 100  | 101 | 102 |

(d)

Figure 5.17: Example of additive-tolerance region growing using different seed pixels ( $T = 3$ ). (a) Original image. (b) The result of region growing (shaded in black) with the seed pixel at  $(2, 2)$ . (c) The result of region growing with the seed pixel at  $(3, 3)$ . (d) The result of region growing with the running-mean algorithm or the “current center pixel” method using any seed pixel within the highlighted region. Figure courtesy of L. Shen.



In order to overcome the dependence of the region on the seed pixel selected, the following modified criterion could be used to determine if a neighboring pixel should be included:

the gray level of a neighboring pixel is compared with the mean gray level, called the *running mean*  $\mu_{R_c}$ , of the region being grown at its current stage,  $R_c$ .

$$|f(m, n) - \mu_{R_c}| \leq T, \quad (5.37)$$

$$\mu_{R_c} = \frac{1}{N_c} \sum_{(m,n) \in R_c} f(m, n), \quad (5.38)$$

where  $N_c$  is the number of pixels in  $R_c$ .



Shen suggested the use of the “current center” pixel as the reference instead of the seed pixel that was used to commence the region-growing procedure.

After the pixel  $C$  is appended to the region, its neighbors (marked as  $N_i, i = 1, 2, \dots, 8$ ) would be checked for inclusion in the region, using

$$|N_i - C| \leq T. \quad (5.39)$$

The pixel  $C$  is called the current center pixel.

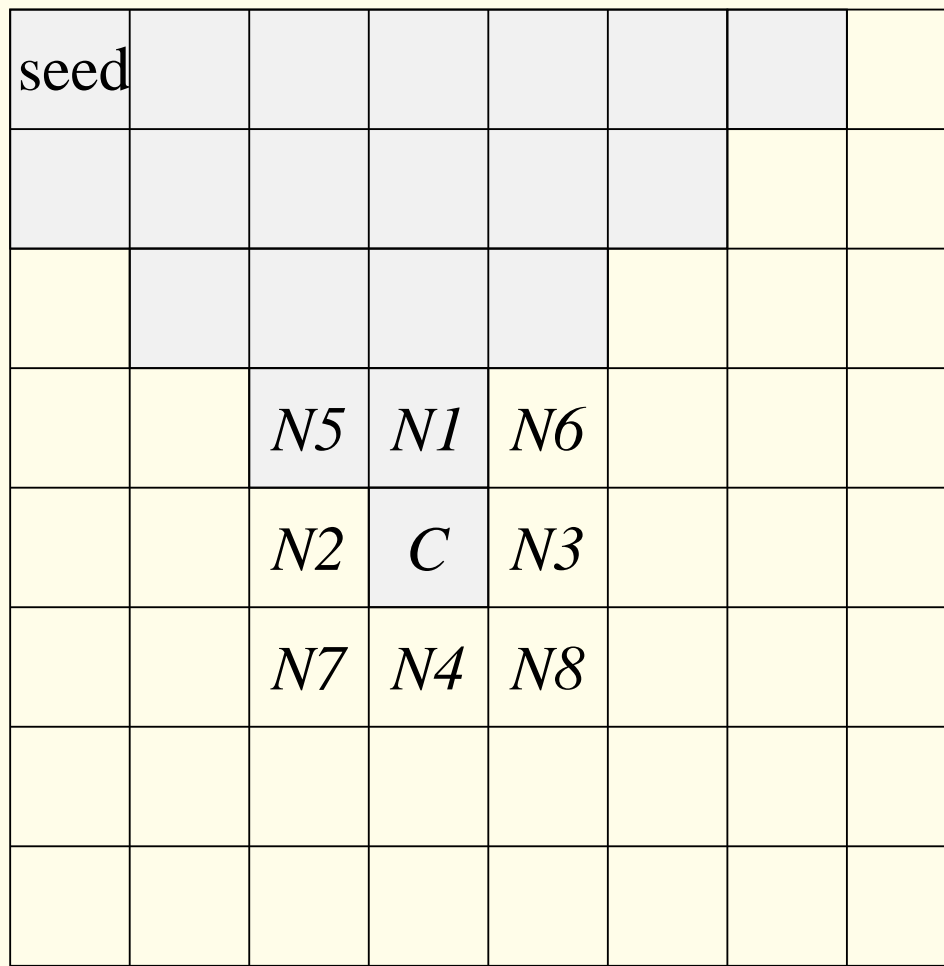


Figure 5.18: Illustration of the concept of the “current center pixel” in region growing. Figure courtesy of L. Shen.



#### 5.4.5 *Region growing using a multiplicative tolerance*

A relative difference is employed, based upon a

*multiplicative tolerance level  $\tau$ :*

$$\frac{|f(m, n) - \mu_{R_c}|}{\mu_{R_c}} \leq \tau \quad (5.40)$$

or

$$2 \frac{|f(m, n) - \mu_{R_c}|}{f(m, n) + \mu_{R_c}} \leq \tau. \quad (5.41)$$

$f(m, n)$ : gray level of the current pixel being checked for inclusion.



$\mu_{R_c}$  could stand for the original seed pixel value, the current center pixel value, or the running-mean gray level.

The two equations above are comparable to the definitions of simultaneous contrast.



#### 5.4.6 *Analysis of region growing in the presence of noise*

Assume that the given image  $\mathbf{g}$  may be modeled as an ideal image  $\mathbf{f}$  plus a noise image  $\boldsymbol{\eta}$ ;

$\mathbf{f}$  consists of a series of strictly uniform, disjoint, or nonoverlapping regions  $R_i, i = 1, 2, \dots, k$ ;

and  $\boldsymbol{\eta}$  includes their corresponding noise parts  $\eta_i, i = 1, 2, \dots, k$ .



The image may be expressed as

$$\mathbf{g} = \mathbf{f} + \boldsymbol{\eta}, \quad (5.42)$$

where

$$\mathbf{f} = \bigcup_i R_i, \quad i = 1, 2, \dots, k, \quad (5.43)$$

and

$$\boldsymbol{\eta} = \bigcup_i \eta_i, \quad i = 1, 2, \dots, k. \quad (5.44)$$



A strictly uniform region  $R_i$  is composed of a set of connected pixels  $f(m, n)$  at positions  $(m, n)$  whose values equal a constant  $\kappa_i$ , that is,

$$R_i = \{ (m, n) \mid f(m, n) = \kappa_i \}. \quad (5.45)$$

The set of regions  $R_i, i = 1, 2, \dots, k$ , is what we expect to obtain as the result of segmentation.



Suppose that the noise parts  $\eta_i$ ,  $i = 1, 2, \dots, k$ , are composed of white noise with zero mean and standard deviation  $\sigma_i$ ; then,

$$\mathbf{g} = \bigcup_i (R_i + \eta_i), \quad i = 1, 2, \dots, k, \quad (5.46)$$

$$\mathbf{f} = \bigcup_i R_i = \mathbf{g} - \bigcup_i \eta_i, \quad i = 1, 2, \dots, k. \quad (5.47)$$



As a special case, when all the noise components have the same standard deviation  $\sigma$ , that is,

$$\sigma_1 = \sigma_2 = \dots = \sigma_k = \sigma \quad (5.48)$$

and

$$\eta_1 \simeq \eta_2 \simeq \dots \simeq \eta_k \simeq \eta, \quad (5.49)$$

where the symbol  $\simeq$  represents statistical similarity,  
the image  $\mathbf{f}$  may be described as

$$\mathbf{g} \simeq \bigcup_i R_i + \eta, \quad i = 1, 2, \dots, k, \quad (5.50)$$

and

$$\mathbf{f} = \bigcup_i R_i \simeq \mathbf{g} - \eta; \quad i = 1, 2, \dots, k. \quad (5.51)$$



Additive-tolerance region growing is well-suited for segmentation of this special type of image, and an additive tolerance level solely determined by  $\sigma$  may be used globally over the image.

However, such special cases are rare in real images.

A given image generally has to be modeled, as in Equation 5.46,

where multiplicative-tolerance region growing may be more suitable, with the expectation that a global multiplicative tolerance level can be derived for all of the regions in the given image.



Because the multiplicative tolerance level could be made a function of  $\frac{\sigma_i}{\kappa_i}$  that is directly related to the SNR,

which can be defined as  $10 \log_{10} \frac{\kappa_i^2}{\sigma_i^2} dB$  for each region  $R_i$ ,

such a global tolerance level can be found if

$$\frac{\sigma_1}{\kappa_1} = \frac{\sigma_2}{\kappa_2} = \dots = \frac{\sigma_k}{\kappa_k}. \quad (5.52)$$



#### **5.4.7 Iterative region growing with multiplicative tolerance**

Shen et al. proposed using the information contained within a region as well as its relationship with the surrounding background to determine the appropriate tolerance level to grow a region.

Such information could be represented by a set of features characterizing the region and its background.

With increasing tolerance levels obtained using a certain step size, it could be expected that the values of the feature set at successive tolerance levels will be either the same or similar.



Suppose that the feature set includes  $M$  features; the feature vector  $\mathbf{V}_k$  at the tolerance level  $k$  is

$$\mathbf{V}_k = [V_{k,1}, V_{k,2}, \dots, V_{k,M}]^T. \quad (5.53)$$

The minimum normalized distance  $d_{\min}$  between the feature vectors at successive tolerance levels could be utilized to select the final region:

$$d_{\min} = \min_k[d_k] = \min_k \left[ \sum_{m=1}^M \frac{(V_{k+1,m} - V_{k,m})^2}{\left( \frac{V_{k+1,m} + V_{k,m}}{2} \right)^2} \right]^{\frac{1}{2}}, \quad (5.54)$$

$k = 1, 2, \dots, K - 1$ ;  $K$  = number of tolerance values used.

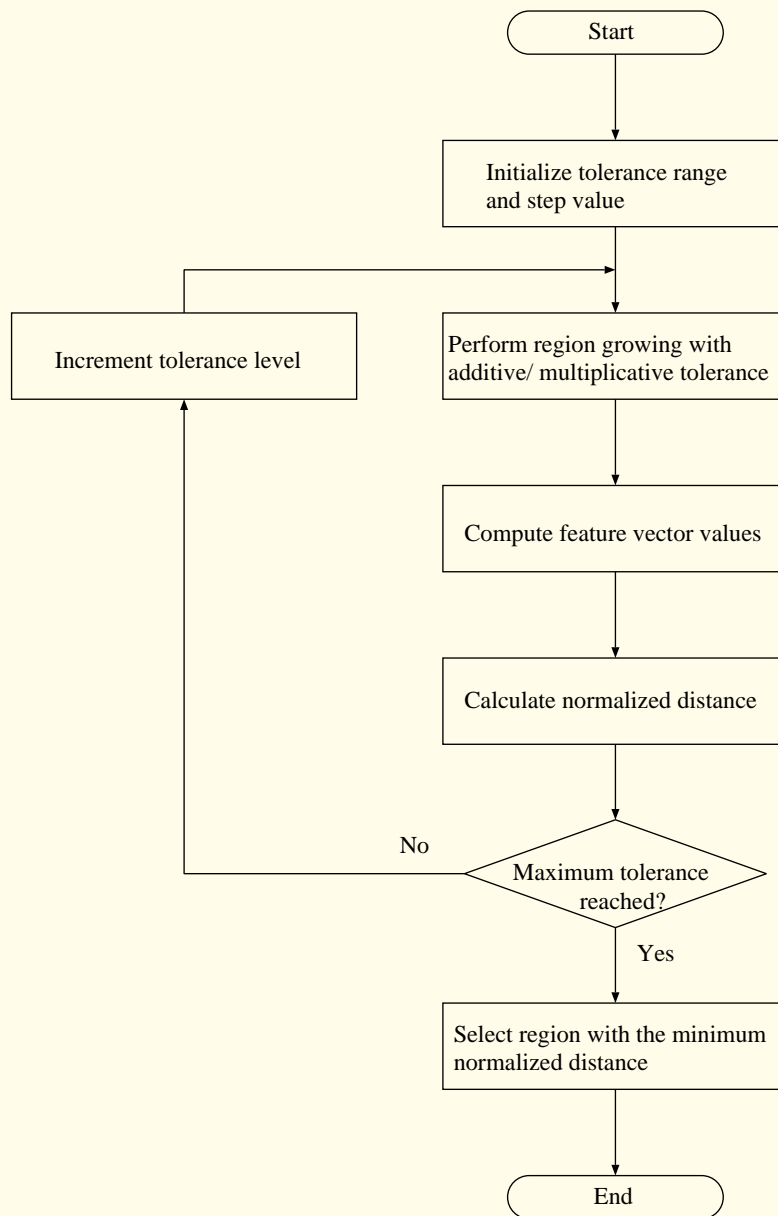


Figure 5.19: Flowchart of the iterative, multitolerance, region-growing algorithm. Figure courtesy of L. Shen.

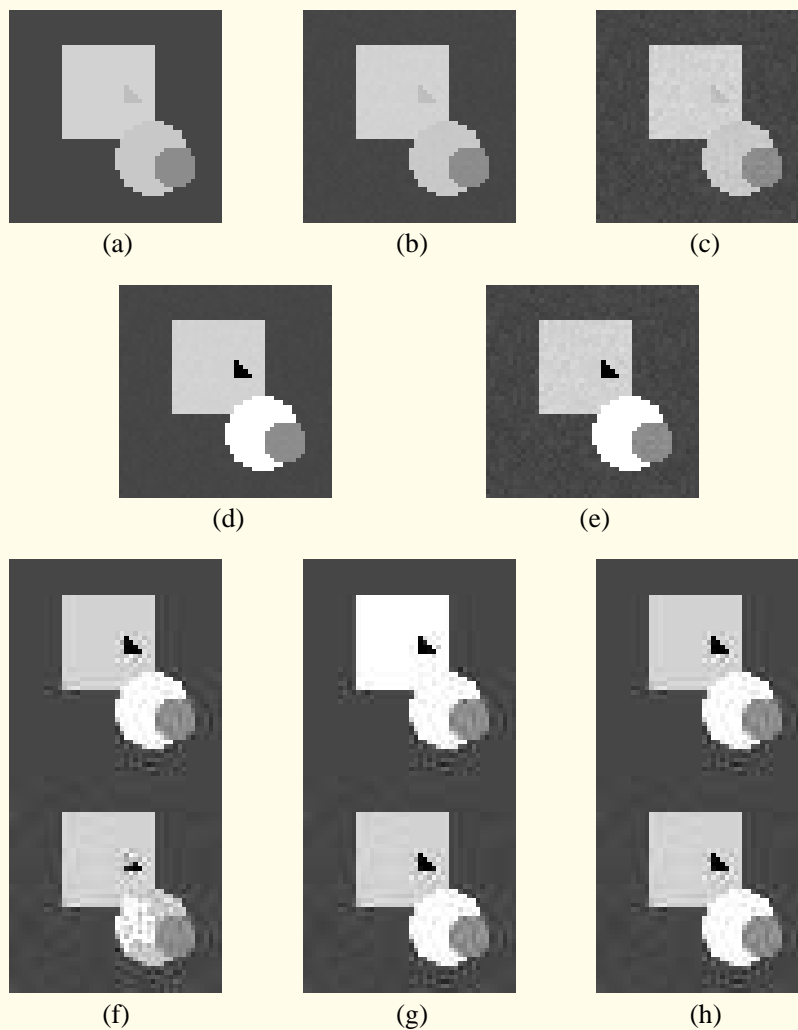


Figure 5.20: Demonstration of the multiplicative-tolerance region-growing algorithm. (a) An ideal test image. (b) Test image with white noise ( $\text{SNR} = 30 \text{ dB}$ ). (c) Test image with white noise ( $\text{SNR} = 20 \text{ dB}$ ). (d) Regions grown with fixed  $\tau = 0.02$  for the image in (b). (e) Regions grown with fixed  $\tau = 0.05$  for the image in (c). (f) Regions grown with fixed  $\tau = 0.02$ . (g) Regions grown with fixed  $\tau = 0.05$ . (h) Regions grown with the iterative algorithm with adaptive  $\tau$ . The original composite images in (f) – (h) were obtained by combining the images in (b) at the top and (c) at the bottom. The detected regions are highlighted in black for the triangle and in white for the occluded circle in figures (d) – (h). Figure courtesy of L. Shen.



#### 5.4.8 *Region growing based upon the human visual system*

The HVS is a nonlinear system with a large dynamic range and a bandpass filter behavior.

The filtering property is characterized by the reciprocal of the threshold contrast  $C_T$  that is a function of both the frequency  $u$  and background luminance  $L$ .

The smallest luminance difference that a human observer can detect when an object of a certain size appears with a certain background luminance level is defined as the JND:

$$JND = L C_T. \quad (5.55)$$



A typical variation of threshold contrast as a function of the background luminance, known as the Weber-Fechner relationship, is graphically depicted in Figure 5.21.

The curve can be typically divided into two asymptotic regions:

the Rose – de Vries region where  $C_T$  decreases when the background luminance increases, with

$$C_T \propto \frac{1}{L^{0.5}}, \quad (5.56)$$



and the Weber region where  $C_T$  is independent of the background luminance, and the relationship obeys Weber's law:

$$C_T = \frac{JND}{L} = C_0 = \text{constant.} \quad (5.57)$$

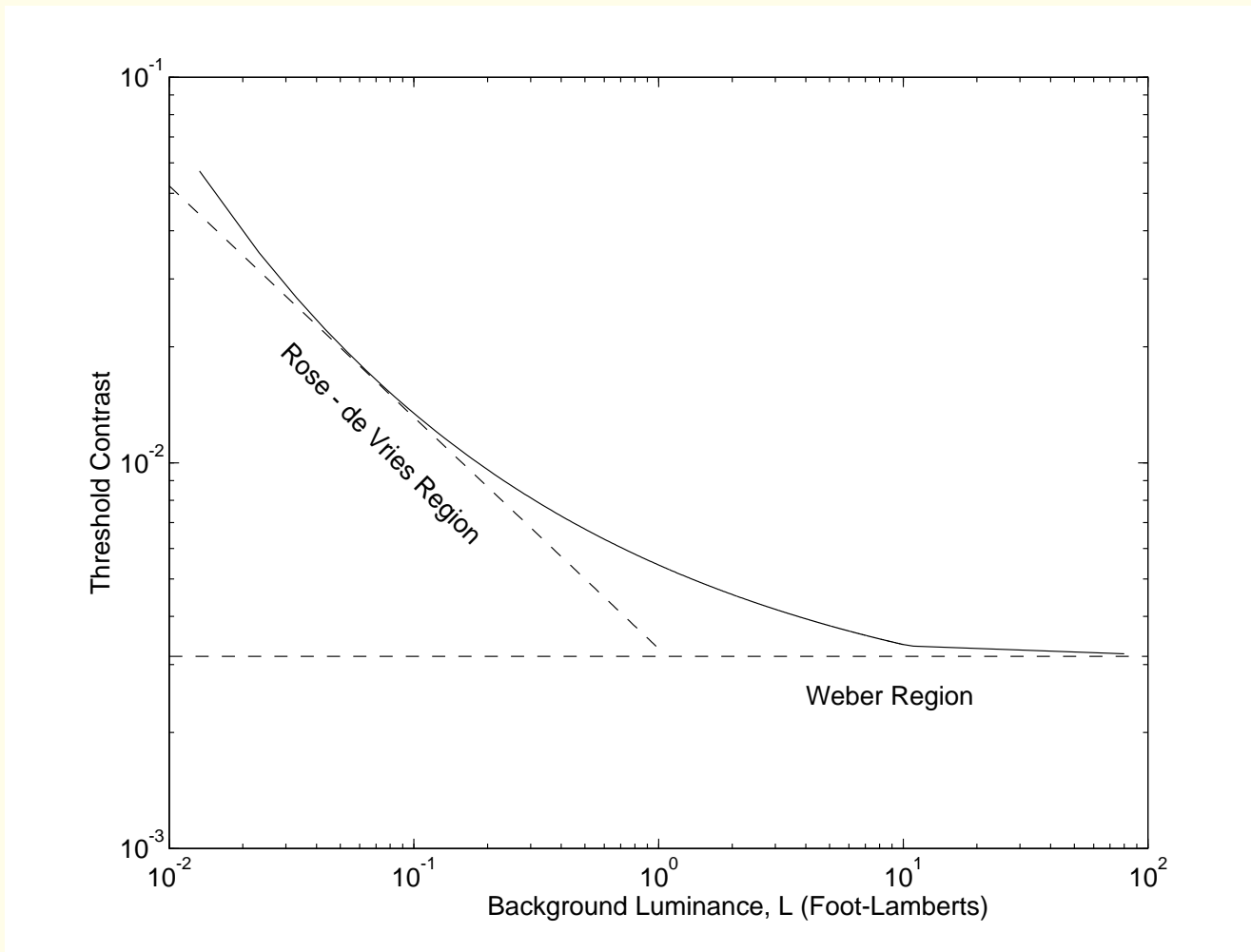


Figure 5.21: A typical threshold contrast curve, known as the Weber-Fechner relationship. Figure courtesy of L. Shen.



It is possible to determine the JND as a function of the background gray level from psychophysical experiments.

In one such study conducted by Shen, a test was set up with various combinations of foreground and background levels using an image containing a series of square boxes,

with the width ranging from 1 pixel to 16 pixels and a fixed space of 7 pixels in between the boxes.

Also included was a series of groups of four, vertical, 64-pixel lines, with the width ranging from 1 pixel to 6 pixels and a spacing of the same number of pixels between any two adjacent lines, and a fixed gap of 12 pixels in between the groups of lines.



Based upon the visibility or detection of up to the 2-pixel-wide square and line group on a monitor, a relationship between the JND and the background gray level was obtained (Figure 5.23).

To obtain a general JND relation, a large number of trials involving the participation of a large number of subjects is necessary, with strict control of the experimental environment.

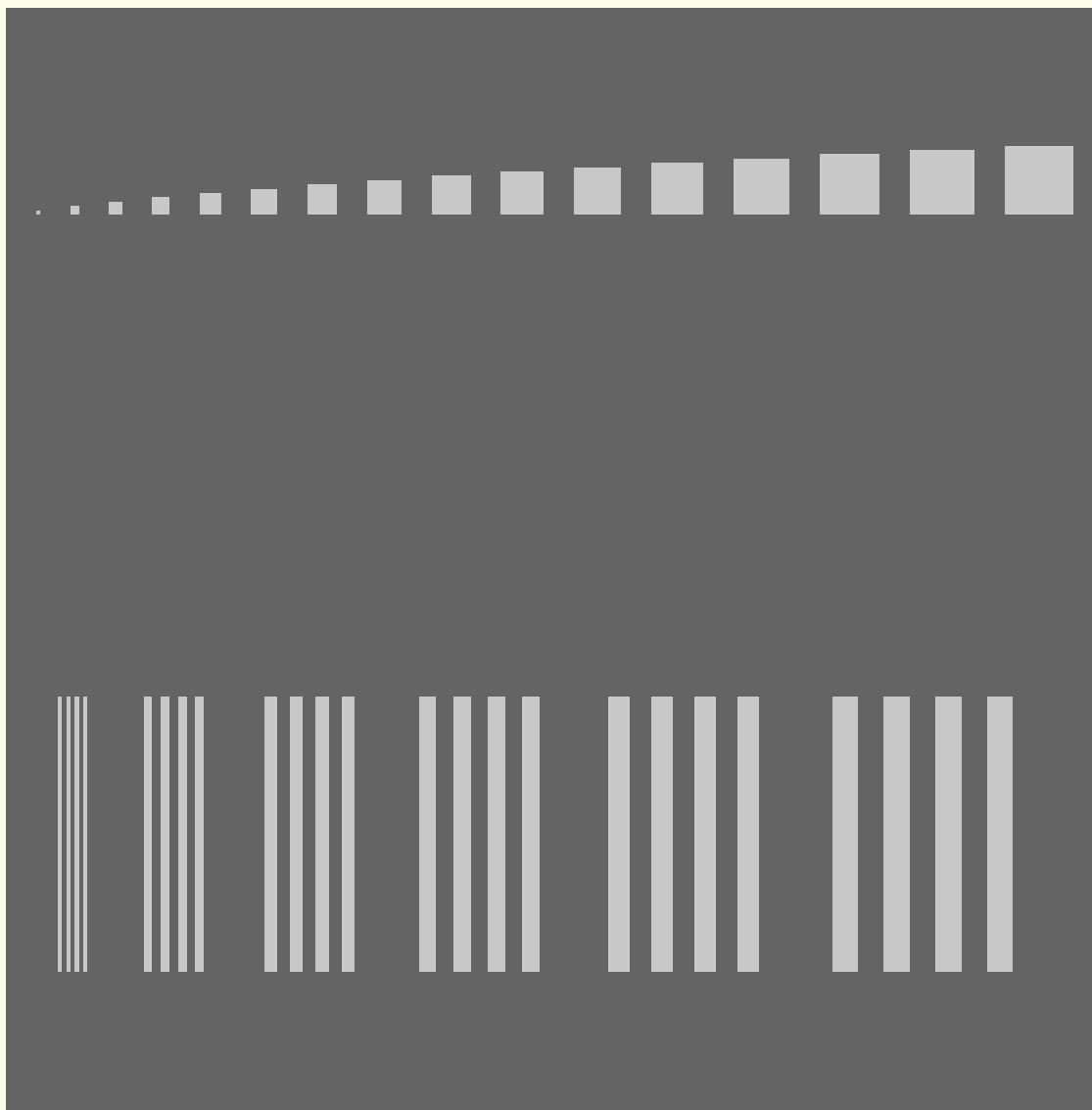


Figure 5.22: Visual test image for determination of the JND as a function of background gray level (foreground is 200 and background is 100 in the displayed image). Figure courtesy of L. Shen.

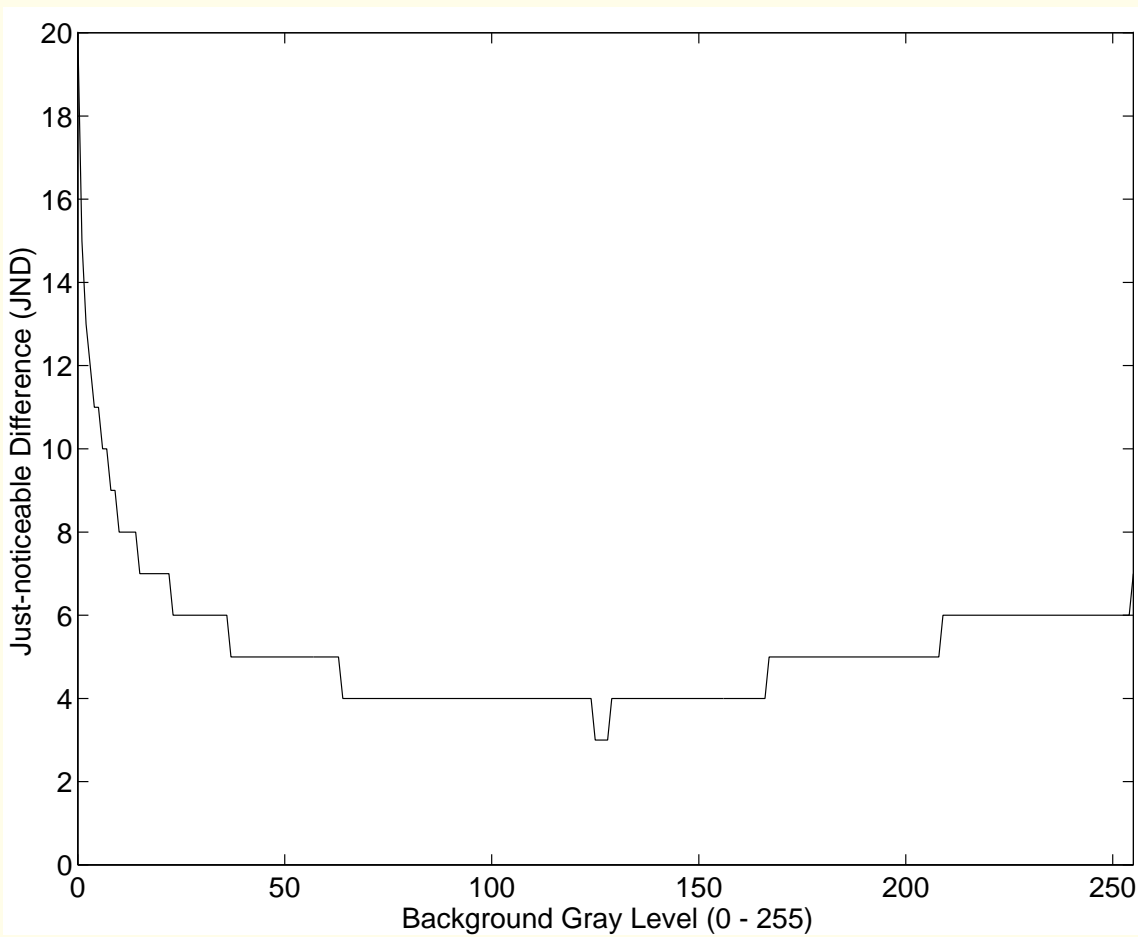


Figure 5.23: A relationship between the JND and the background gray level based upon a psychophysical experiment. Figure courtesy of L. Shen.



The HVS-based region-growing algorithm starts with a 4-connected neighbor-pixel grouping based upon the JND relationships of adjacent pixel gray levels.

The JND condition is defined as

$$|p_1 - p_2| \leq \min\{JND(p_1), JND(p_2)\}, \quad (5.58)$$

where  $p_1$  and  $p_2$  are two connected pixels.



This step is followed by the removal of small regions by merging with a connected region with the minimum mean gray-level difference.

Then, merging of connected regions is performed if any of two neighboring regions meet the JND condition, with  $p_1$  and  $p_2$  representing the regions' mean values.

The procedure is iterated until no neighboring region satisfies the JND condition.

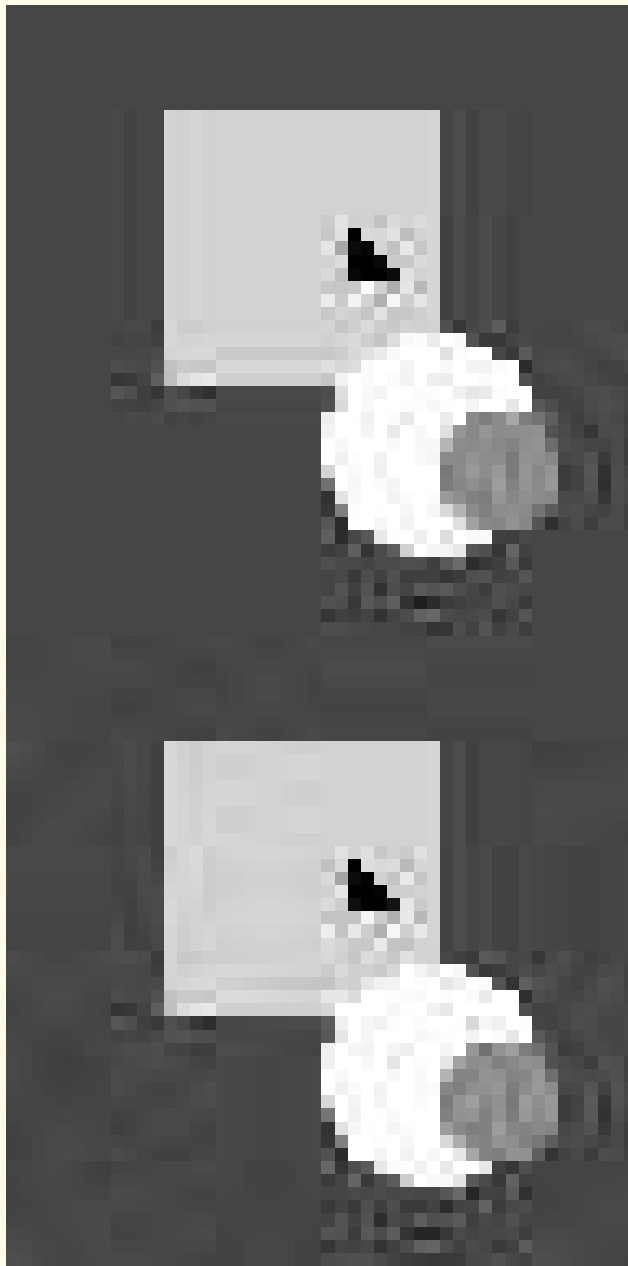


Figure 5.24: Results of the HVS-based region-growing algorithm with the same test image as in Figure 5.20 (f). Figure courtesy of L. Shen.



#### 5.4.9 *Detection of calcifications by multitolerance region growing*

Shen et al. reported on a method to detect and classify mammographic calcifications based upon a multitolerance region-growing procedure, shape analysis, and neural networks.

The calcification detection algorithm consists of three steps:

1. selection of seed pixels;
2. detection of potential calcification regions; and
3. confirmation of calcification regions.

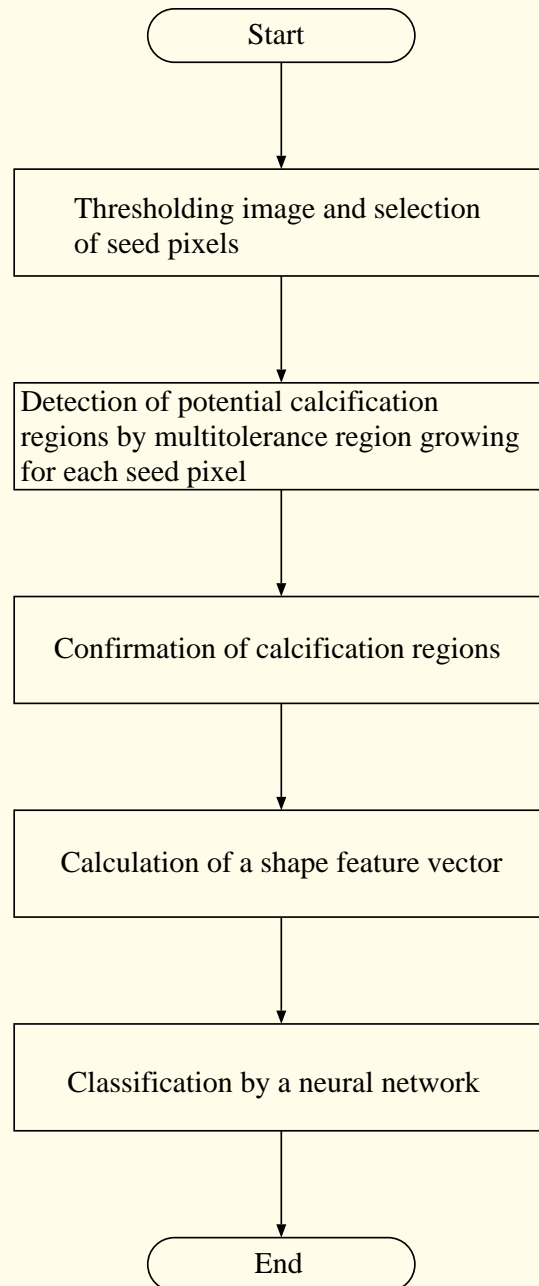


Figure 5.25: Flowchart of a method for the detection and classification of mammographic calcifications. Figure courtesy of L. Shen.



## Selection of seed pixels:

Calcifications in mammograms are relatively bright due to the higher X-ray attenuation coefficient (or density) of calcium as compared with other normal breast tissues.

Every pixel with a value greater than the median gray level of the mammogram is identified as a potential seed pixel for the next two steps of calcification detection.

The pixels identified as above are processed in sequence by selecting the highest intensity pixel remaining, in raster-scan order,

as long the pixel has not been included in any of the regions already labeled as calcifications.



## Detection of potential calcification regions:

The algorithm starts a region-growing procedure with each seed pixel selected as above.

Every 4-connected neighbor  $f(m, n)$  of the pixels belonging to the region is checked for the following condition:

$$0.5(1+\tau)(R_{\max}+R_{\min}) \geq f(m, n) \geq 0.5(1-\tau)(R_{\max}+R_{\min}), \quad (5.59)$$

where  $R_{\max}$  and  $R_{\min}$  are the current maximum and minimum pixel values of the region being grown, and  $\tau$  is the growth tolerance.



The fractional tolerance value  $\tau$  for region growing is increased from 0.01 to 0.40 with a step size determined as the inverse of the seed-pixel's gray level.

A feature vector including

compactness, defined as  $c = 1 - 4\pi \frac{area}{perimeter^2}$ ,

the  $(x, y)$  coordinates of the centroid, and

the size or area in number of pixels,

is calculated for the region obtained at each tolerance level.



The normalized distance between the feature vectors for successive tolerance levels is computed.

The feature set with the minimum distance is selected as the final set, and the corresponding region considered to be a potential calcification region.



## Confirmation of calcification regions:

Condition on the size  $S$  in pixels:

$$5 < S < 2,500 \quad (5.60)$$

The upper limit on the area corresponds to about  $6.25 \text{ mm}^2$  with a pixel resolution of  $50 \text{ }\mu\text{m}$ .

Condition on contrast  $C$ :

$$C > 0.20. \quad (5.61)$$

The background region required to compute  $C$  is formed by using pixels circumscribing the region contour to a thickness of 3 pixels.



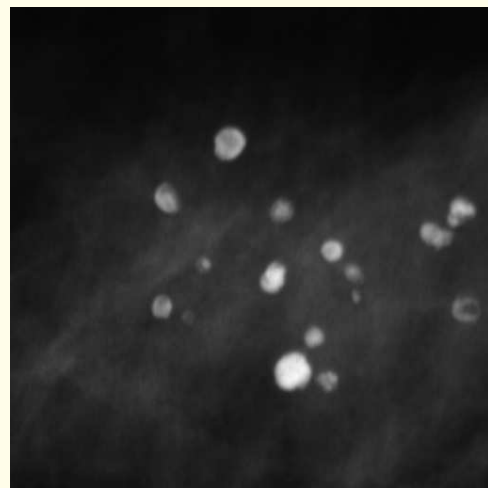
## Examples:

Sections of size  $1,024 \times 768$ ,  $768 \times 512$ ,  $512 \times 768$ , and  $512 \times 768$  pixels of four typical mammograms from complete images of up to  $2,560 \times 4,096$  pixels with biopsy-proven calcifications.

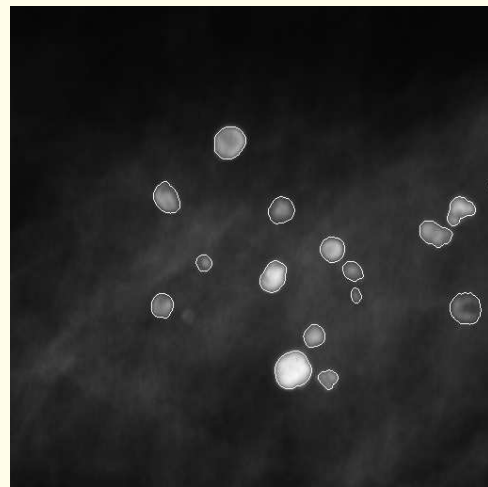
Two of the sections had a total of 58 benign calcifications; the other two contained  $241 \pm 10$  malignant calcifications.

Based upon visual inspection by a radiologist, the detection rates of the multitolerance region-growing algorithm were

81% with 0 false calcifications for the benign mammograms, and 85  $\pm$  3% with 29 false calcifications for the malignant cases.

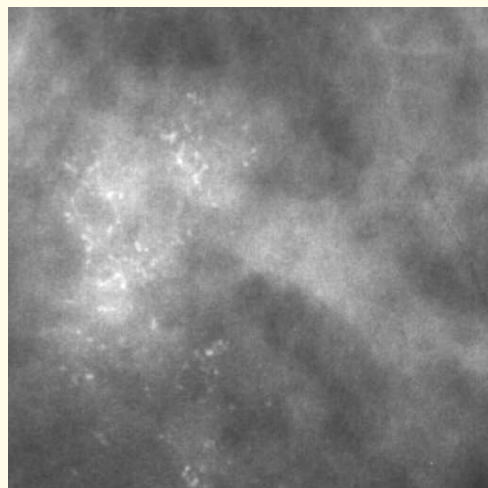


(a)

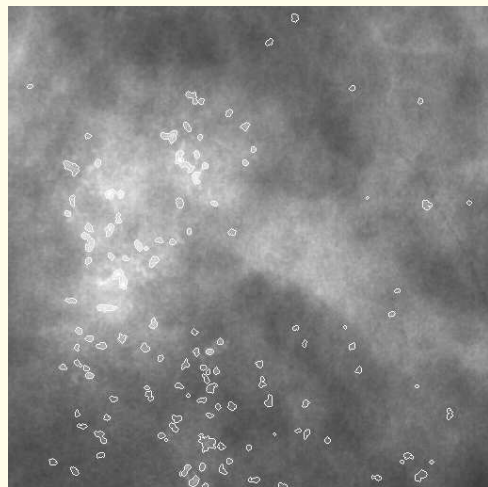


(b)

Figure 5.26: Mammogram section with benign calcifications. (a) Original image. (b) Image with the contours of the calcification regions detected. The section shown is of size  $512 \times 512$  pixels (approximately  $2.25 \text{ cm} \times 2.25 \text{ cm}$ ), out of the full matrix of  $1,536 \times 4,096$  pixels of the complete mammogram. Reproduced with permission from L. Shen, R.M. Rangayyan, and J.E.L. Desautels, “Detection and classification of mammographic calcifications”, *International Journal of Pattern Recognition and Artificial Intelligence*, 7(6): 1403–1416, 1993. © World Scientific Publishing Co.



(a)



(b)

Figure 5.27: Mammogram section with malignant calcifications. (a) Original image. (b) Image with the contours of the calcification regions detected. The section shown is of size  $512 \times 512$  pixels (approximately  $2.25 \text{ cm} \times 2.25 \text{ cm}$ ), out of the full matrix of  $1,792 \times 4,096$  pixels of the complete mammogram. Reproduced with permission from L. Shen, R.M. Rangayyan, and J.E.L. Desautels, “Detection and classification of mammographic calcifications”, *International Journal of Pattern Recognition and Artificial Intelligence*, 7(6): 1403–1416, 1993. © World Scientific Publishing Co.



#### 5.4.10 *Application: Detection of calcifications by linear prediction error*

The simple seed selection method used by Shen et al. encounters limitations in the case of calcifications present in or superimposed by dense breast tissue.

Serrano et al. proposed a method to detect seed pixels for region growing based upon the error of linear prediction.

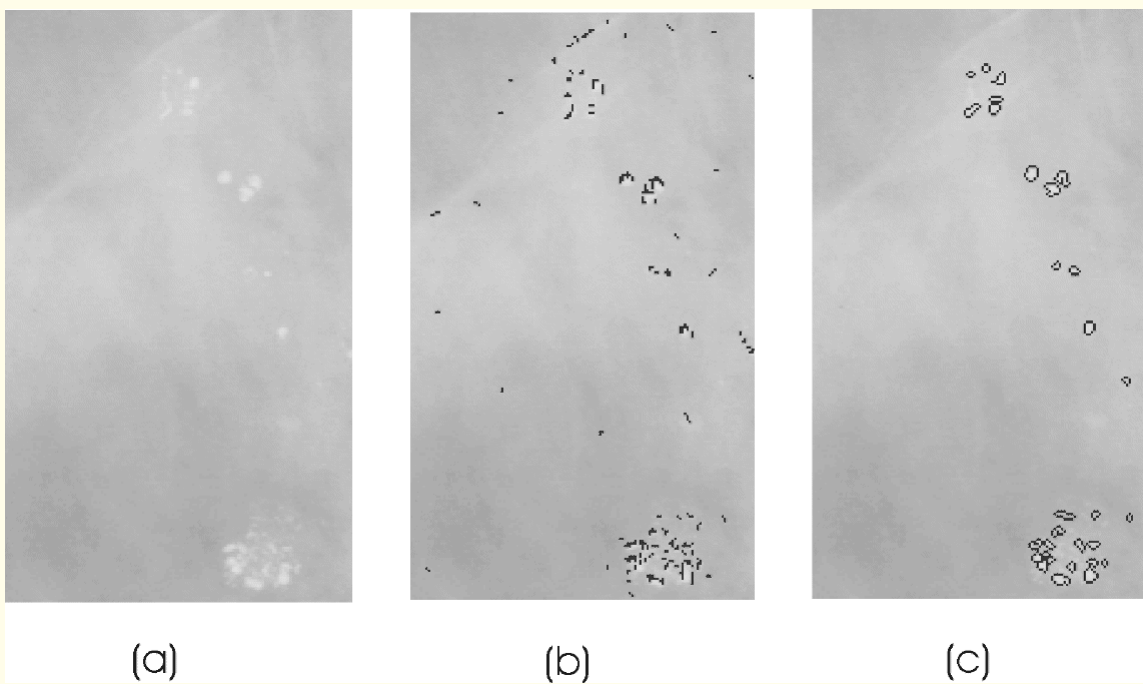


Figure 5.28: (a) Mammogram section with malignant calcifications;  $234 \times 137$  pixels with a resolution of  $160 \mu\text{m}$ . (b) Seed pixels detected by thresholding the prediction error (marked in black). (c) Image with the contours of the calcification regions detected by region growing from the seed pixels in (b). Reproduced with permission from C. Serrano, J.D. Trujillo, B. Acha, and R.M. Rangayyan, “Use of 2D linear prediction error to detect microcalcifications in mammograms”, *CDROM Proceedings of the II Latin American Congress on Biomedical Engineering*, Havana, Cuba, 23–25 May 2001. © Cuban Society of Bioengineering.



## 5.5 Fuzzy-set-based Region Growing to Detect Breast Tumors

Classical segmentation techniques attempt to define precisely the ROI.

Tumors often do not have distinct boundaries.

An alternative to address the problem of detecting breast masses is to represent tumor or mass regions by fuzzy sets.



Guliato et al. proposed two segmentation methods that incorporate fuzzy concepts:

The first method determines the boundary of a tumor or mass by region growing after a preprocessing step based on fuzzy sets to enhance the ROI.

The second segmentation method is a fuzzy region-growing method that takes into account the uncertainty present around the boundaries of tumors.



### 5.5.1 *Preprocessing based upon fuzzy sets*

A mass or tumor typically appears on a mammogram as a relatively dense region, whose properties could be characterized using local density, gradient, texture, and other measures.

A set of such local properties could be used to define a feature vector of a mass ROI and/or a pixel belonging to the ROI.



Given a feature vector, a pixel whose properties are similar to those represented by the feature vector of the mass could be assigned a high intensity; if not, the pixel intensity could be made low.

At the end of such a process, the pixels in and around the ROI will be displayed according to their degree of similarity with respect to the features of the mass ROI.



A fuzzy set may be defined by assigning to each element considered from the universal set  $\Omega$  a value representing its grade of membership in the fuzzy set.

The grade corresponds to the degree with which the element is similar to or compatible with the concept represented by the fuzzy set.

Let  $\Gamma : \Omega \rightarrow L$  be a membership function that maps  $\Omega$  into  $L$ , where  $L$  denotes any set that is at least partially ordered.

The most commonly used range of values for membership functions is the unit real interval  $[0, 1]$ .

Crisp sets can be seen as a particular case of fuzzy sets where  $\Gamma : \Omega \rightarrow \{0, 1\}$ ; that is, only the discrete values 0 and 1.



Enhancement of an ROI may be achieved by defining a membership function that evaluates the similarity between the properties of the pixel being considered and those of the ROI.

In this procedure, the original image is mapped to a fuzzy set according to the membership function, which:

- assigns a membership degree equal to 1 to those pixels that possess the same properties as the mass ROI;
- represents the degree of similarity between the features of the mass ROI and those of the pixel being considered;
- exhibits symmetry with respect to the difference between the features of the ROI and those of the pixel being considered;
- decreases monotonically from 1 to 0.



Guliato et al. considered the mean intensity of a seed region, identified by the user, as the ROI feature.

Membership function:

$$\Gamma(p) = \frac{1}{1 + \beta | \mathbf{A} - \mathbf{B} |}, \quad (5.62)$$

where  $p$  is the pixel being processed,

$\mathbf{A}$  is the feature vector of the mass (gray level),

$\mathbf{B}$  is the feature vector of the pixel being analyzed,

$\beta$  defines the opening of the membership function.



Large  $\beta$ : opening is narrow, the function is strict.

Small  $\beta$ : opening is wide, the function is permissive.

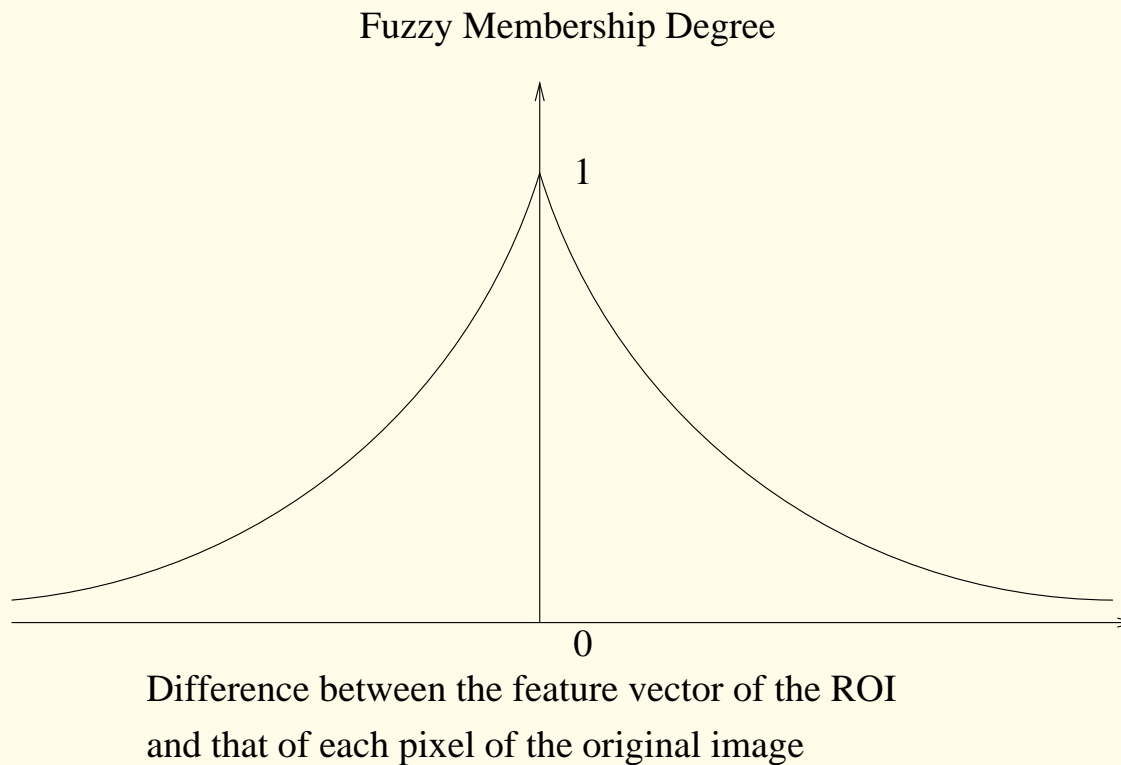


Figure 5.29: Fuzzy membership function for preprocessing. Reproduced with permission from D. Guliato, R.M. Rangayyan, W.A. Carnielli, J.A. Zuffo, and J.E.L. Desautels, “Segmentation of breast tumors in mammograms using fuzzy sets”, *Journal of Electronic Imaging*, 12(3): 369 – 378, 2003. © SPIE and IS&T.



The fuzzy set obtained represents pixels whose properties are close to those of the mass with a high membership degree; the opposite case results in a low membership degree.

The membership degree may be used as a scale factor to obtain gray levels and display the result as an image.

The contrast of the ROI in the resulting image depends upon the parameter  $\beta$ .

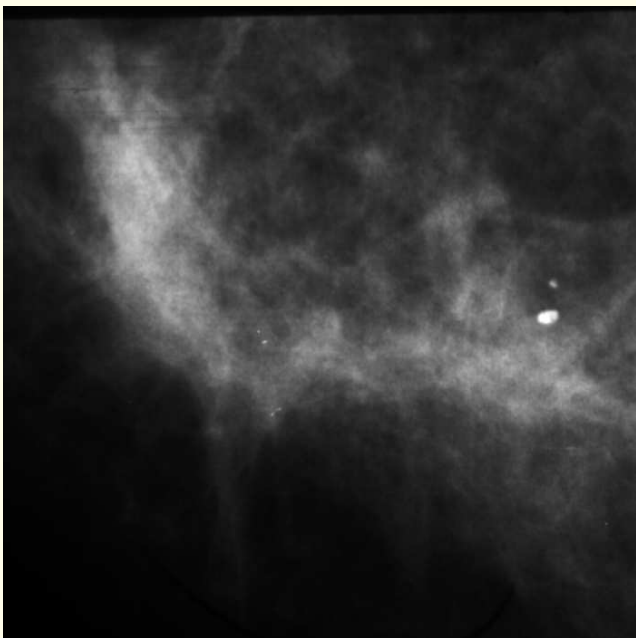


Figure 5.30 (a)



Figure 5.30 (b)

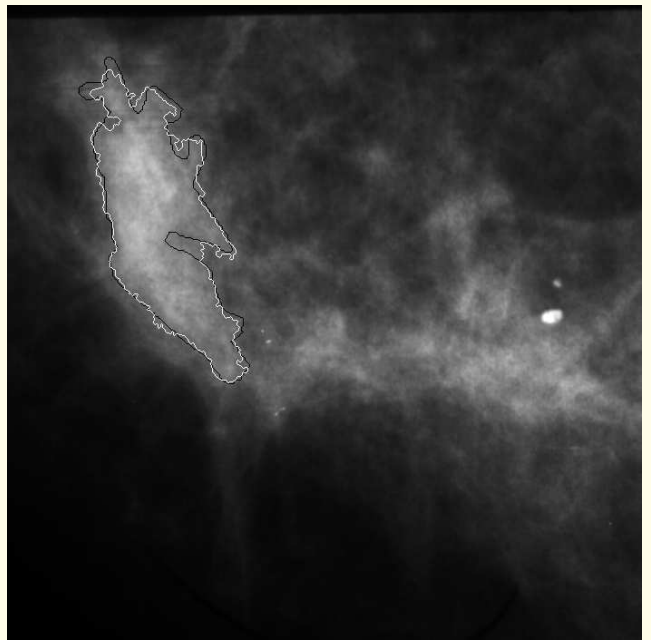
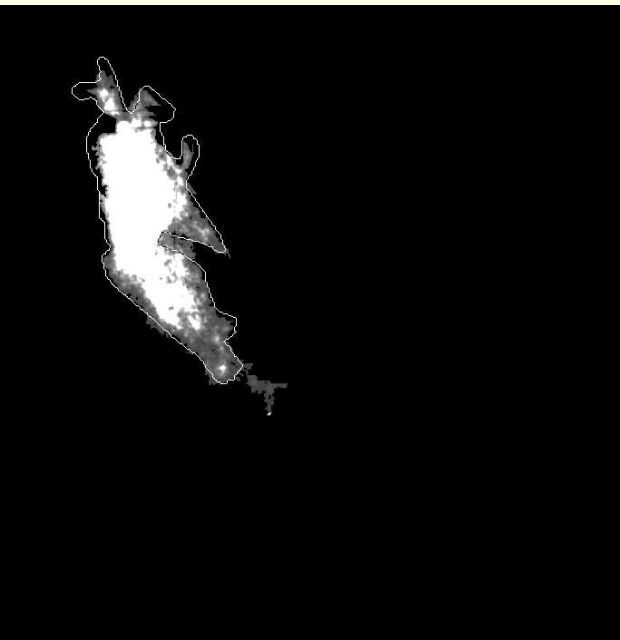


Figure 5.30 (c)



(d)

Figure 5.30: (a) A  $700 \times 700$ -pixel portion of a mammogram with a spiculated malignant tumor. Pixel size =  $62.5 \mu\text{m}$ . (b) Fuzzy-set-based ROI enhancement with  $\beta = 0.007$ . (c) Contour extracted (white line) by region growing with the result in (b). The black line represents the boundary drawn by a radiologist (shown for comparison).  $\beta = 0.007$ , threshold = 0.63. (d) Result of fuzzy region growing with the image in (a) with  $\Delta\mu_{\max} = 45$ ,  $\Delta CV_{\max} = 0.01$ ,  $\beta = 0.07$ . The contour drawn by the radiologist is superimposed for comparison. Reproduced with permission from D. Guliato, R.M. Rangayyan, W.A. Carnielli, J.A. Zuffo, and J.E.L. Desautels, “Segmentation of breast tumors in mammograms using fuzzy sets”, *Journal of Electronic Imaging*, 12(3): 369 – 378, 2003. © SPIE and IS&T.



### 5.5.2 *Fuzzy segmentation based upon region growing*

The pixel values in the fuzzy-set preprocessed image represent the membership degrees of pixels with respect to the ROI as defined by the seed region.

To perform contour extraction, the region-growing algorithm needs a threshold value and a seed region that lies inside the ROI.

The region-growing process starts with the seed region.



Four-connected neighboring pixels that are above the threshold are labeled as zero, the neighbors of the pixels labeled as zero are inspected, and the procedure continued.

If the connected pixel is less than the threshold, it is labeled as one, indicating a contour pixel, and its neighborhood is not processed.

The recursive process continues until all spatially connected pixels fail the test for inclusion in the region.

A post-processing step is included to remove isolated pixels and regions that lie within the outermost contour.

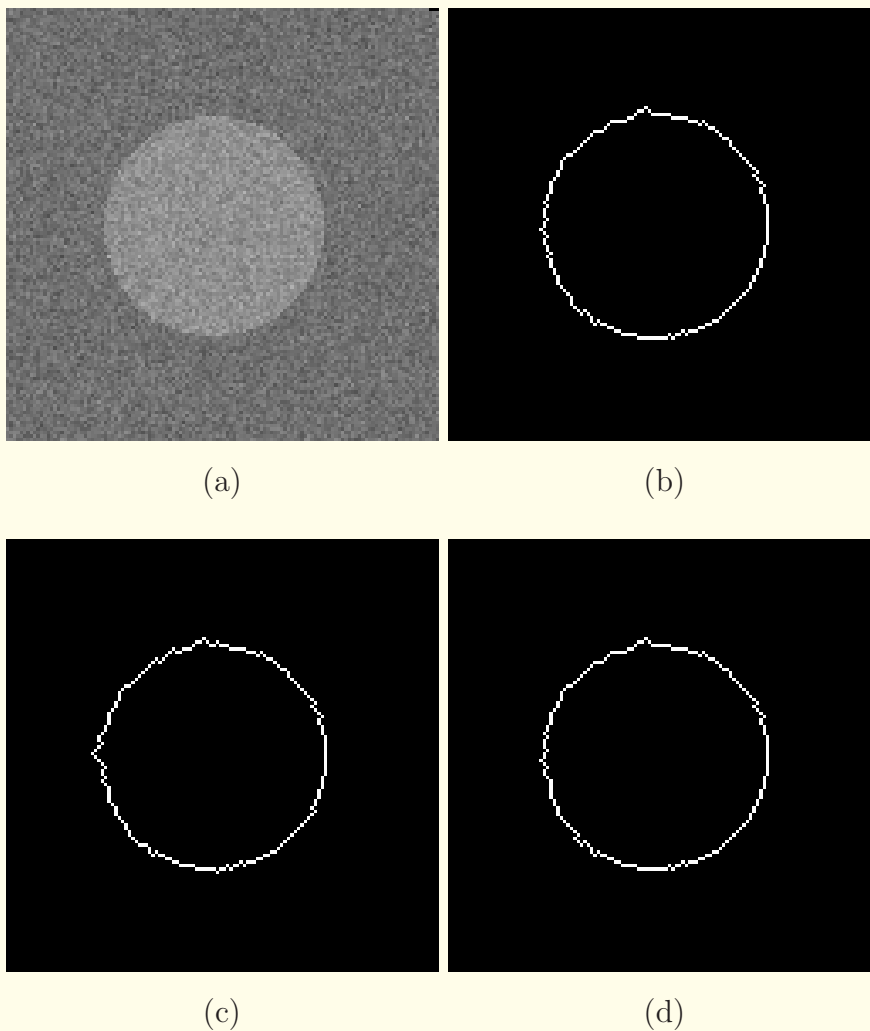


Figure 5.31: Illustration of the effects of seed pixel and threshold selection on fuzzy-set preprocessing and region growing. (a) Original image ( $128 \times 128$  pixels) with additive Gaussian noise, with  $\sigma = 12$  and SNR = 2.66. Results with (b) seed pixel (60, 60) and threshold = 0.82; (c) seed pixel (68, 60) and threshold = 0.85; (d) seed pixel (68, 80) and threshold = 0.85. Reproduced with permission from D. Gulianto, R.M. Rangayyan, W.A. Carnielli, J.A. Zuffo, and J.E.L. Desautels, “Segmentation of breast tumors in mammograms using fuzzy sets”, *Journal of Electronic Imaging*, 12(3): 369 – 378, 2003. © SPIE and IS&T.

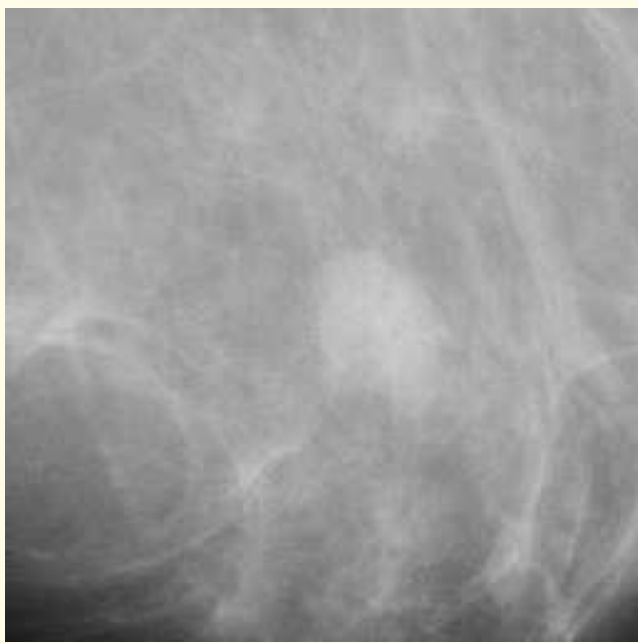


Figure 5.32 (a)

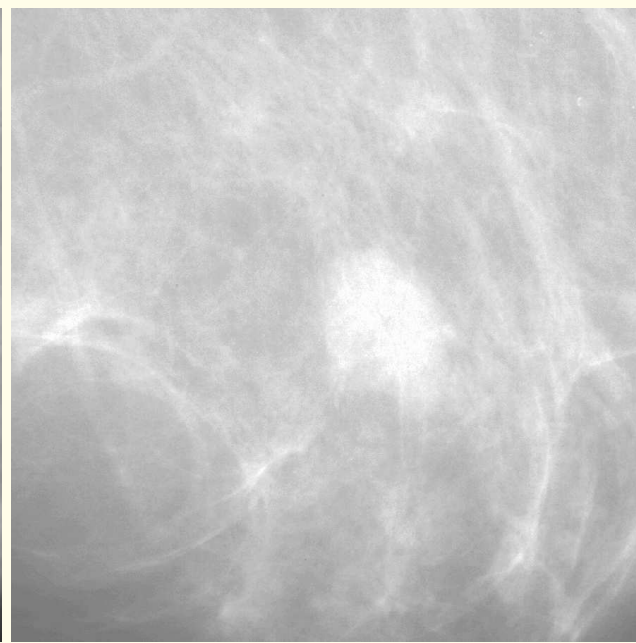


Figure 5.32 (b)

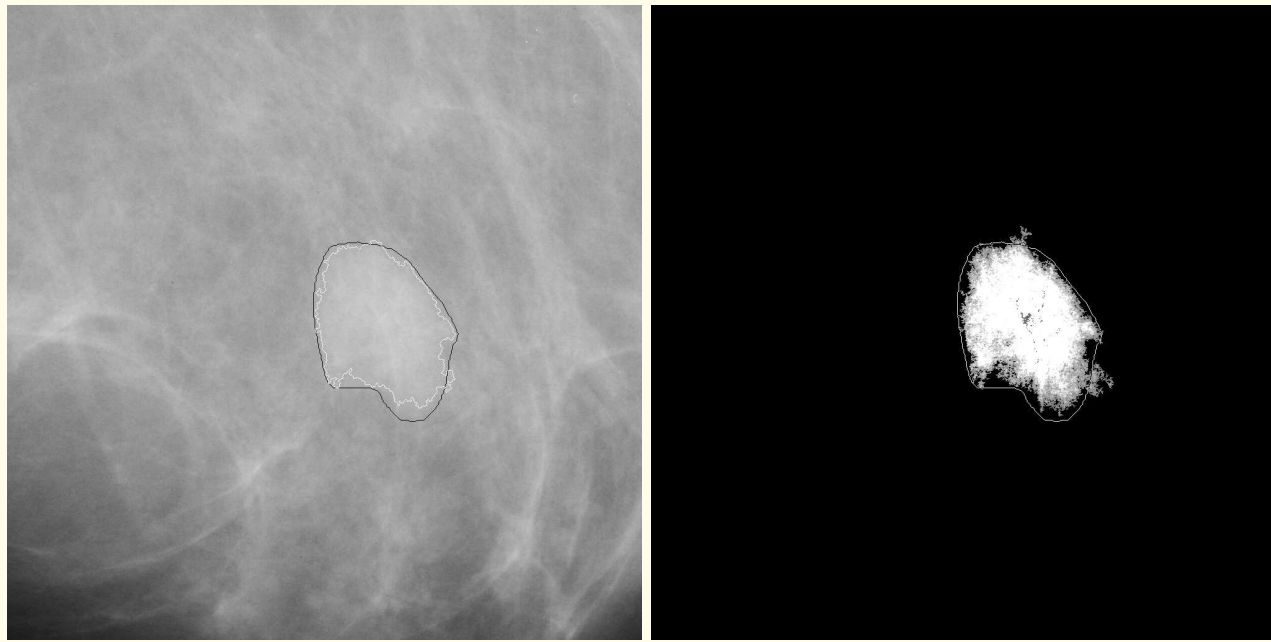


Figure 5.32 (c)

(d)

Figure 5.32: (a) A  $1,024 \times 1,024$ -pixel portion of a mammogram with a circumscribed benign mass. Pixel size =  $50 \mu\text{m}$ . (b) Fuzzy-set-based ROI enhancement with  $\beta = 0.007$ . (c) Contour extracted (white line) by region growing with the result in (b). The black line represents the boundary drawn by a radiologist (shown for comparison).  $\beta = 0.007$ , threshold = 0.87. (d) Result of fuzzy region growing with the image in (a) with  $\Delta\mu_{\max} = 15$ ,  $\Delta CV_{\max} = 0.01$ ,  $\beta = 0.07$ . The contour drawn by the radiologist is superimposed for comparison. Reproduced with permission from D. Guliato, R.M. Rangayyan, W.A. Carnielli, J.A. Zuffo, and J.E.L. Desautels, “Segmentation of breast tumors in mammograms using fuzzy sets”, *Journal of Electronic Imaging*, 12(3): 369 – 378, 2003. © SPIE and IS&T.



## Results of application to mammograms:

Guliato et al. tested their method with 47 mammograms including 25 malignant tumors and 22 benign masses.

Good agreement was observed between the contours given by the method and those drawn independently by a radiologist.

The seed region and threshold value were selected manually for each case; the threshold values varied between 0.57 and 0.90.

The same value of the membership function parameter  $\beta = 0.007$  was used to process all of the images in the study.



## Measure of fuzziness:

To compare the results obtained by segmentation with the contours drawn by the radiologist, Guliato et al. developed a method to aggregate the segmented region with the reference contour.

The method uses a fuzzy fusion operator that generalizes classical intersection of sets, producing a fuzzy set that represents the agreement present among the two inputs.



The result of fusion was evaluated by a measure of fuzziness:

$$f(X) = \frac{\sum_{p \in X} [1 - |2\Gamma(p) - 1|]}{|X|}, \quad (5.63)$$

where  $X$  is the result of aggregation, and

$\Gamma(p)$  is the degree of membership of the pixel  $p$ .

The denominator normalizes the measure with respect to the area of the result of fusion, resulting in a value in the range  $[0, 1]$ :

zero represents perfect agreement and unity indicates no intersection between the two inputs.



The values of the measure of fuzziness obtained for the 47 mammograms in the study were in the range (0.13, 0.85), with the mean and standard deviation being 0.42 and 0.17.

The measure of fuzziness was less than 0.5 for 34 out of the 47 cases.

In most cases where the measure of fuzziness was greater than 0.5, the segmented region was smaller than, but contained within, the region indicated by the contour drawn by the radiologist.



## Assessment of the results by pattern classification:

In order to derive a parameter for discriminating between benign masses and malignant tumors, the following procedure was applied by Guliato et al.:

Morphological erosion with a square structuring element of size equal to 25% of the shorter dimension of the smallest rectangle containing the contour was applied to the contour:

the core of the ROI was separated from the boundary.



A parameter  $DCV$  was computed from the fuzzy-set preprocessed image, as the difference between the coefficient of variation ( $CV$ ) of the entire ROI and that of its core.

A high value of  $DCV$  represents an inhomogeneous ROI, which could be indicative of a malignant tumor.

The probability of malignancy based upon  $DCV$  was computed using logistic regression.

The cut point of 0.02 resulted in all 22 benign masses and 16 out of the 25 malignant tumors being correctly classified, yielding a high specificity of 1.0 but a low sensitivity of 0.64.

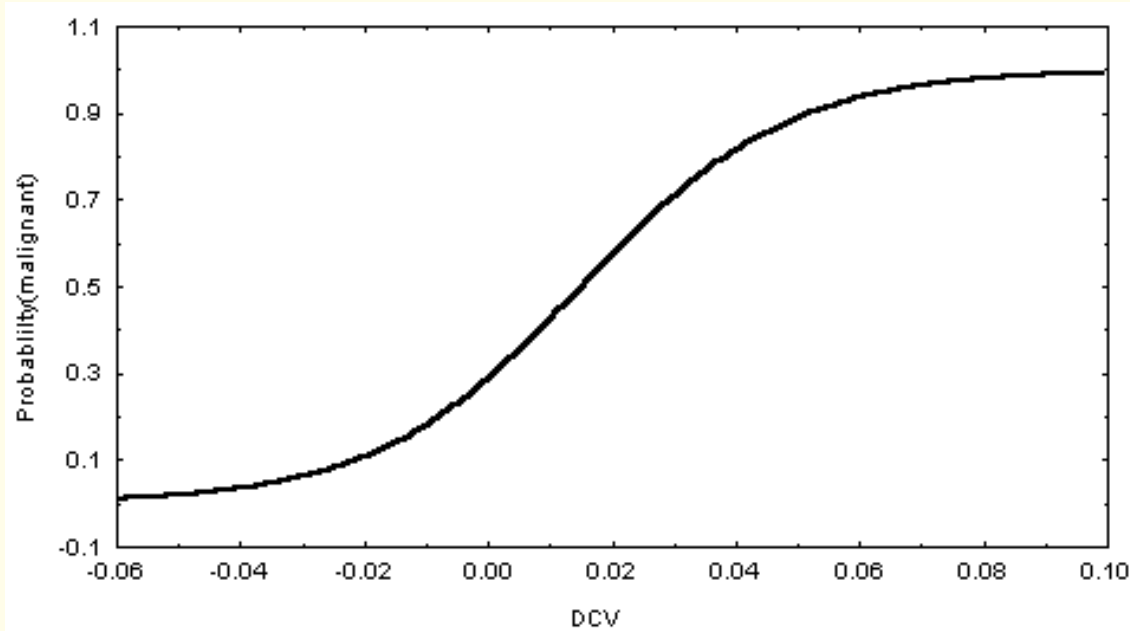


Figure 5.33: The probability of malignancy (vertical axis) derived from the parameter *DCV* (horizontal axis). Reproduced with permission from D. Guliato, R.M. Rangayyan, W.A. Carnielli, J.A. Zuffo, and J.E.L. Desautels, “Segmentation of breast tumors in mammograms using fuzzy sets”, *Journal of Electronic Imaging*, 12(3): 369 – 378, 2003. © SPIE and IS&T.



### 5.5.3 Fuzzy region growing

Guliato et al. also proposed a fuzzy region-growing algorithm to obtain mass regions in mammograms.

In this method, an adaptive similarity criterion is used for region growing, with the mean and the standard deviation of the pixels in the region being grown as control parameters.

The region is represented by a fuzzy set to preserve the transition information around boundary regions.



The algorithm starts with a seed region that lies inside the ROI and spreads by adding to the region 8-connected pixels that have similar properties.

The homogeneity of the region is evaluated by calculating the mean ( $\mu$ ), standard deviation ( $\sigma$ ), and the coefficient of variation  $CV = \frac{\sigma}{\mu}$ .



$\Delta\mu_{\max}$ ,  $\Delta CV_{\max}$ ,  $\beta$ : control parameters for region growing.

$\Delta\mu_{\max}$  specifies the maximum allowed difference between the value of the pixel being analyzed and the mean of the subregion already grown.

$\Delta CV_{\max}$  indicates the desired degree of homogeneity between two subregions;

$\beta$  defines the opening of the membership function.

Let  $p$  be the next pixel to be analyzed and  $I(p)$  be the value of  $p$ .



The segmentation algorithm is executed in two steps:

$$1. |I(p) - \mu| \leq \Delta\mu_{\max}.$$

If this condition is not satisfied, then the pixel is labeled as rejected.

If the condition is satisfied,  $p$  is temporarily added to the subregion and  $\mu_{new}$  and  $\sigma_{new}$  are calculated.

$$2. \left| \frac{\sigma}{\mu} - \frac{\sigma_{new}}{\mu_{new}} \right| \leq \Delta CV_{\max}.$$

If the condition is satisfied, then  $p$  must definitely be added to the subregion and labeled as accepted, and  $\mu$  and  $\sigma$  must be updated, that is,  $\mu = \mu_{new}$  and  $\sigma = \sigma_{new}$ .

If the condition is not satisfied,  $p$  is added to the subregion with the label *accepted with restriction*, and  $\mu$  and  $\sigma$  are not modified.



The second step given above analyzes the distortion that the pixel  $p$  can produce if added to the subregion.

At the beginning of the process, the region includes all the pixels in the seed region, and the standard deviation is set to zero.

While the standard deviation of the region being grown is zero, a specific procedure is executed in the second step:

$$\left| \frac{\sigma}{\mu} - \frac{\sigma_{new}}{\mu_{new}} \right| \leq 2 \Delta CV_{max}.$$

The parameter  $\Delta CV_{max}$  works as a filter that avoids the possibility that the mean and standard deviation measures suffer undesirable modification during the region-growing process.



The algorithm processes pixels in expanding concentric squares around the seed region, evaluating each pixel only once.

These steps provide stability to the algorithm.

The membership function that maps the pixel values of the region resulting from the preceding procedure to the unit interval  $[0, 1]$  could be based upon the mean of the region.

Pixels that are close to the mean will have a high membership degree, and in the opposite case, a low membership degree.



The desirable characteristics of the membership function are:

- the membership degree of the seed pixel or region must be 1;
- the membership degree of a pixel labeled as rejected must be 0;
- the membership function must be as independent of the seed pixel or region as possible;
- the membership degree must represent the proximity between a pixel labeled as accepted or accepted with restriction and the mean of the resulting region;
- the function must be symmetric with respect to the difference between the mean and the pixel value; and
- the function must decrease monotonically from 1 to 0.



Membership function  $\Gamma$  used by Guliato et al.: Figure 5.34.

$a = | mean\_seed\_region + standard\_deviation\_seed\_region - \mu |$  and

$b = \Delta\mu_{\max}$ .

The value of a pixel  $p$  is mapped to the fuzzy membership degree  $\Gamma(p)$  as follows:

if  $| I(p) - \mu | \leq a$  then  $\Gamma(p) = 1$

else if  $| I(p) - \mu | > b$  then  $\Gamma(p) = 0$

else  $\Gamma(p) = \frac{1}{1+\beta |I(p)-\mu|}.$

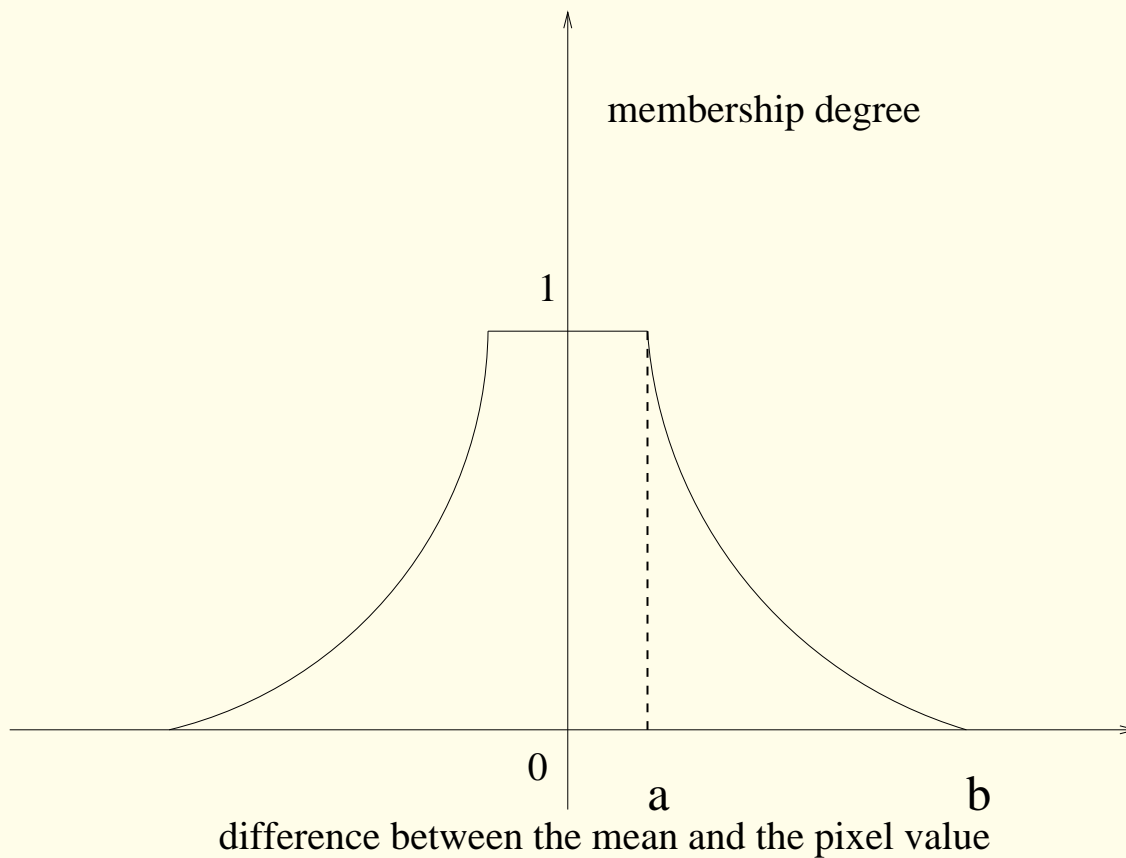
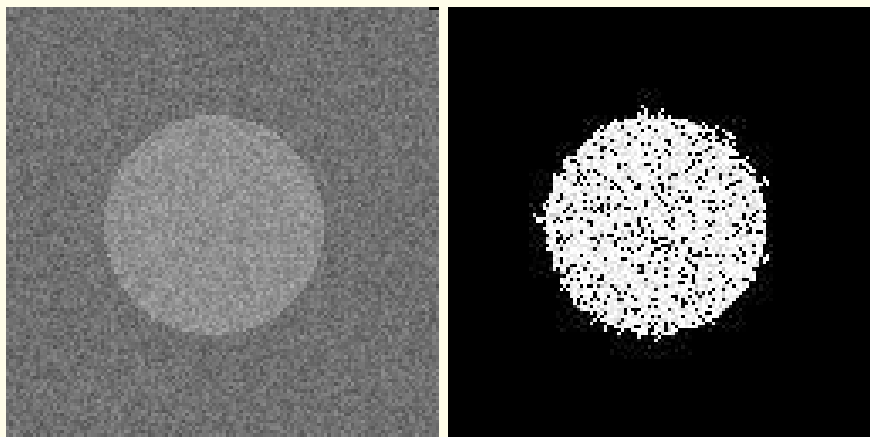
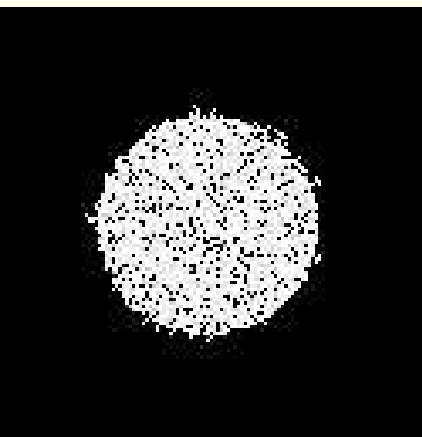


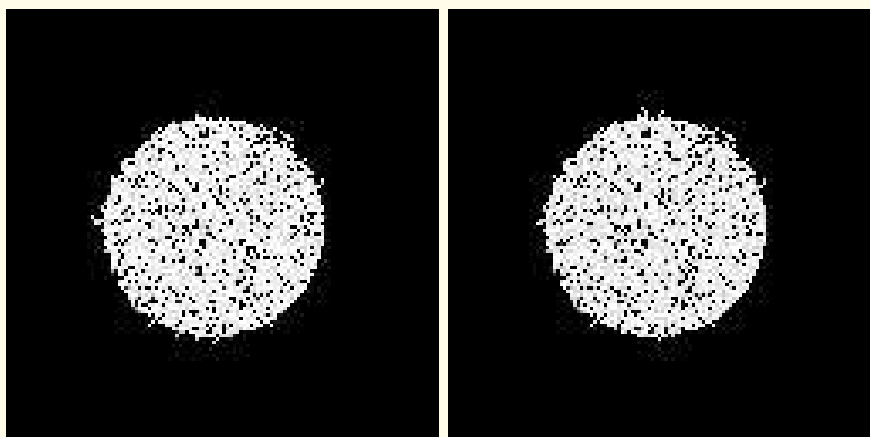
Figure 5.34: Fuzzy membership function for region growing, where  $a = | \text{mean\_seed\_region} + \text{standard\_deviation\_seed\_region} - \mu |$ , and  $b = \Delta\mu_{\max}$ . Reproduced with permission from D. Guliato, R.M. Rangayyan, W.A. Carnielli, J.A. Zuffo, and J.E.L. Desautels, “Segmentation of breast tumors in mammograms using fuzzy sets”, *Journal of Electronic Imaging*, 12(3): 369 – 378, 2003. © SPIE and IS&T.



(a)



(b)



(c)

(d)

Figure 5.35: Illustration of the effects of seed pixel selection on fuzzy region growing. (a) Original image ( $128 \times 128$  pixels) with Gaussian noise, with  $\sigma = 12$  and SNR = 2.66. Results with (b) seed pixel  $(60, 60)$ ,  $\Delta\mu_{\max} = 18$ ,  $\Delta CV_{\max} = 0.007$ ,  $\beta = 0.01$ ; (c) seed pixel  $(68, 60)$ ,  $\Delta\mu_{\max} = 18$ ,  $\Delta CV_{\max} = 0.007$ ,  $\beta = 0.01$ ; (d) seed pixel  $(68, 80)$ ,  $\Delta\mu_{\max} = 18$ ,  $\Delta CV_{\max} = 0.007$ ,  $\beta = 0.01$ . Reproduced with permission from D. Guliato, R.M. Rangayyan, W.A. Carnielli, J.A. Zuffo, and J.E.L. Desautels, “Segmentation of breast tumors in mammograms using fuzzy sets”, *Journal of Electronic Imaging*, 12(3): 369 – 378, 2003. © SPIE and IS&T.



Guliato et al. applied the fuzzy region-growing method to 47 test images maintaining the same values of  $\beta = 0.07$  and  $\Delta CV_{\max} = 0.01$ , and varying only the parameter  $\Delta\mu_{\max}$ .

The values of the parameters were selected by comparing the results of segmentation with the contours drawn by a radiologist.

The  $\Delta\mu_{\max}$  parameter ranged from 5 to 48 for the 47 masses and tumors analyzed.



The fuzzy regions obtained for the 47 mammograms were compared objectively with the corresponding contours drawn by the radiologist, by computing the measure of fuzziness.

The values were distributed over the range (0.098, 0.82), with the mean and standard deviation being 0.46 and 0.19, respectively.

The measure of fuzziness was smaller than 0.5 in 27 of the 47 cases analyzed.



## Assessment of the results by pattern classification:

In order to derive parameters for pattern classification, Guliato et al. analyzed the characteristics of a *fuzzy ribbon*:

connected region whose pixels possess membership degrees less than unity and separate the tumor core from the background.

The uncertainty present in and/or around the ROI is maintained.

The fuzzy ribbon of the malignant tumor in Figure 5.36 (a) contains more pixels with low values than that of the benign mass in part (b) of the same figure:

most malignant tumors possess ill-defined boundaries, whereas benign masses are well-circumscribed.



Based upon this observation, Guliato et al. computed the coefficient of variation  $CV_{fr}$  of the membership values of the pixels lying only within the fuzzy ribbon,

and the ratio  $\nu_{fr}$  of the number of pixels with membership degree less than 0.5 to the total number of pixels within the fuzzy ribbon.

It was expected that the fuzzy ribbons of malignant tumors would possess higher  $CV_{fr}$  and  $\nu_{fr}$  than those of benign masses.

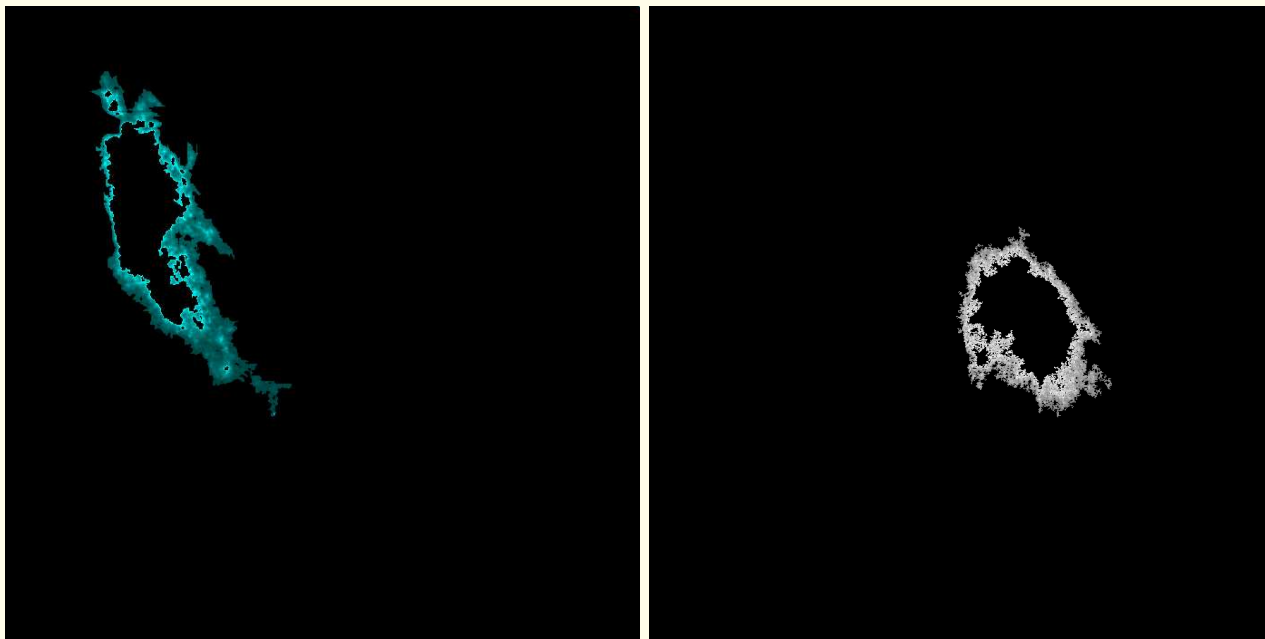


Figure 5.36 (a)

(b)

Figure 5.36: The fuzzy ribbons of (a) the malignant tumor in Figure 5.30 (a) and (b) the benign mass in Figure 5.32 (a). Reproduced with permission from D. Guliato, R.M. Rangayyan, W.A. Carnielli, J.A. Zuffo, and J.E.L. Desautels, “Segmentation of breast tumors in mammograms using fuzzy sets”, *Journal of Electronic Imaging*, 12(3): 369 – 378, 2003. © SPIE and IS&T.



In pattern classification experiments, discrimination between benign masses and malignant tumors with the parameter  $\nu_{fr}$  had no statistical significance.

The probability of malignancy curve based upon  $CV_{fr}$ , computed using the logistic regression method is illustrated in Figure 5.37.

The cut point of 0.18 resulted in the correct classification of 20 out of 25 malignant tumors and 20 out of 22 benign masses processed, leading to a sensitivity of 0.8 and a specificity of 0.9.

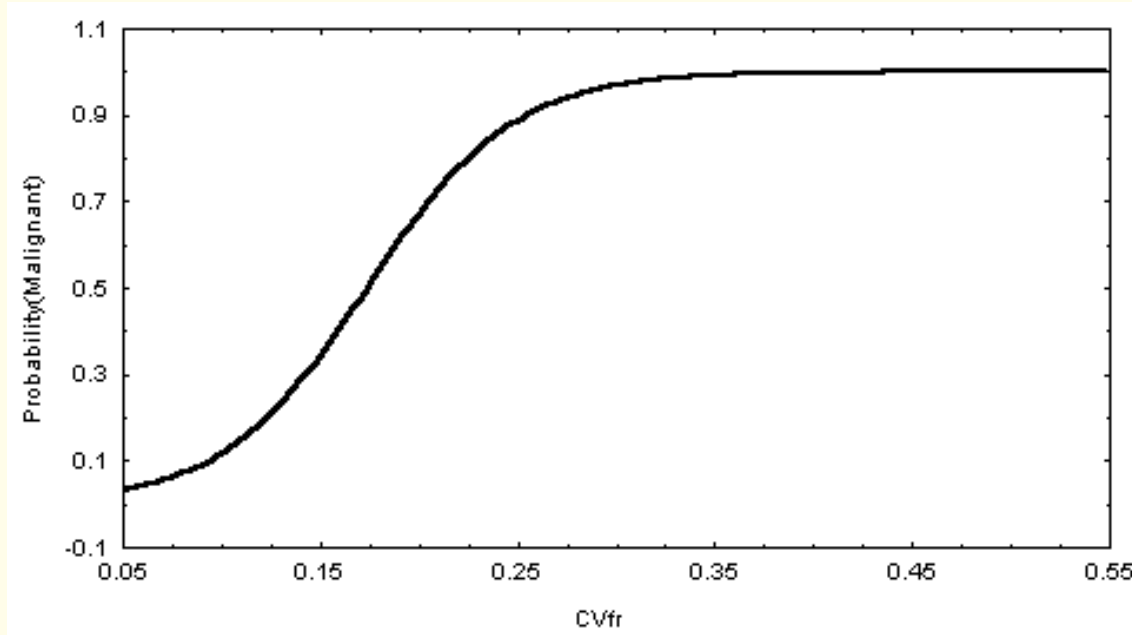


Figure 5.37: The probability of malignancy (vertical axis) derived from the parameter  $CV_{fr}$  (horizontal axis). Reproduced with permission from D. Guliato, R.M. Rangayyan, W.A. Carnielli, J.A. Zuffo, and J.E.L. Desautels, “Segmentation of breast tumors in mammograms using fuzzy sets”, *Journal of Electronic Imaging*, 12(3): 369 – 378, 2003. © SPIE and IS&T.



## 5.6 Detection of Objects of Known Geometry

Images may contain objects that may be represented in an analytical form, such as straight-line segments, circles, ellipses, and parabolas.

The edge of the pectoral muscle appears as an almost-straight line in MLO mammograms.

Benign calcifications and masses appear as almost-circular or oval objects in mammograms.

Most cells in pathology specimens have circular or elliptic boundaries, and some may have nearly rectangular shapes.



Parts of the boundaries of malignant breast tumors may be represented using parabolas.

The detection, modeling, and characterization of objects as above may be facilitated by prior knowledge of their shapes.



### 5.6.1 The Hough transform

Hough proposed a method to detect straight lines in images based upon the representation of straight lines in the image  $(x, y)$  space using the slope-intercept equation

$$y = m x + c, \quad (5.64)$$

where  $m$  is the slope and

$c$  is the position where the line intercepts the  $y$  axis;

In the Hough domain or parameter space, straight lines are characterized by the pair of parameters  $(m, c)$ .

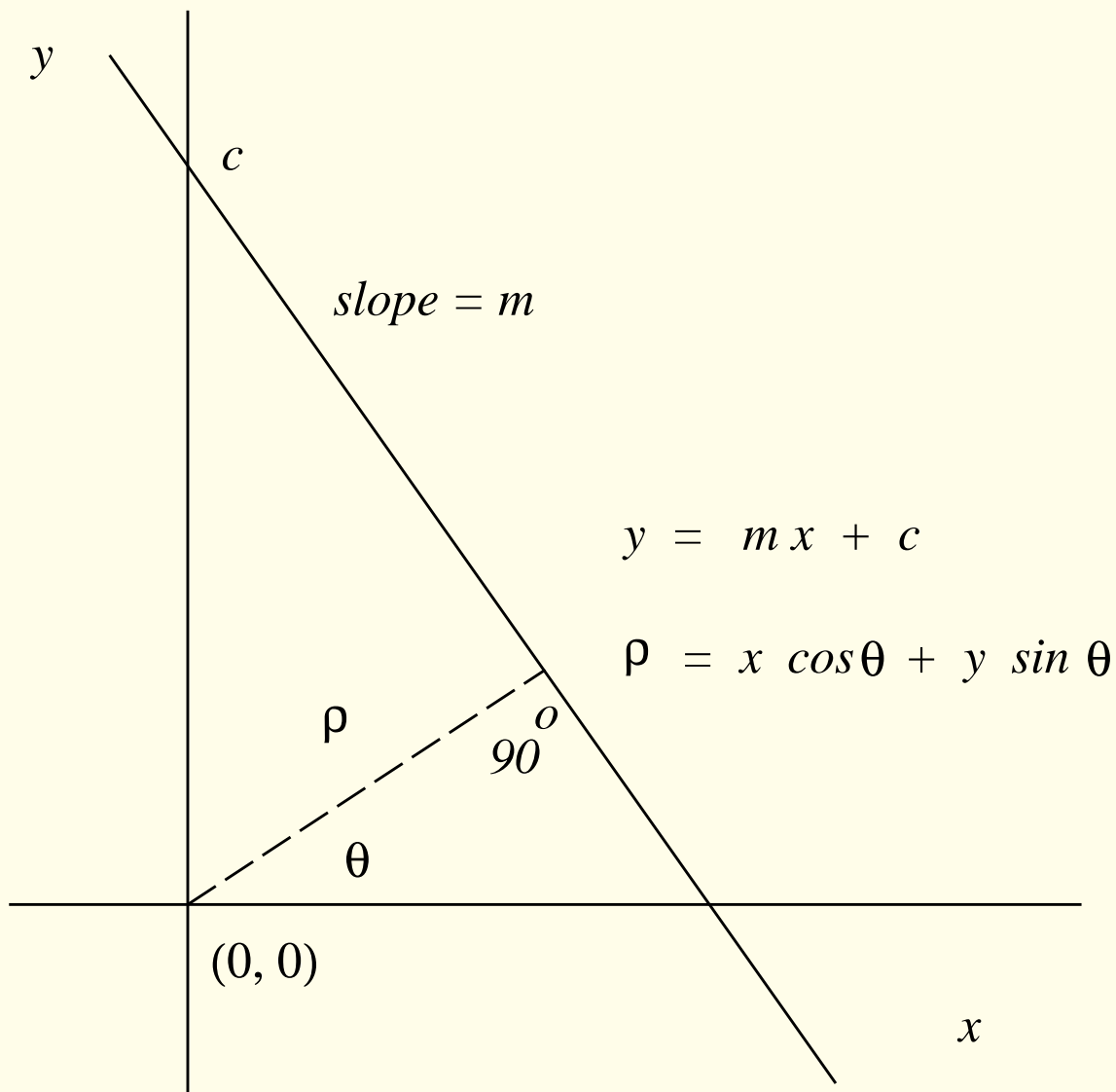


Figure 5.38: Parametric representation of a straight line in three coordinate systems:  $(x, y)$ ,  $(m, c)$ , and  $(\rho, \theta)$ .



Disadvantage: both  $m$  and  $c$  have unbounded ranges;

creates practical difficulties in the computational representation of the  $(m, c)$  space.

To overcome this limitation, Duda and Hart proposed the representation of straight lines using the parameters  $(\rho, \theta)$  of the normal (perpendicular) to the line as

$$\rho = x \cos \theta + y \sin \theta. \quad (5.65)$$



Advantage:  $\theta$  is limited to the range  $[0, \pi]$  or  $[0, 2\pi]$  and

$\rho$  is limited by the size of the given image.

The origin may be chosen to be at the center of the given image or at any other convenient point; the limits of the parameters  $(\rho, \theta)$  are affected by the choice of the origin.



### 5.6.2 *Detection of straight lines*

Suppose we are given a digital image that contains a straight line.

Let the pixels along the line be represented as  $\{x(n), y(n)\}$ ,  
 $n = 0, 1, 2, \dots, N - 1$ ;  $N$  = number of pixels along the line.

It is assumed that the image has been binarized, such that the pixels that belong to the line have the value 1, and all other pixels have the value 0.

It is advantageous if the line is one-pixel thick;  
otherwise, several lines could exist within a thick line.



If the normal parameters of the line are  $(\rho_0, \theta_0)$ , all pixels along the line satisfy the relationship

$$\rho_0 = x(n) \cos \theta_0 + y(n) \sin \theta_0. \quad (5.66)$$

For a given pixel  $\{x(n), y(n)\}$ , this represents a sinusoidal curve in the  $(\rho, \theta)$  parameter space;

it follows that the curves for all the  $N$  pixels intersect at the point  $(\rho_0, \theta_0)$ .



The following properties of the above representation follow:

- A point in the  $(x, y)$  space corresponds to a sinusoidal curve in the  $(\rho, \theta)$  parameter space.
- A point in the  $(\rho, \theta)$  space corresponds to a straight line in the  $(x, y)$  space.
- Points lying on the same straight line in the  $(x, y)$  space correspond to curves through a common point in the parameter space.
- Points lying on the same curve in the parameter space correspond to lines through a common point in the  $(x, y)$  space.



Procedure to detect straight lines:

1. Discretize the  $(\rho, \theta)$  parameter space into bins by quantizing  $\rho$  and  $\theta$  as  $\rho_k$ ,  $k = 0, 1, 2, \dots, K - 1$ , and  $\theta_l$ ,  $l = 0, 1, 2, \dots, L - 1$ ;

the bins are commonly referred to as accumulator cells.

Suitable limits may be imposed on the ranges of the parameters  $(\rho, \theta)$ .

2. For each point in the given image that has a value of 1, increment by 1 each accumulator cell in the  $(\rho, \theta)$  space that satisfies the relationship  $\rho = x(n) \cos \theta + y(n) \sin \theta$ .

Note that exact equality needs to be translated to a range of acceptance depending upon the discretization step size of the parameter space.



3. The coordinates of the point of intersection of all the curves in the parameter space provide the parameters of the line.  
This point will have the highest count in the parameter space.

The procedure given above assumes the existence of a single straight line in the image.

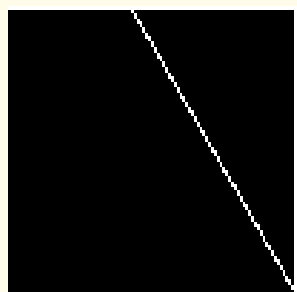


If several lines exist, there will be the need to search for all possible points of intersection of several curves (or the local maxima).

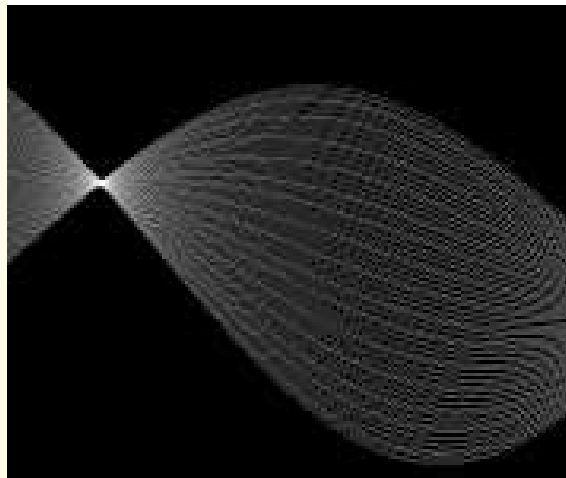
Note that the count in a given accumulator cell represents the number of pixels that lie on a straight line or several straight-line segments that have the corresponding  $(\rho, \theta)$  parameters.

A threshold may be applied to detect only lines that have a certain minimum length (number of pixels).

All cells in the parameter space that have counts above the threshold may be taken to represent straight lines (or segments) with the corresponding  $(\rho, \theta)$  values and numbers of pixels.



(a)



(b)

Figure 5.39: (a) Image with a straight line with  $(\rho, \theta) = (20, 30^\circ)$ . The limits of the  $x$  and  $y$  axes are  $\pm 50$ , with the origin at the center of the image. (b) Hough transform parameter space for the image. The display intensity is  $\log(1 + \text{accumulator cell value})$ . The horizontal axis represents  $\theta = [0, 180^\circ]$ ; the vertical axis represents  $\rho = [-75, 75]$ .

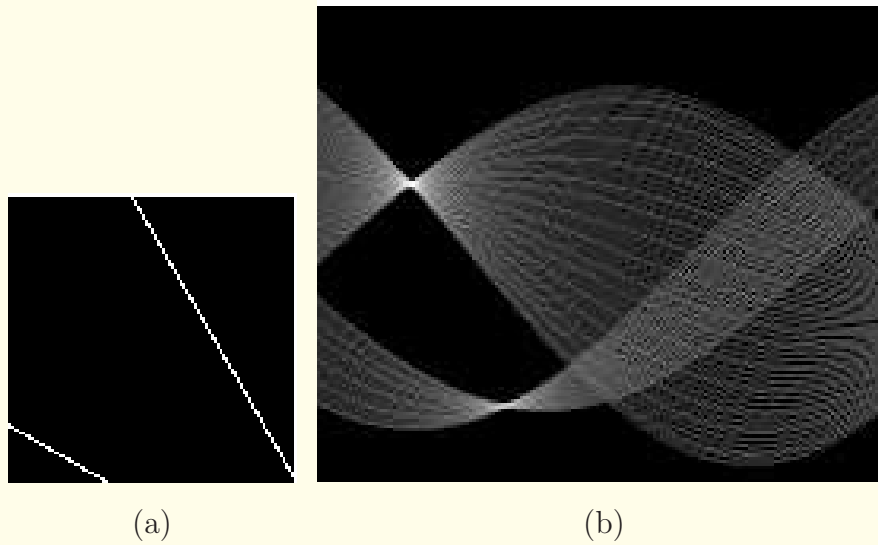


Figure 5.40: (a) Image with two straight lines with  $(\rho, \theta) = (20, 30^\circ)$  and  $(-50, 60^\circ)$ . The limits of the  $x$  and  $y$  axes are  $\pm 50$ , with the origin at the center of the image. (b) Hough transform parameter space for the image. The display intensity is  $\log(1 + \text{accumulator cell value})$ . The horizontal axis represents  $\theta = [0, 180^\circ]$ ; the vertical axis represents  $\rho = [-75, 75]$ .



### 5.6.3 *Detection of circles*

All points along the perimeter of a circle of radius  $c$  centered at  $(x, y) = (a, b)$  satisfy the relationship

$$(x - a)^2 + (y - b)^2 = c^2. \quad (5.67)$$

Any circle is represented by a single point in the 3D  $(a, b, c)$  parameter space.

The points along the perimeter of a circle in the  $(x, y)$  plane describe a right-circular cone in the  $(a, b, c)$  parameter space.

The algorithm for the detection of straight lines may be easily extended for the detection of circles using this representation.

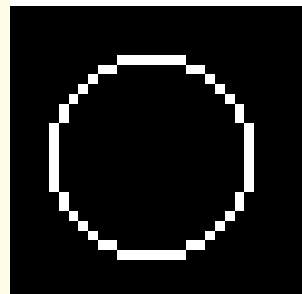


Figure 5.41: A  $30 \times 30$  image with a circle of radius 10 pixels, centered at  $(x, y) = (15, 15)$ .

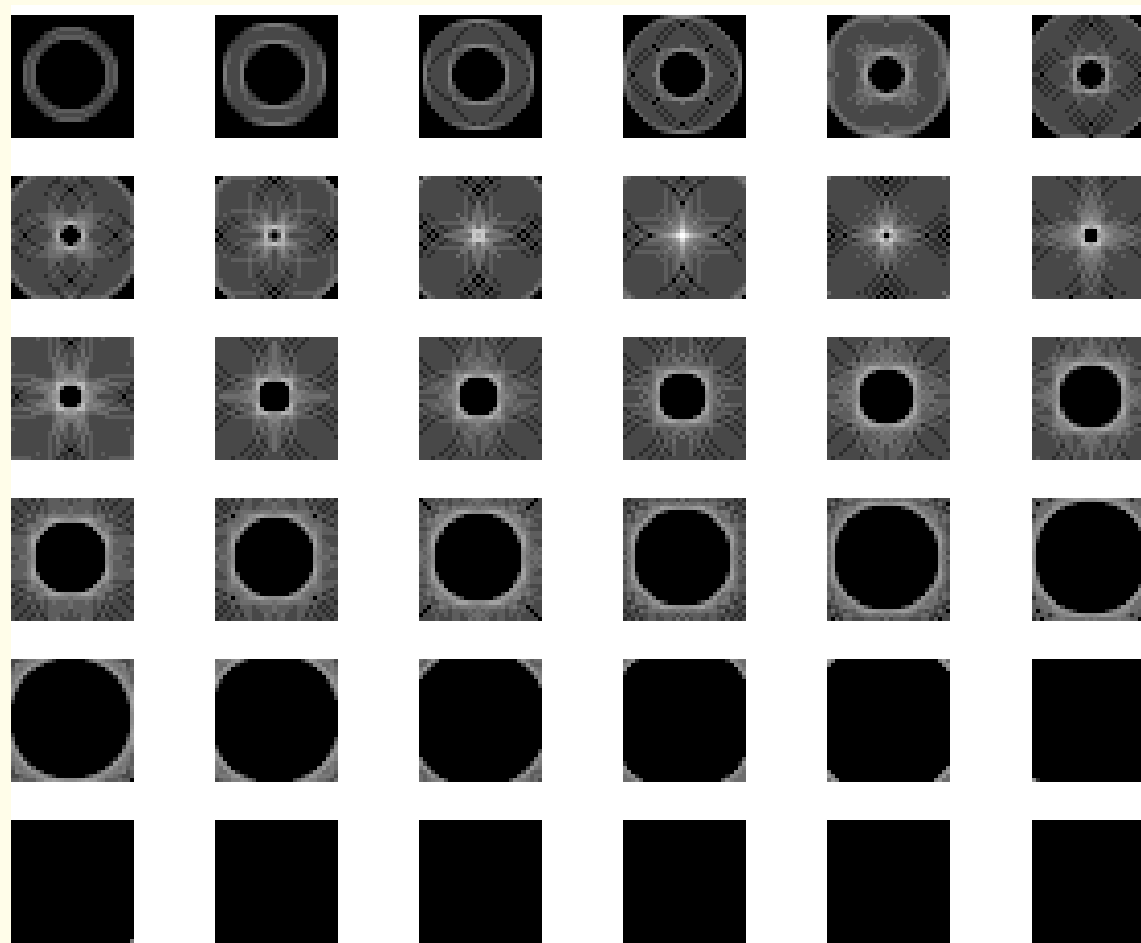


Figure 5.42: Hough parameter  $(a, b, c)$  space of the circle image in Figure 5.41. Each image is of size  $30 \times 30$  pixels, and represents the range of the  $(a, b)$  coordinates of the center of a potential circle. The series of images represents the various planes of the  $(a, b, c)$  parameter space with  $c = 1, 2, \dots, 36$ , going left to right and top to bottom, representing the radius of potential circles. The intensity of the parameter space values has been enhanced with the log operation. The maximum value in the Hough space is located at the center of the plane for  $c = 10$ .

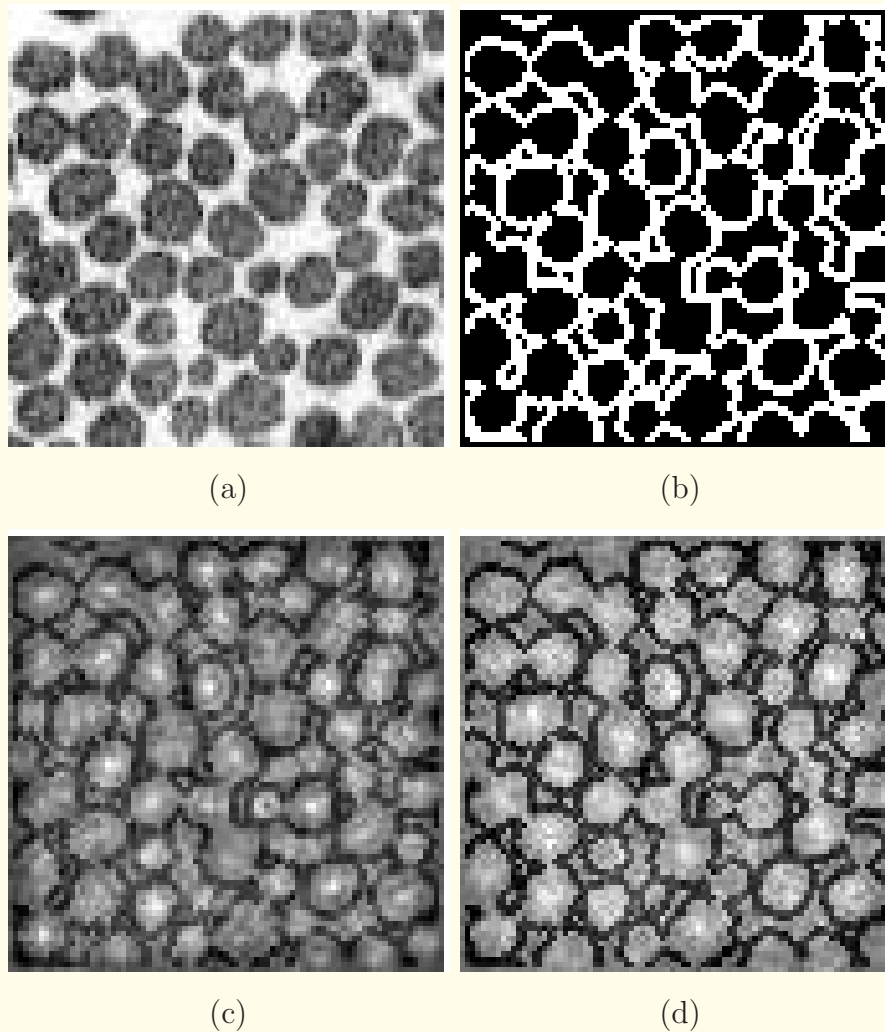


Figure 5.43: (a) TEM image showing collagen fibers in cross-section. The image is of size  $85 \times 85$  pixels. (b) Edges extracted from the image in (a). (c) Negative version of the image in (b), overlaid with 10 times the  $c = 5$  plane of the Hough transform parameter space. (d) Same as in (c) but with the  $c = 7$  plane. See also Figure 5.44.

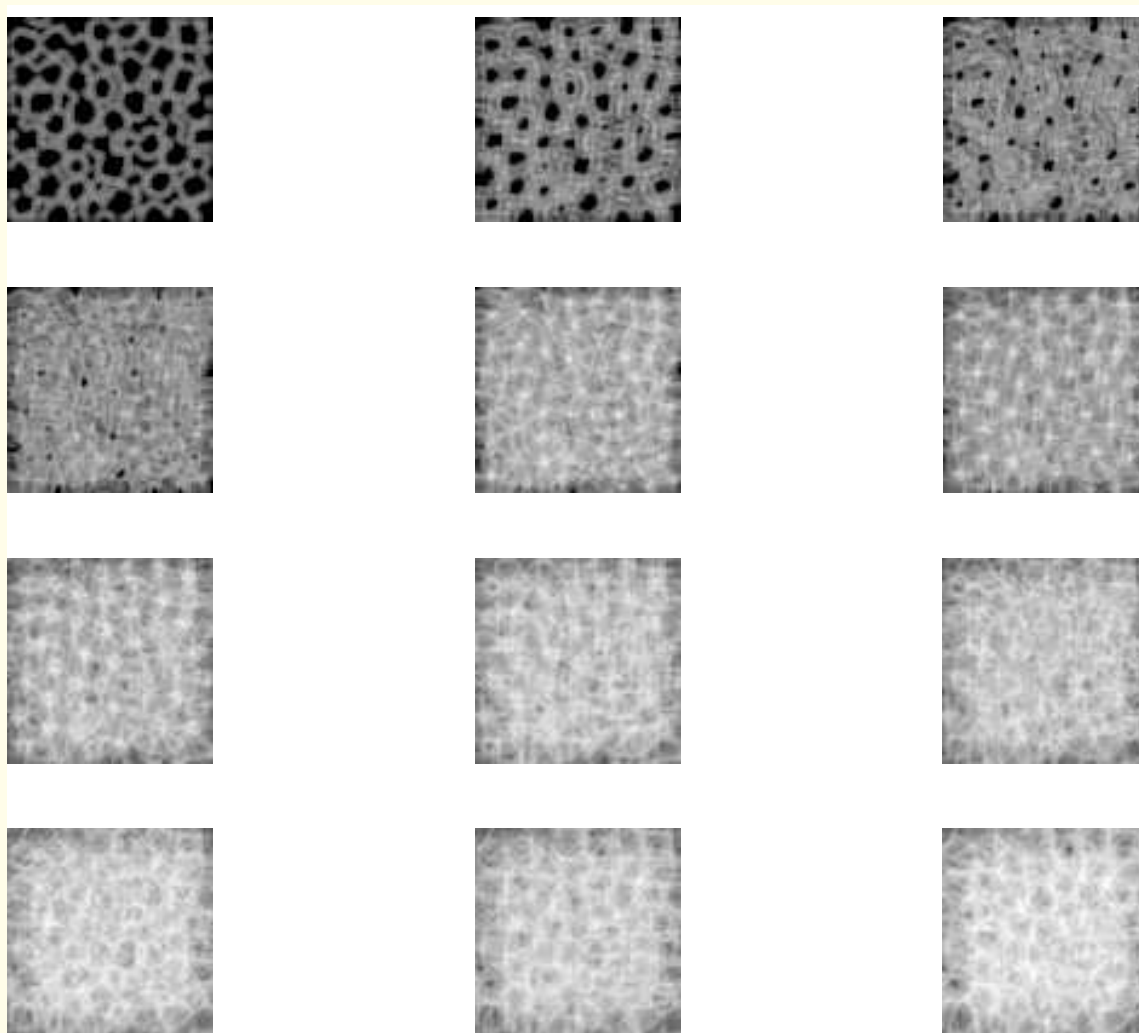


Figure 5.44: Hough parameter  $(a, b, c)$  space of the image in Figure 5.43 (b). Each image is of size  $85 \times 85$  pixels, and represents the range of the  $(a, b)$  coordinates of the center of a potential circle. The series of images represents the various planes of the  $(a, b, c)$  parameter space with  $c = 1, 2, \dots, 12$ , going left to right and top to bottom, representing the radius of potential circles. The intensity of the parameter space values has been enhanced with the log operation.

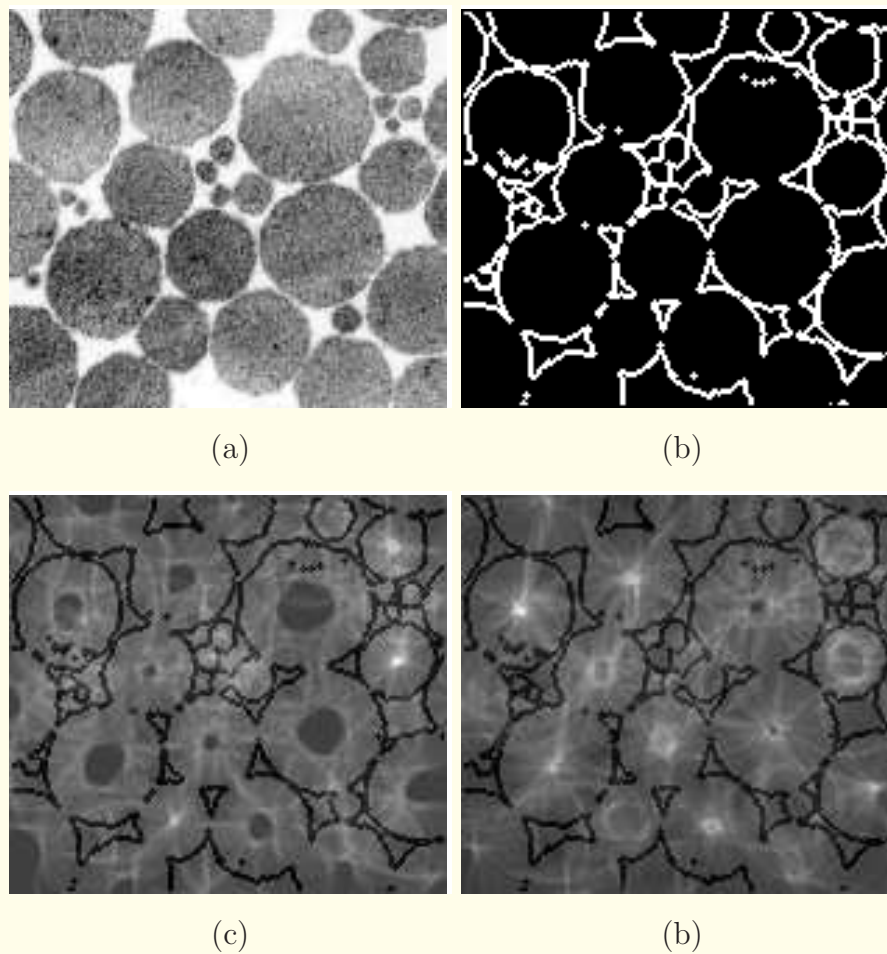


Figure 5.45: (a) TEM image showing collagen fibers in cross-section [a part of the image in Figure 1.5 (a)]. The image is of size  $143 \times 157$  pixels. (b) Edges extracted from the image in (a). (c) Negative version of the image in (b), overlaid with 10 times the  $c = 13$  plane of the Hough transform parameter space. (d) Same as in (c) but with the  $c = 20$  plane. See also Figure 5.46.

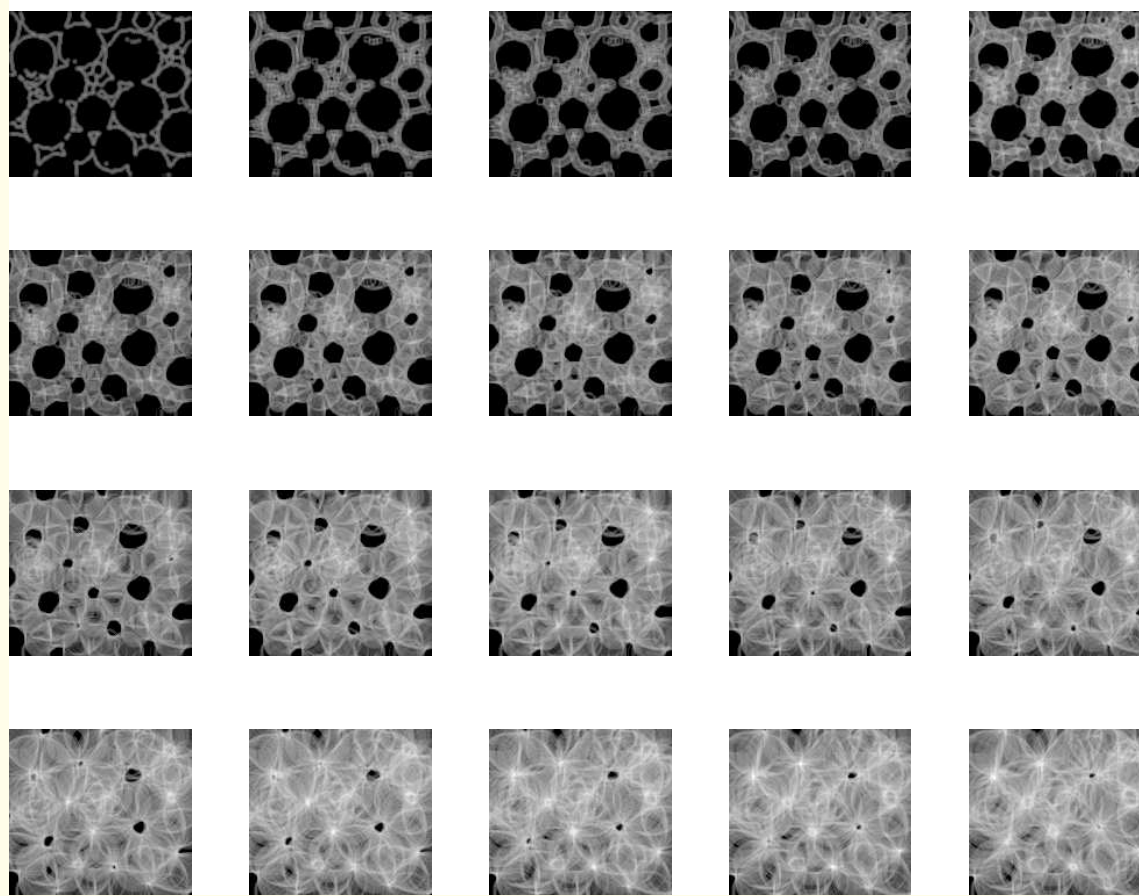


Figure 5.46: Hough parameter  $(a, b, c)$  space of the image in Figure 5.45 (b). Each image is of size  $143 \times 157$  pixels, and represents the range of the  $(a, b)$  coordinates of the center of a potential circle. The series of images represents the various planes of the  $(a, b, c)$  parameter space with  $c = 1, 2, \dots, 20$ , going left to right and top to bottom, representing the radius of potential circles. The intensity of the parameter space values has been enhanced with the log operation.



## 5.7 Methods for the Improvement of Contour or Region Estimates

It is often the case that the contour of an ROI provided by an image processing technique does not satisfy the user.

The user may wish to impose conditions, such as smoothness, on the contour.

It may also be desirable to have the result authenticated by an expert in the field of application.

In such cases, the need may arise to modify the contour.



Techniques that may assist in these tasks:

- Polygonal and parabolic models.
- B-spline and Bezier curves.
- Active contour models or “snakes”.
- The “live wire”.
- Fusion of multiple results of segmentation.



## 5.8 Application: Detection of the Spinal Canal

The spine, spinal cord, and spinal canal form important landmarks in procedures for image-guided surgery, image-guided therapy, the development of human body atlases, and the design of algorithms to detect/ segment other organs.

In an application to analyze CT images of neuroblastoma, the spinal canal was observed to interfere with the segmentation of the tumor using the fuzzy connectivity algorithm.

In order to address this problem, a method was developed to detect the center of the spinal canal in each CT slice, grow the 3D region containing the spinal canal, and remove the structure.



The initializing seeds for the region-growing procedure were automatically obtained with the following procedure.

The outer region in the CT volume containing materials outside the patient, the skin, and peripheral fat was first segmented and removed.

The CT volume was then thresholded at  $+800 \text{ HU}$  to detect the high-density bone structures.

All voxels not within  $8 \text{ mm}$  from the inner boundary of the peripheral fat layer were rejected.

Regions were grown using each remaining voxel, and all of the resulting regions were merged to form the bone volume.



The inclusion criteria were in terms of the CT values being within  $+800 \pm 2\sigma \text{ HU}$ , with  $\sigma = 103 \text{ HU}$  being the standard deviation of bone, and spatial connectivity.

The resulting CT volume was cropped to limit the scope of further analysis, as follows.

The width of the image was divided into three equal parts, and the outer thirds were rejected.

The height of the image was divided into six equal parts, and the lower fourth and fifth parts were included in the cropped region.

In the interslice direction, the first 13% of the slices were removed, and the subsequent 20 slices were included in the cropped volume.



Note: The spinal canal is nearly circular in the thoracic region, but nearly triangular in the cervical region.

The cropped, binarized bone volume was subjected to a 3D derivative operator to produce the edges of the bone structures.

The vertebral column is not continuous, but made up of interlocking elements: the bone-edge map could be sparse.

The Hough transform for the detection of circles was applied to each slice of the bone-edge map.

The radius in the Hough space was limited to the range  $6 - 10 \text{ mm}$ .



Because of the possibility of partial structures and edges in a given image, the global maximum in the Hough space may not relate to the inner circular edge of the spinal canal, as desired.

CT values used as constraints:

bone marrow  $\mu = +142 \text{ HU}$  and  $\sigma = 48 \text{ HU}$ ;

spinal canal  $\mu = +30 \text{ HU}$  and  $\sigma = 8 \text{ HU}$ .

If the center of the circle corresponding to the Hough-space maximum was not within the specified  $\text{HU}$  range, the circle was rejected, and the next maximum was evaluated.

This process was continued until a suitable circle was detected.



The centers of the circles detected were used as the seed voxels in a fuzzy connectivity algorithm to segment the spinal canal.

The mean and standard deviation required were estimated using a  $7 \times 7 \times 2$  neighborhood around each seed voxel.

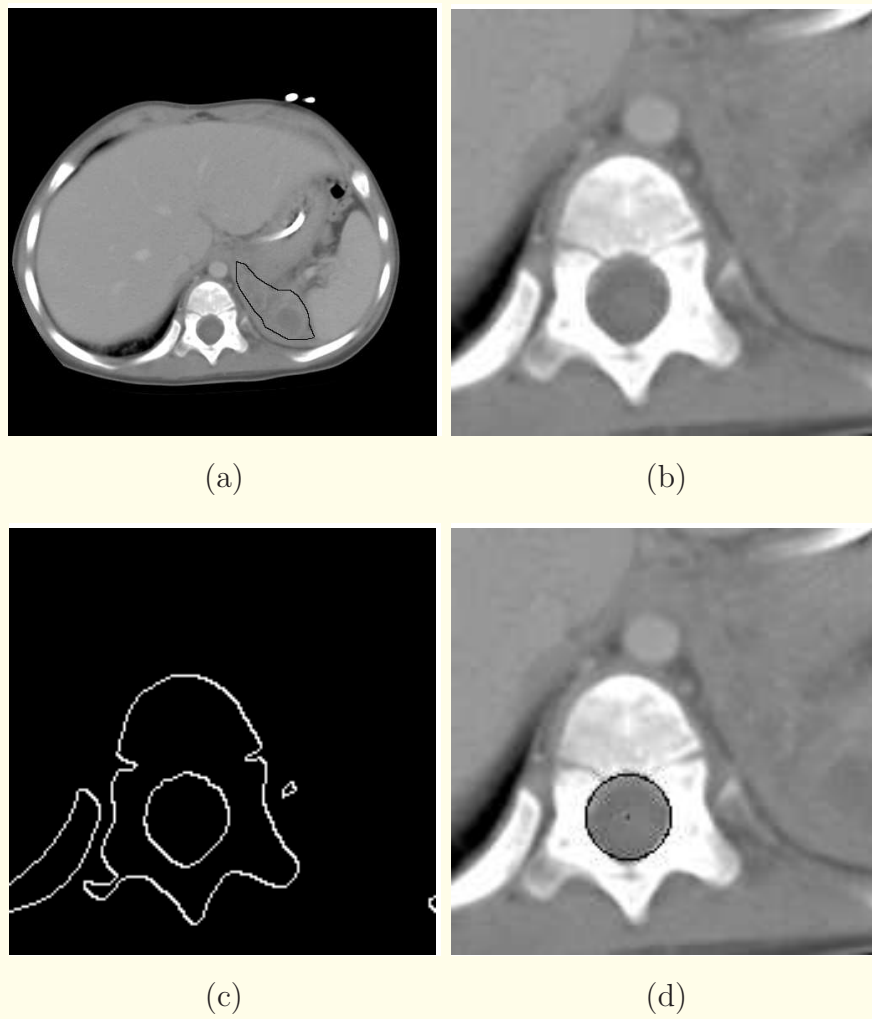


Figure 5.47: (a) A  $512 \times 512$  CT image slice of a patient with neuroblastoma. Pixel width =  $0.41\text{ mm}$ . The tumor boundary drawn by a radiologist is shown in black. (b) Cropped area for further processing. (c) Edge map of the binarized bone volume. (d) Best-fitting circle as determined by Hough-space analysis. The circle has a radius of  $6.6\text{ mm}$ . Figures courtesy of the Alberta Children's Hospital and H.J. Deglint.

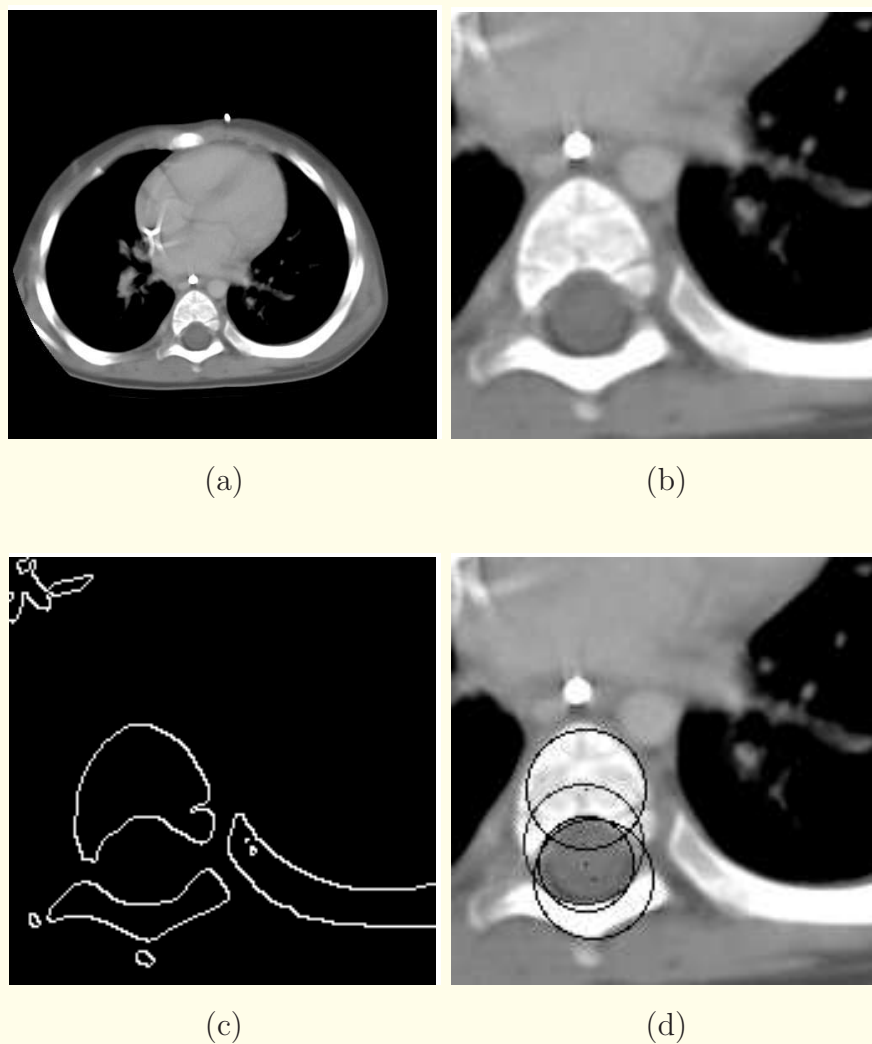


Figure 5.48: (a) A  $512 \times 512$  CT image slice of a patient with neuroblastoma. Pixel width =  $0.41\text{ mm}$ . (b) Cropped area for further processing. (c) Edge map of the binarized bone volume. (d) The four circles corresponding to the first four peaks in the Hough space. The radii of the circles range from  $6.6\text{ mm}$  to  $9.8\text{ mm}$ . See also Figure 5.49. Figures courtesy of the Alberta Children's Hospital and H.J. Deglint.

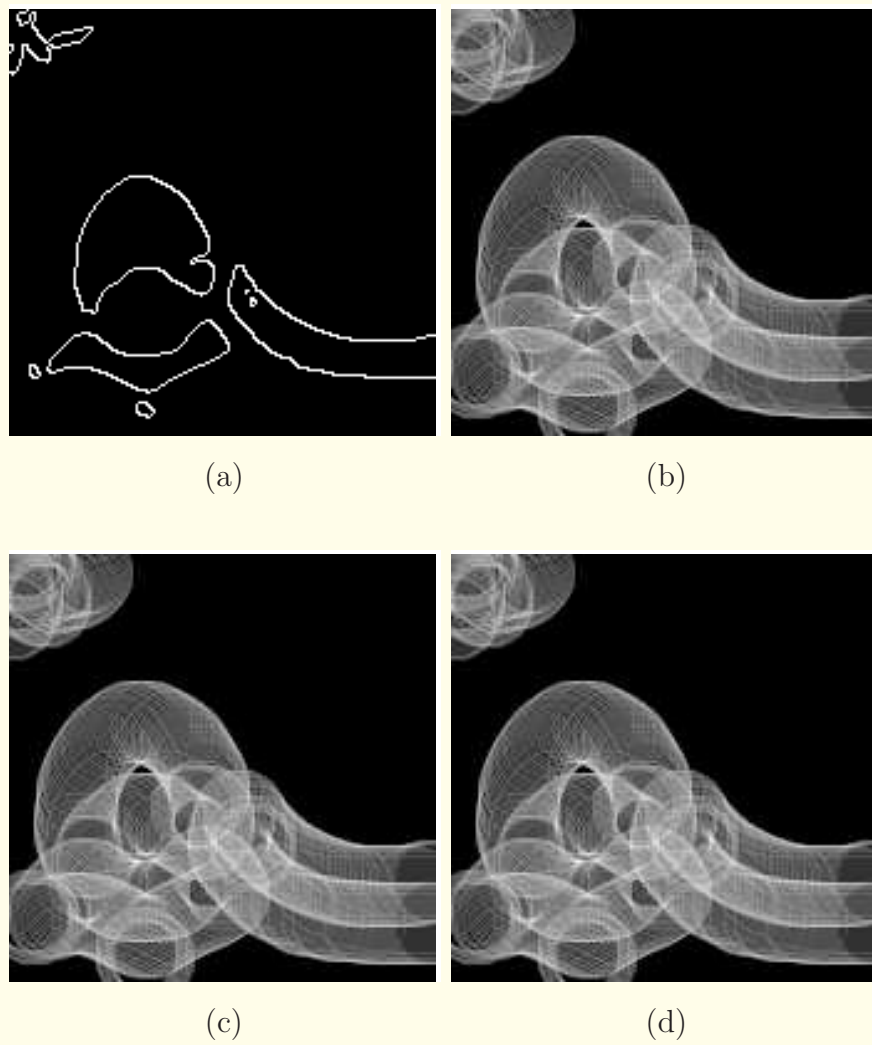


Figure 5.49: (a) Edge map of the binarized bone volume related to the ROI of the CT image in Figure 5.48. Hough-space slices related to the detection of circles of radius (b) 15, (c) 17, and (d) 19 pixels, with the pixel width being [0.41 mm](#). Figures courtesy of H.J. Deglindt.

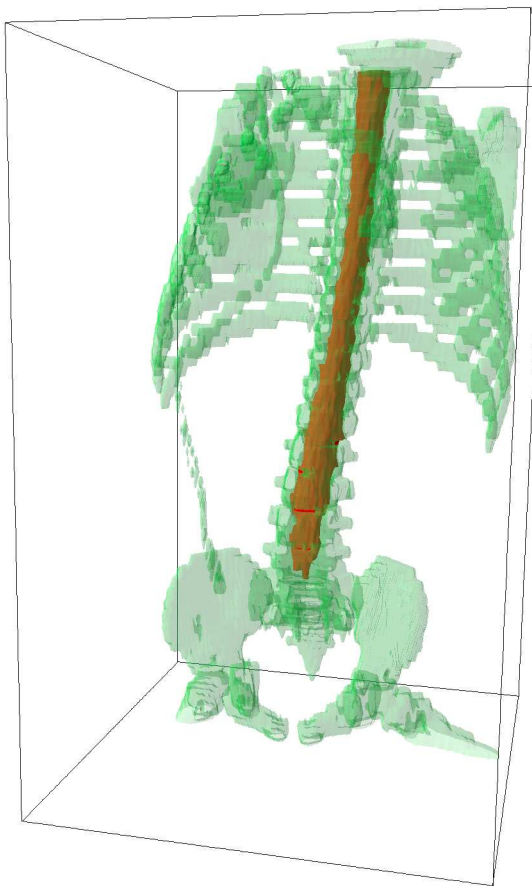


Figure 5.50: 3D rendition of the spinal canal detected for the case related to the CT slices shown in Figures 5.47 and 5.48. The spinal canal is shown in a relatively dark shade of gray against the bone volume for reference.



## 5.9 Application: Detection of the Breast Boundary in Mammograms

Identification of the breast boundary is important in order to demarcate the breast region on a mammogram.

By identifying the boundary of the breast, it is possible to remove any artifact present outside the breast area, such as patient markings and noise, which can affect the performance of image analysis and pattern recognition techniques.



### 5.9.1 *Detection using the traditional active deformable contour model*

Ferrari et al. used the traditional active deformable contour model or snakes for the detection of the breast boundary: Figure 5.51.

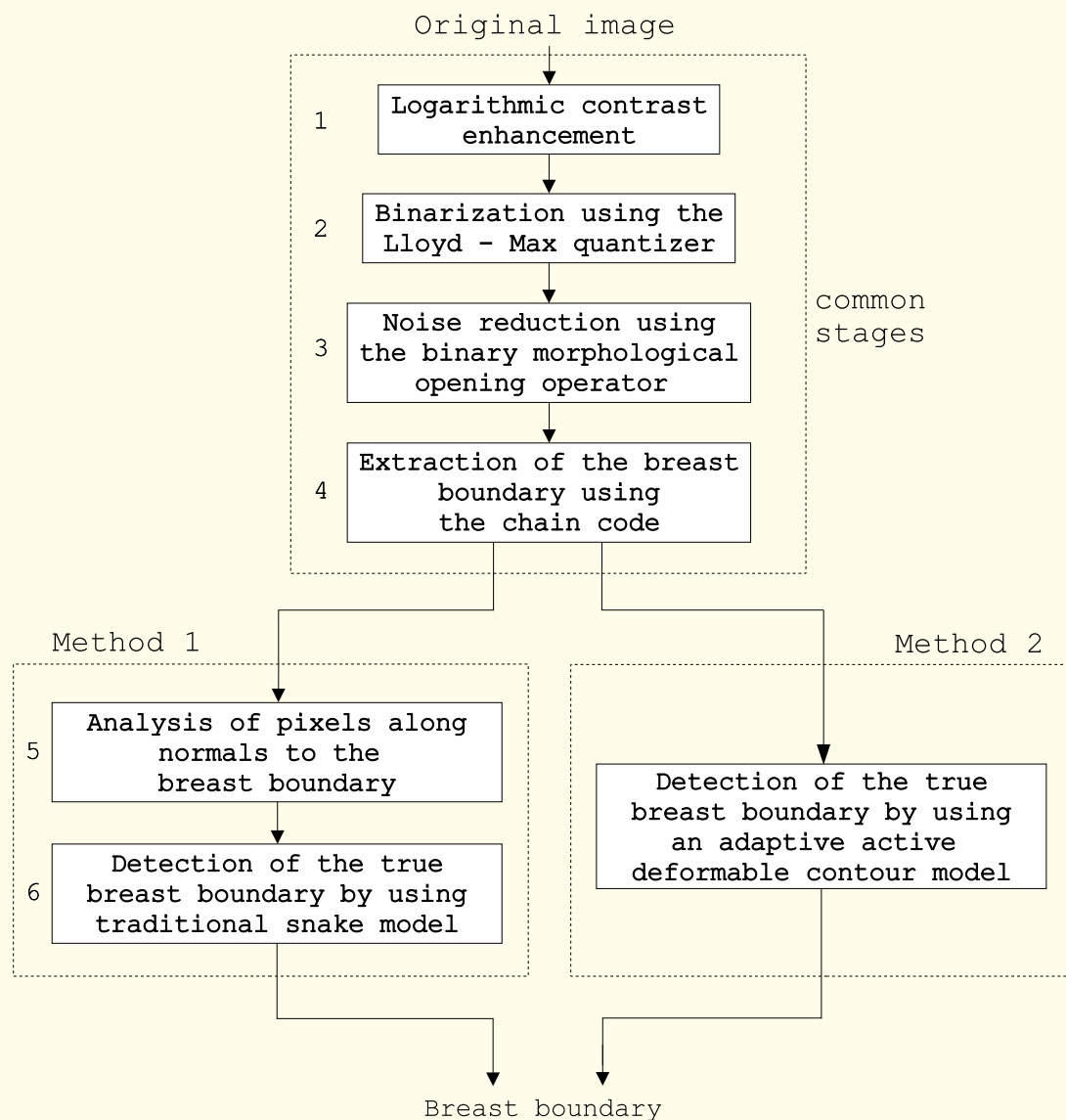


Figure 5.51: Flowchart of the procedures for identification of the skin-air boundary of the breast in mammograms. Reproduced with permission from R.J. Ferrari, R.M. Rangayyan, J.E.L. Desautels, R.A. Borges, and A.F. Frère, “Identification of the breast boundary in mammograms using active contour models”, *Medical and Biological Engineering and Computing*, 42: 201 – 208, 2004. © IFMBE.



**Stage 1:** Image contrast enhanced by using the log operation:

$$g(x, y) = \log[1 + f(x, y)]. \quad (5.68)$$

Provides dynamic range compression and enhances the contrast of the regions near the breast boundary in mammograms, which are characterized by low density and poor definition of details.

See Figures 5.52 (a) and 5.52 (b).

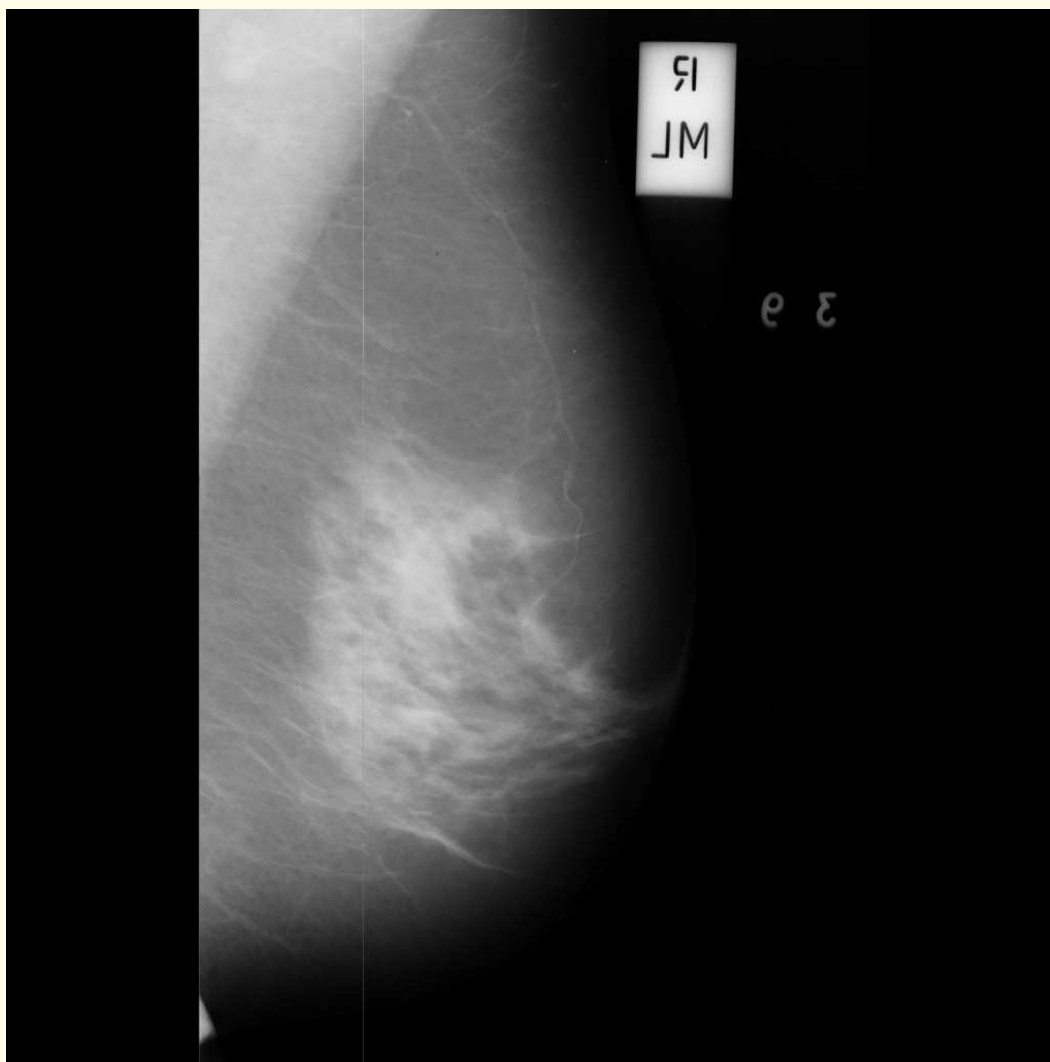


Figure 5.52 (a)

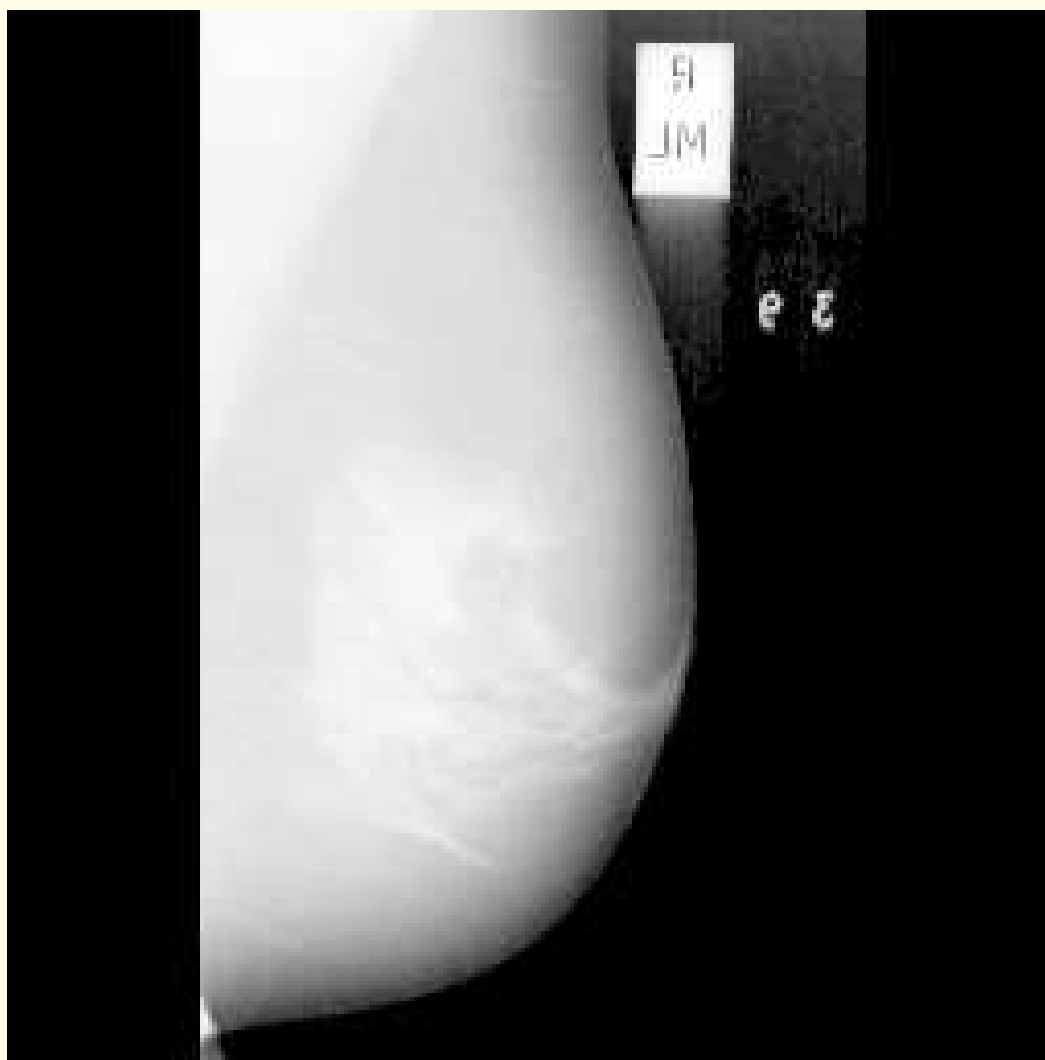


Figure 5.52 (b)

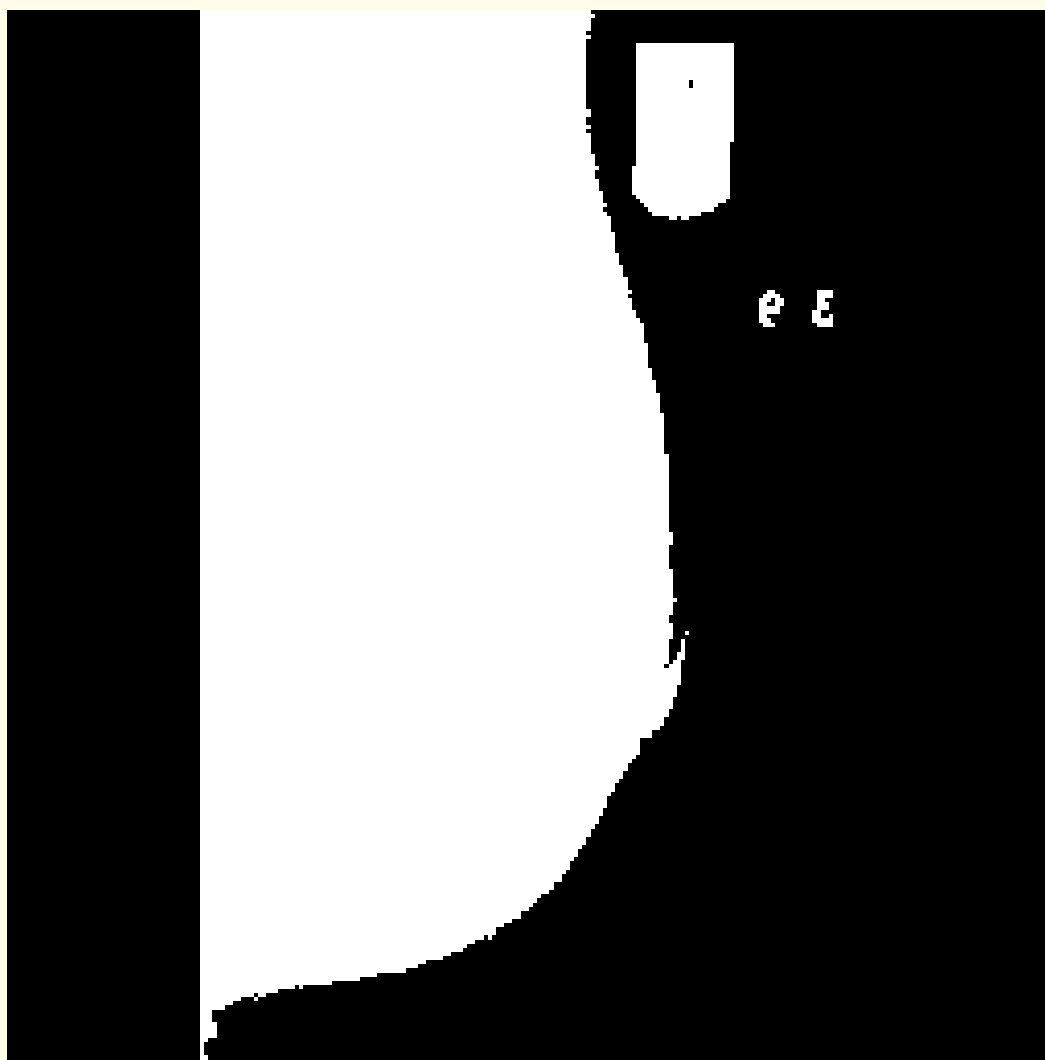


Figure 5.52 (c)

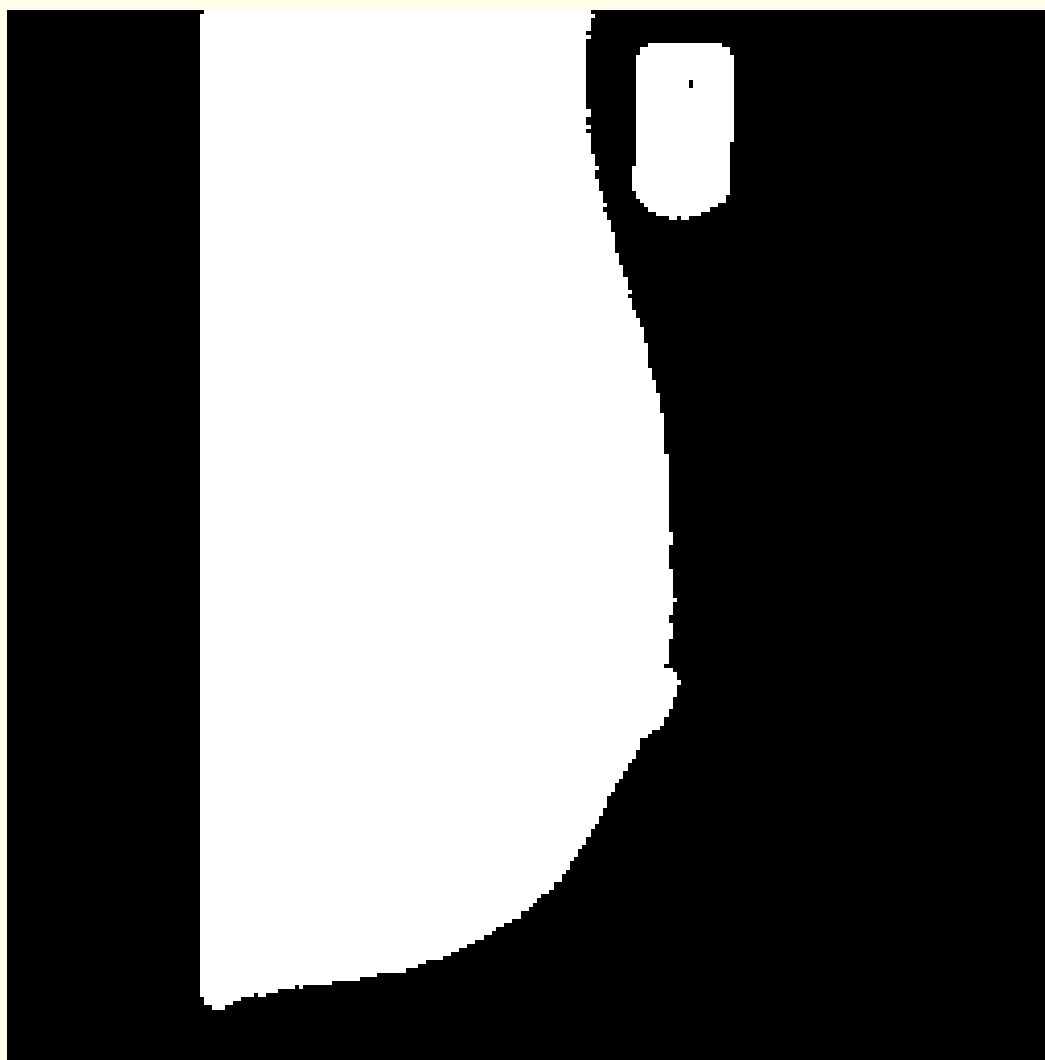


Figure 5.52 (d)

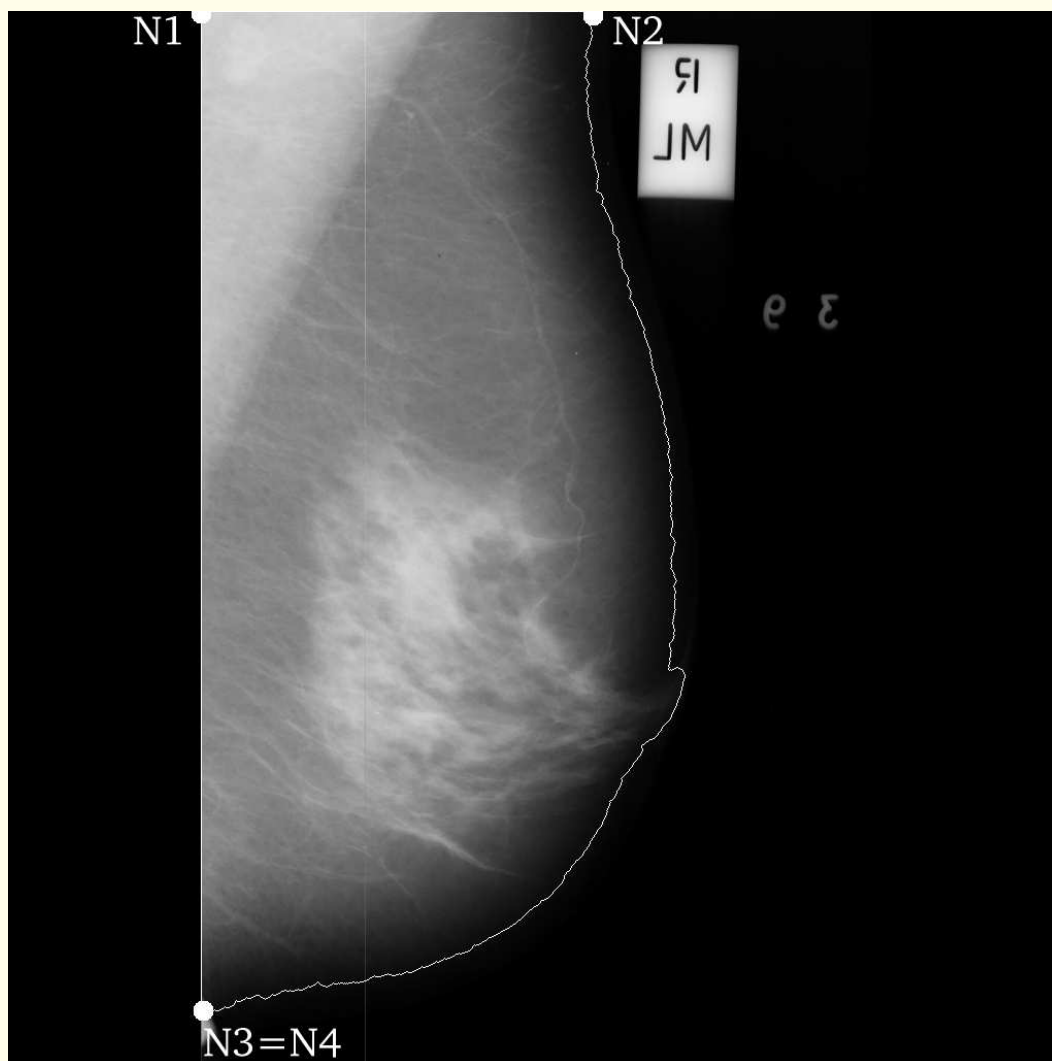


Figure 5.52 (e)

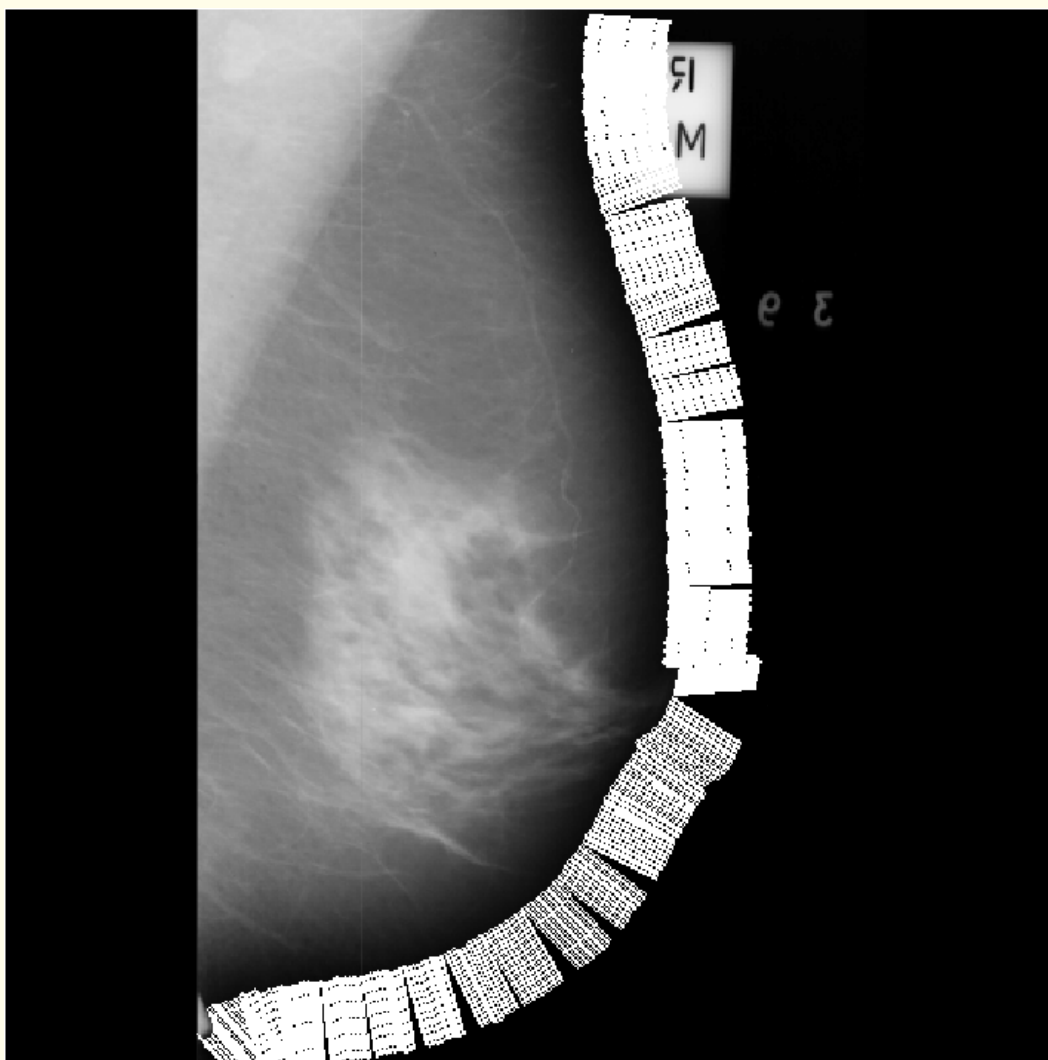


Figure 5.52 (f)

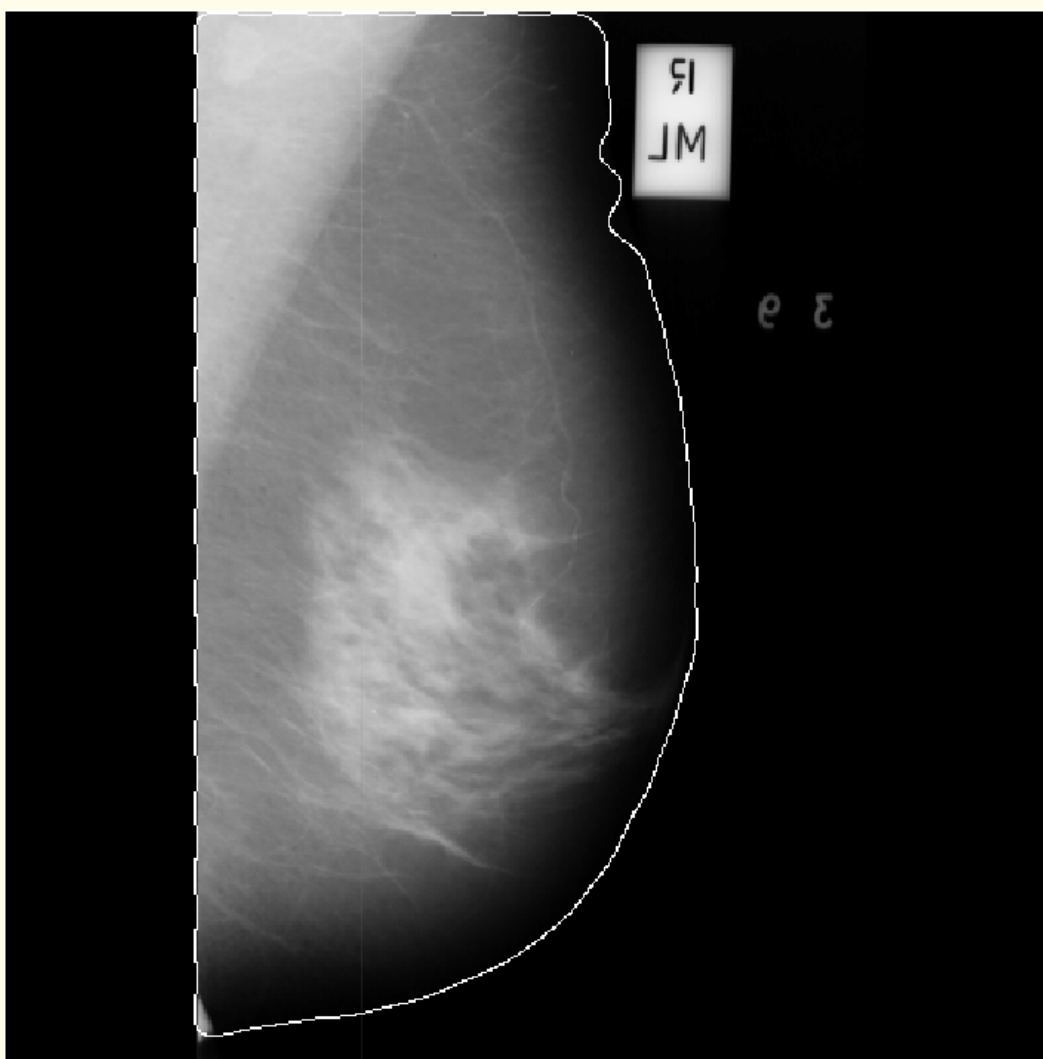
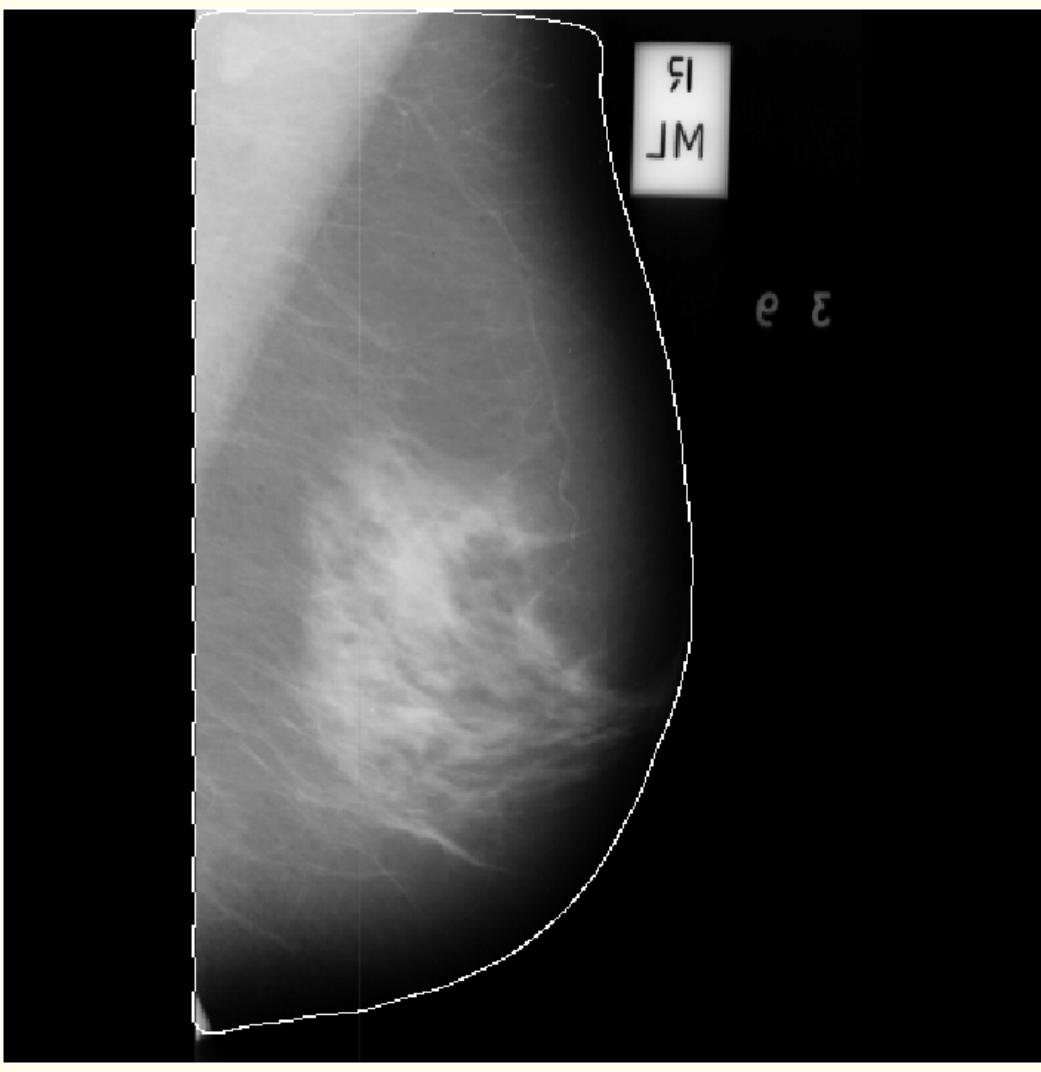


Figure 5.52 (g)



(h)

Figure 5.52: Results of each stage of the method for identification of the breast boundary. (a) Image mdb042 from the Mini-MIAS database. (b) Image after the logarithmic operation. (c)–(d) Binary image before and after applying the binary morphological opening operator. (e) Control points N1 to N4 (automatically determined) used to limit the breast boundary. (f) Normal lines computed from each pixel on the skin-air boundary. (g) Boundary after histogram-based analysis of the normal lines. (h) Final boundary. Reproduced with permission from R.J. Ferrari, R.M. Rangayyan, J.E.L. Desautels, R.A. Borges, and A.F. Frère, “Identification of the breast boundary in mammograms using active contour models”, *Medical and Biological Engineering and Computing*, 42: 201 – 208, 2004. © IFMBE.



**Stage 2:** A binarization procedure using the Lloyd–Max quantization algorithm is applied to the image.

See Figure 5.52 (c).

**Stage 3:** Spurious details generated by the binarization step are removed by using a morphological opening operator with a circular structuring element of diameter 7 pixels.

See Figure 5.52 (d).



**Stage 4:** An approximate contour  $C_{appr}$  of the breast is extracted by using the chain-code method.

The starting point of  $C_{appr}$  is obtained by following the horizontal path that starts at the centroid of the image and is directed toward the chest wall until a background pixel is found.

This procedure avoids selecting an initial boundary from artifacts or patient labels that may be present in the image.



Four control points [see Figure 5.52 (e)] are automatically determined and used to limit the breast boundary:

N1: the top-left corner pixel of the boundary loop;

N2: the farthest point on the boundary from N3  
(in terms of the Euclidean distance through the breast);

N3: the lowest pixel on the left-hand edge of the boundary loop;

N4: the farthest point on the skin-air boundary loop from N1.



**Stage 5:** Pixels along lines of length 40 pixels  
(length = 0.8 cm at a sampling resolution of 200  $\mu\text{m}$ )  
are identified at each point of the approximate skin-air boundary  
in the original image in the direction normal to the boundary;  
see Figure 5.52 (f).

The gray-level histogram of the pixels along each normal line is computed, and the skin-air intersection is defined as the first pixel, while traversing along the normal line from inside the breast toward the outside, that has the gray level associated with the maximum value in the histogram; see Figure 5.53.

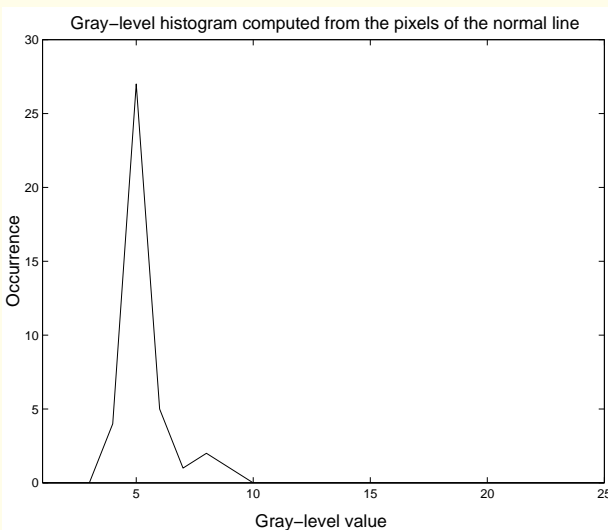
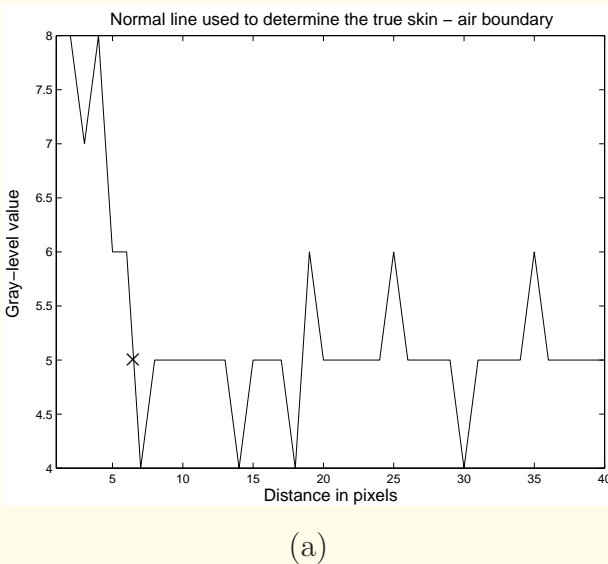


Figure 5.53: (a) Profile of a sample normal line used to determine an approximate skin-air boundary. The symbol  $\times$  indicates the skin-air intersection determined in Stage 5 of the method. (b) Histogram computed from (a). Reproduced with permission from R.J. Ferrari, R.M. Rangayyan, J.E.L. Desautels, R.A. Borges, and A.F. Frère, “Identification of the breast boundary in mammograms using active contour models”, *Medical and Biological Engineering and Computing*, 42: 201 – 208, 2004. © IFMBE.



**Stage 6:** The traditional snakes model is applied to define the true breast boundary.

The contour determined in the previous stage is used as the input to a traditional parametric active contour or snakes model.

The contour is moved through the spatial domain of the image in order to minimize the energy functional

$$E = \int_0^1 \left[ \frac{1}{2} \left\{ \alpha |v'(s)|^2 + \beta |v''(s)|^2 \right\} + E_{ext} \{v(s)\} \right] ds. \quad (5.69)$$



$\alpha$  and  $\beta$  are weighting parameters that control, respectively, the tension and rigidity of the snake.

$v'(s)$  and  $v''(s)$  denote the first and second derivatives of  $v(s)$  with respect to  $s$ , where  $v(s)$  indicates the continuous representation of the contour, and  $s$  represents distance along the contour, normalized to the range  $[0, 1]$ .



The external energy function  $E_{ext} \{v(s)\}$  is derived from the original image  $f(x, y)$  as

$$E_{ext}(x, y) = -\|\nabla f(x, y)\|^2, \quad (5.70)$$

where  $\nabla$  is the gradient operator.

The values  $\alpha = 0.001$  and  $\beta = 0.09$  were experimentally derived by Ferrari et al.



## Results of application to mammograms:

Sixty-six images from the Mini-MIAS database were used to assess the performance of the method.

The results were subjectively analyzed by an expert radiologist.

The method accurately detected the breast boundary in 50 images, and reasonably well in 11 images.

See Figure 5.52 (a) – (h).

The method failed in five images because of distortions and artifacts present near the breast boundary (see Figure 5.54).

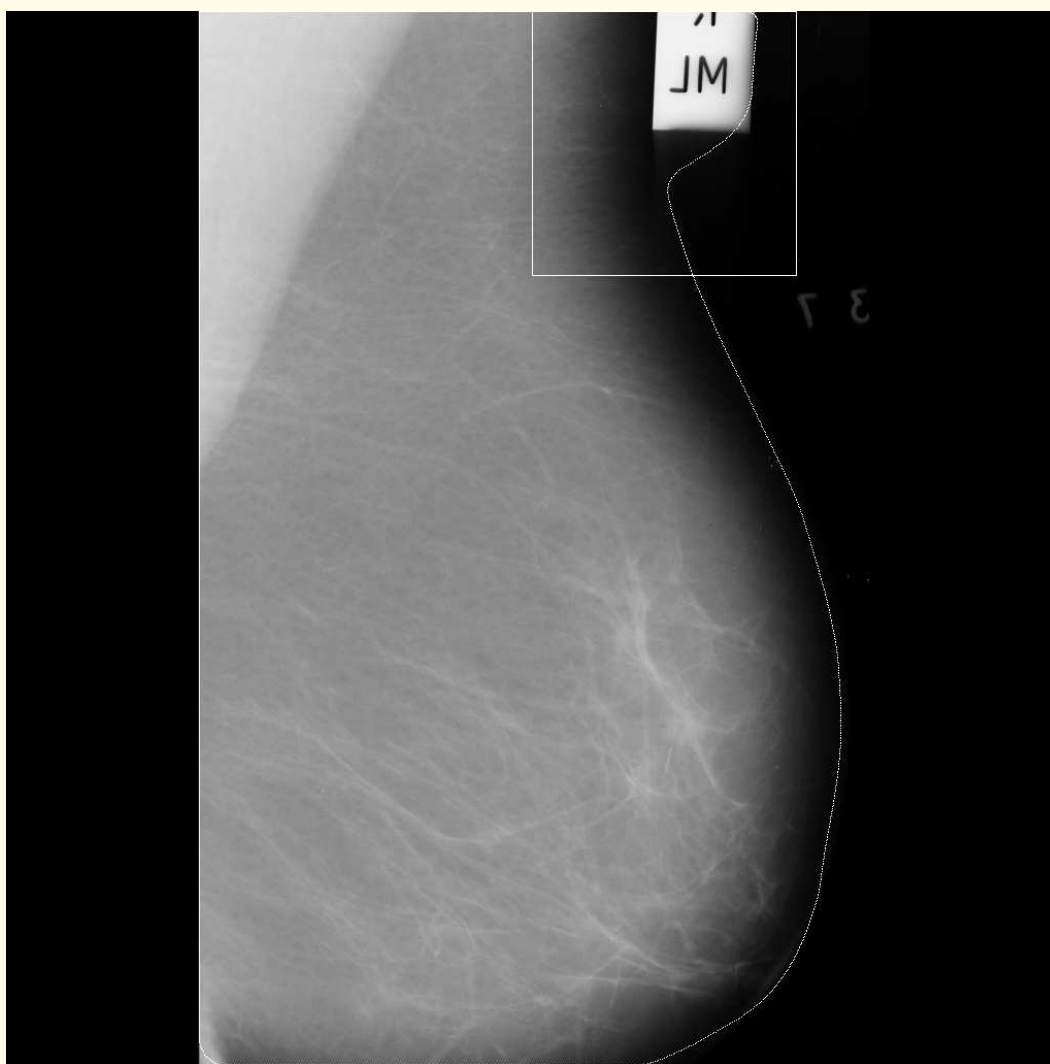
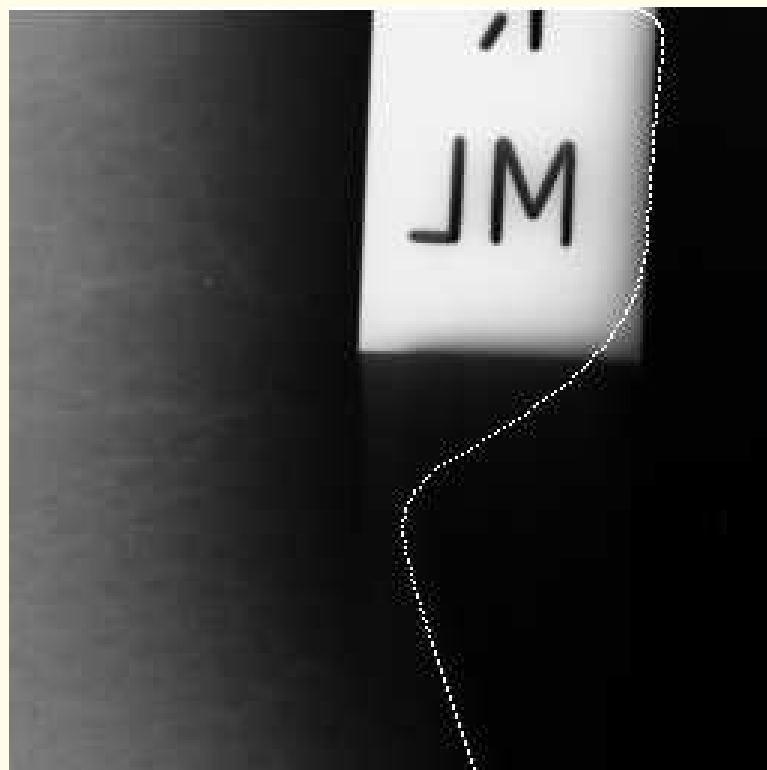


Figure 5.54 (a)



(b)

Figure 5.54: Result of the segmentation algorithm showing wrong convergence of the breast contour to a region of high gradient value. (a) Breast boundary detected, superimposed on the original image mdb006 from the Mini-MIAS database. (b) Details of the breast contour attracted to the image identification marker, corresponding to the boxed region in (a). Compare with Figure 5.59. Reproduced with permission from R.J. Ferrari, R.M. Rangayyan, J.E.L. Desautels, R.A. Borges, and A.F. Frère, “Identification of the breast boundary in mammograms using active contour models”, *Medical and Biological Engineering and Computing*, 42: 201 – 208, 2004. © IFMBE.



### 5.9.2 *Adaptive active deformable contour model*

Ferrari et al. proposed an improved method by replacing the traditional snakes algorithm with an adaptive active deformable contour model (AADCM); see Figure 5.51.

The algorithm includes a balloon force in an energy formulation that minimizes the influence of the initial contour on the convergence of the algorithm.

In the energy formulation, the external energy is also designed to be locally adaptive.



Stages 1 – 4 of the initial method described in the preceding section are used to find an approximate breast boundary.

The approximate contour  $V = v_1, v_2, \dots, v_N$ , with an ordered collection of  $N$  points  $v_i = (x_i, y_i)$ ,  $i = 1, 2, \dots, N$ , is obtained from Stage 4 of the previous method by sampling the approximate contour  $C_{appr}$  [see Figure 5.55 (a)];

used as the initial contour in the AADCM; see Figure 5.55 (b).

Only 10% of the total number of points present in  $C_{appr}$  are used in the sampled contour.

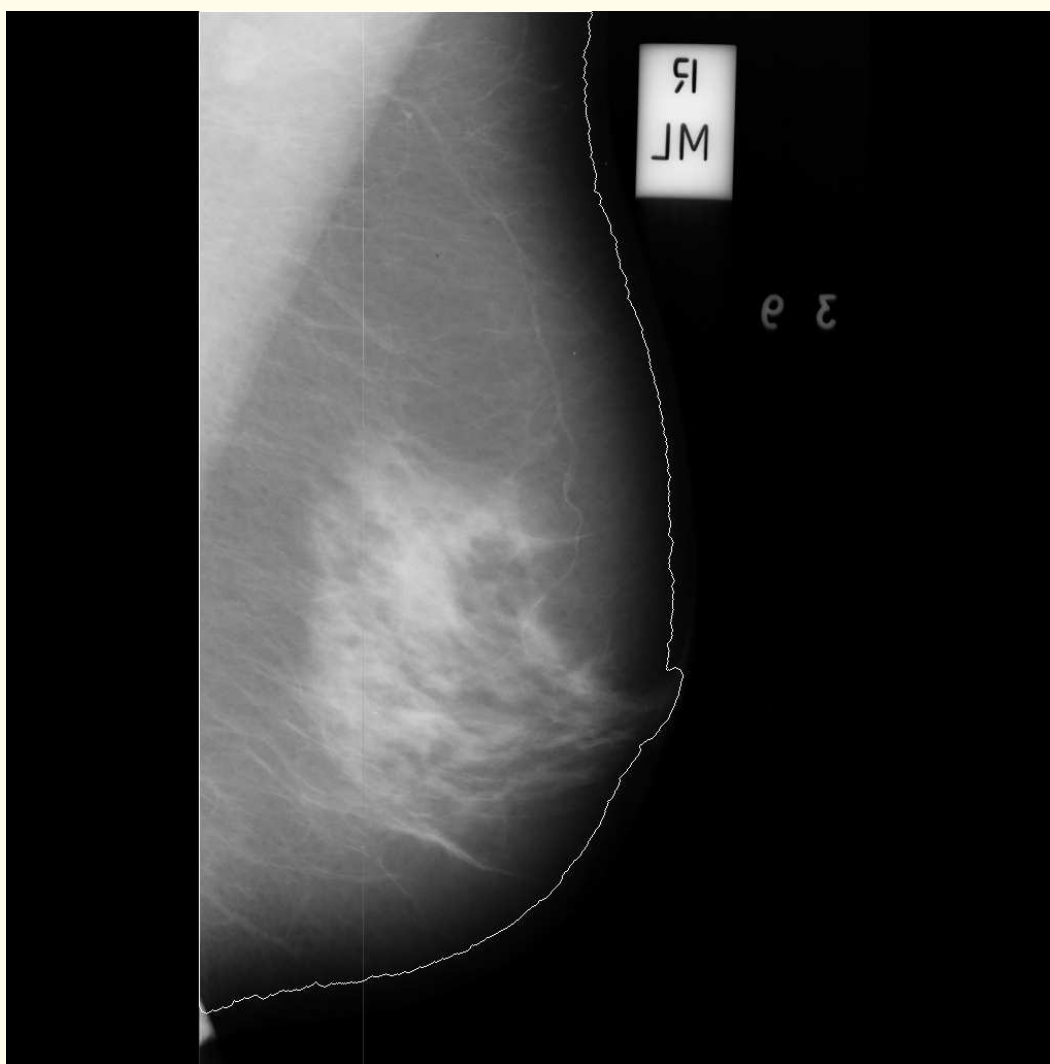
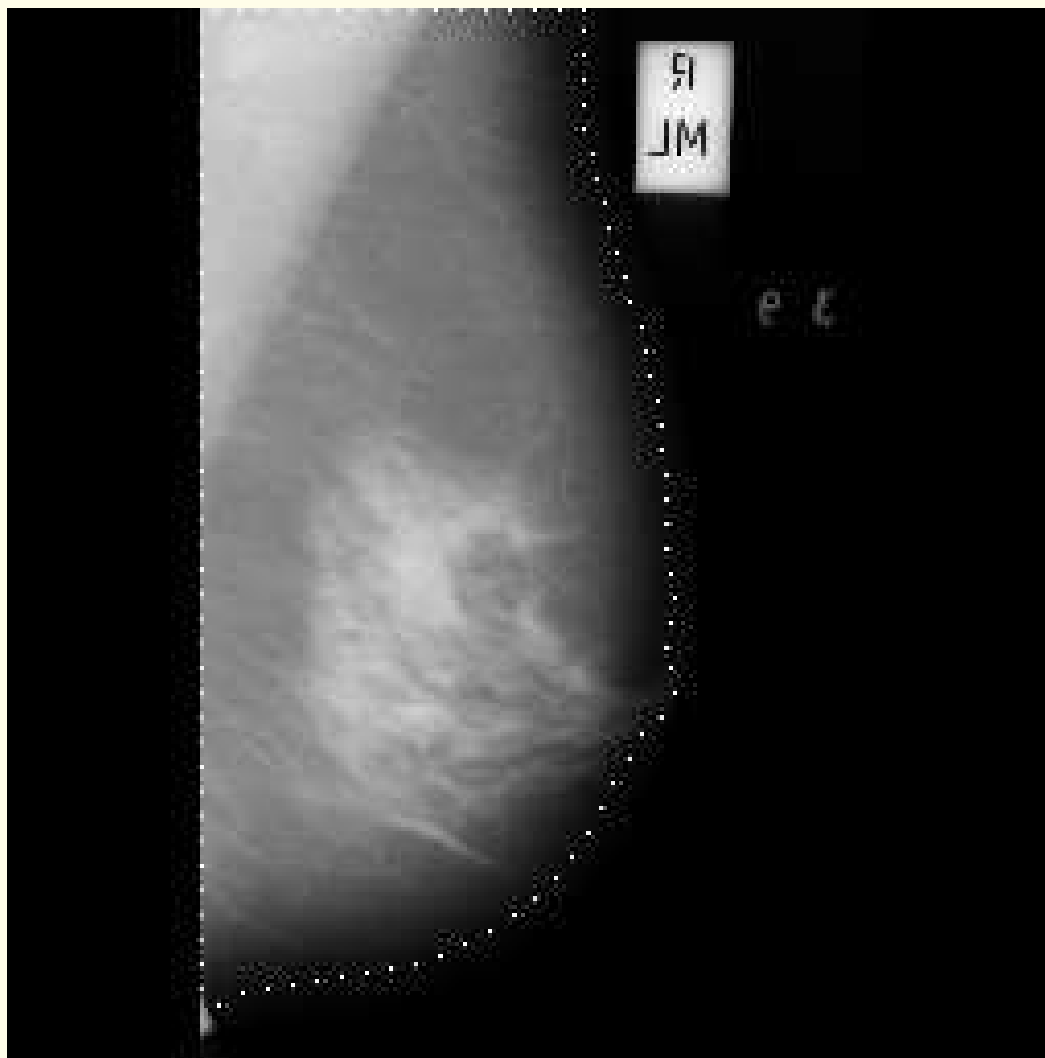


Figure 5.55 (a)



(b)

Figure 5.55: (a) Approximate breast contour obtained from Stage 4 of the method described in Section 5.9.1, for the image mdb042. (b) Sampled breast contour used as the input to the AADCM. Reproduced with permission from R.J. Ferrari, R.M. Rangayyan, J.E.L. Desautels, R.A. Borges, and A.F. Frère, “Identification of the breast boundary in mammograms using active contour models”, *Medical and Biological Engineering and Computing*, 42: 201 – 208, 2004. © IFMBE.



In the AADCM, the contour is moved through the spatial domain of the image to minimize the following functional of energy:

$$E_{total} = \sum_{i=1}^N [\alpha E_{internal}(v_i) + \beta E_{external}(v_i)] , \quad (5.71)$$

where  $\alpha$  and  $\beta$  are weighting parameters that control the internal and external energies  $E_{internal}$  and  $E_{external}$ , respectively, at each point  $v_i$ .



The internal energy is composed of two terms:

$$E_{internal}(v_i) = a E_{continuity}(v_i) + b E_{balloon}(v_i). \quad (5.72)$$

This energy component ensures a stable shape for the contour and constrains to keep constant the distance between the points in the contour.



In the work of Ferrari et al., the weighting parameters  $a$  and  $b$  were initially set to unity ( $a = b = 1$ ), because the initial contours present smooth shapes and are close to the true boundary in most cases.

For each element  $(m, n)$  in a neighborhood of  $7 \times 7$  pixels of  $v_i$ , the continuity term  $e_{c(m,n)}(v_i)$  is computed as

$$e_{c(m,n)}(v_i) = \frac{1}{l(V)} |p_{(m,n)}(v_i) - \rho(v_{i-1} + v_{i+1})|^2. \quad (5.73)$$



$l(V) = \frac{1}{N} \sum_{i=1}^N |v_{i+1} - v_i|^2$  is a normalization factor that makes the continuity energy independent of the size, location, and orientation of  $V$ ;

$p_{(m,n)}(v_i)$  is the point in the image at the position  $(m, n)$  in the  $7 \times 7$  neighborhood of  $v_i$ ;

$\rho = [2 \cos(\frac{2\pi}{N})]^{-1}$  is a constant factor to keep the location of the minimum energy lying on the circle connecting  $v_{i-1}$  and  $v_{i+1}$ , in the case of closed contours; see Figure 5.56.

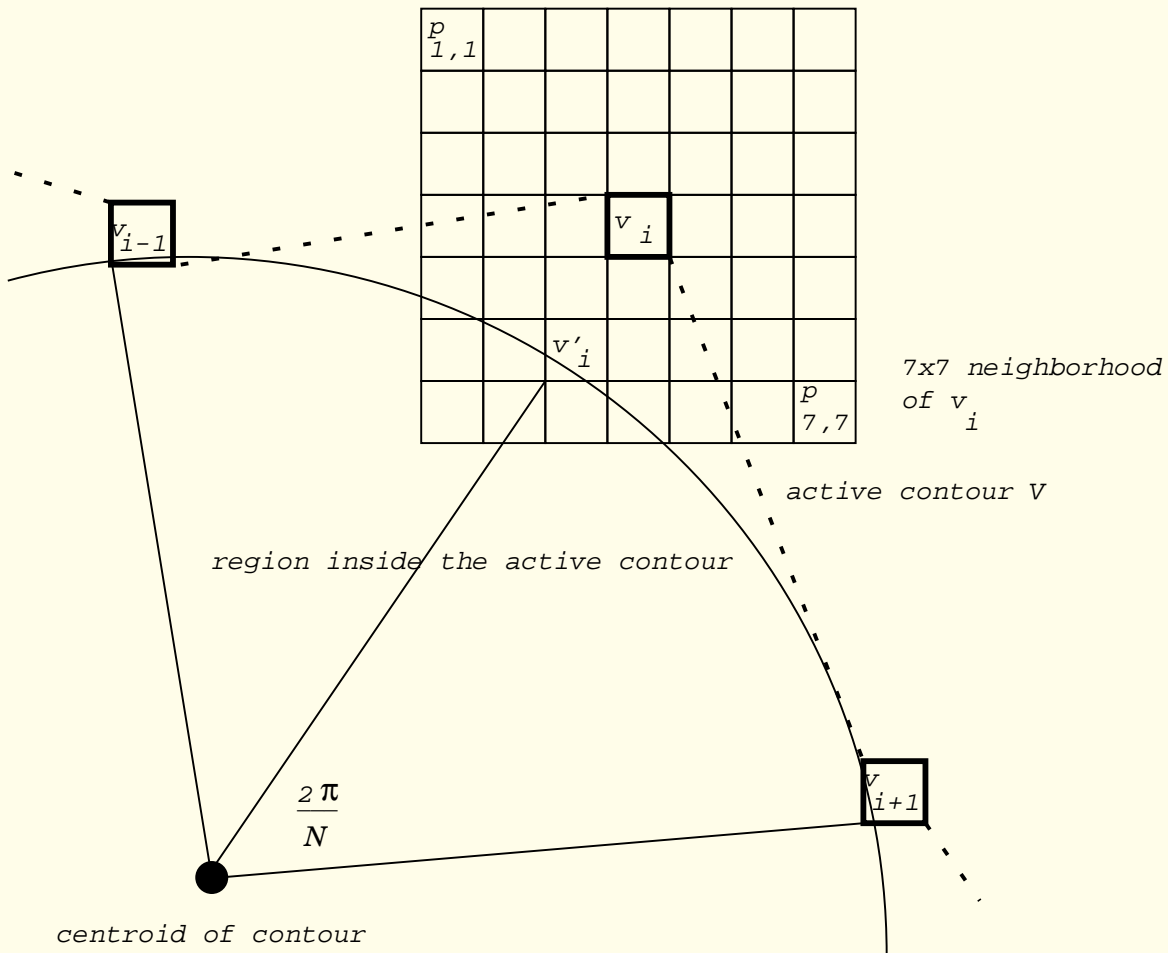


Figure 5.56: Characteristics of the continuity energy component in the adaptive active deformable contour model.  
Figure adapted with permission from B.T. Mackiewich.



The balloon force is used to force the expansion of the initial contour toward the breast boundary.

The balloon force was made adaptive to the magnitude of the image gradient, causing the contour to expand faster in homogeneous regions and slower near the breast boundary.

The balloon energy term  $e_{b(m,n)}(v_i)$  is defined as

$$e_{b(m,n)}(v_i) = \mathbf{n}_i \bullet \{v_i - p_{(m,n)}(v_i)\}. \quad (5.74)$$



$\mathbf{n}_i$  is the outward unit normal vector of  $V$  at the point  $v_i$ ;

the symbol  $\bullet$  indicates the dot product.

$\mathbf{n}_i$  is computed by rotating the vector

$$\mathbf{t}_i = \frac{\mathbf{v}_i - \mathbf{v}_{i-1}}{|\mathbf{v}_i - \mathbf{v}_{i-1}|} + \frac{\mathbf{v}_{i+1} - \mathbf{v}_i}{|\mathbf{v}_{i+1} - \mathbf{v}_i|},$$

which is the tangent vector at the point  $v_i$ , by  $90^\circ$ ; see Figure 5.57.

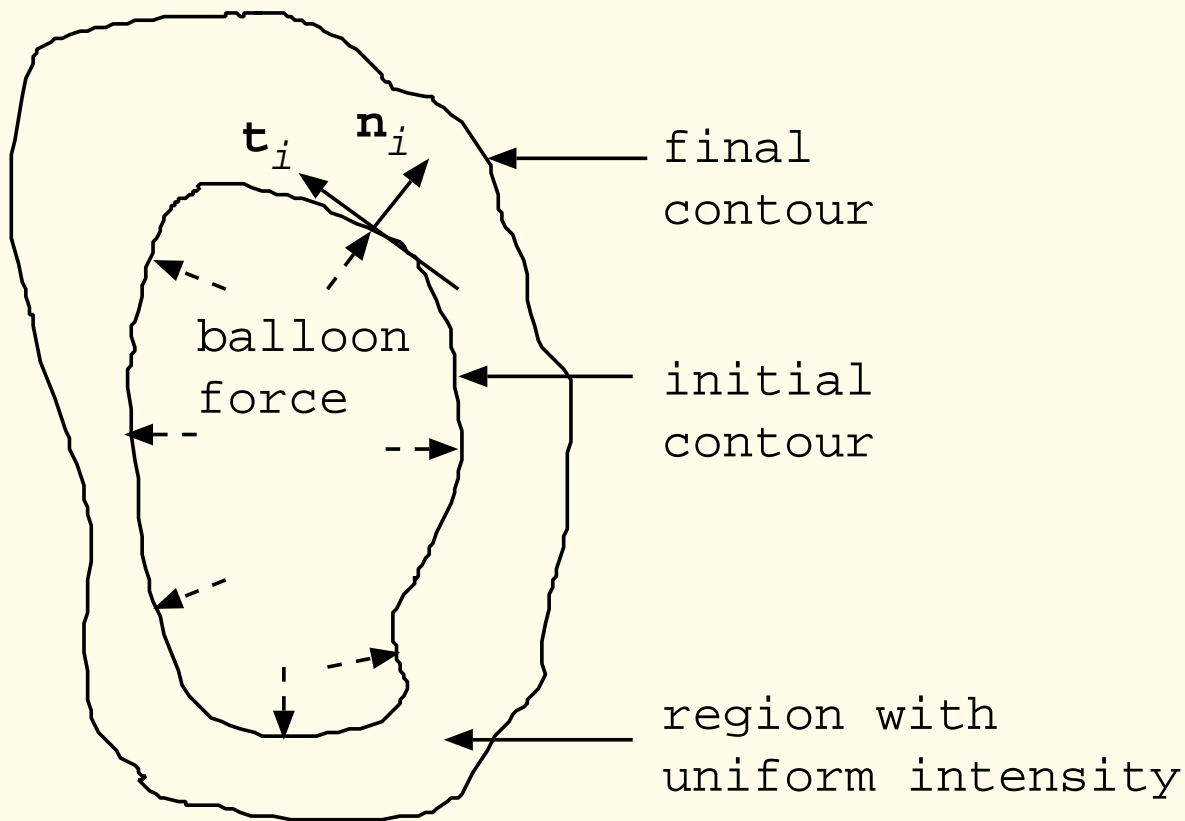


Figure 5.57: Characteristics of the balloon energy component in the adaptive active deformable contour model.  
Figure adapted with permission from B.T. Mackiewich.



The external energy is based upon the magnitude and direction of the image gradient, and is intended to attract the contour to the breast boundary:

$$e_{e(m,n)}(v_i) = -\mathbf{n}_i \bullet \nabla f\{p_{(m,n)}(v_i)\}, \quad (5.75)$$

where  $\nabla f\{p_{(m,n)}(v_i)\}$  is the image gradient vector at  $(m, n)$  in the  $7 \times 7$  neighborhood of  $v_i$ ; see Figure 5.58.



The direction of the image gradient is used to avoid the attraction of the contour by edges that may be located near the true breast boundary, such as identification marks and small artifacts; see Figure 5.59.

In this situation, the gradient direction at the position  $(m, n)$  on an edge near the breast boundary and the direction of the unit normal of the contour will have opposite signs, which makes the functional of energy present a large value at  $(m, n)$ .

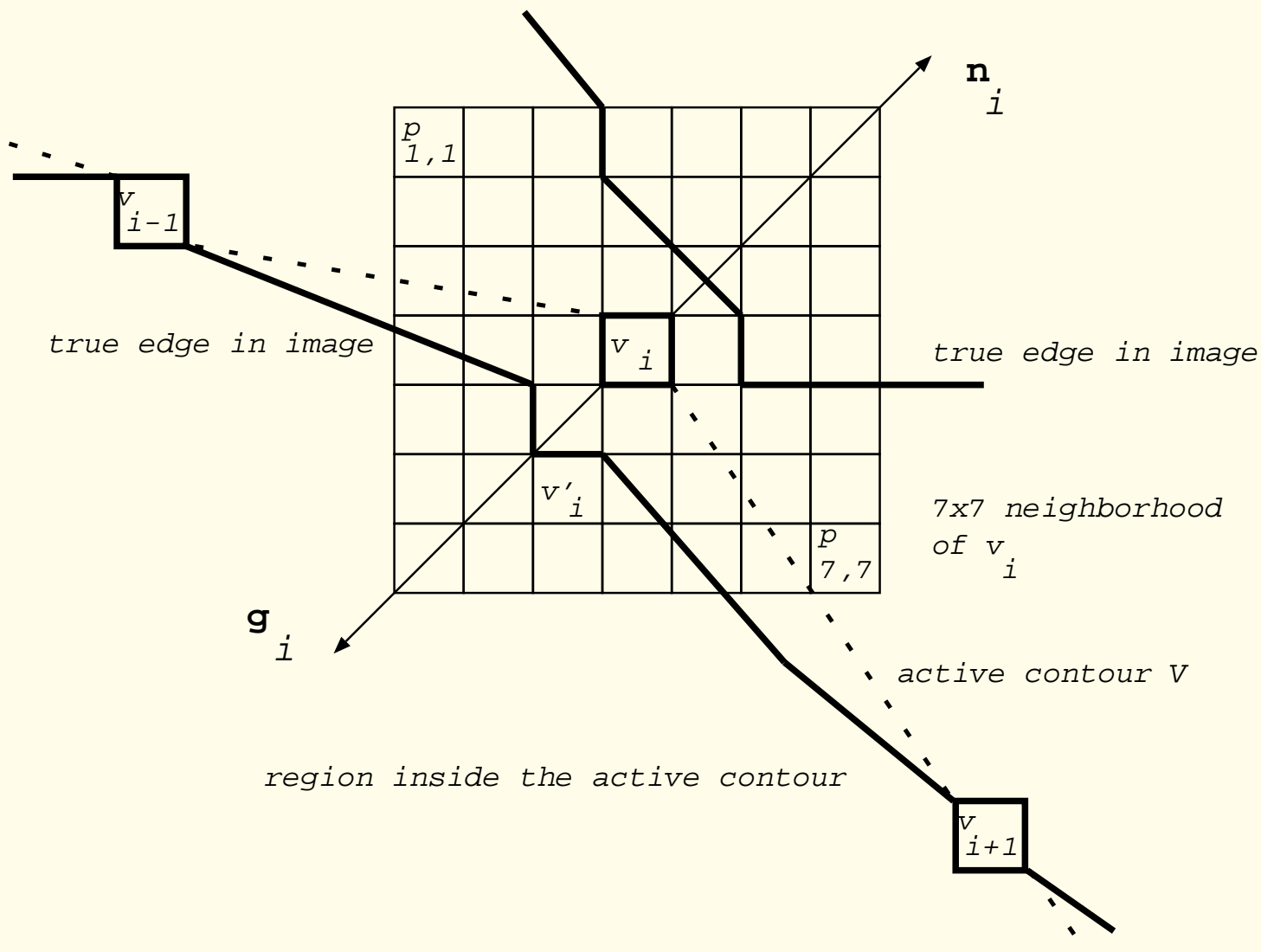
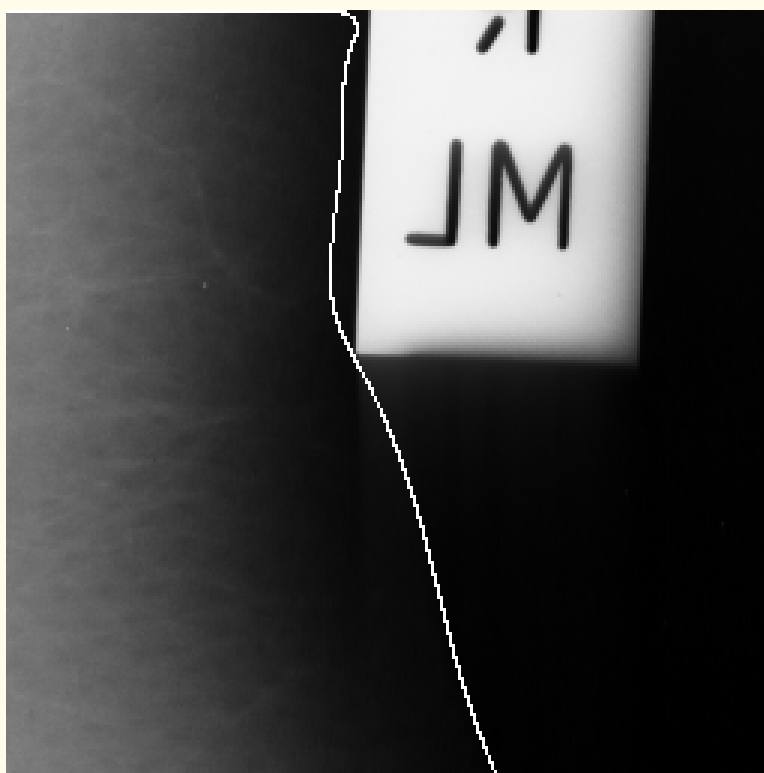


Figure 5.58: Characteristics of the external energy component in the adaptive active deformable contour model. Figure adapted with permission from B.T. Mackiewich.



Figure 5.59 (a)



(b)

Figure 5.59: Application of the gradient direction information to avoid the attraction of the boundary to objects near the true boundary. (a) Breast boundary detected automatically, superimposed on the original image mdb006 from the Mini-MIAS database. (b) Details of the detected breast boundary close to the image identification marker, corresponding to the boxed region in the original image. Compare with Figure 5.54. Reproduced with permission from R.J. Ferrari, R.M. Rangayyan, J.E.L. Desautels, R.A. Borges, and A.F. Frère, “Identification of the breast boundary in mammograms using active contour models”, *Medical and Biological Engineering and Computing*, 42: 201 – 208, 2004. © IFMBE.



## Minimization of the energy functionals:

In order to allow comparison between the various energy components described above, each energy parameter was scaled to the range  $[0, 1]$  as follows:

$$E_{continuity}(v_i) = \frac{e_{c(m,n)}(v_i) - e_{c\min}(v_i)}{e_{c\max}(v_i) - e_{c\min}(v_i)}; \quad (5.76)$$

$$E_{balloon}(v_i) = \frac{e_{b(m,n)}(v_i) - e_{b\min}(v_i)}{e_{b\max}(v_i) - e_{b\min}(v_i)} \left( 1 - \frac{\|\nabla f(v_i)\|}{\|\nabla f\|_{\max}} \right); \quad (5.77)$$



$$E_{external}(v_i) = \frac{e_{e(m,n)}(v_i) - e_{e\min}(v_i)}{\max[e_{e\max}(v_i) - e_{e\min}(v_i), \|\nabla f\|_{\max}]} \quad (5.78)$$

$e_{\min}$  and  $e_{\max}$  indicate the minimum and maximum of the energy component in the  $7 \times 7$  neighborhood of  $v_i$ .

$\|\nabla f\|_{\max}$  is the maximum gradient magnitude in the image.



Ferrari et al. used the Greedy algorithm of Williams and Shah, to minimize the functional of energy in Equation 5.71.

Although this algorithm has the drawback of not guaranteeing a global-minimum solution, it is faster than the other methods proposed in the literature such as dynamic programming, variational calculus, and finite elements.

It also allows the insertion of hard constraints, such as curvature evaluation, as described below.



Convergence of the AADCM is achieved in two stages by smoothing the original image with two different Gaussian kernels defined with  $\sigma_x = \sigma_y = 3$  pixels, and  $\sigma_x = \sigma_y = 1.5$  pixels.

At each stage, the iterative process is stopped when the total energy of the contour increases between consecutive iterations.

This coarse-to-fine representation is expected to provide more stability to the contour.



In order to allow the deformable contour to adjust to corner regions, such as the upper-right limit of the breast boundary, a constraint was inserted at the end of each iteration, to relax the continuity term defined in Equation 5.73.

The curvature value  $C(v_i)$  at each point  $v_i$  of the contour was computed as

$$C(v_i) = 2 \sin\left(\frac{\theta}{2}\right) = \left\| \frac{\mathbf{u}_i}{\|\mathbf{u}_i\|} - \frac{\mathbf{u}_{i-1}}{\|\mathbf{u}_{i-1}\|} \right\|^2, \quad (5.79)$$

where  $\mathbf{u}_i = (v_{i+1} - v_i)$  is the vector joining two neighboring contour elements and  $\theta$  is the external angle between such vectors sharing a common contour element.



This definition of curvature has three important advantages over other curvature measures:

it requires only simple computation,

gives coherent values, and

depends solely on relative direction.



At each  $v_i$ , the weight values for the continuity term and the external energy are set, respectively, to zero ( $a = 0$ ) and to twice the initial value ( $\beta \leftarrow 2\beta$ )

if  $[C(v_i) > C(v_{i-1})]$

and  $[C(v_i) > C(v_{i+1})]$

and  $[C(v_i) > T]$ .

The threshold value  $T$  was set equal to 0.25, which corresponds to an external angle of approximately  $29^\circ$ .

See Figures 5.60 (b) and (c): example without and with the curvature constraint to correct corner effects.

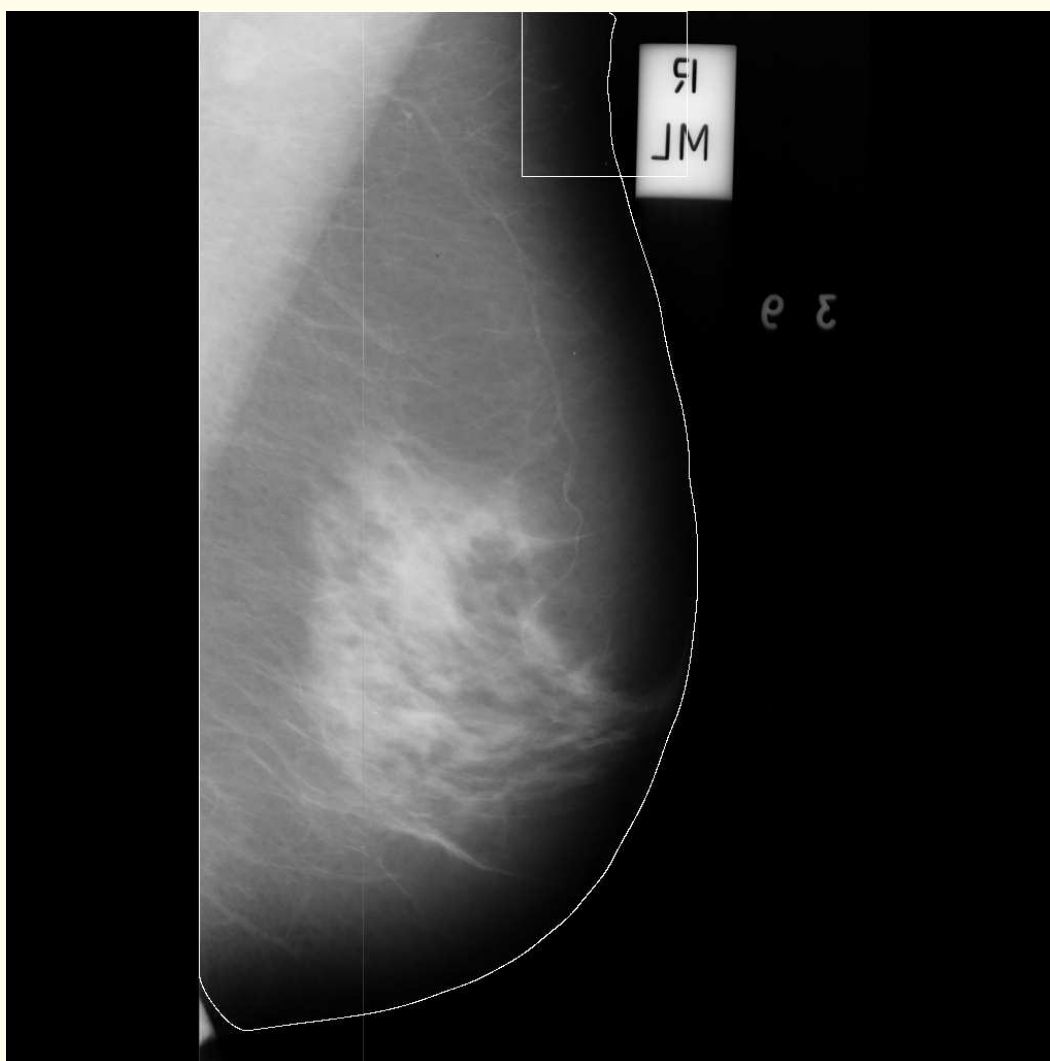


Figure 5.60 (a)

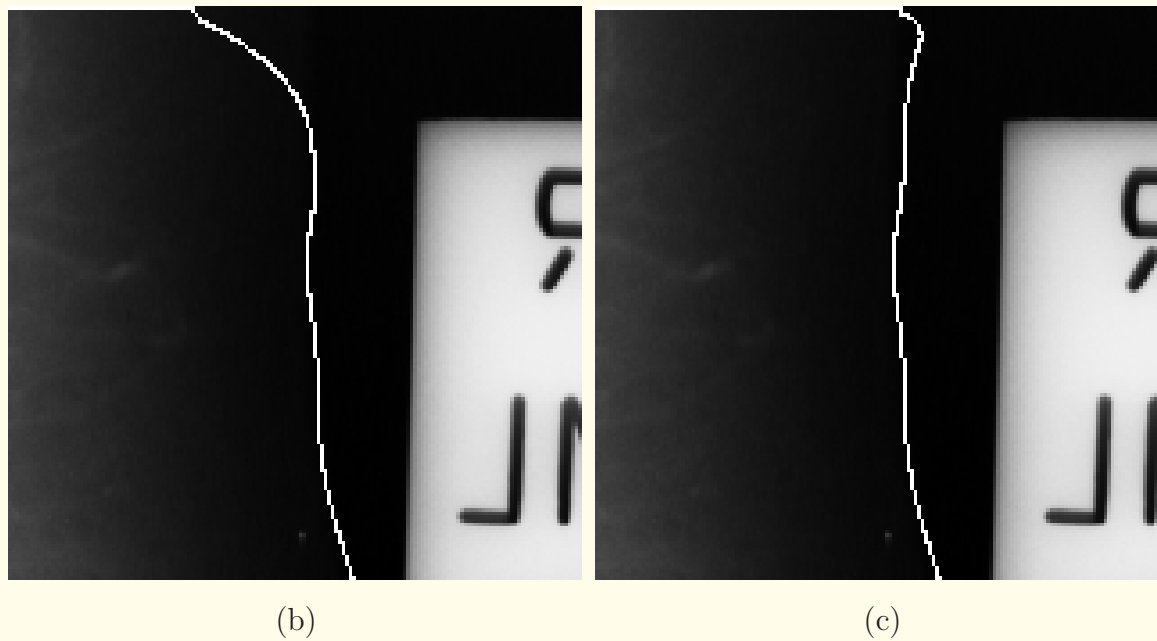


Figure 5.60: Example of the constraint used in the active contour model to prevent smoothing effects at corners. (a) Original image; the box indicates the region of concern. (b) – (c) Details of the breast contour without and with the constraint for corner correction, respectively. Reproduced with permission from R.J. Ferrari, R.M. Rangayyan, J.E.L. Desautels, R.A. Borges, and A.F. Frère, “Identification of the breast boundary in mammograms using active contour models”, *Medical and Biological Engineering and Computing*, 42: 201 – 208, 2004. © IFMBE.



In the work of Ferrari et al., the weighting parameters  $\alpha$  and  $\beta$  in Equation 5.71 were initialized to 0.2 and 1.0, respectively, for each contour element.

A larger weight was given to the gradient energy to favor contour deformation toward the breast boundary rather than smoothing due to the internal force.



### 5.9.3 *Results of application to mammograms*

Ferrari et al. applied their methods to 84 images randomly chosen from the Mini-MIAS database.

All images were MLO views with  $200 \mu\text{m}$  sampling interval and 8-bit gray-level quantization.

For reduction of processing time, all images were downsampled to  $256 \times 256$  pixels.

The results were mapped to the original mammograms for subsequent analysis and display.

The results were evaluated in consultation with two radiologists experienced in mammography.



The test images were displayed on a computer monitor with a diagonal size of *47.5 cm* and dot pitch of *0.27 mm*.

By using the Gimp program, the contrast and brightness of each image were manually enhanced so that the breast contour could be easily visualized.

The breast boundary was manually drawn under the supervision of a radiologist, and the results printed on paper by using a laser printer with *600 dpi* resolution.

The zoom option of the Gimp program was used to aid in drawing the contours.



The breast boundaries of all images were visually checked by a radiologist using the printed images (hardcopy) along with the displayed images (softcopy).

The segmentation results were evaluated based upon the number of false-positive (FP) and false-negative (FN) pixels identified and normalized with reference to the corresponding areas demarcated by the manually drawn contours.

The FP and FN average percentages and the corresponding standard deviation values obtained for the 84 images were  $0.41 \pm 0.25\%$  and  $0.58 \pm 0.67\%$ , respectively.



Thirty-three images had both FP and FN < 0.5%;

38 images had FP and FN between 0.5% and 1%;

FP and FN were greater than 1% for 13 images.

The most common cause of FN pixels was related to missing the nipple region, as illustrated by the example in Figure 5.61 (c).

The breast boundary was used by Ferrari et al. in the analysis of bilateral asymmetry.

Other applications:

image compression by using only the effective area of the breast;  
image registration.

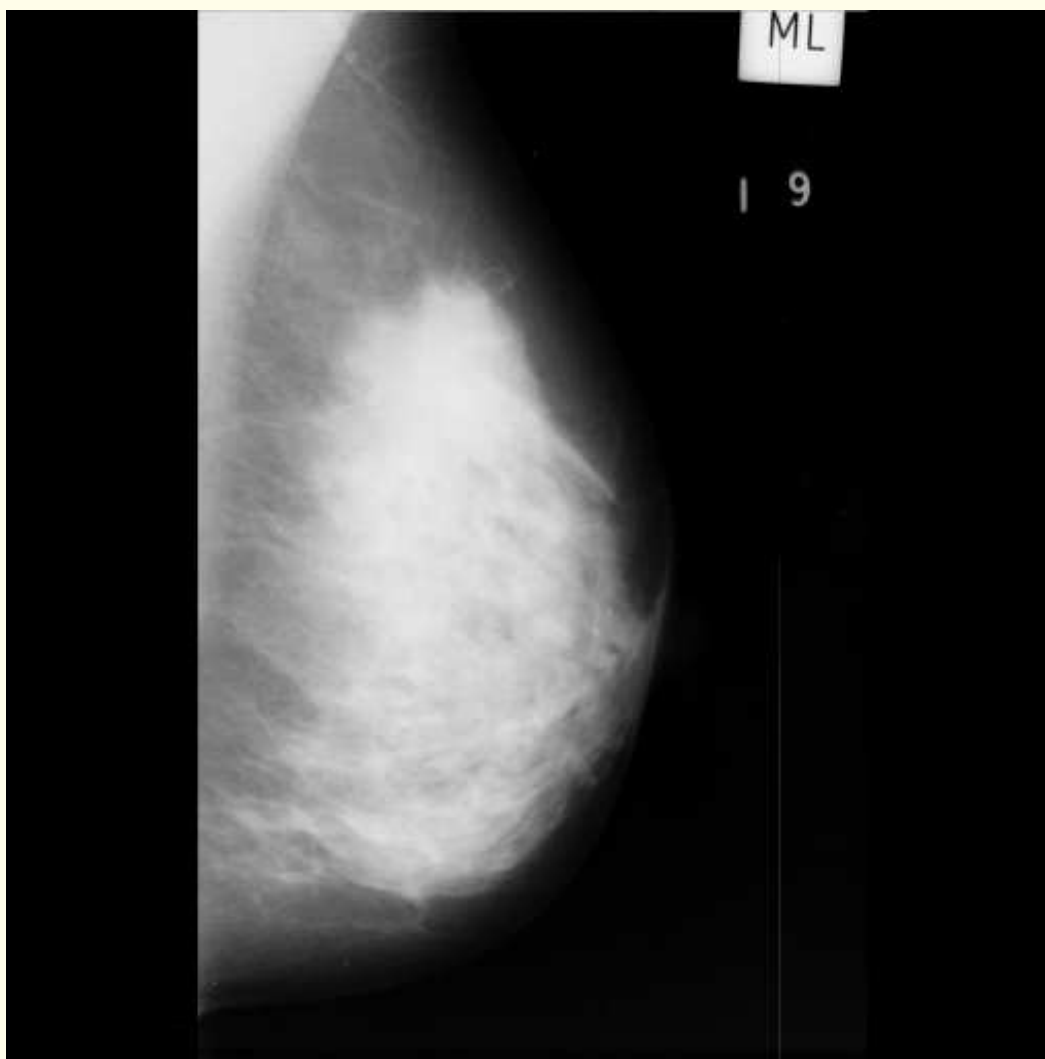


Figure 5.61 (a)

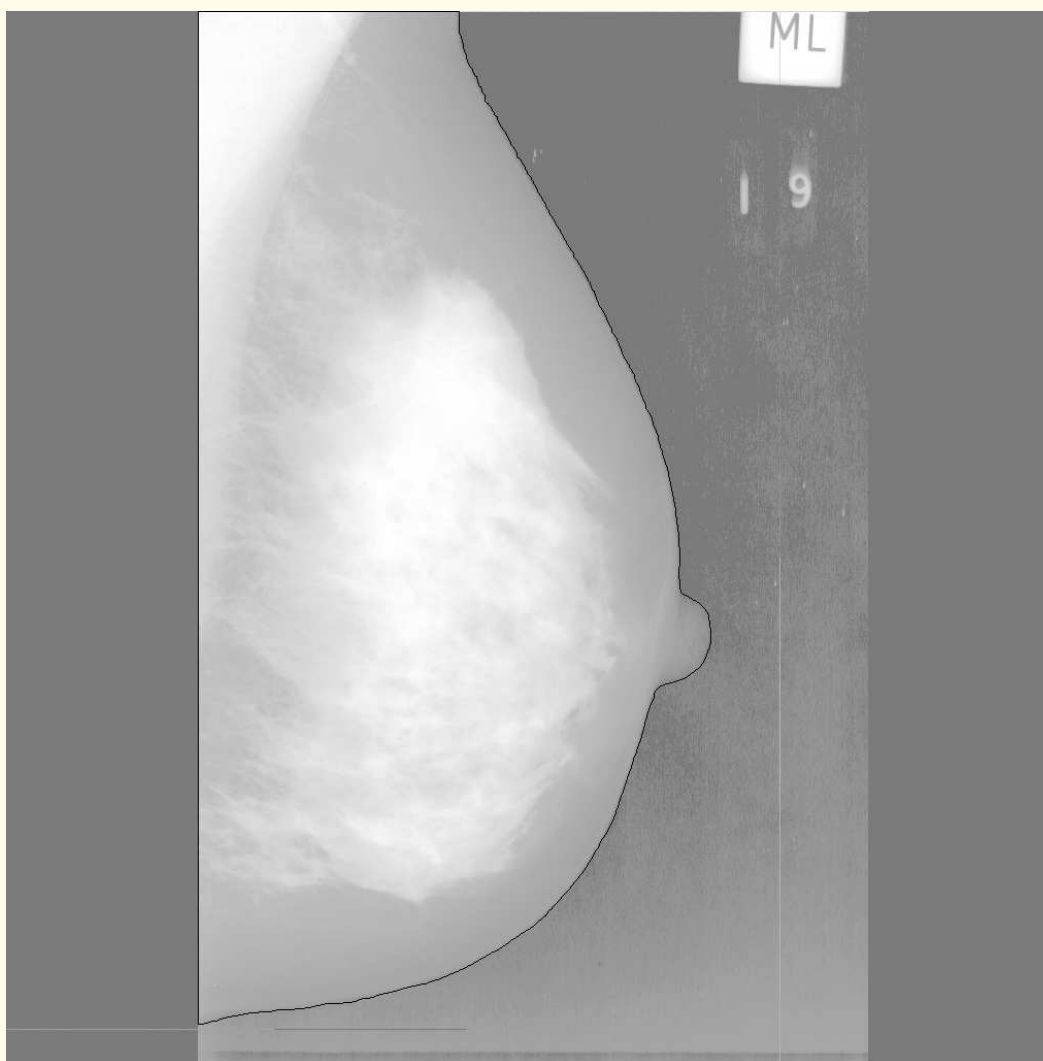
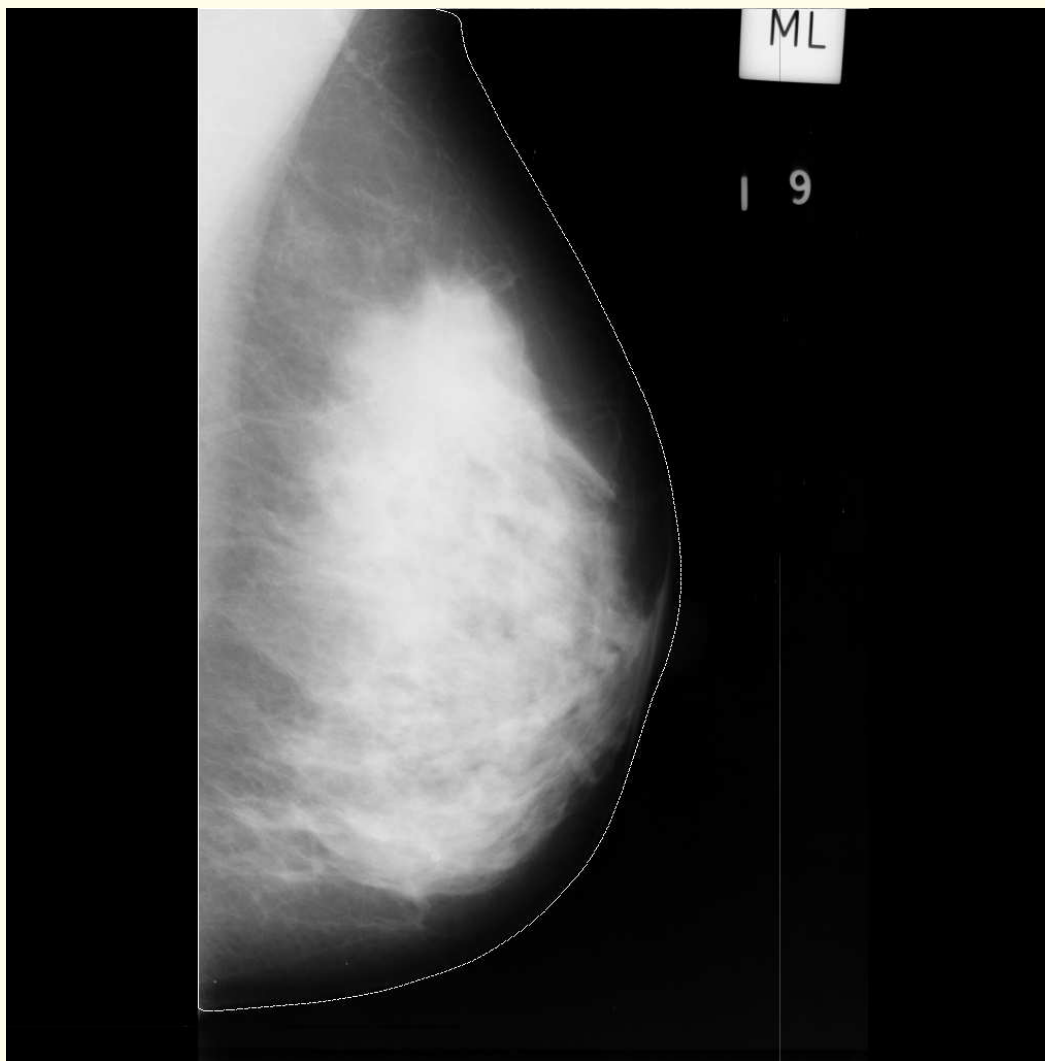


Figure 5.61 (b)



(c)

Figure 5.61: Results obtained for the image mdb003 from the Mini-MIAS database. (a) Original image. (b) Hand-drawn boundary superimposed on the histogram-equalized image. (c) Breast boundary detected, superimposed on the original image. Reproduced with permission from R.J. Ferrari, R.M. Rangayyan, J.E.L. Desautels, R.A. Borges, and A.F. Frère, “Identification of the breast boundary in mammograms using active contour models”, *Medical and Biological Engineering and Computing*, 42: 201 – 208, 2004. © IFMBE.

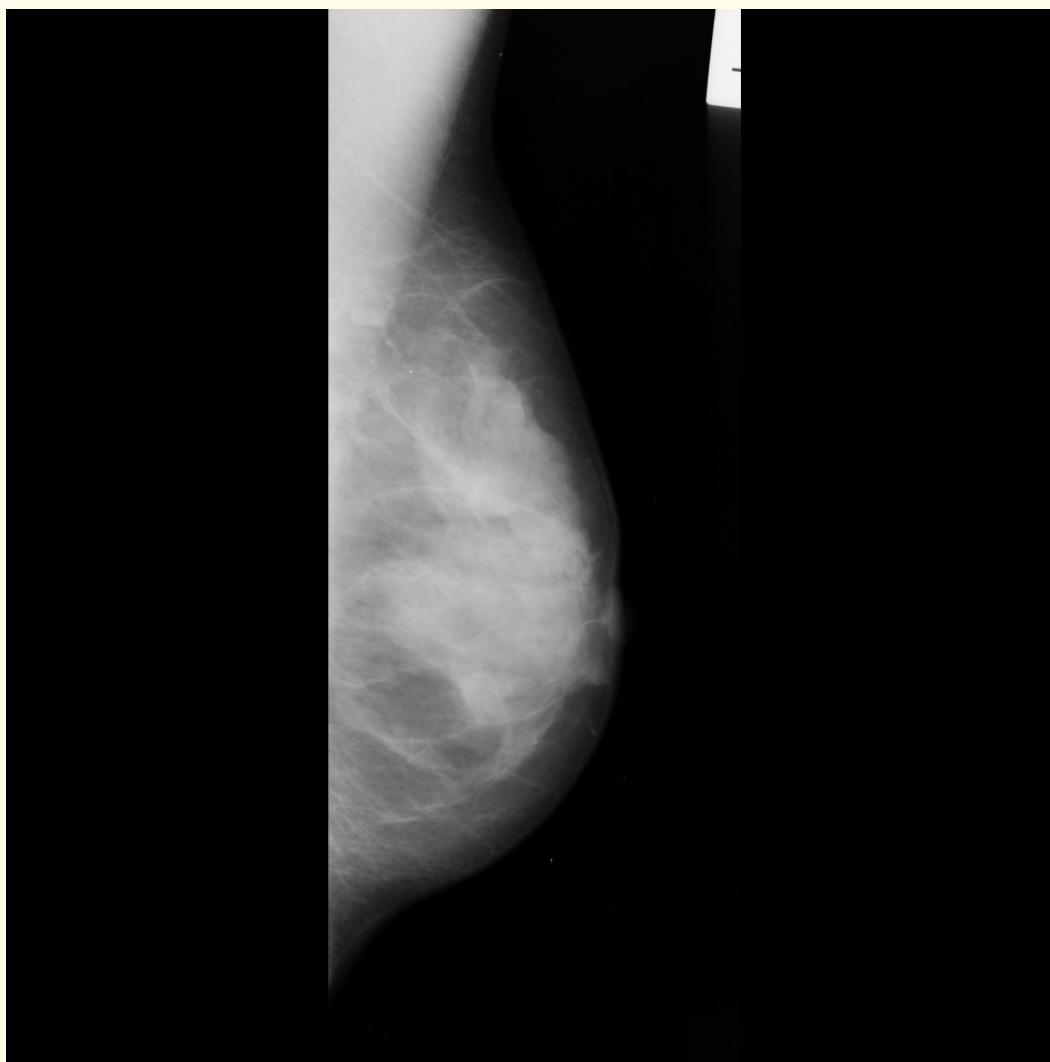


Figure 5.62 (a)

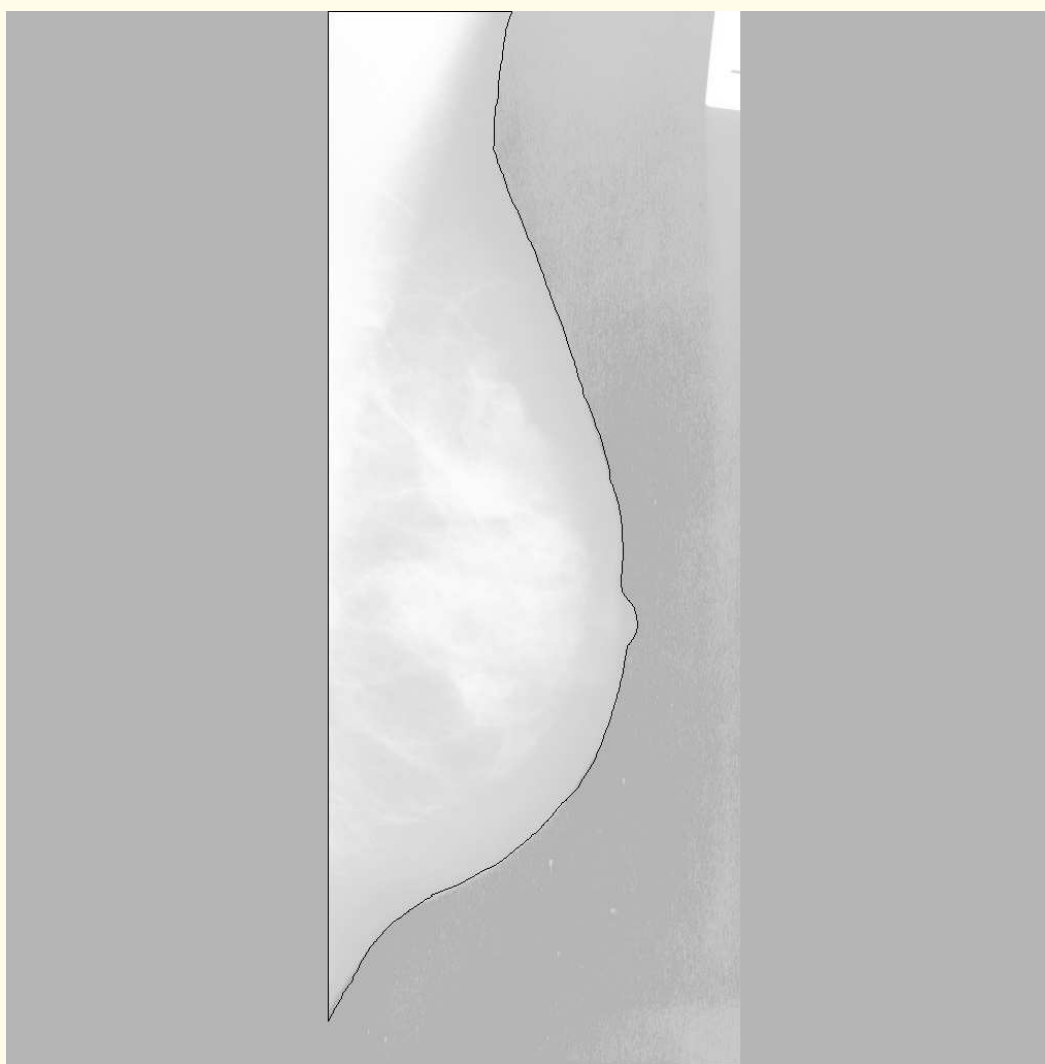
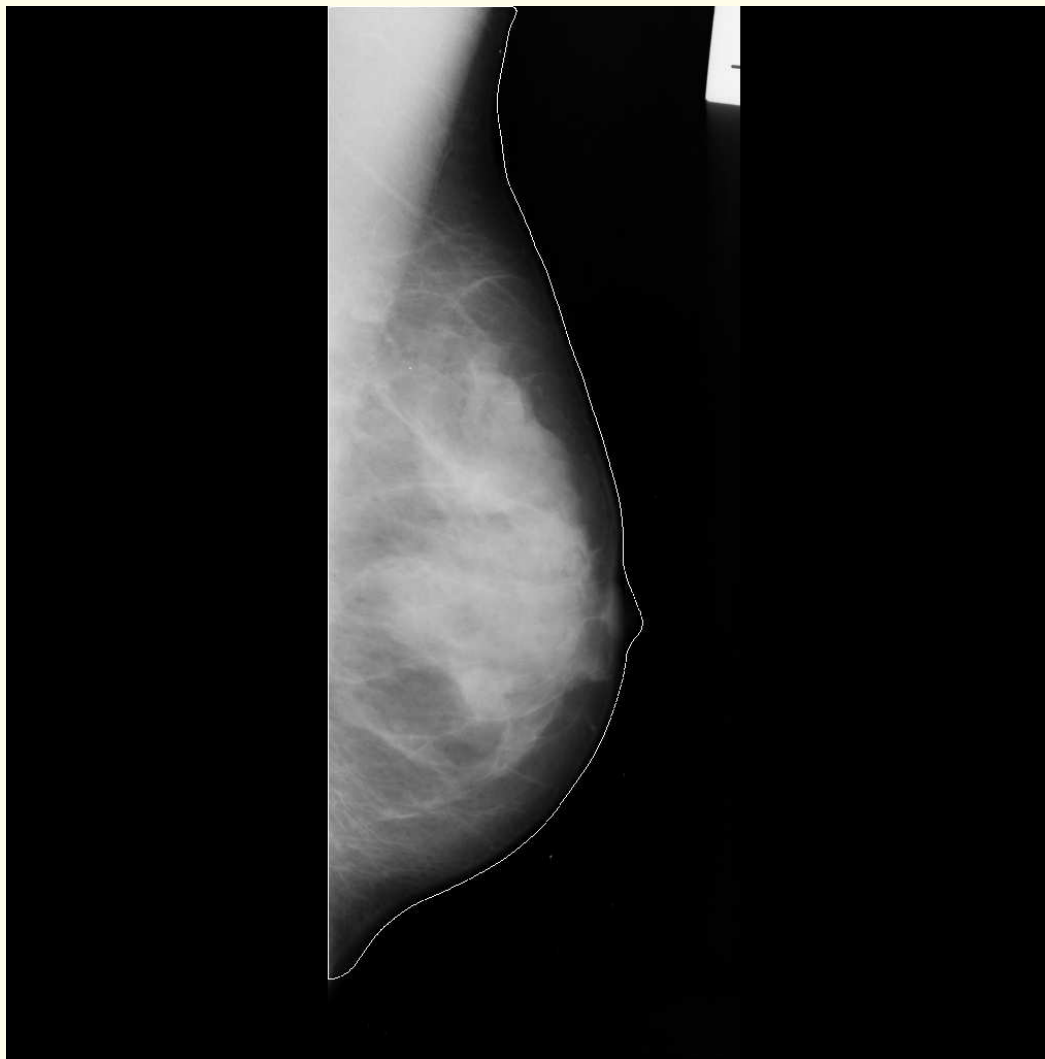


Figure 5.62 (b)



(c)

Figure 5.62: Results obtained for the image mdb114 from the Mini-MIAS database. (a) Original image. (b) Hand-drawn boundary superimposed on the histogram-equalized image. (c) Breast boundary detected, superimposed on the original image. Reproduced with permission from R.J. Ferrari, R.M. Rangayyan, J.E.L. Desautels, R.A. Borges, and A.F. Frère, “Identification of the breast boundary in mammograms using active contour models”, *Medical and Biological Engineering and Computing*, 42: 201 – 208, 2004. © IFMBE.



## 5.10 Application: Detection of the Pectoral Muscle in Mammograms

The pectoral muscle represents a predominant density region in most MLO views of mammograms, and can affect the results of image processing methods.

Analysis of the pectoral muscle could be used to identify the presence of abnormal axillary lymph nodes, which may be the only manifestation of occult breast carcinoma in some cases.



### 5.10.1 *Detection using the Hough transform*

Method to identify the pectoral muscle proposed by Ferrari et al.:  
Figure 5.63.

Starts by automatically identifying an appropriate ROI containing the pectoral muscle: Figure 5.64.

An approximate breast contour delimiting the control points is obtained by using a method for the detection of the skin-air boundary, described in Section 5.9.

Six control points N1–N6 used to define the ROI are determined.



1. N1: the top-left corner pixel of the boundary loop;
2. N5: the lowest pixel on the left-hand edge of the boundary loop;
3. N3: the mid-point between N1 and N5;
4. N2: the farthest point on the boundary from N5 in terms of the Euclidean distance through the breast  
(if this point is not located on the upper edge of the mammogram, it is projected vertically to the upper edge);
5. N4: the point that completes a rectangle with N1, N2, and N3 (not necessarily on the boundary loop);
6. N6: the farthest point on the boundary loop from N1. In the case of the mammogram in Figure 5.64, the points N5 and N6 have coincided.



The ROI is defined by the rectangular region delimited by the points N1, N2, N3, and N4: Figure 5.64.

Although, in some cases, this region may not include the total length of the pectoral muscle, the portion of the muscle present is adequate to define a straight line to represent its edge.

By limiting the size of the ROI as described above, the bias that could be introduced by other linear structures that may be present in the fibroglandular disc is minimized.

Geometric and anatomical constraints were incorporated into the method, as follows.

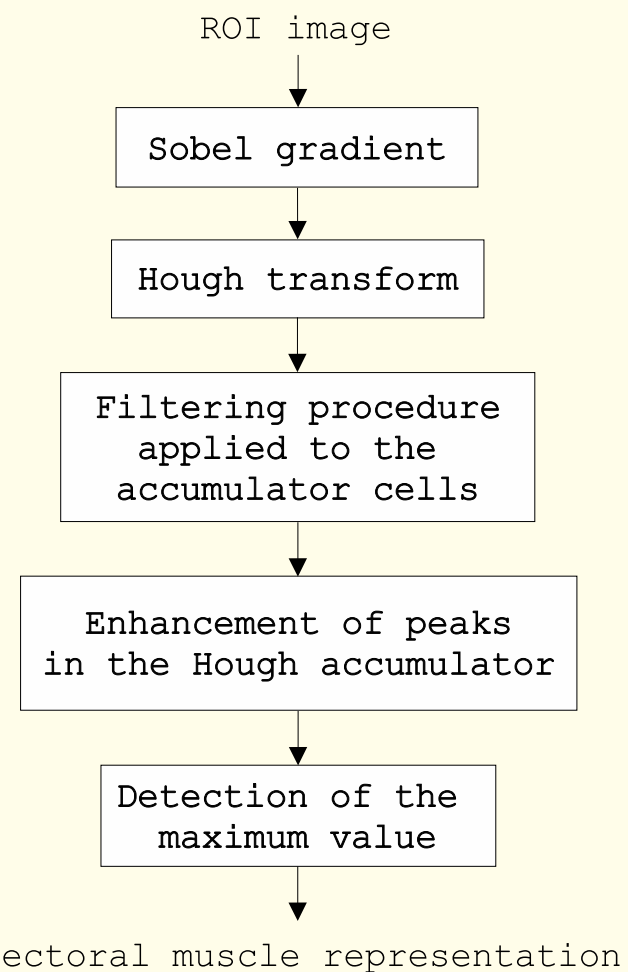


Figure 5.63: Procedure for the identification of the pectoral muscle by using the Hough transform. Reproduced with permission from R.J. Ferrari, R.M. Rangayyan, J.E.L. Desautels, R.A. Borges, and A.F. Frère, “Automatic identification of the pectoral muscle in mammograms”, *IEEE Transactions on Medical Imaging*, 23: 232 – 245, 2004. © IEEE.

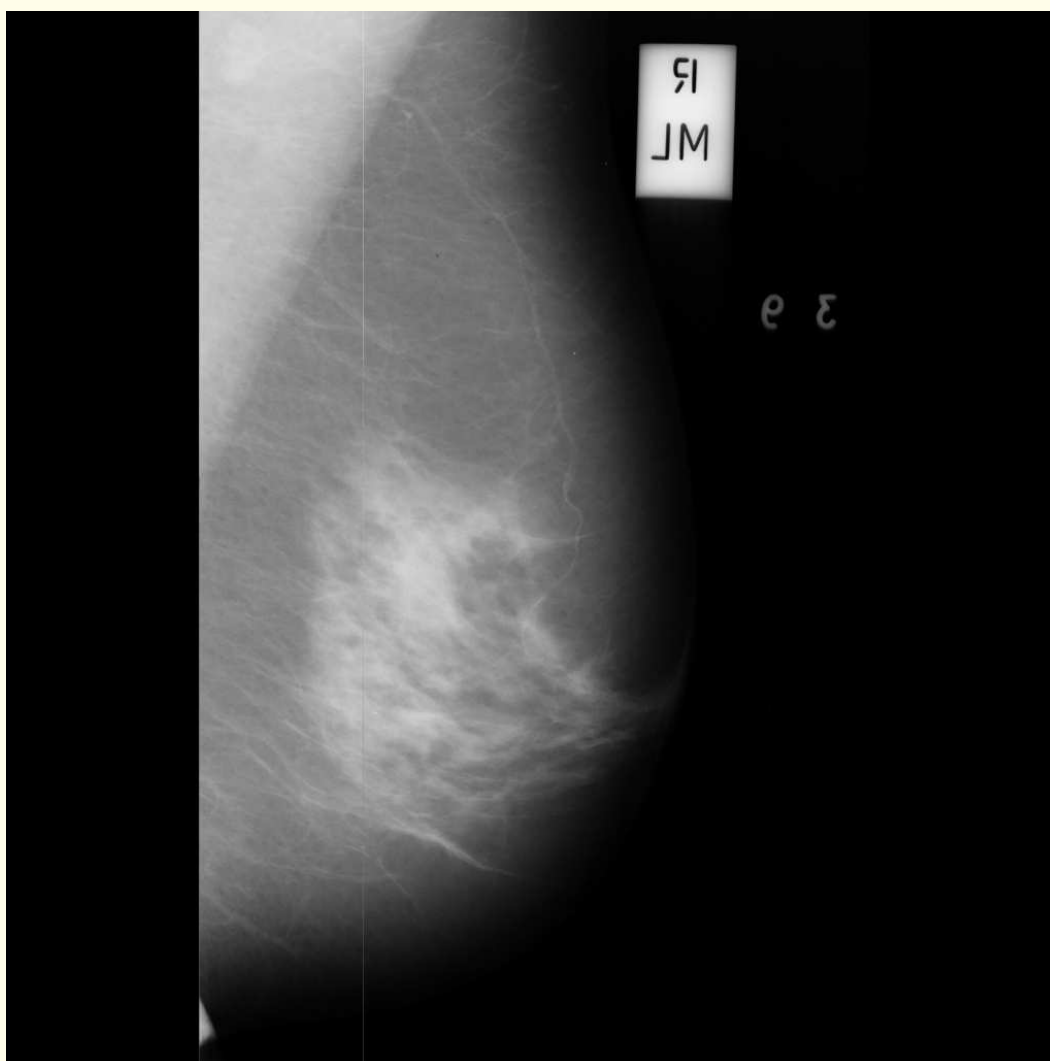
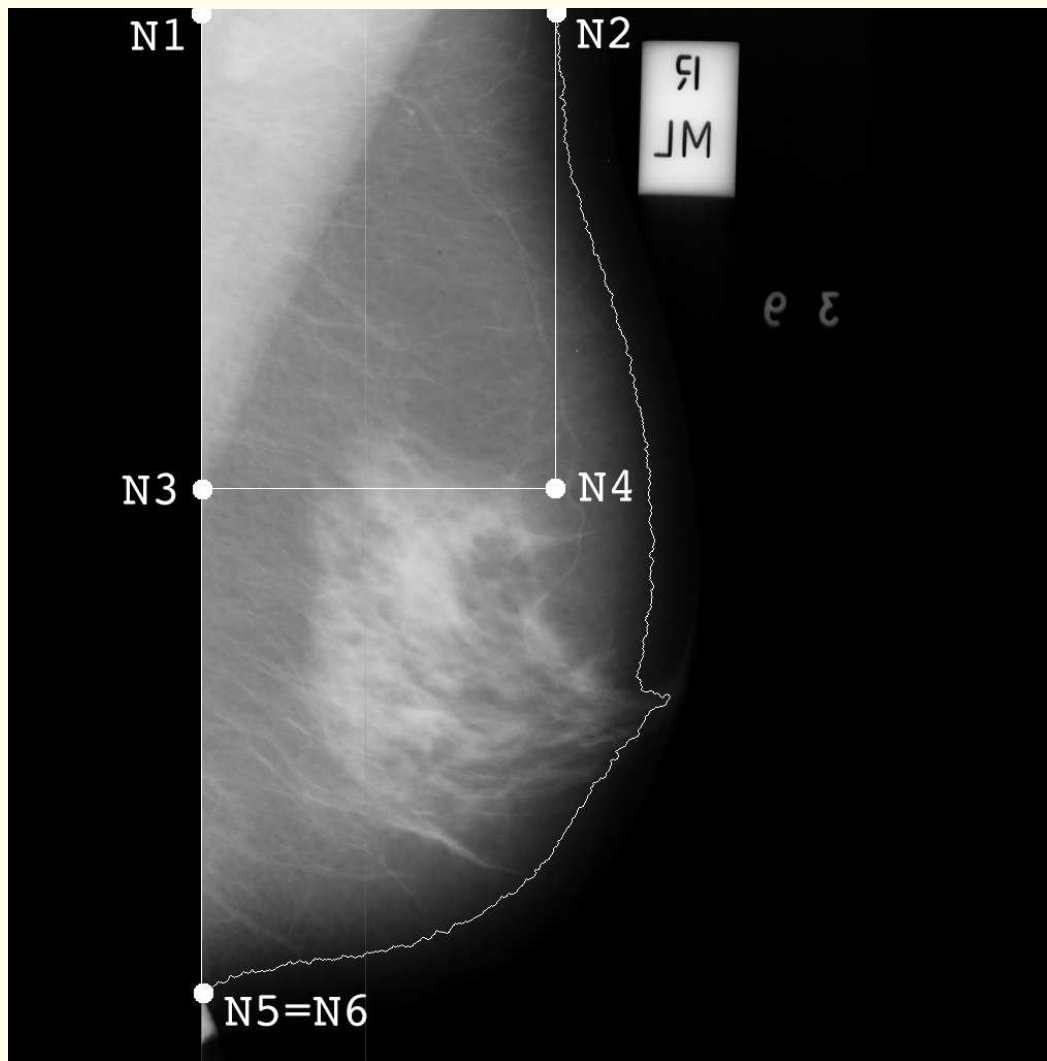


Figure 5.64 (a)



(b)

Figure 5.64: (a) Image mdb042 from the Mini-MIAS database. (b) Approximate boundary of the breast along with the automatically determined control points N1 – N6 used to limit the ROI (rectangle marked) for the detection of the pectoral muscle. Reproduced with permission from R.J. Ferrari, R.M. Rangayyan, J.E.L. Desautels, R.A. Borges, and A.F. Frère, “Automatic identification of the pectoral muscle in mammograms”, *IEEE Transactions on Medical Imaging*, 23: 232 – 245, 2004. © IEEE.



1. The pectoral muscle is considered to be a straight line limited to an angle  $\theta$  between  $120^\circ$  and  $170^\circ$ , with the angle computed as indicated in Figure 5.65. Mammograms of right breasts are flipped (mirrored) before processing.
2. The pectoral line intercepts the line segment N1 – N2, as indicated in Figure 5.64.
3. The pectoral line is present, in partial or total length, in the ROI defined as the rectangular region delimited by the points N1, N2, N3, and N4, as illustrated in Figure 5.64.
4. The pectoral muscle appears on mammograms as a dense region with homogeneous gray-level values.

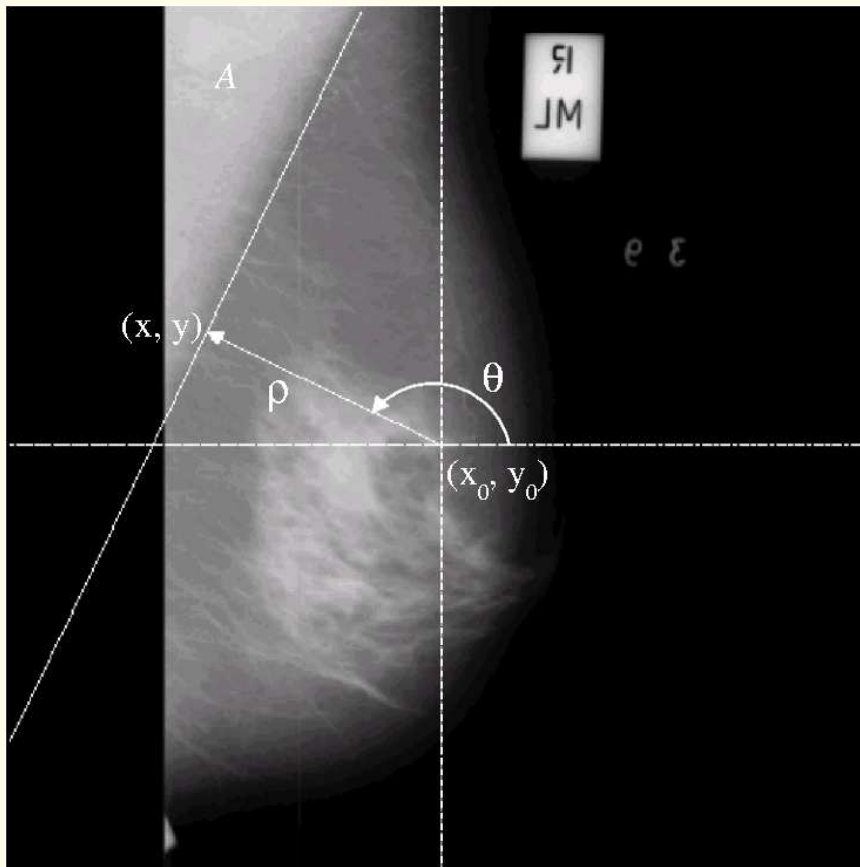


Figure 5.65: Coordinate system used to compute the Hough transform. The pectoral muscle line detected is also shown. Reproduced with permission from R.J. Ferrari, R.M. Rangayyan, J.E.L. Desautels, R.A. Borges, and A.F. Frère, “Automatic identification of the pectoral muscle in mammograms”, *IEEE Transactions on Medical Imaging*, 23: 232 – 245, 2004. © IEEE.



A Gaussian filter with  $\sigma_x = \sigma_y = 4$  pixels is used to smooth the ROI in order to remove the high-frequency noise in the image.

The Hough transform is then applied to the Sobel gradient of the ROI to detect the edge of the pectoral muscle.

Representation of a straight line for the Hough transform:

$$\rho = (x - x_0) \cos \theta + (y - y_0) \sin \theta, \quad (5.80)$$

where  $(x_0, y_0)$  is the origin of the coordinate system defined as the center of the image, and  $\rho$  and  $\theta$  represent, respectively, the distance and angle between  $(x_0, y_0)$  and the coordinates  $(x, y)$  of the pixel being analyzed, as in Figure 5.65.



The Hough accumulator is quantized to 45 bins of  $4^\circ$  each by using the constraint  $|\phi_{x,y} - \theta| < 2^\circ$ , where  $\phi_{x,y}$  is the orientation of the Sobel gradient at the pixel  $(x, y)$ .

The accumulator cells are incremented using the magnitude of the gradient instead of unit increments; thus, pixels with a strong gradient have larger weights.

Only values of  $\theta$  in the range  $[120^\circ, 170^\circ]$  were considered in the analysis, because the pectoral muscle of the mammogram was positioned on the left-hand side of the image before computing the Hough transform (see Figure 5.65).



A filtering procedure is applied in the Hough space to eliminate all lines (pairs of parameters  $\rho$  and  $\theta$ ) that are unlikely to represent the pectoral muscle.

All lines intercepting the top of the image outside the N1 – N2 line segment (see Figure 5.64) or with slopes outside the range  $[120^\circ, 170^\circ]$  are removed.

The  $x$  axis corresponds to  $0^\circ$ , and the chest wall is positioned on the left-hand side; see Figure 5.65.



Each remaining accumulator cell is multiplied by the factor

$$\alpha = \frac{\mu}{\sigma^2} A \Big|_{\theta, \rho} . \quad (5.81)$$

$\mu$  and  $\sigma^2$  : mean and variance of the gray-level values in the area  $A$  of the pectoral muscle (Figure 5.65), defined by the straight line specified by the parameters  $\theta$  and  $\rho$ .

This procedure was applied in order to enhance the Hough transform peaks that define dense, homogeneous regions.

The weight related to the area was designed to differentiate the true pectoral muscle from the pectoralis minor.



Finally, the parameters  $\rho$  and  $\theta$  of the accumulator cell with the maximum value are taken to represent the pectoral muscle line.

Figure 5.66 shows the Hough accumulator cells at the different stages of the procedure described above for the mammogram in Figure 5.64 (a).

The pectoral muscle line detected for the mammogram in Figure 5.64 (a) is shown in Figure 5.65.

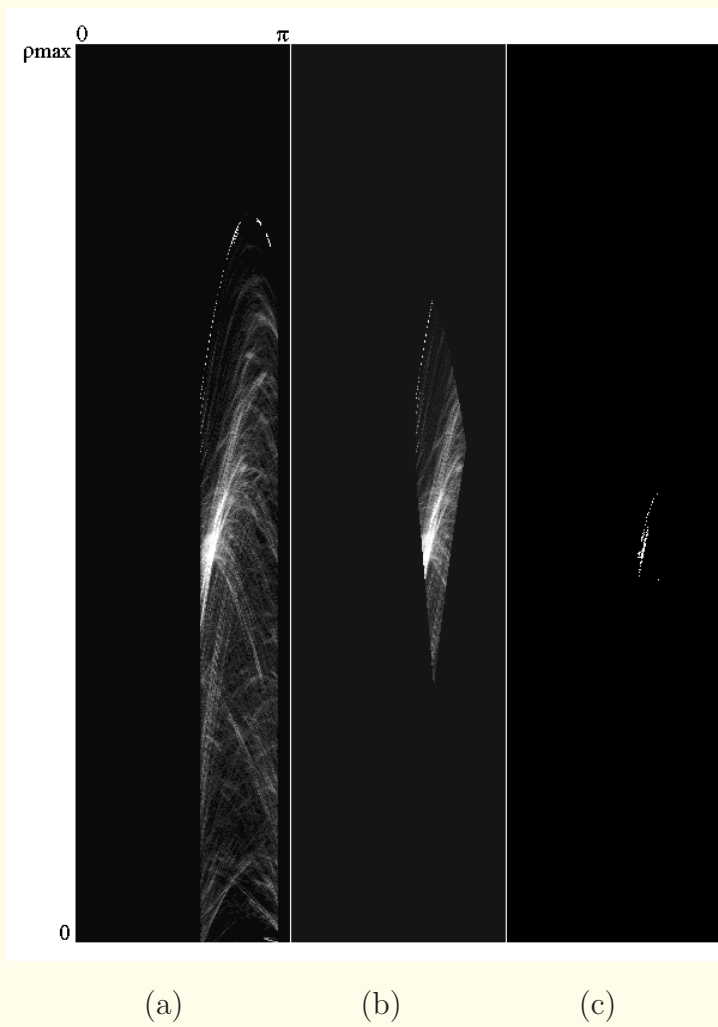


Figure 5.66: Hough accumulator cells obtained at three stages of the procedure to detect the pectoral muscle. The contrast of the images has been modified for improved visualization. (a) Accumulator cells obtained by using the constraint  $|\phi_{x,y} - \theta| < 2^\circ$  and  $120^\circ \leq \theta \leq 170^\circ$ . (b) After removing the lines intercepting the top of the image outside the region defined by the control points N1 – N2 (see Figure 5.65). (c) After applying the multiplicative factor  $\alpha = \frac{\mu}{\sigma^2} A \Big|_{\theta, \rho}$ . Reproduced with permission from R.J. Ferrari, R.M. Rangayyan, J.E.L. Desautels, R.A. Borges, and A.F. Frère, “Automatic identification of the pectoral muscle in mammograms”, *IEEE Transactions on Medical Imaging*, 23: 232 – 245, 2004. © IEEE.



### 5.10.2 *Detection using Gabor wavelets*

Improved method to detect the pectoral muscle edge: Figure 5.67.

Ferrari et al. designed a bank of Gabor filters to enhance the directional, piecewise-linear structures that are present in an ROI containing the pectoral muscle.

The ROI is defined to contain the entire pectoral muscle region.



Figure 5.68 (b) shows the ROI for a mammogram —

defined automatically as the rectangle formed by the chest wall as the left-hand edge, and a vertical line through the upper-most point on the skin-air boundary drawn along the entire height of the mammogram as the right-hand edge —

to be used for the detection of the pectoral muscle.

Decomposition of the ROI into components with different scale and orientation is performed by convolution of the ROI image with a bank of tunable Gabor filters.

The magnitude and phase components of the filtered images are then combined and used.

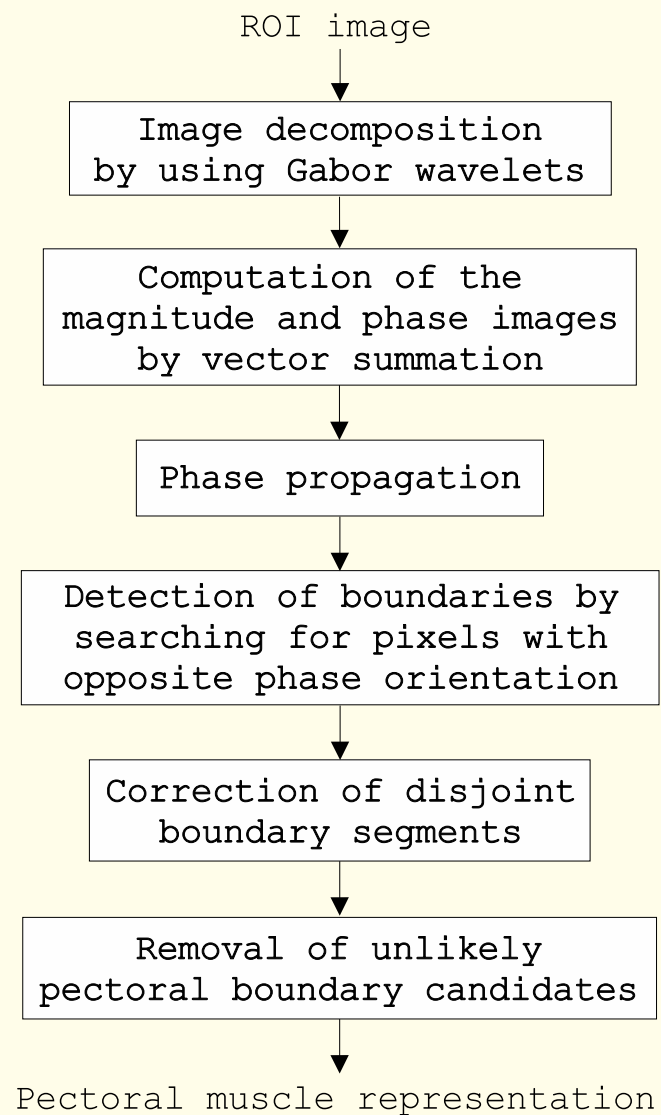


Figure 5.67: Flowchart of the procedure for the identification of the pectoral muscle by using Gabor wavelets. Reproduced with permission from R.J. Ferrari, R.M. Rangayyan, J.E.L. Desautels, R.A. Borges, and A.F. Frère, “Automatic identification of the pectoral muscle in mammograms”, *IEEE Transactions on Medical Imaging*, 23: 232 – 245, 2004. © IEEE.

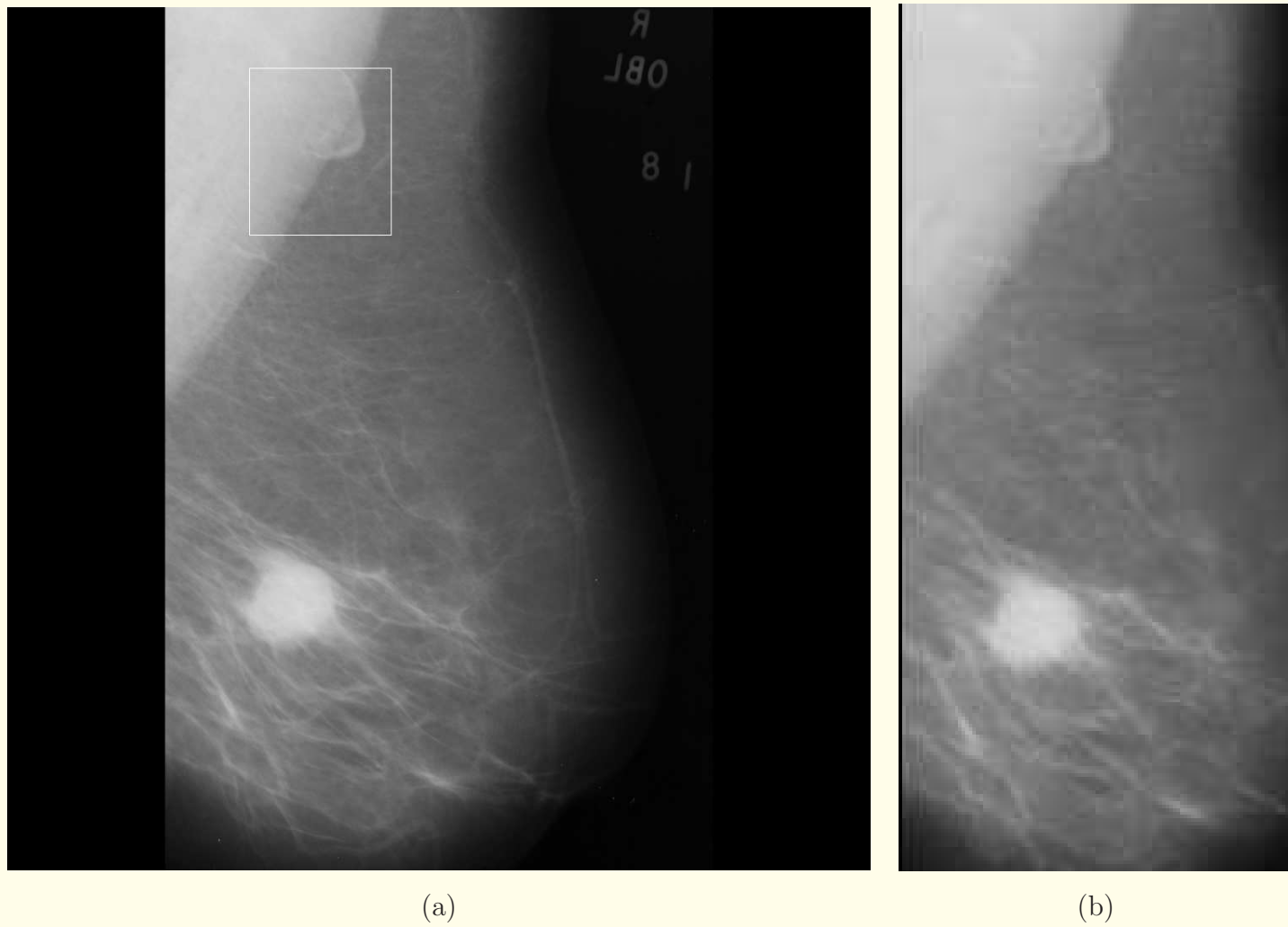


Figure 5.68: (a) Image mdb028 from the Mini-MIAS database. (b) The ROI used to search for the pectoral muscle region, defined by the chest wall and the upper limit of the skin-air boundary. The box drawn in (a) is not related to the ROI in (b). Reproduced with permission from R.J. Ferrari, R.M. Rangayyan, J.E.L. Desautels, R.A. Borges, and A.F. Frère, “Automatic identification of the pectoral muscle in mammograms”, *IEEE Transactions on Medical Imaging*, 23: 232 – 245, 2004. © IEEE.



## Gabor wavelets:

A 2D Gabor function is a Gaussian modulated by a complex sinusoid, specified by the frequency of the sinusoid  $W$  and the standard deviations  $\sigma_x$  and  $\sigma_y$  of the Gaussian envelope as

$$\psi(x, y) = \frac{1}{2\pi\sigma_x\sigma_y} \exp \left[ -\frac{1}{2} \left( \frac{x^2}{\sigma_x^2} + \frac{y^2}{\sigma_y^2} \right) + j2\pi Wx \right]. \quad (5.82)$$



Gabor wavelets are obtained by dilation and rotation of  $\psi(x, y)$  as in Equation 5.82 by using the generating function

$$\psi_{m,n}(x, y) = a^{-m} \psi(x', y'), \quad a > 1, \quad m, n = \text{integers},$$

$$\begin{aligned} x' &= a^{-m} [ (x - x_0) \cos \theta_n + (y - y_0) \sin \theta_n ] , \\ y' &= a^{-m} [ -(x - x_0) \sin \theta_n + (y - y_0) \cos \theta_n ] . \end{aligned} \tag{5.83}$$



$(x_0, y_0)$  is the center of the filter in the spatial domain;

$$\theta_n = \frac{n\pi}{K}, n = 1, 2, \dots, K;$$

$K$  is the number of orientations desired; and

$m$  and  $n$  indicate the scale and orientation, respectively.



The Gabor filter used by Ferrari et al. is expressed in the frequency domain as

$$\Psi(u, v) = \frac{1}{2\pi\sigma_u\sigma_v} \exp \left\{ -\frac{1}{2} \left[ \frac{(u - W)^2}{\sigma_u^2} + \frac{v^2}{\sigma_v^2} \right] \right\}, \quad (5.84)$$

where  $\sigma_u = \frac{1}{2\pi\sigma_x}$  and  $\sigma_v = \frac{1}{2\pi\sigma_y}$ .

Design strategy: project the filters so as to ensure that the half-peak magnitude supports of the filter responses in the frequency spectrum touch one another, as shown in Figure 5.69;

capture maximum information with minimum redundancy.



In order for the bank of Gabor filters to be a family of admissible 2D Gabor wavelets, the filters  $\psi(x, y)$  must satisfy the admissibility condition of finite energy:

their Fourier transforms are pure bandpass functions having zero response at DC.

This condition is achieved by setting the DC gain of each filter as

$$\Psi(0, 0) = 0.$$

The filters do not respond to regions with constant intensity.

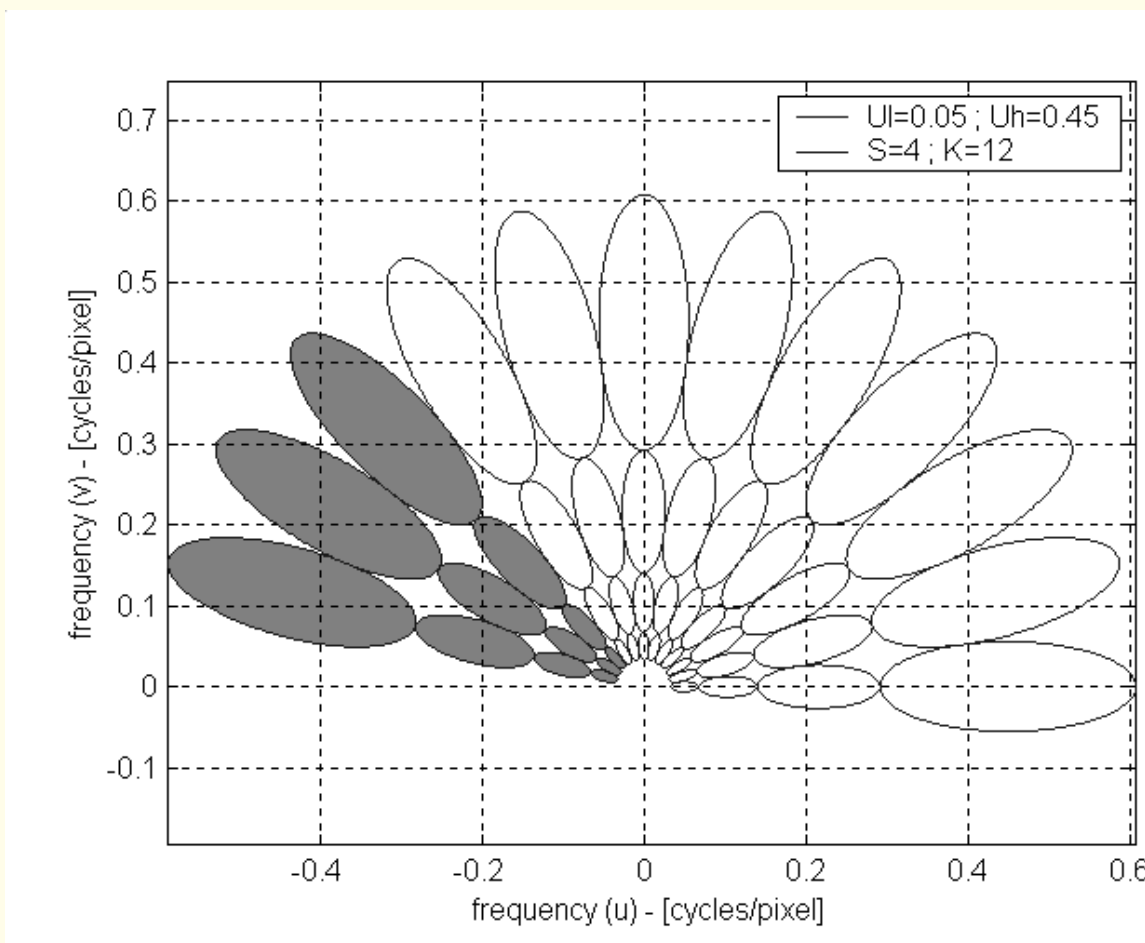


Figure 5.69: Bank of Gabor filters designed in the frequency domain. Each ellipse represents the range of the corresponding filter response from 0.5 to 1.0 in squared magnitude (only one half of the response is shown for each filter). The sampling of the frequency spectrum can be adjusted by changing the  $U_l$ ,  $U_h$ ,  $S$ , and  $K$  parameters of the Gabor wavelets. Only the filters shown shaded are used to enhance the directional piecewise-linear structures present in the ROI images. The frequency axes are normalized. Reproduced with permission from R.J. Ferrari, R.M. Rangayyan, J.E.L. Desautels, R.A. Borges, and A.F. Frère, “Automatic identification of the pectoral muscle in mammograms”, *IEEE Transactions on Medical Imaging*, 23: 232 – 245, 2004. © IEEE.



The following formulas provide the filter parameters  $\sigma_u$  and  $\sigma_v$ :

$$a = \left( \frac{U_h}{U_l} \right)^{\frac{1}{S-1}}, \quad (5.85)$$

$$\sigma_u = \frac{(a - 1)U_h}{(a + 1)\sqrt{2 \ln 2}}, \quad (5.86)$$

$$\sigma_v = \frac{\tan\left(\frac{\pi}{2K}\right) \left[ U_h - \left( \frac{\sigma_u^2}{U_h} \right) 2 \ln 2 \right]}{\left[ 2 \ln 2 - \frac{(2 \ln 2)^2 \sigma_u^2}{U_h^2} \right]^{\frac{1}{2}}}. \quad (5.87)$$



$U_l$  and  $U_h$  : lower and upper center frequencies of interest.

$K$  and  $S$  : number of orientations and number of scales in the desired multiresolution decomposition procedure.

Sinusoid frequency  $W$  set equal to  $U_h$ .

$m = 0, 1, \dots, S - 1$ .



In the application being considered, interest lies only in image analysis, without the requirement of exact reconstruction or synthesis of the image from the filtered components.

Therefore, instead of using the wavelet coefficients, Ferrari et al. used the magnitude of the filter response, computed as

$$a_{m,n}(x, y) = |f(x, y) * \psi^{even}_{m,n} (x, y)|. \quad (5.88)$$



$\psi^{even}_{m,n}(x, y)$  indicates the even-symmetric part of the complex Gabor filter,

$f(x, y)$  is the ROI being filtered, and

\* represents 2D convolution.

The phase and magnitude images, indicating the local orientation, were composed by vector summation of the  $K$  filtered images.



The area of each ellipse indicated in Figure 5.69 represents the frequency spectrum covered by the corresponding Gabor filter.

The choice of the number of scales and orientations is made in order to cover the range of the spectrum as required.

By selecting  $U_l = 0.05$ ,  $U_h = 0.45$ ,  $S = 4$ , and  $K = 12$  for processing mammographic images, Ferrari et al. adjusted the Gabor wavelets to have a frequency bandwidth of approximately one octave and angular bandwidth of  $15^\circ$ .



All images were initially oriented so that the chest wall was always positioned on the left-hand side;

then, the pectoral muscle edge in correctly acquired MLO views will be located between  $45^\circ$  and  $90^\circ$ .

The orientation of the pectoral muscle edge is defined as the angle between the horizontal line and an imaginary straight line representing the pectoral muscle edge.

For this reason, Ferrari et al. used only the Gabor filters with the mean orientation of their responses in the image domain at  $45^\circ$ ,  $60^\circ$ , and  $75^\circ$ ; the corresponding frequency-domain responses are shown shaded in Figure 5.69.



## Post-processing and pectoral muscle edge detection:

After computing the phase and magnitude images by vector summation, the relevant edges in the ROI are detected by using an algorithm for edge-flow propagation.

The magnitude  $A(x, y)$  and phase  $\phi(x, y)$  at each location  $(x, y)$  are used to represent the edge-flow vector instead of the predictive coding model of Ma and Manjunath.

The phase at each point in the image is propagated until it reaches a location where two opposite directions of flow encounter each other, as follows:



1. Set  $n = 0$  and

$$\mathbf{E}_0(x, y) = [A(x, y) \cos \phi(x, y), A(x, y) \sin \phi(x, y)].$$

2. Set the edge-flow vector  $\mathbf{E}_{n+1}(x, y)$  at iteration  $n + 1$  to zero.

3. At each image location  $(x, y)$ , identify the neighbor  $(x', y')$  that has the same direction  $\theta$  as that of the edge-flow vector  $\mathbf{E}_n(x, y)$ . The direction  $\theta$  is computed as  $\theta = \tan^{-1} \frac{(y'-y)}{(x'-x)}$ .

4. If  $\mathbf{E}_n(x', y') \bullet \mathbf{E}_n(x, y) > 0$

then  $\mathbf{E}_{n+1}(x', y') = \mathbf{E}_{n+1}(x', y') + \mathbf{E}_n(x, y)$

else  $\mathbf{E}_{n+1}(x, y) = \mathbf{E}_{n+1}(x, y) + \mathbf{E}_n(x, y)$ ,

where the symbol  $\bullet$  indicates the dot-product operation.

5. If nothing has been changed

then stop iterating

else go to Step 2 and repeat the procedure.

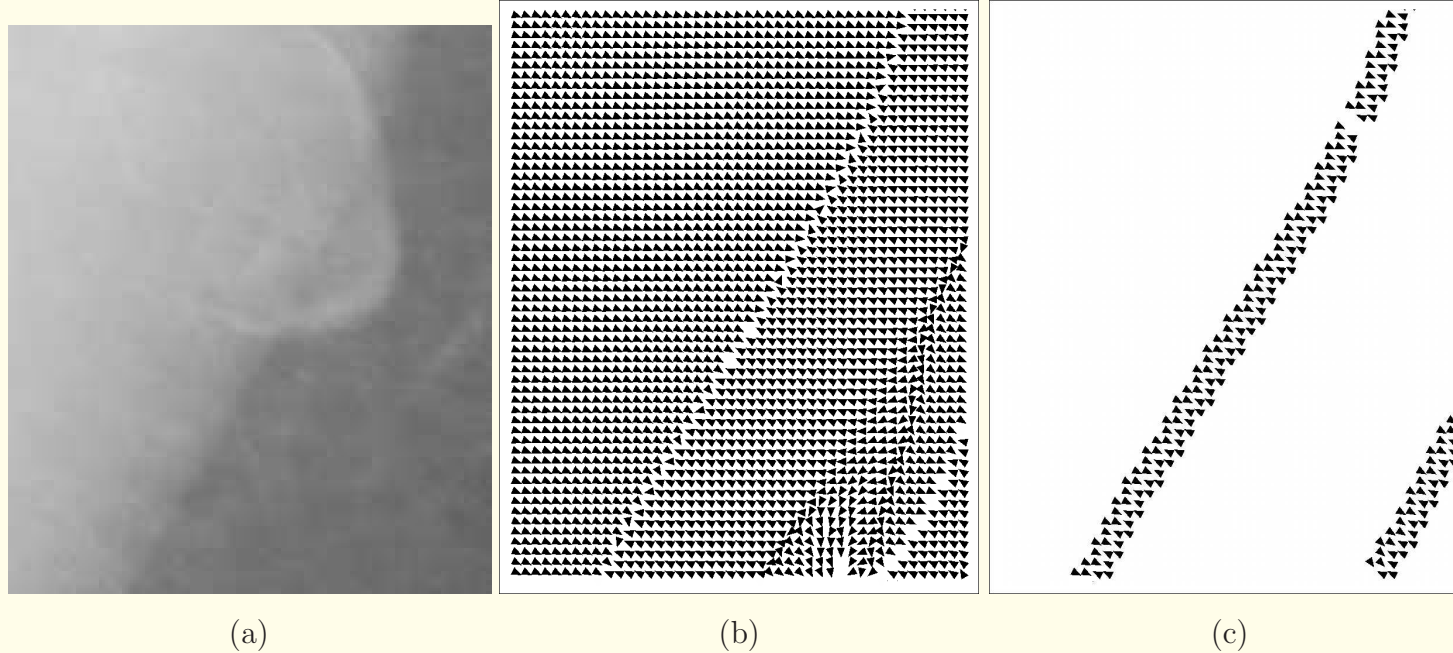
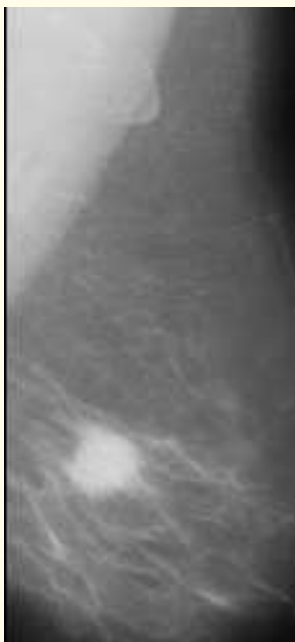


Figure 5.70: (a) Region indicated by the box in Figure 5.68 (a) containing a part of the pectoral muscle edge. (b) and (c) Edge-flow map before and after propagation. Each arrowhead represents the direction of the edge-flow vector at the corresponding position in the image. Reproduced with permission from R.J. Ferrari, R.M. Rangayyan, J.E.L. Desautels, R.A. Borges, and A.F. Frère, “Automatic identification of the pectoral muscle in mammograms”, *IEEE Transactions on Medical Imaging*, 23: 232 – 245, 2004. © IEEE.



After propagating the edge-flow vector, boundary candidates for the pectoral muscle are obtained by identifying the locations that have nonzero edge-flow arriving from two opposite directions.

Weak edges are eliminated by thresholding the ROI image with a threshold of 10% of the maximum gray-level value in the ROI.



(a)



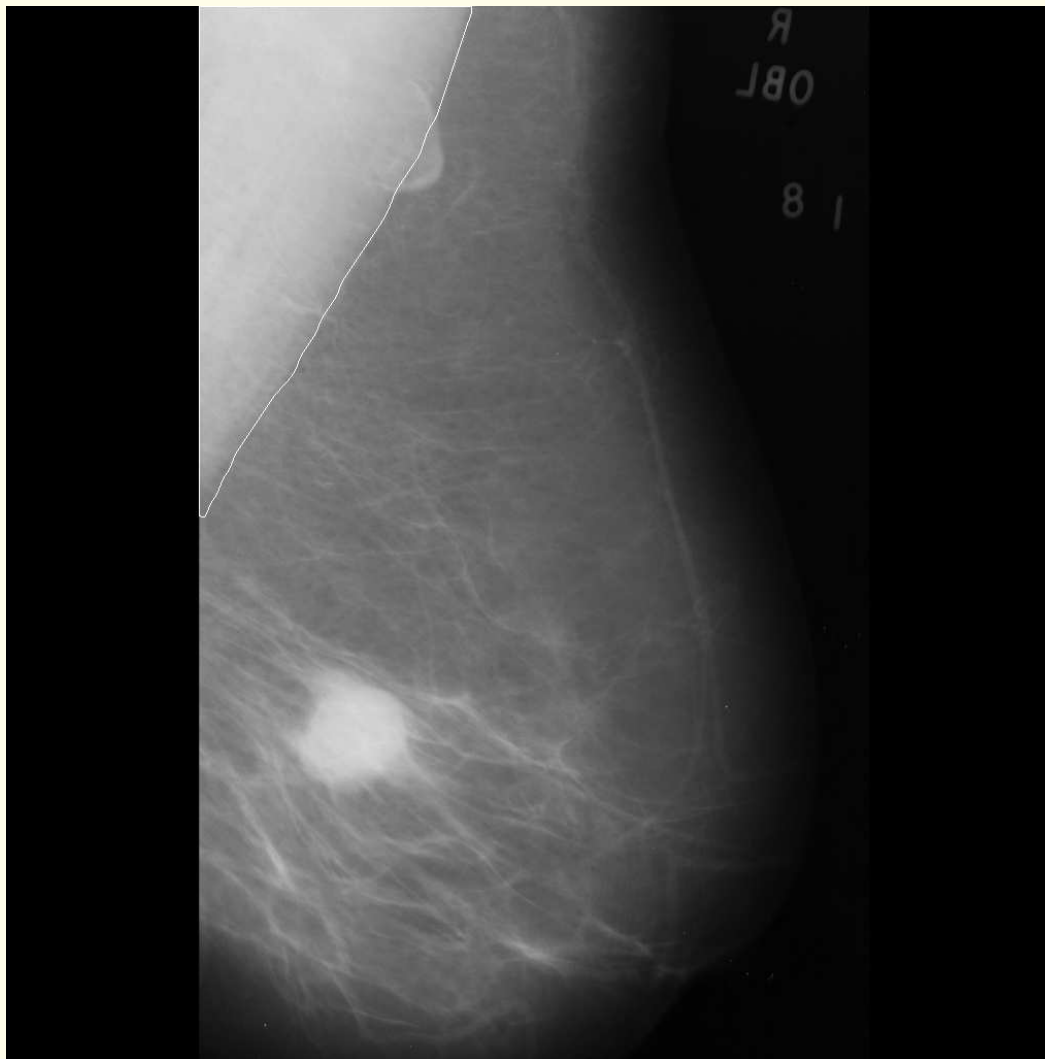
(b)



Figure 5.71 (c)



(d)



(e)

Figure 5.71: Result of each stage of the Gabor-wavelet-based method: (a) ROI used. (b) Image magnitude after filtering and vector summation, enhanced by gamma correction ( $\gamma = 0.7$ ). (c)–(d) Results before and after the post-processing stage. (e) Final boundary. Reproduced with permission from R.J. Ferrari, R.M. Rangayyan, J.E.L. Desautels, R.A. Borges, and A.F. Frère, “Automatic identification of the pectoral muscle in mammograms”, *IEEE Transactions on Medical Imaging*, 23: 232 – 245, 2004. © IEEE.



In order to connect the disjoint boundary segments that are usually present in the image after the edge-flow propagation step, a half-elliptical neighborhood is defined with its center located at each boundary pixel being processed.

The half-ellipse is adjusted to be proportional to the length of the contour, with

$$R_1 = 0.2 C_{len} \text{ and } R_2 = 5 \text{ pixels},$$

where  $R_1$  and  $R_2$  are, respectively, the major and minor axes of the half-ellipse, and  $C_{len}$  is the length of the boundary,

with its major axis oriented along the direction of the contour line.



If an ending or a starting pixel of an unconnected line segment is found in the defined neighborhood, it is connected by linear interpolation.

The iterative method stops when all disjoint lines are connected.

Next, the false edges that may result in the filtered images due to structures inside the fibroglandular disc or due to the filtering process [see Figure 5.71 (c)–(d)] are removed by checking

if their limiting points are far away from the upper and left-hand side of the ROI, or if the straight line having the same slope as the pectoral muscle edge candidate intercepts outside the upper and left-hand limits of the ROI.

Finally, the largest line in the ROI is selected to represent the pectoral muscle edge; see Figure 5.71 (e).



### 5.10.3 *Results of application to mammograms*

Ferrari et al. tested their methods with 84 images randomly chosen from the Mini-MIAS database.

All images were MLO views with  $200 \mu\text{m}$  sampling interval and 8-bit gray-level quantization.

For reduction of processing time, all images were downsampled to  $256 \times 256$  pixels.

The results were mapped to the original  $1,024 \times 1,024$  mammograms.



The results were evaluated in consultation with two radiologists experienced in mammography.

The test images were displayed on a computer monitor with diagonal size of *47.5 cm* and dot pitch of *0.27 mm*.

The contrast and brightness were manually enhanced so that the pectoral muscle edge could be easily visualized.

Then, the pectoral muscle edges were manually drawn and the results printed on paper by using a laser printer at *600 dpi*.

The pectoral muscle edges of all images were checked by a radiologist using the printed images (hardcopy) along with the displayed images (softcopy).



The segmentation results were evaluated based upon the number of FP and FN pixels normalized with reference to the corresponding numbers of pixels in the regions demarcated by the manually drawn edges.

The reference region for the pectoral muscle was defined as the region contained between the left-hand edge of the image and the hand-drawn pectoral muscle edge.

An FP pixel was defined as a pixel outside the reference region that was included in the pectoral region segmented; an FN pixel was defined as a pixel in the reference region that was not present within the segmented region.

Detection of the pectoral muscle was used as a preprocessing step in segmentation of the fibroglandular discs in mammograms for the analysis of bilateral asymmetry by Ferrari et al.



Table 5.1: Average False-positive and False-negative Rates in the Detection of the Pectoral Muscle by the hough-transform-based and Gabor-wavelet-based Methods.

| Method                              | Hough               | Gabor             |
|-------------------------------------|---------------------|-------------------|
| $FP \pm \sigma$                     | $1.98 \pm 6.09\%$   | $0.58 \pm 4.11\%$ |
| $FN \pm \sigma$                     | $25.19 \pm 19.14\%$ | $5.77 \pm 4.83\%$ |
| <hr/>                               |                     |                   |
| Number of images with               |                     |                   |
| $(FP \text{ and } FN) < 5\%$        | 10                  | 45                |
| $5\% < (FP \text{ and } FN) < 10\%$ | 8                   | 22                |
| $(FP \text{ and } FN) > 10\%$       | 66                  | 17                |

Reproduced with permission from R.J. Ferrari, R.M. Rangayyan, J.E.L. Desautels, R.A. Borges, and A.F. Frère, “Automatic identification of the pectoral muscle in mammograms”, IEEE Transactions on Medical Imaging, 23: 232 – 245, 2004. © IEEE.

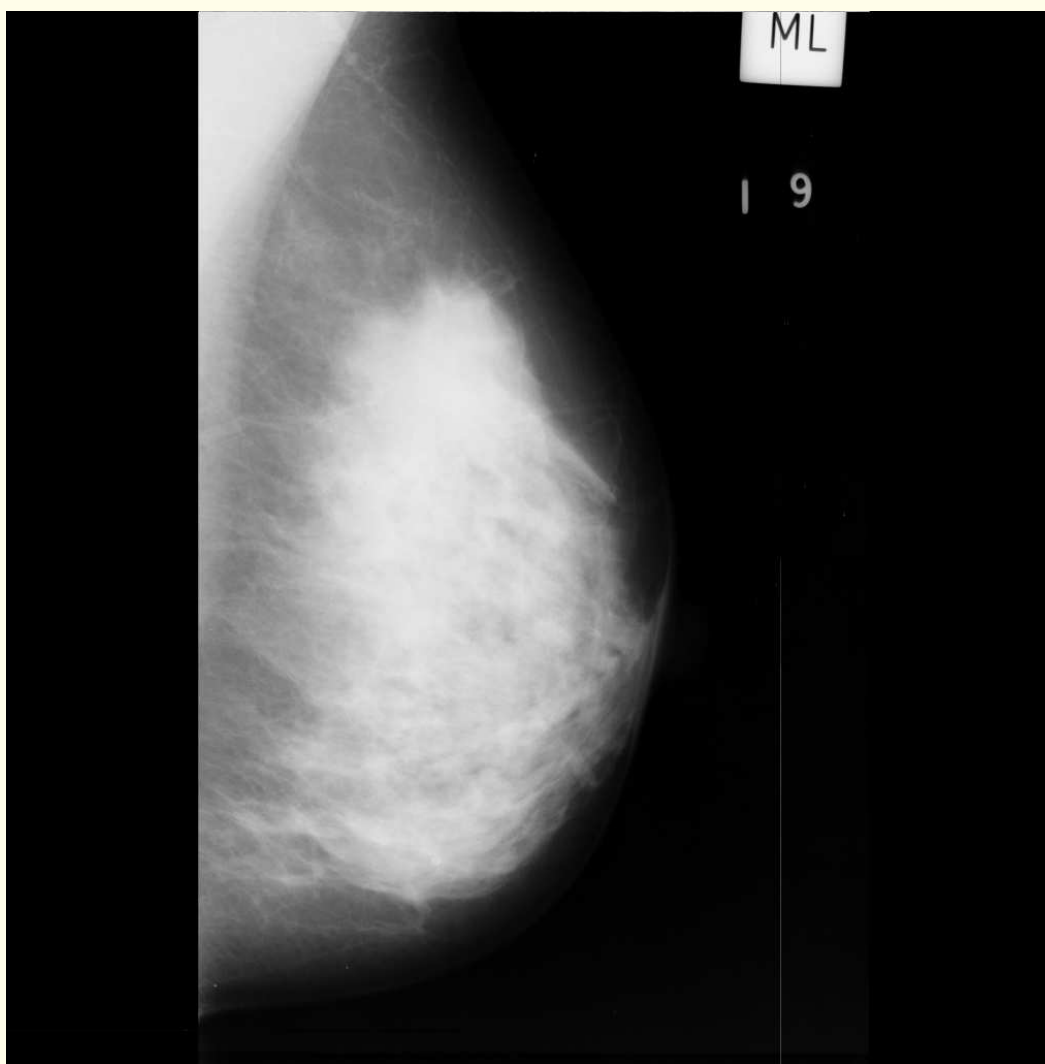


Figure 5.72 (a)

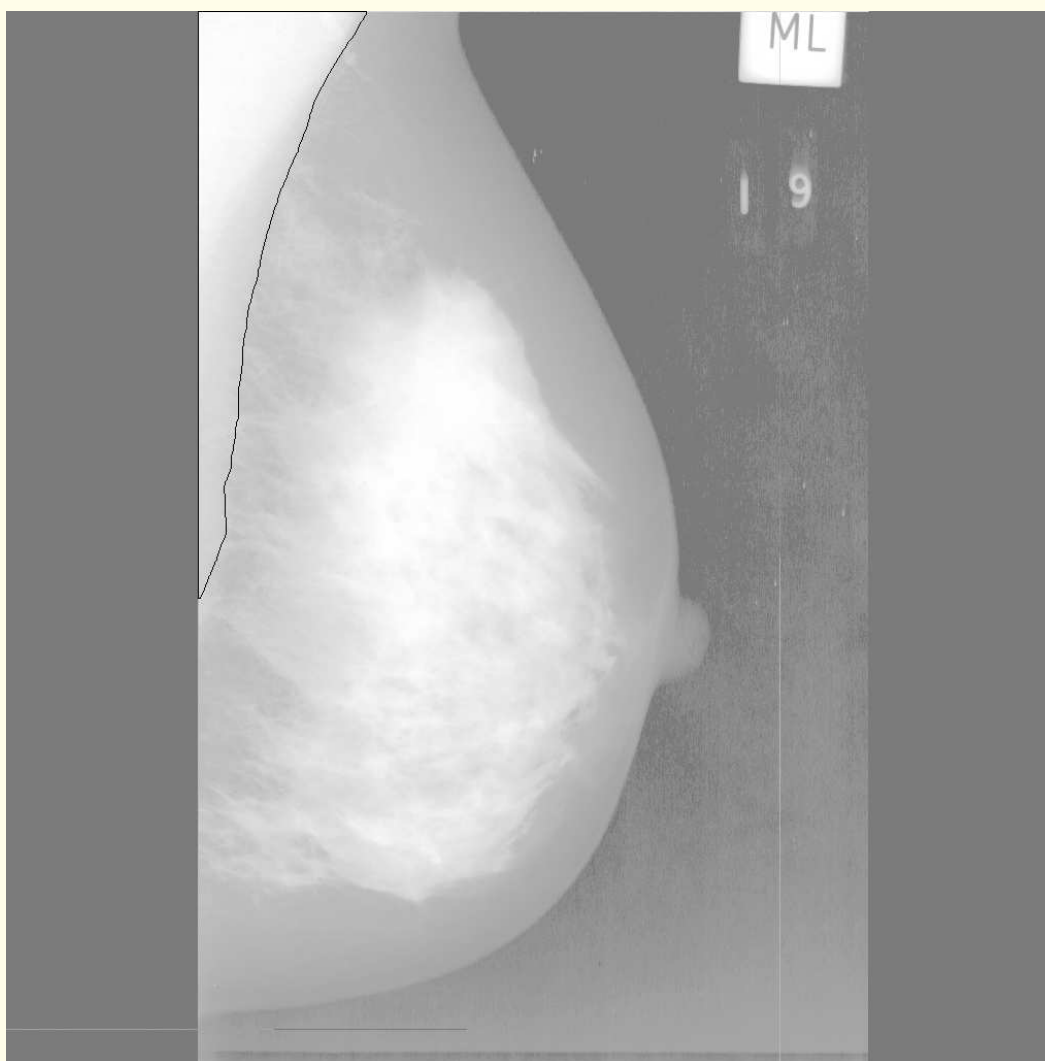


Figure 5.72 (b)

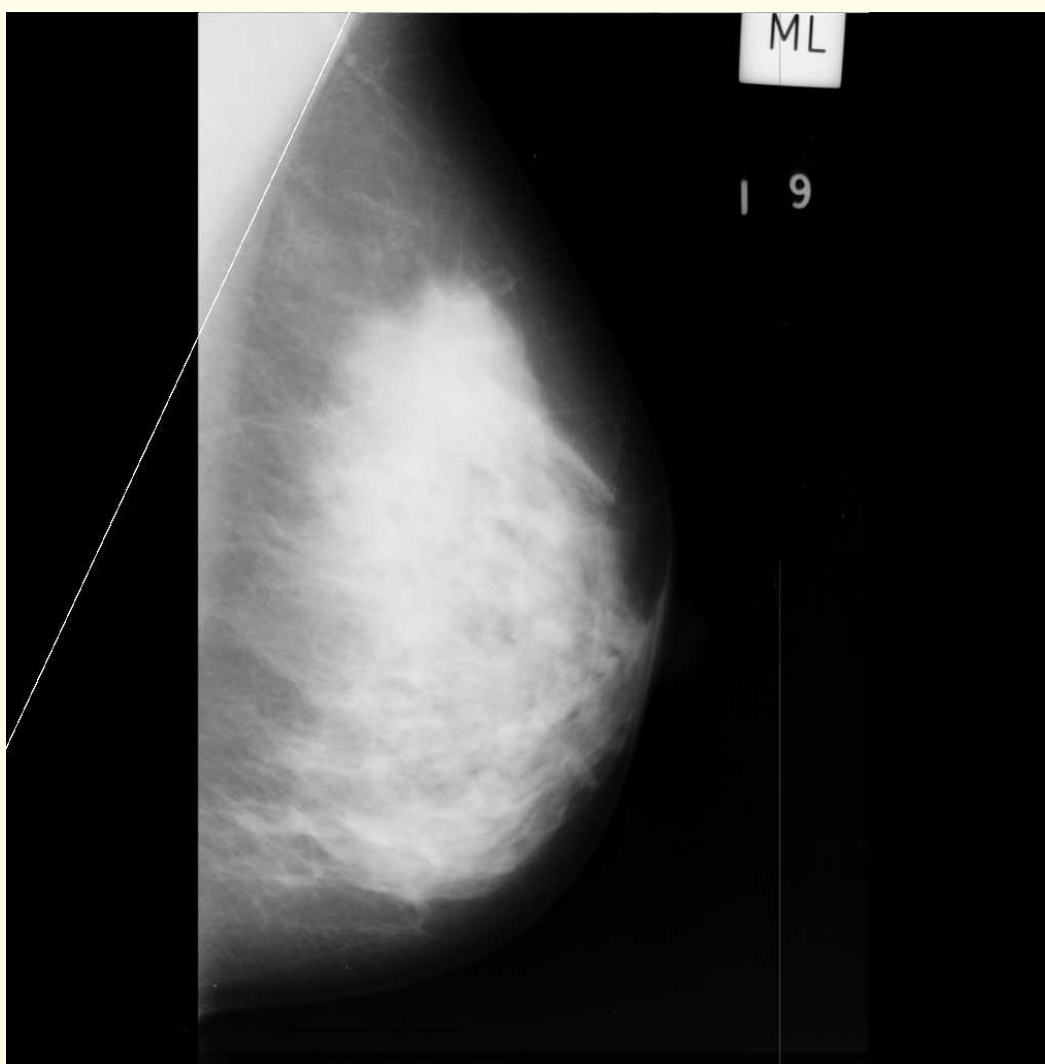
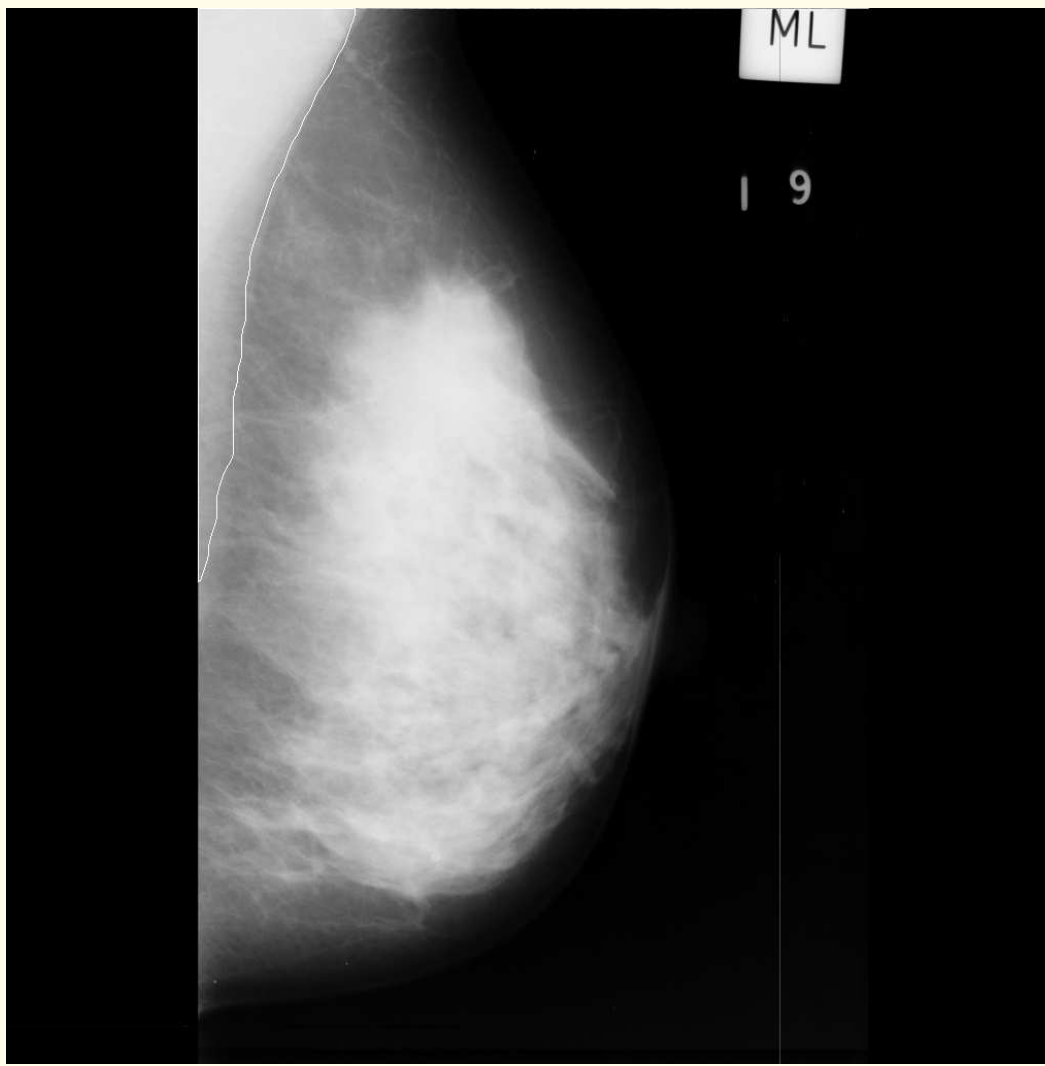


Figure 5.72 (c)



(d)

Figure 5.72: Results obtained for the image mdb003 from the Mini-MIAS database. (a) Original image. (b) Hand-drawn pectoral muscle edge superimposed on the histogram-equalized image. (c) and (d) Pectoral muscle edges detected by the Hough-transform-based and Gabor-wavelet-based methods, respectively, superimposed on the original image. Reproduced with permission from R.J. Ferrari, R.M. Rangayyan, J.E.L. Desautels, R.A. Borges, and A.F. Frère, “Automatic identification of the pectoral muscle in mammograms”, *IEEE Transactions on Medical Imaging*, 23: 232 – 245, 2004. © IEEE.

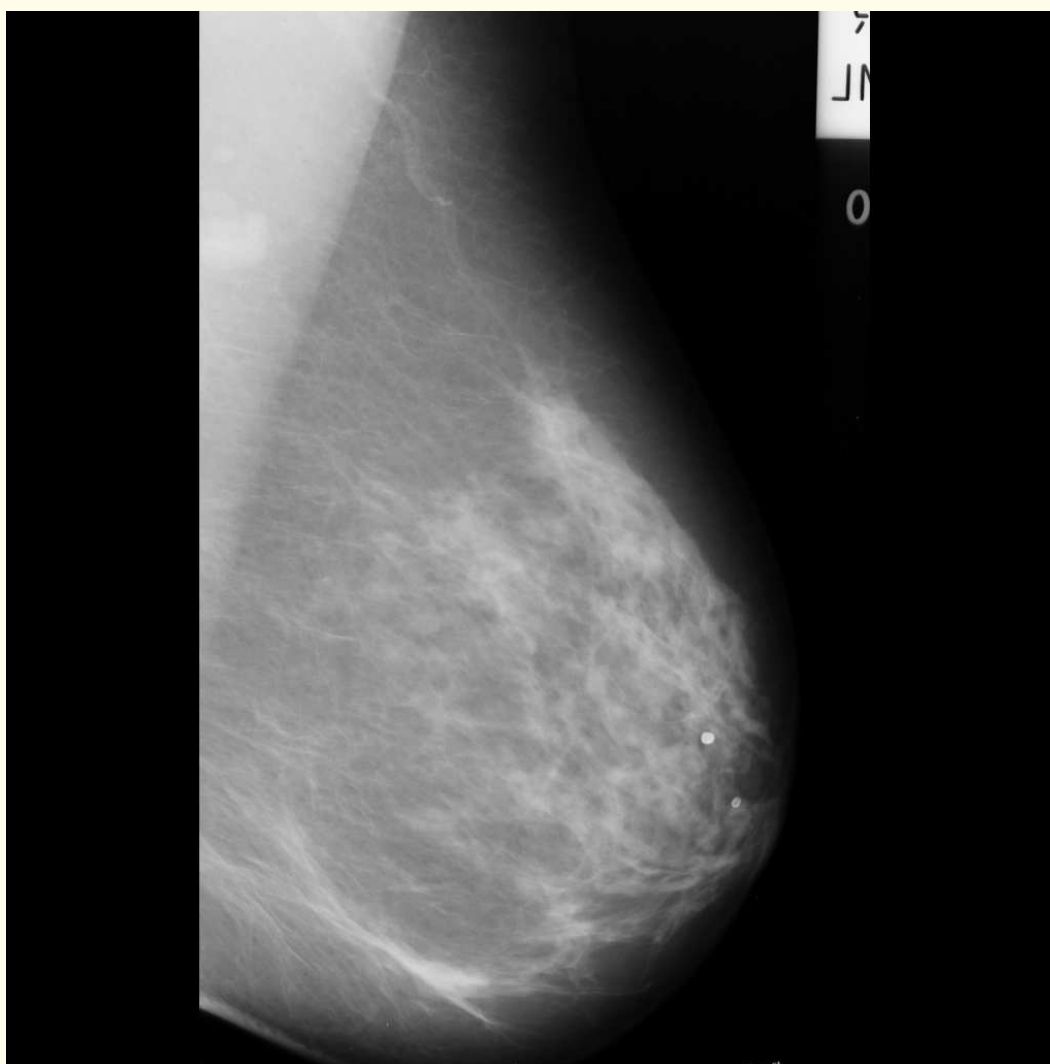


Figure 5.73 (a)

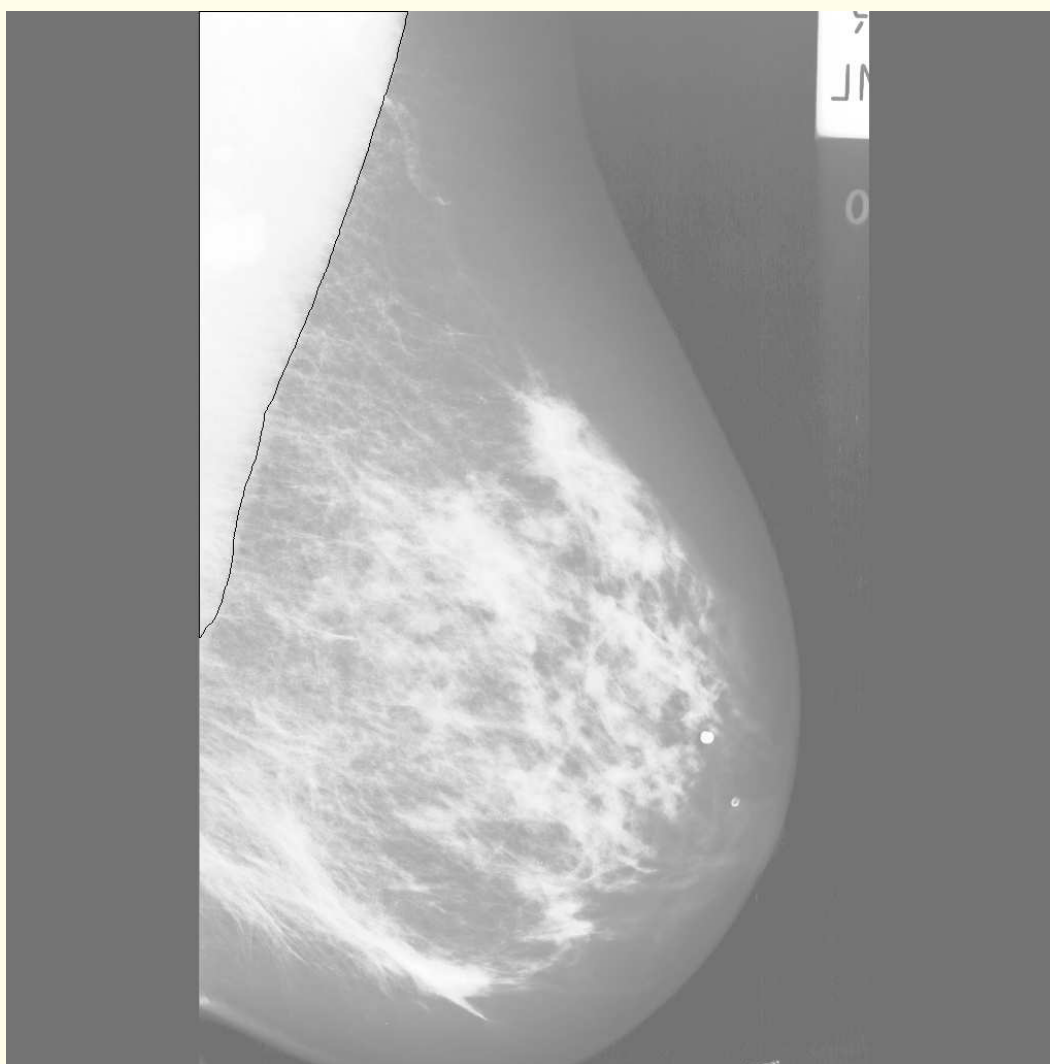


Figure 5.73 (b)

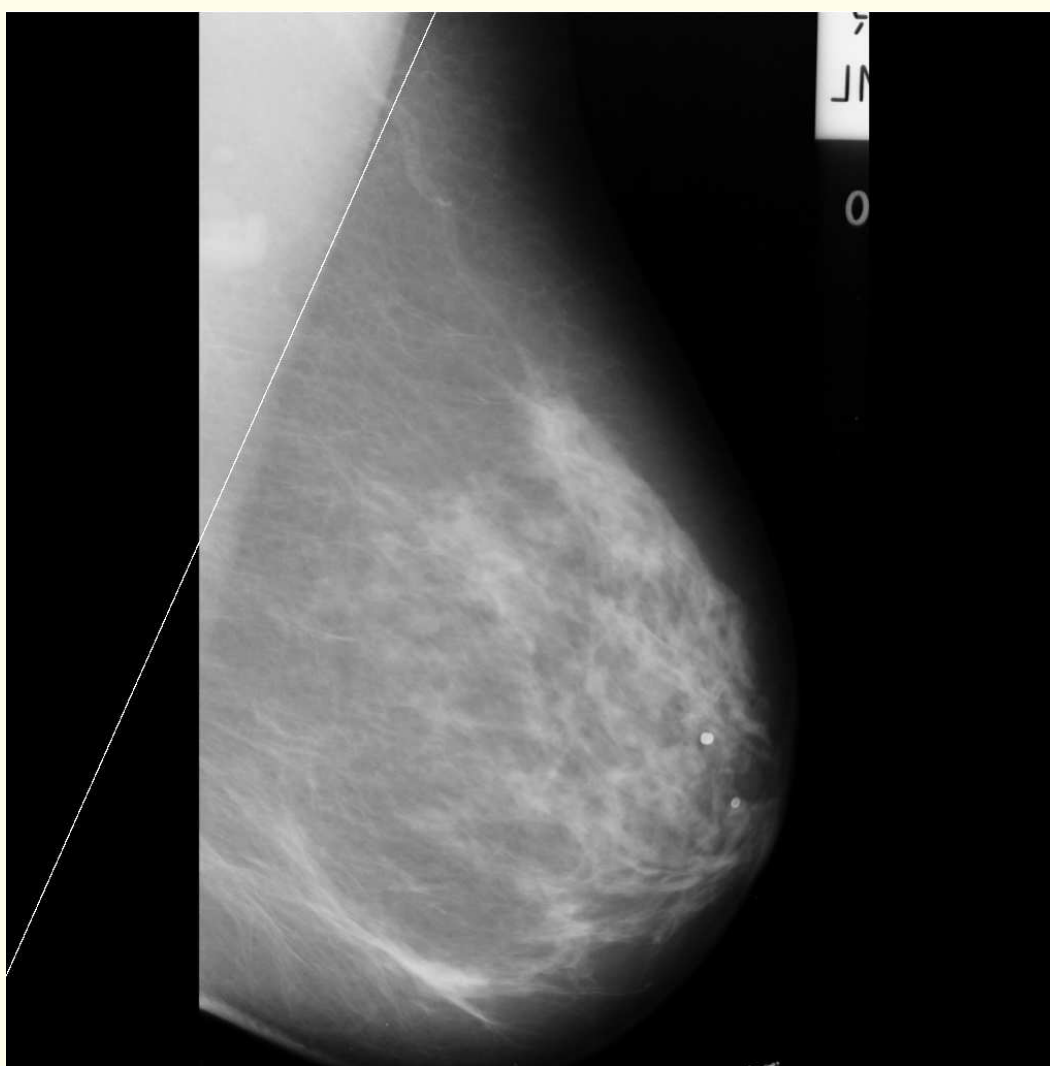
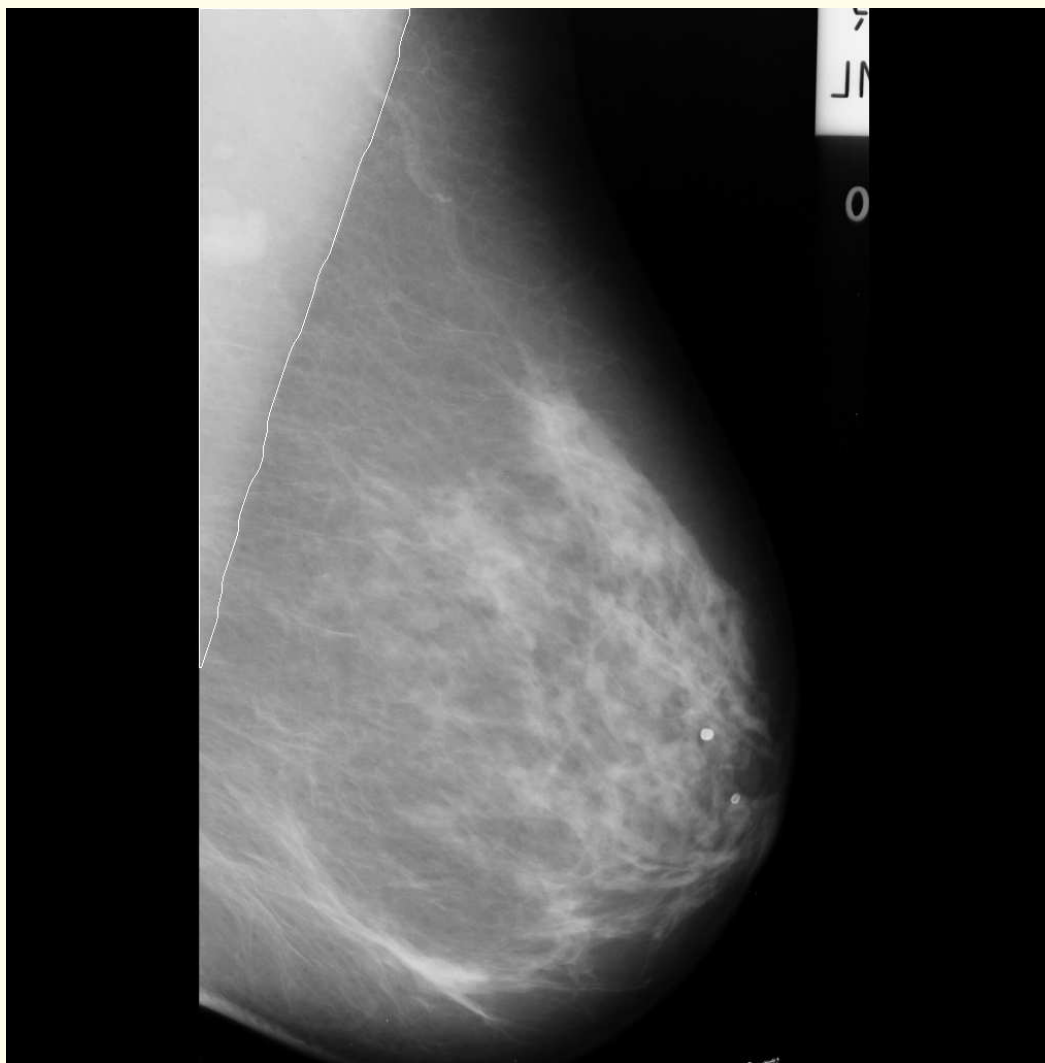
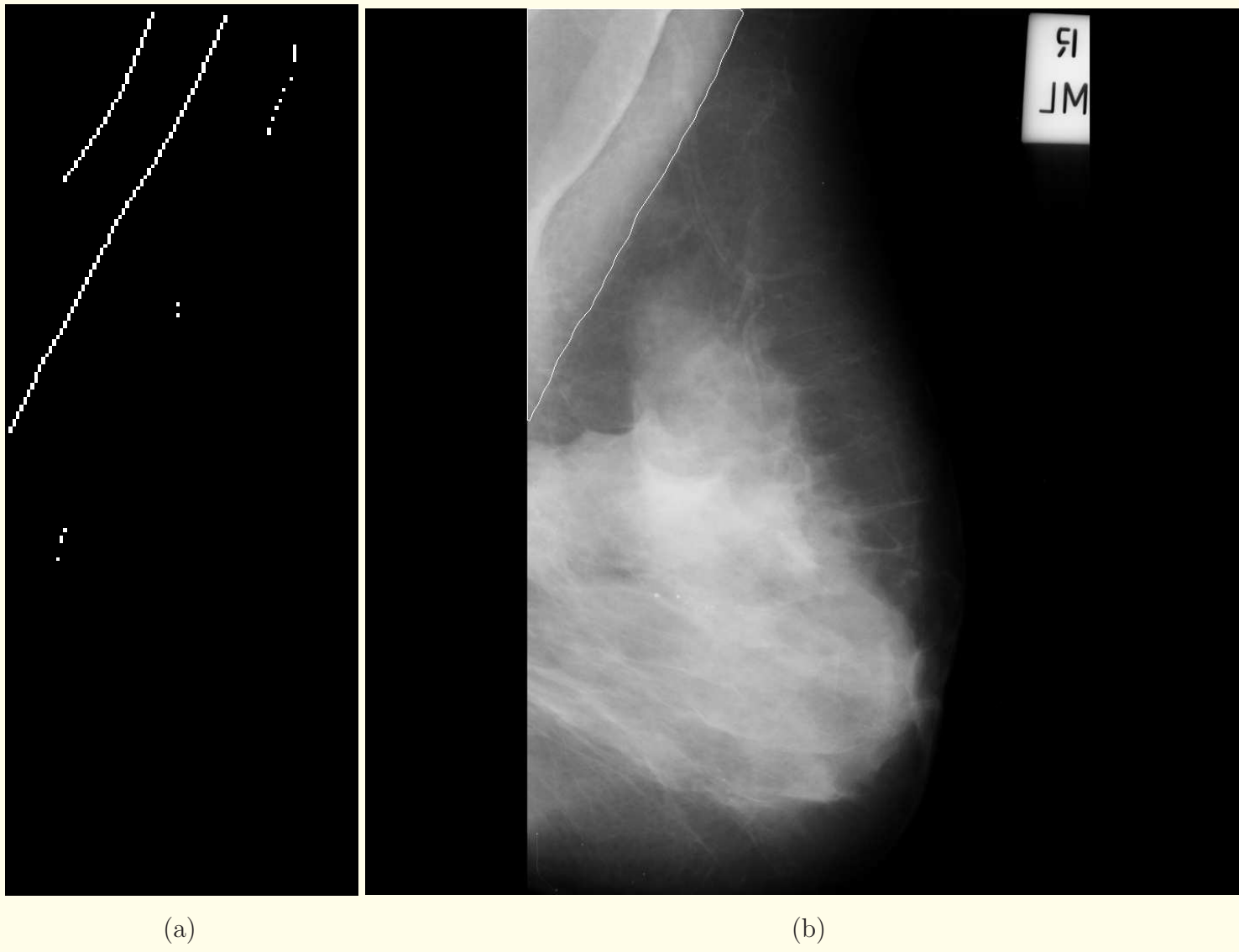


Figure 5.73 (c)



(d)

Figure 5.73: Results obtained for the image mdb008 from the Mini-MIAS database. (a) Original image. (b) Hand-drawn pectoral muscle edge superimposed on the histogram-equalized image. (c) and (d) Pectoral muscle edges detected by the Hough-transform-based and Gabor-wavelet-based methods, respectively, superimposed on the original image. Reproduced with permission from R.J. Ferrari, R.M. Rangayyan, J.E.L. Desautels, R.A. Borges, and A.F. Frère, “Automatic identification of the pectoral muscle in mammograms”, *IEEE Transactions on Medical Imaging*, 23: 232 – 245, 2004. © IEEE.



(a)

(b)

Figure 5.74: Image mdb110 from the Mini-MIAS database, showing the result of the detection of the pectoral muscle in the presence of the pectoralis minor. (a) Edge candidates after the post-processing stage. (b) Final boundary detected by the Gabor-wavelet-based method. Reproduced with permission from R.J. Ferrari, R.M. Rangayyan, J.E.L. Desautels, R.A. Borges, and A.F. Frère, “Automatic identification of the pectoral muscle in mammograms”, *IEEE Transactions on Medical Imaging*, 23: 232 – 245, 2004. © IEEE.



## 5.11 Application: Improved Segmentation of Breast Masses by Fuzzy-set-based Fusion of Contours and Regions

Given the difficult nature of the problem of the detection of masses and tumors in a mammogram, the question arises

“Can the problem benefit from the use of multiple approaches?”

Guliato et al. proposed two approaches to the problem:

one based upon contour detection,

and the other based upon a fuzzy region-growing method.



The former method is simple and easy to implement, always produces closed contours, and yields good results even in the presence of high levels of noise (see Section 5.5.2);

the latter produces a fuzzy representation of the ROI, and preserves the uncertainty around the boundaries of tumors (see Section 5.5.3).

As a follow-up, Guliato et al. considered the following question:

How may we combine the results of the two approaches — which may be considered to be complementary — so as to obtain a possibly better result?

Guliato et al. proposed a general fusion operator, oriented by a finite automaton, to combine information from different sources.



## Elementary concepts of fusion operators:

A *fusion operator* over fuzzy sets is formally defined as a function  $h : [0, 1]^n \rightarrow [0, 1]$ , where  $n \geq 2$  represents the number of sources of input information.

Fusion operators may be classified according to their behavior into three classes —

conjunctive, disjunctive, and compromise operators:



- An operator is said to be *conjunctive* if

$$h(a_1, a_2, \dots, a_n) \leq \min \{a_1, a_2, \dots, a_n\}, a_i \in [0, 1].$$

Conjunctive operators are those that represent a consensus between the items of information being combined.

They generalize classical intersection, and agree with the source that offers the smallest measure while trying to obtain simultaneous satisfaction of its criteria.

Conjunctive operators present a *severe* behavior.



- An operator is said to be *disjunctive* if

$$h(a_1, a_2, \dots, a_n) \geq \max \{a_1, a_2, \dots, a_n\}.$$

Disjunctive operators generalize classical union.

They agree with the source that offers the greatest measure, and express redundancy between criteria.

They present a *permissive* behavior.



- An operator is said to be a *compromise operator* if

$$\begin{aligned} \min\{a_1, a_2, \dots, a_n\} &\leq h(a_1, a_2, \dots, a_n) \\ &\leq \max\{a_1, a_2, \dots, a_n\}. \end{aligned}$$

Compromise operators produce an intermediate measure between items of information obtained from several sources.

They present *cautious* behavior.



Context-independent, constant-behavior operators:  
maintain the same behavior independent of the input variables.

Context-independent, variable-behavior operators:  
behavior varies according to the input variables.

Context-dependent operators: behavior varies as in the previous case, also taking into account the agreement between the sources and their reliability.

The following paragraphs provide the description of a class of fusion operators that generalize context-dependent operators,

taking into consideration different degrees of confidence in the sources, specific knowledge, and spatial context while operating with conceptually distinct sources.



## Considerations in the fusion of the results of complementary segmentation techniques:

Figure 5.75 illustrates an overlay of two segmentation results obtained by two complementary techniques —

region growing represented by a fuzzy set  $S_r$ , and

closed-contour detection represented by a fuzzy set  $S_c$  —

for the same ROI.

The straight line within  $S_r$  indicates a possible artifact.

The results are not the same: different segmentation algorithms may produce different results for the same ROI.



A fusion operator designed to aggregate such entities should produce a third entity that takes into consideration the inputs and is better than either input on its own.

In order to realize this, the fusion operator must be able to identify regions of certainty and uncertainty during its execution.

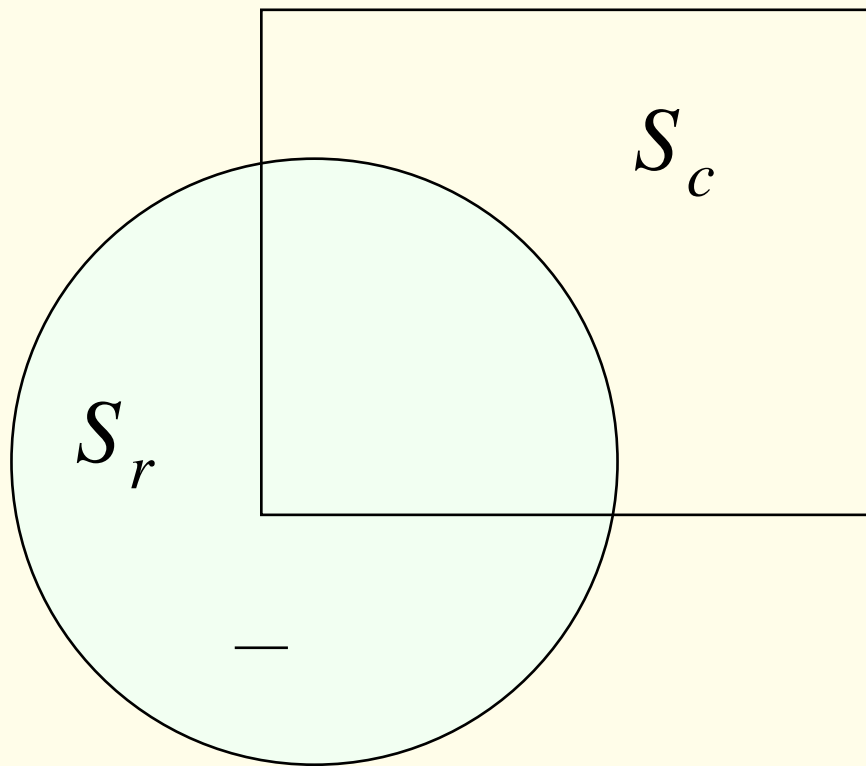


Figure 5.75: Superimposition of the results of two complementary segmentation techniques. The circular region  $S_r$  represents the result of region growing. The square box  $S_c$  represents the result of contour detection. Reproduced with permission from D. Guliato, R.M. Rangayyan, W.A. Carnielli, J.A. Zuffo, and J.E.L. Desautels, “Fuzzy fusion operators to combine results of complementary medical image segmentation techniques”, *Journal of Electronic Imaging*, 12(3): 379 – 389, 2003. © SPIE and IS&T.

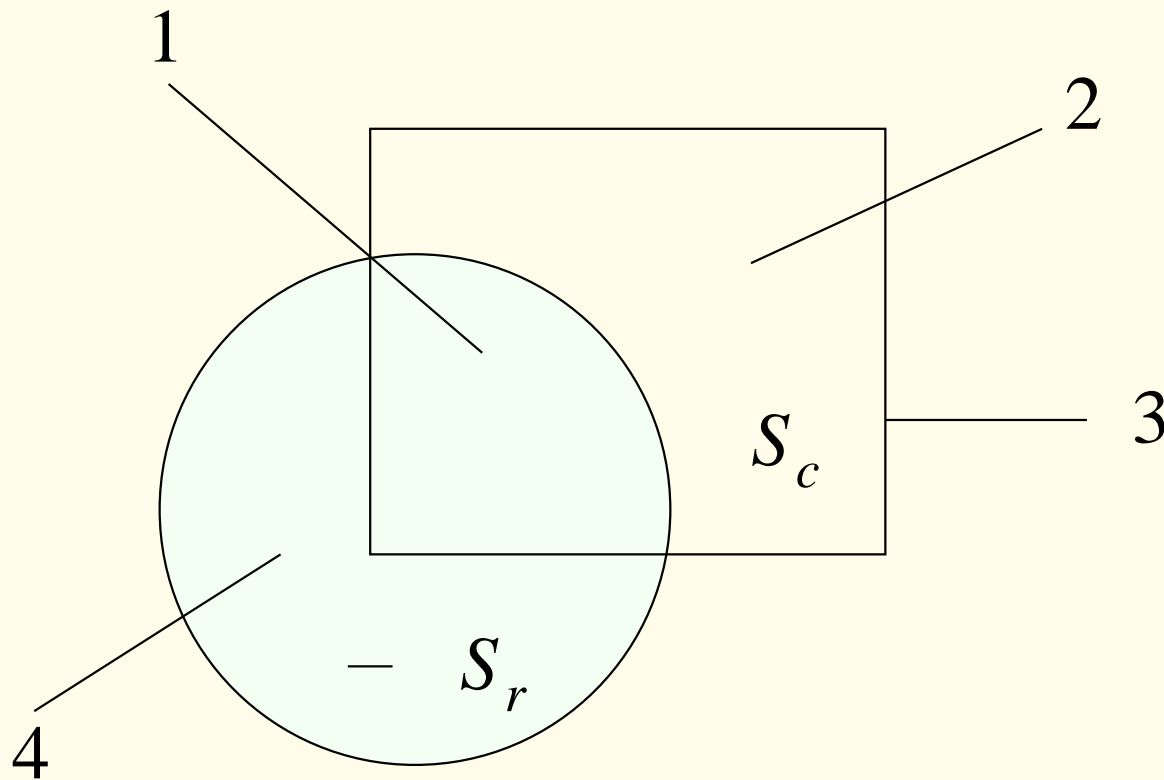


Figure 5.76: The four different situations treated by the fusion operator. Reproduced with permission from D. Gulianto, R.M. Rangayyan, W.A. Carnielli, J.A. Zuffo, and J.E.L. Desautels, “Fuzzy fusion operators to combine results of complementary medical image segmentation techniques”, *Journal of Electronic Imaging*, 12(3): 379 – 389, 2003. © SPIE and IS&T.



Considering a pixel  $p$  being analyzed, let  $\Gamma_{S_r}(p)$  be the membership degree of  $p$ , such that  $S_r = \Gamma_{S_r} : I \rightarrow [0, 1]$ , where  $I$  is the original image.

Also, let  $\Gamma_{S_c}(p)$  be the membership degree of  $p$ , such that  $S_c = \Gamma_{S_c} : I \rightarrow [0, 1]$ .

It is important to note that  $\Gamma_{S_c}(p)$  is zero when the pixel  $p$  is inside or outside of  $S_c$ , and that  $\Gamma_{S_c}(p)$  possesses a high value when  $p$  is on the contour represented by  $S_c$ .

Similarly,  $\Gamma_{S_r}(p)$  is high when  $p$  belongs to the region, and  $\Gamma_{S_r}(p)$  is low or zero when  $p$  does not belong to the region.



With respect to the fusion operator, four situations may be identified considering the position of  $p$  (see Figure 5.76):

1.  $p$  belongs to the intersection of  $S_r$  and  $S_c$

[that is,  $\Gamma_{S_r}(p)$  is high and  $\Gamma_{S_c}(p)$  is zero].

In this case the pixel  $p$  belongs to the final segmentation result with a high membership degree.

The sources agree with respect to the inclusion of the pixel  $p$  in the final result.

This is a case of certainty.



2.  $p$  does not belong to  $S_r$  or belongs to  $S_r$  with a low membership degree, and is inside  $S_c$

[that is,  $\Gamma_{S_r}(p)$  is low or zero and  $\Gamma_{S_c}(p)$  is zero].

In this case the sources disagree with respect to the inclusion of the pixel  $p$  in the final result.

This is a case of uncertainty.



3.  $p$  belongs to the contour line of  $S_c$  [that is,  $\Gamma_{S_c}(p)$  is high] and does not belong to  $S_r$  [that is,  $\Gamma_{S_r}(p)$  is low or zero].

As in Item 2 above, this is an uncertainty situation.

Note that although the inputs are different from those presented in Item 2 above, the result of the fusion operator is expected to represent uncertainty.



4.  $p$  belongs to  $S_r$  [that is,  $\Gamma_{S_r}(p)$  is high] and is outside of  $S_c$  [that is,  $\Gamma_{S_c}(p)$  is zero].

Here again we have an uncertainty case.

Observe that although the inputs are similar to those in Item 1 [that is,  $\Gamma_{S_r}(p)$  is high and  $\Gamma_{S_c}(p)$  is zero], the result of the fusion operator is expected to be different.



A practically applicable fusion operator should be composed of a number of basic fusion operators.

The spatial position of the pixel being analyzed is an important item of information that should be used in determining the basic fusion operator to be applied to the pixel.

Based upon these observations, Guliato et al. proposed a general fusion operator oriented by a finite automaton:

the finite set of states of the automaton is determined by the spatial position of the pixel being analyzed;

the transition function (to be defined later) depends on the strategy used to traverse the image.



An important question to be considered in fusion is the reliability of the sources (original segmentation results).

The result of the fusion operator depends on how good the original segmentation results are.

The evaluation of the individual segmentation results is not a component of the fusion procedure;

parameters are included in the definitions of the operators to represent the reliability of the sources;

it is assumed that the parameters are determined using other methods.



## General finite-automaton-oriented fusion operators:

Formally, a *fusion operator oriented by a finite automaton* that aggregates  $n$  sources may be defined as an ordered pair  $\langle H, M \rangle$ , where:

- $H = \{h_1, h_2, \dots, h_k\}$  is a finite set of *basic fusion operators*, where  $h_i$  are functions that map  $[0, 1]^n \rightarrow [0, 1]$ ,  $n \geq 2$ .



- $M = (Q, \Sigma, \delta, q_0, F)$  is a finite automaton, where:
  - $Q$  is a finite set of states,
  - $\Sigma$  is a finite input alphabet,
  - $\delta$  is a transition function that maps  $Q \times \Sigma \rightarrow Q$ ,  
where  $\times$  is the Cartesian product operator,
  - $q_0 \in Q$  is an initial state, and
  - $F \subset Q$  is the set of final states.



In the present case, the alphabet  $\Sigma$  is given by a finite collection of labels associated with the Cartesian product of finite partitions of the interval  $[0, 1]$ .

For example, suppose that, coming from different motivations, we are dividing  $[0, 1]$  into two finite partitions  $P_1$  and  $P_2$ , where  $P_1$  divides the values between ‘low’ and ‘high’, and  $P_2$  between ‘good’ and ‘bad’.

Our alphabet may be composed of  $\Sigma = \{0, 1, 2\}$  representing the combinations (low, good), (low, bad), and (high, good), respectively, for example.

We are not necessarily using the whole set of possibilities.



The interpretation of the transition function  $\delta$  of a finite automaton is the following:

$\delta(q_i, a) = q_j$  is a valid transition if, and only if, the automaton can go from the state  $q_i$  to  $q_j$  through the input  $a$ .

Sometimes,  $q_i$  and  $q_j$  could be the same state.

If there is a transition from the state  $q_i$  to  $q_j$  through the input  $a$ , then there is a directed arc from  $q_i$  to  $q_j$  with the label  $a$  in the graphical representation (transition diagram) of the specific automaton; see Figure 5.77.

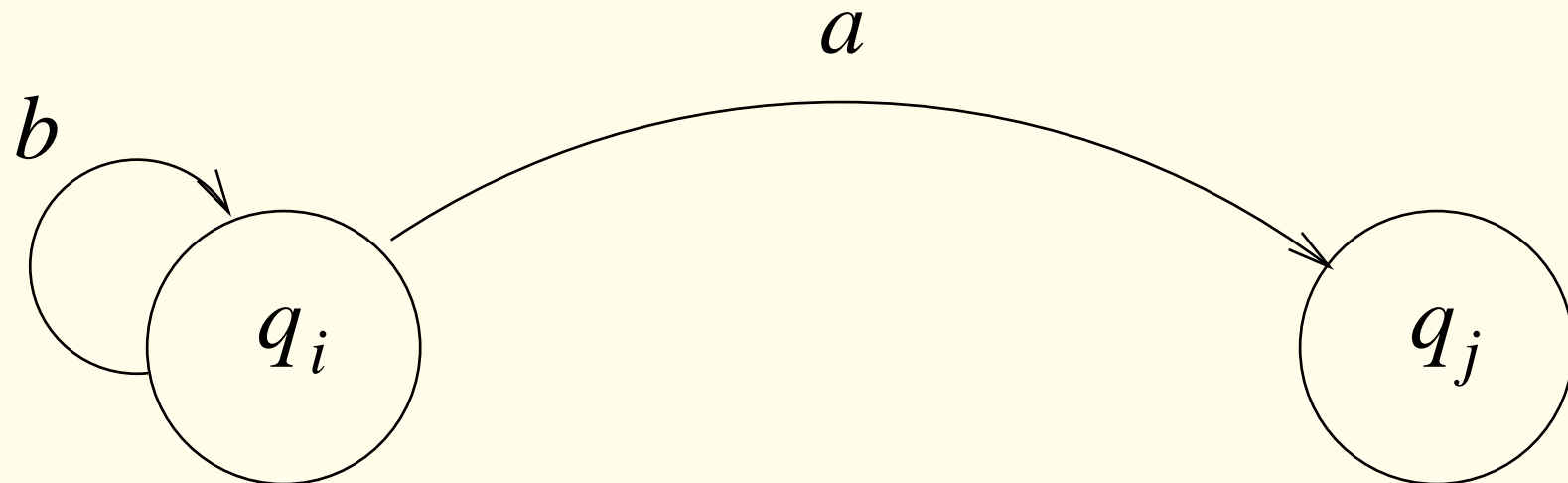


Figure 5.77: Graphical representation of the transition function given by  $\delta(q_i, a) = q_j$  and  $\delta(q_i, b) = q_i$ . Reproduced with permission from D. Guliato, R.M. Rangayyan, W.A. Carnielli, J.A. Zuffo, and J.E.L. Desautels, “Fuzzy fusion operators to combine results of complementary medical image segmentation techniques”, *Journal of Electronic Imaging*, 12(3): 379 – 389, 2003. © SPIE and IS&T.



## Application of the fusion operator to image segmentation:

The fusion operator proposed by Guliato et al. is designed to combine the results obtained from two segmentation techniques that explore complementary characteristics of the image:

one based on region growing, and

the other based on closed-contour detection.

The result of fusion obtained is a fuzzy set that represents the agreement or disagreement between the input sources.



Let  $S_r$ , based on region growing, and

$S_c$ , based on closed-contour detection

represent the two segmented images to be combined,  
as shown in Figure 5.75.

The process starts with a seed pixel selected by the user.

The seed pixel must belong to the intersection  $S_r \cap S_c$ .

It is assumed that  $S_r$  and  $S_c$  are each endowed with a  
reliability measure, given by a number in the interval  $[0, 1]$ .



The fusion operator is represented by  $\mathcal{O} = \langle H, M \rangle$ ,

where  $H = \{h_1, h_2, \dots, h_6\}$  is a collection of six basic fusion operators that take into consideration the reliability measures of the sources, and

$M$  is a finite automaton that governs the actions of the operator.

The parameters  $C_r$  and  $C_c$  range within the interval  $[0, 1]$  and denote the reliability measures of the sources  $S_r$  and  $S_c$ .

The parameters are used to indicate the influence that a given source should have on the final result of the fusion operation: the higher the value, the larger the influence of the source.



The result of each basic fusion operator should give information about the agreement among the sources being analyzed.

The absence of conflict is represented by a membership degree equal to 1 or 0; that is, both the sources agree or do not agree with respect to the membership of the given pixel in the ROI.

Maximal conflict is represented by membership degree = 0.5; the sources do not agree with respect to the membership of the given pixel.

Intermediate membership degrees denote proportionately intermediate degrees of agreement.



Let  $p_{ij}$  be the  $j^{th}$  pixel of the segmented image  $S_i$  and

$\Gamma_{S_i}(p_{ij})$  be the membership degree of the pixel  $p_{ij}$ ,

where  $i \in \{r, c\}$ ,  $j = 1, 2, \dots, m$ , and

$m$  is the total number of pixels in the image  $I$ .

**Note:** In the present section, we are using only one index  $j$  to represent the position of a pixel in an image.



Then, the basic fusion operators are defined as follows:

$$1. h_1 = \max\{C_r \Gamma_{S_r}(p_{rj}), C_c, 0.5\}.$$

This is a disjunctive operator that associates with the pixels in  $S_r \cap S_c$  new membership degrees taking into account the source with the greater reliability measure;  
see  $h_1$  in Figure 5.78.



2. if  $\max(C_r, C_c) \leq 0.5$

then  $h_2 = 0.5$

else if ( $C_r \leq 0.5$ )

then  $h_2 = C_c \Gamma_{S_c}(p_{cj})$

else if ( $C_c < 0.5$ )

then  $h_2 = C_r \Gamma_{S_r}(p_{rj})$

else  $h_2 = \frac{1}{(C_r+C_c)} [C_r \Gamma_{S_r}(p_{rj}) + C_c \Gamma_{S_c}(p_{cj})]$ .

This is a compromise operator that acts on the pixels in the transition region between the interior and the exterior of the result of contour detection; see  $h_2$  in Figure 5.78.



3. if  $\max(C_r, C_c) \leq 0.5$

then  $h_3 = 0.5$

else if ( $C_r \leq 0.5$ )

then  $h_3 = C_c$

else if ( $C_c \leq 0.5$ )

then  $h_3 = C_r \Gamma_{S_r}(p_{rj})$

else  $h_3 = \frac{1}{(C_r+C_c)} [C_r \Gamma_{S_r}(p_{rj}) + C_c]$ .

This is a compromise operator that acts on the pixels lying outside the result of region growing and in the interior of the result of contour detection; see  $h_3$  in Figure 5.78.



4. if  $\max(C_r, C_c) \leq 0.5$

then  $h_4 = 0.5$

else if ( $C_r \leq 0.5$ )

then  $h_4 = 0$

else if ( $C_c \leq 0.5$ )

then  $h_4 = C_r \Gamma_{S_r}(p_{rj})$

else  $h_4 = \frac{1}{(C_r+C_c)} \{C_r \Gamma_{S_r}(p_{rj}) + [1 - \sqrt{C_c}]^2\}.$



$h_4$  is a compromise operator that acts on the pixels lying outside the result of contour detection and belonging to the interior of the result of region growing; see  $h_4$  in Figure 5.78. Artifacts within the region-growing result are rejected (the line segment inside the circle in Figure 5.78).



$$5. h_5 = \max\{C_r \Gamma_{S_r}(p_{rj}), C_c \Gamma_{S_c}(p_{cj}), 0.5\}.$$

This is a disjunctive operator that acts on the transition pixels lying in the intersection  $S_r \cap S_c$ ; see  $h_5$  in Figure 5.78.



6. if  $\max(C_r, C_c) \leq 0.5$

then  $h_6 = 0.0$

else if ( $C_r \leq 0.5$ )

then  $h_6 = 0.0$

else if ( $C_c \leq 0.5$ )

then  $h_6 = C_r \Gamma_{S_r}(p_{rj})$

else  $h_6 = \min\{C_r \Gamma_{S_r}(p_{rj}), [1 - C_c]\}$ .

This is a conjunctive operator that acts on the exterior of  $S_r \cup S_c$  and determines a limiting or stopping condition for the operator (see  $h_6$  in Figure 5.78).

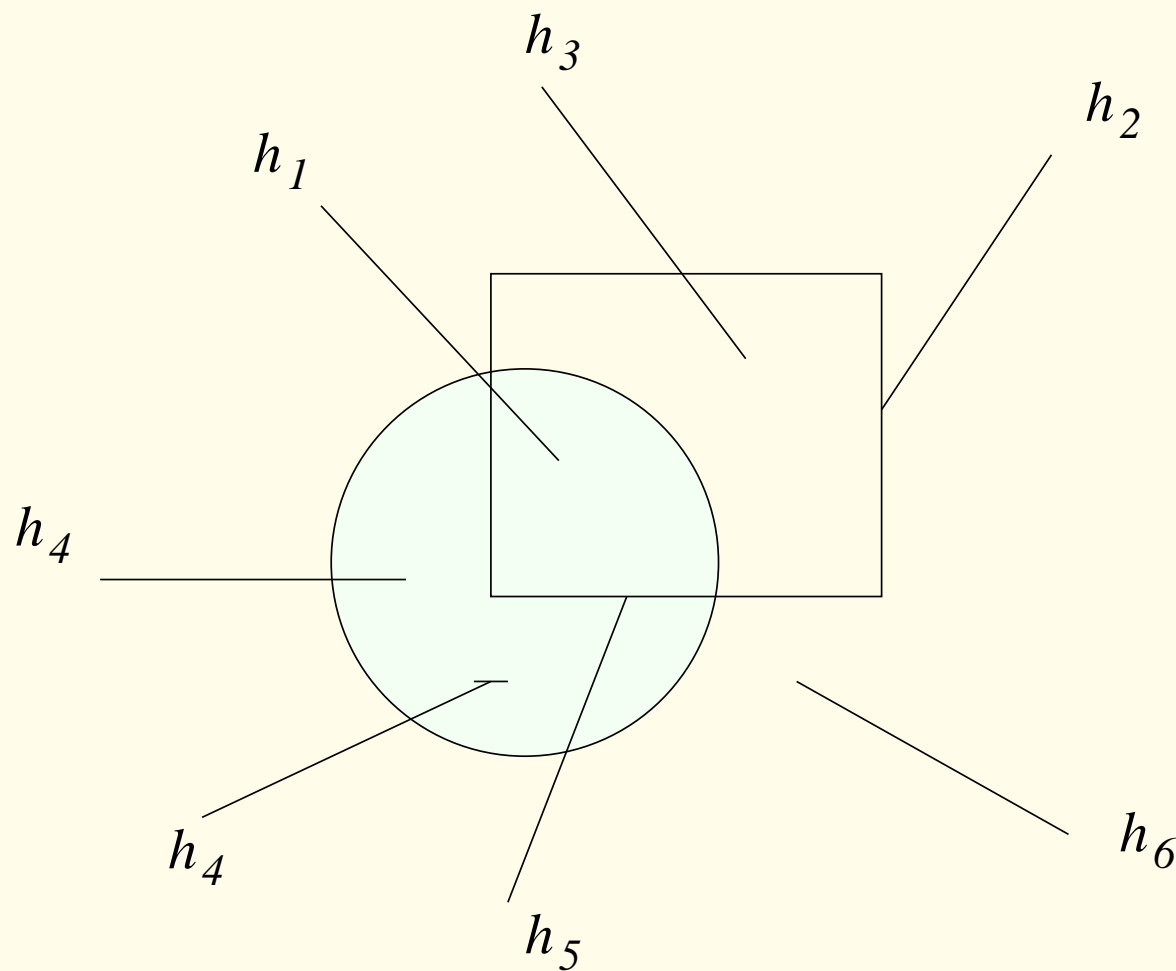


Figure 5.78: The regions where the six basic fusion operators are applied are indicated by  $\{h_1, h_2, h_3, h_4, h_5, h_6\}$ . Reproduced with permission from D. Guliato, R.M. Rangayyan, W.A. Carnielli, J.A. Zuffo, and J.E.L. Desautels, “Fuzzy fusion operators to combine results of complementary medical image segmentation techniques”, *Journal of Electronic Imaging*, 12(3): 379 – 389, 2003. © SPIE and IS&T.



## Description of the finite automaton:

The finite automaton  $M = (Q, \Sigma, \delta, q_0, F)$  in  $\mathcal{O}$  is defined by the following entities:

- A set of finite states  $Q = \{a, b, c\}$ , where
  - state  $a$  indicates that the pixel being analyzed belongs to the interior of the contour,
  - state  $b$  indicates that the pixel being analyzed belongs to the contour, and
  - state  $c$  indicates that the pixel being analyzed belongs to the exterior of the contour (see Figure 5.79).



- A finite input alphabet  $\Sigma = \{I_1, I_2, I_3, I_4\}$ .

Let  $\pi_1$  and  $\pi_2$  be two finite partitions of  $[0, 1]$ , where  $\pi_1 = \pi_2 = \{\text{high}, \text{low}\}$ .

We can choose the classes **high** and **low** as follows:

$$\text{low} = [0, 0.5),$$

$$\text{high} = [0.5, 1.0];$$

$p_{ij} \in \text{high}$  if  $\Gamma_{S_i}(p_{ij}) \geq 0.5$  for  $j = 1, 2, \dots, m$ , and

$p_{ij} \in \text{low}$  if  $\Gamma_{S_i}(p_{ij}) < 0.5$  for  $j = 1, 2, \dots, m$ ,

where  $p_{ij}$ ,  $i \in \{r, c\}$ , and  $j = 1, 2, \dots, m$ , identify the  $i^{th}$  source and the  $j^{th}$  pixel; and

$\Gamma_{S_i}(p_{ij})$  is the membership degree of the pixel  $p_j$  in  $S_i$ .



The finite input alphabet  $\Sigma$  is produced by the function

$\mu : \pi_1 \times \pi_2 \rightarrow \Sigma$ , where:

–  $\mu(\text{high}, \text{low}) = I_1$ .

The pixel being analyzed presents a high membership degree in the region-growing segmentation result and a low membership degree in the closed-contour result.

This input represents a certainty or uncertainty situation depending on the spatial position of the pixel being analyzed; see Figure 5.80.



$$-\mu(\text{high}, \text{high}) = I_2.$$

The pixel being analyzed presents a high membership degree in the region-growing segmentation result and a high membership degree in the closed-contour result.

This indicates an intersection case; see Figure 5.80.



$$-\mu(\text{low}, \text{high}) = I_3.$$

The pixel being analyzed presents a low membership degree in the region-growing segmentation result and a high membership degree in the closed-contour result.

This indicates an uncertainty case; see Figure 5.80.



$$-\mu(\text{low}, \text{low}) = I_4.$$

The pixel being analyzed presents a low membership degree in the region-growing segmentation result and a low membership degree in the closed-contour result.

This indicates an uncertainty case if the pixel belongs to the interior of the contour;  
in the opposite case, this indicates a stopping or limiting condition of the fusion operator; see Figure 5.80.



- A transition diagram  $\delta$  of  $M$ , as shown in Figure 5.81.

The transition diagram illustrates the situations when the basic fusion operator is executed.

The analysis begins with a pixel that belongs to the intersection of the two segmentation results.

The first input must be of type  $I_1$ ; the initial state of the automaton is  $a$ , which corresponds to the fact that the pixel belongs to the interior of the contour.

The analysis procedure is first applied to all of the pixels inside the contour.

While the inputs are  $I_1$  or  $I_4$ , the operators  $h_1$  or  $h_3$  will be applied and the automaton remains in state  $a$ .



When an input of type  $I_2$  or  $I_3$  arrives, the automaton goes to state  $b$  to inform the analysis process that the pixel being processed is on the boundary given by contour detection.

At this stage, all the pixels on the contour are processed.

While the inputs are  $I_2$  or  $I_3$  and the operators  $h_5$  or  $h_2$  are applied, the automaton will remain in state  $b$ .

If, while in state  $b$ , the input  $I_1$  or  $I_4$  occurs, and the operators  $h_4$  or  $h_6$  applied, the automaton goes to state  $c$ , indicating that the pixel being analyzed is outside the contour.



All the pixels outside the contour are processed at this stage.

Observe that, depending upon the state of the automaton, different fusion operators may be applied to the same inputs.

As indicated by the transition diagram in Figure 5.81, all of the pixels in the interior of the contour are processed first; all of the pixels on the contour are processed next, followed by the pixels outside the contour.



- The initial state  $q_0 \in Q$ , with  $q_0 = \{a\}$ .
- The set of final states  $F = \{c\}$ , where  $F \subseteq Q$ .  
In the present case,  $F$  has only one element.

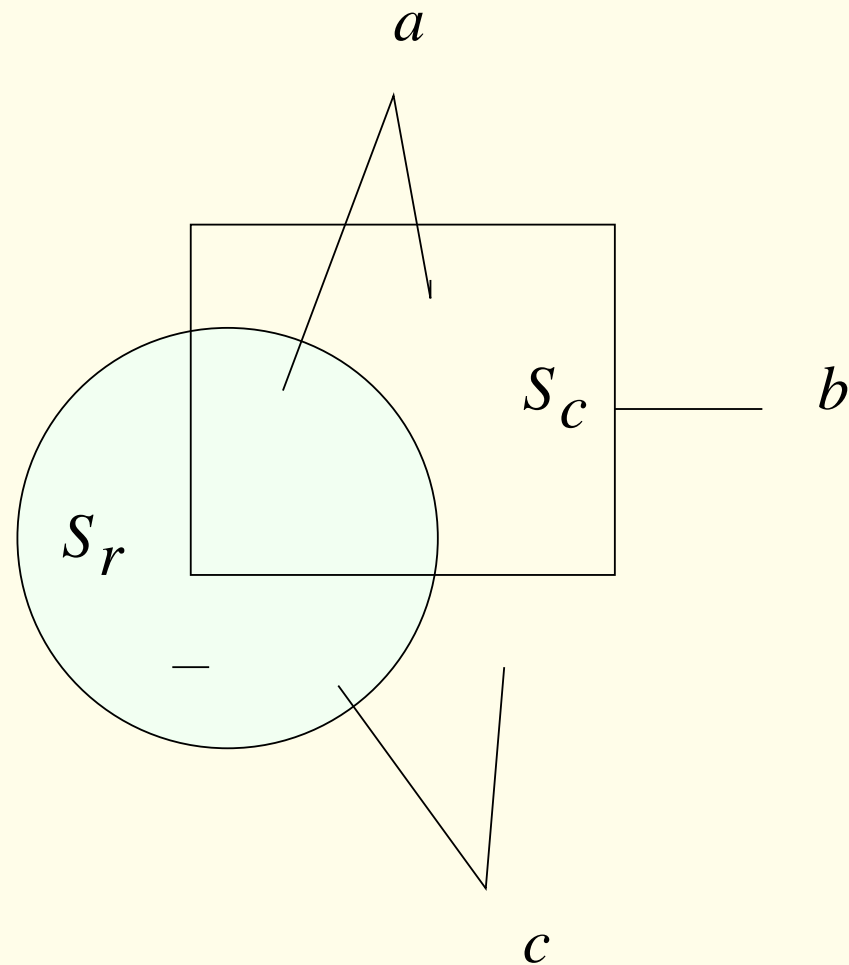


Figure 5.79: The three states of the automaton. Reproduced with permission from D. Guliato, R.M. Rangayyan, W.A. Carnielli, J.A. Zuffo, and J.E.L. Desautels, “Fuzzy fusion operators to combine results of complementary medical image segmentation techniques”, *Journal of Electronic Imaging*, 12(3): 379 – 389, 2003. © SPIE and IS&T.

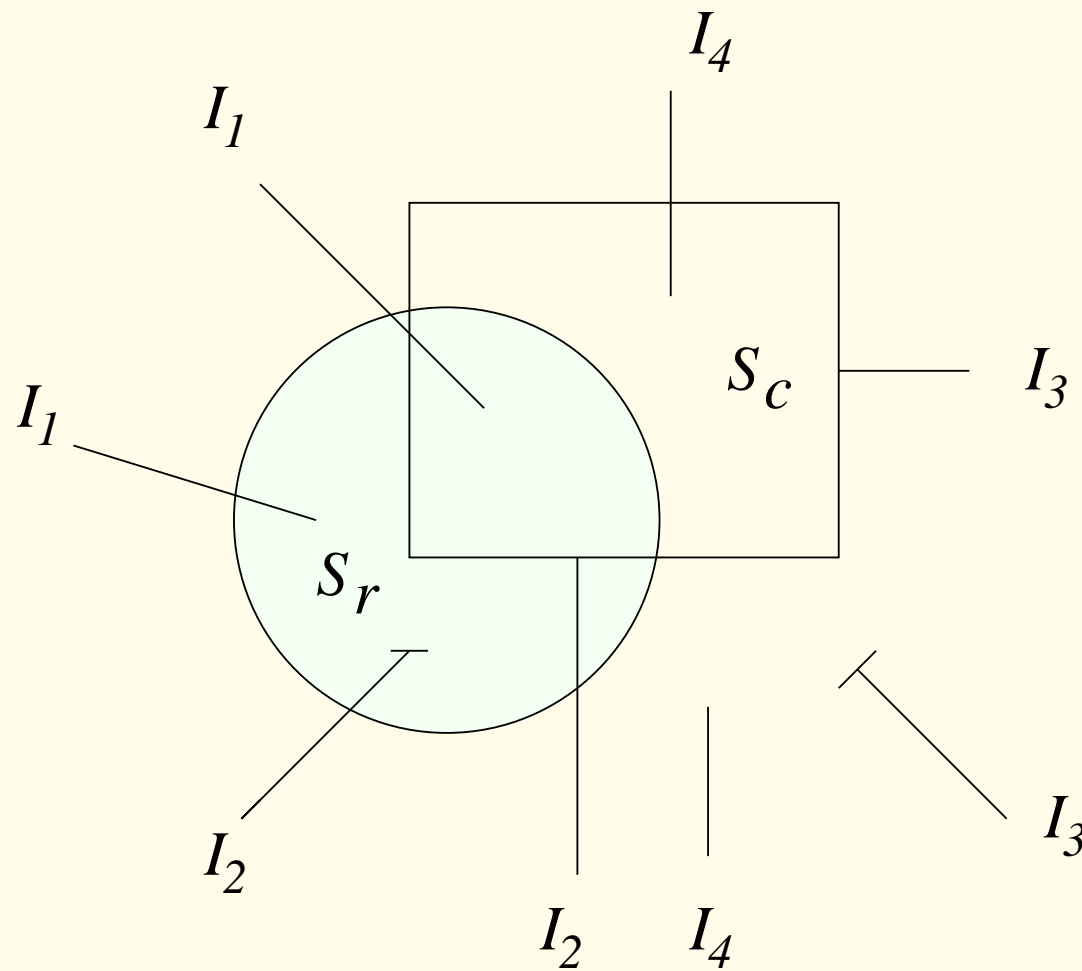


Figure 5.80: The four possible input values  $\{I_1, I_2, I_3, I_4\}$  for the fusion operator. The short line segments with the labels  $I_2$  and  $I_3$  represent artifacts in the segmentation result. Reproduced with permission from D. Guliato, R.M. Rangayyan, W.A. Carnielli, J.A. Zuffo, and J.E.L. Desautels, “Fuzzy fusion operators to combine results of complementary medical image segmentation techniques”, *Journal of Electronic Imaging*, 12(3): 379 – 389, 2003. © SPIE and IS&T.

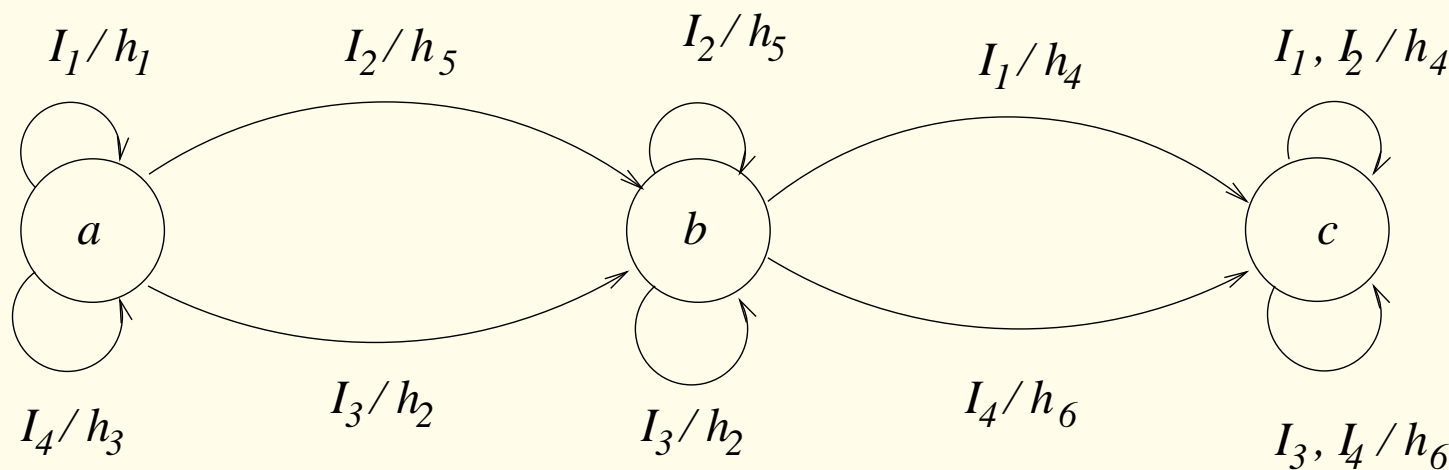


Figure 5.81: Transition diagram that governs the actions of the fusion operator. Reproduced with permission from D. Guliato, R.M. Rangayyan, W.A. Carnielli, J.A. Zuffo, and J.E.L. Desautels, “Fuzzy fusion operators to combine results of complementary medical image segmentation techniques”, *Journal of Electronic Imaging*, 12(3): 379 – 389, 2003. © SPIE and IS&T.



## Behavior of the basic fusion operators:

The fusion operator described above can combine several results of segmentation, two at a time.

The result yielded by the fusion operator is a fuzzy set that identifies the certainty and uncertainty present in the inputs to the fusion process.

It is expected that maximal certainty will be represented by a membership degree equal to 1 or 0;

that is, the pixel being analyzed certainly belongs to or does not belong to the final segmentation result.



When individual segmentation results disagree with respect to a pixel belonging or not belonging to the final result,

or when both sources do not present sufficient reliability,

the fusion operator yields a membership degree equal to 0.5 to represent a situation with maximal uncertainty.

Other situations are represented by membership degrees ranging in the interval  $(0, 0.5)$  and  $(0.5, 1)$ , depending on the evidence with respect to the membership of the analyzed pixel in the ROI and the reliability of the sources.



Two illustrative studies on the behavior of the basic fusion operators  $h_1$  and  $h_2$  are presented below, taking into consideration a limited set of entries:

- State  $a$  of the automaton (inside the contour), entry 1 (*high, low*), basic fusion operator  $h_1 = \max\{C_r \Gamma_{S_r}(p_{rj}), C_c, 0.5\}$ .

This is the starting condition of the fusion operator; see Figure 5.81.

The starting pixel must lie in the intersection of  $S_r$  and  $S_c$  (see Figures 5.78 and 5.79).



In this case,  $\Gamma_{S_r}(p_{rj}) \geq 0.5$

(that is,  $p$  belongs to the region-growing result with a high membership degree) and

$\Gamma_{S_c}(p_{cj}) < 0.5$

(that is,  $p$  is inside the contour).

This situation represents the condition that both sources agree with respect to the pixel  $p$  belonging to the ROI.

Table 5.2 provides explanatory comments describing the behavior of  $h_1$  for several values of the reliability parameters and inputs from the two sources.



- State  $a$  of the automaton (inside the contour)

or state  $b$  (on the contour),

entry 3 (*low, high*),

basic fusion operator  $h_2$ .

The operator  $h_2$  is applied when the automaton is in the state  $a$  or  $b$  and a transition occurs from a pixel inside the contour to a pixel on the contour [that is,  $\delta(a, I_3) \rightarrow b$ ]

or from a pixel on the contour to a neighboring pixel on the contour [that is,  $\delta(b, I_3) \rightarrow b$ ].

In this case,  $\Gamma_{S_r}(p_{rj}) < 0.5$

(that is,  $p$  does not belong to the region-growing result or belongs with a low membership degree),

and  $\Gamma_{S_c}(p_{cj}) > 0.5$  (that is,  $p$  is on the contour).



This situation represents the condition where the sources disagree with respect to the pixel  $p$  belonging to the ROI.

The result of  $h_2$  is a weighted average of the input membership values.

Table 5.3 provides explanatory comments describing the behavior of  $h_2$  for several values of the reliability parameters and inputs from the two sources.

Table 5.2: Behavior of the Basic Fusion Operator  $h_1$ .

| $C_r$ | $\Gamma_{S_r}(p_{rj})$ | $C_c$ | $\Gamma_{S_c}(p_{cj})$ | $h_1$ | Comments   |
|-------|------------------------|-------|------------------------|-------|--|
| 1.0   | 1.0                    | 1.0   | 0.0                    | 1.0   | $p$ belongs to the ROI with maximal certainty            |
| 1.0   | 1.0                    | 0.0   | 0.0                    | 1.0   | Result depends on the source with the higher reliability |
| 0.0   | 1.0                    | 1.0   | 0.0                    | 1.0   | Result depends on the source with the higher reliability |
| 0.0   | 1.0                    | 0.0   | 0.0                    | 0.5   | Both sources do not present reliability                  |
| 0.8   | 1.0                    | 1.0   | 0.0                    | 1.0   | Source $S_c$ presents the higher reliability             |
| 0.8   | 1.0                    | 0.8   | 0.0                    | 0.8   | Result depends on the source with the higher reliability |
| 0.9   | 1.0                    | 0.3   | 0.0                    | 0.9   | Result depends on the source with the higher reliability |

Reproduced with permission from D. Guliato, R.M. Rangayyan, W.A. Carnielli, J.A. Zuffo, and J.E.L. Desautels, “Fuzzy fusion operators to combine results of complementary medical image segmentation techniques”, Journal of Electronic Imaging, 12(3): 379 – 389, 2003. © SPIE and IS&T.

Table 5.3: Behavior of the Basic Fusion Operator  $h_2$ .

| $C_r$ | $\Gamma_{S_r}(p_{rj})$ | $C_c$ | $\Gamma_{S_c}(p_{cj})$ | $h_2$ | Comments  |
|-------|------------------------|-------|------------------------|-------|---|
| 1.0   | 0.0                    | 1.0   | 1.0                    | 0.5   | Weighted averaging  |
| 1.0   | 0.0                    | 0.0   | 1.0                    | 0.0   | Result depends on the source<br>with the higher reliability     |
| 0.0   | 0.0                    | 1.0   | 1.0                    | 1.0   | Result depends on the source<br>with the higher reliability     |
| 0.0   | 0.0                    | 0.0   | 1.0                    | 0.5   | Both sources do not present<br>reliability; maximal uncertainty |
| 0.8   | 0.0                    | 1.0   | 1.0                    | 0.56  | Weighted averaging  |

Reproduced with permission from D. Guliato, R.M. Rangayyan, W.A. Carnielli, J.A. Zuffo, and J.E.L. Desautels, “Fuzzy fusion operators to combine results of complementary medical image segmentation techniques”, Journal of Electronic Imaging, 12(3): 379 – 389, 2003. © SPIE and IS&T.



## Application of the fusion operator to the segmentation of breast tumors:

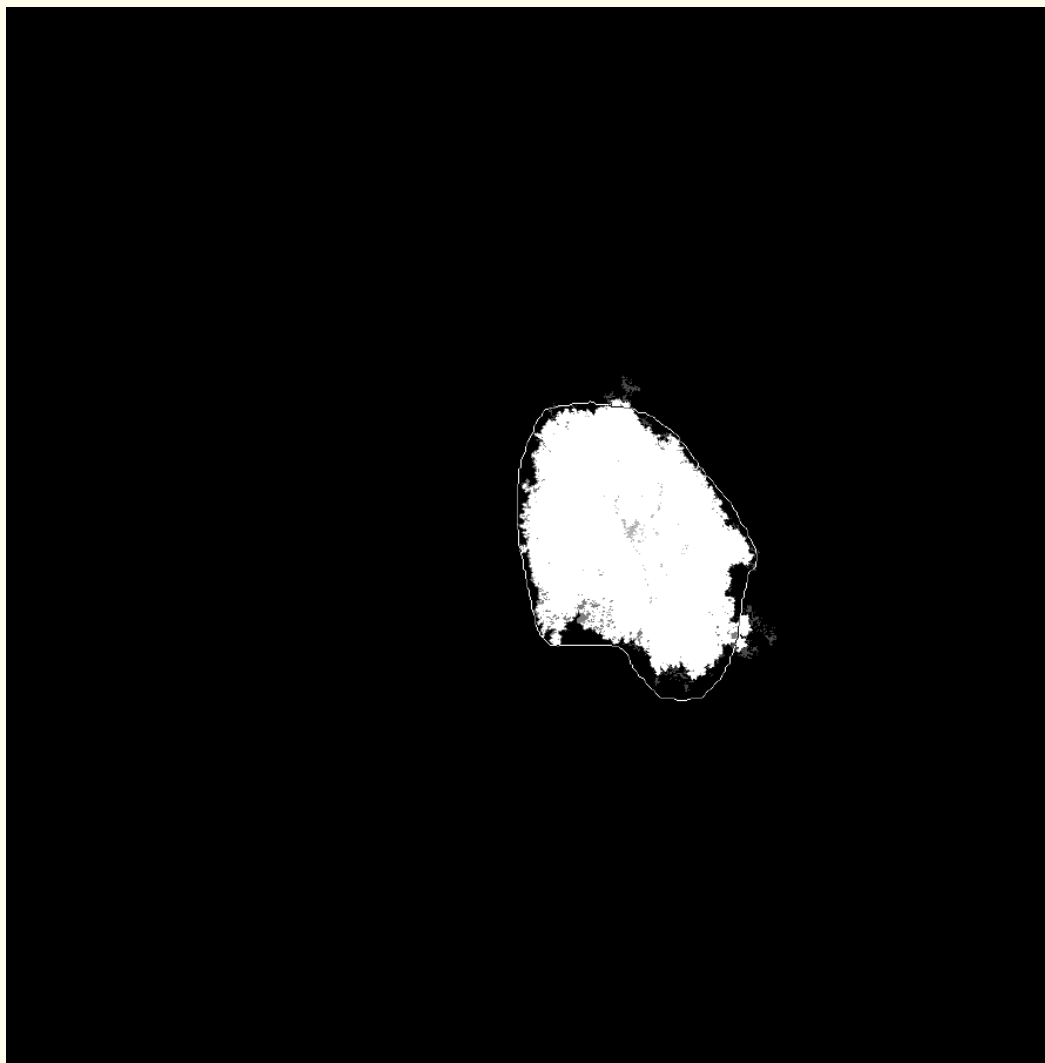
The fusion results reduce the uncertainty present in the interior of the regions, but also reduce the certainty of the boundaries.

The features of the results of the individual segmentation procedures contribute to the fusion results,

allowing the postponement of a crisp decision (if necessary) on the ROI or its boundary to a higher level of image analysis.



Figure 5.82 (a)



(b)

Figure 5.82: Result of the fusion of the contour and region (a) in Figures 5.30 (c) and (d) for the case with a malignant tumor; and (b) in Figures 5.32 (c) and (d) for the case with a benign mass, with  $C_r = 1.0$ ,  $C_c = 1.0$ . The contours drawn by the radiologist are superimposed for comparison. Reproduced with permission from D. Guliato, R.M. Rangayyan, W.A. Carnielli, J.A. Zuffo, and J.E.L. Desautels, “Fuzzy fusion operators to combine results of complementary medical image segmentation techniques”, *Journal of Electronic Imaging*, 12(3): 379 – 389, 2003. © SPIE and IS&T.

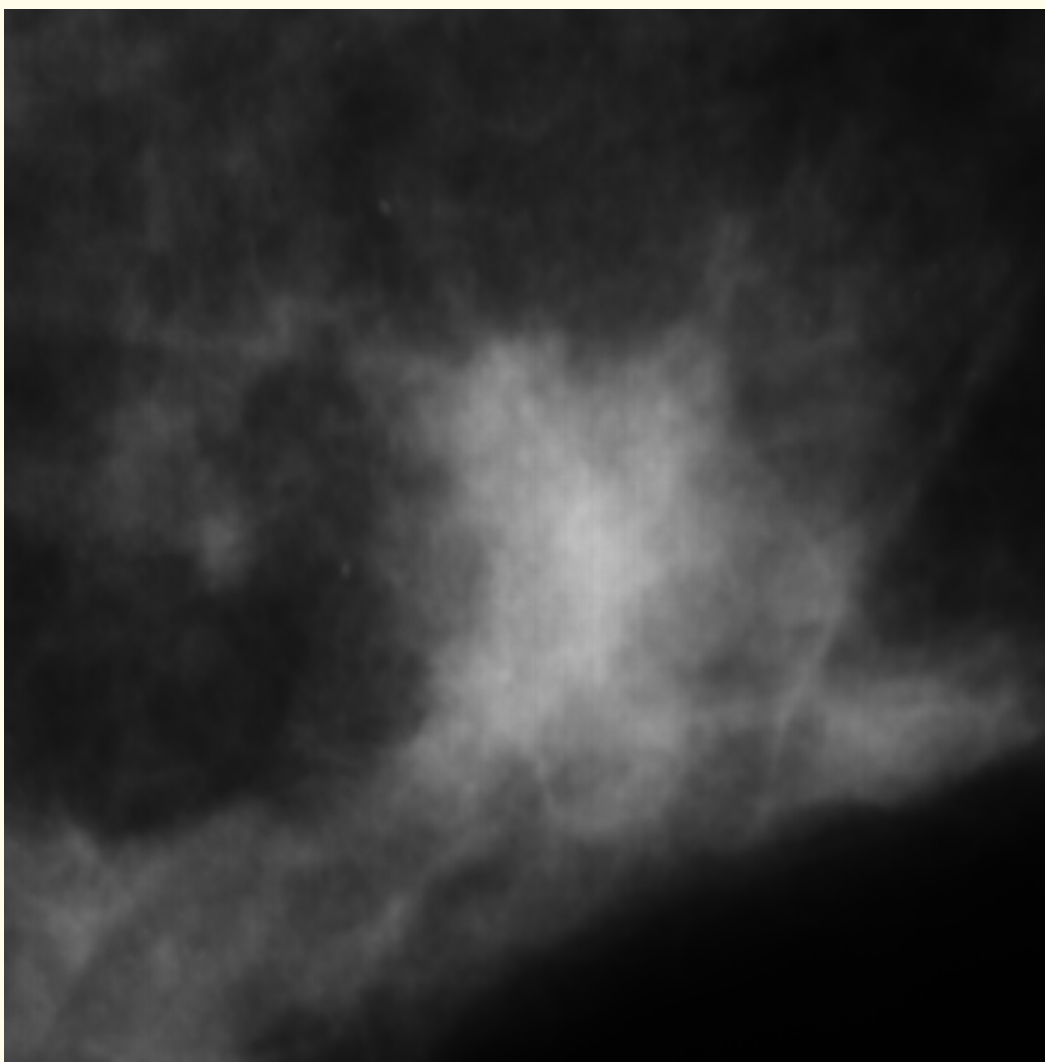


Figure 5.83 (a)

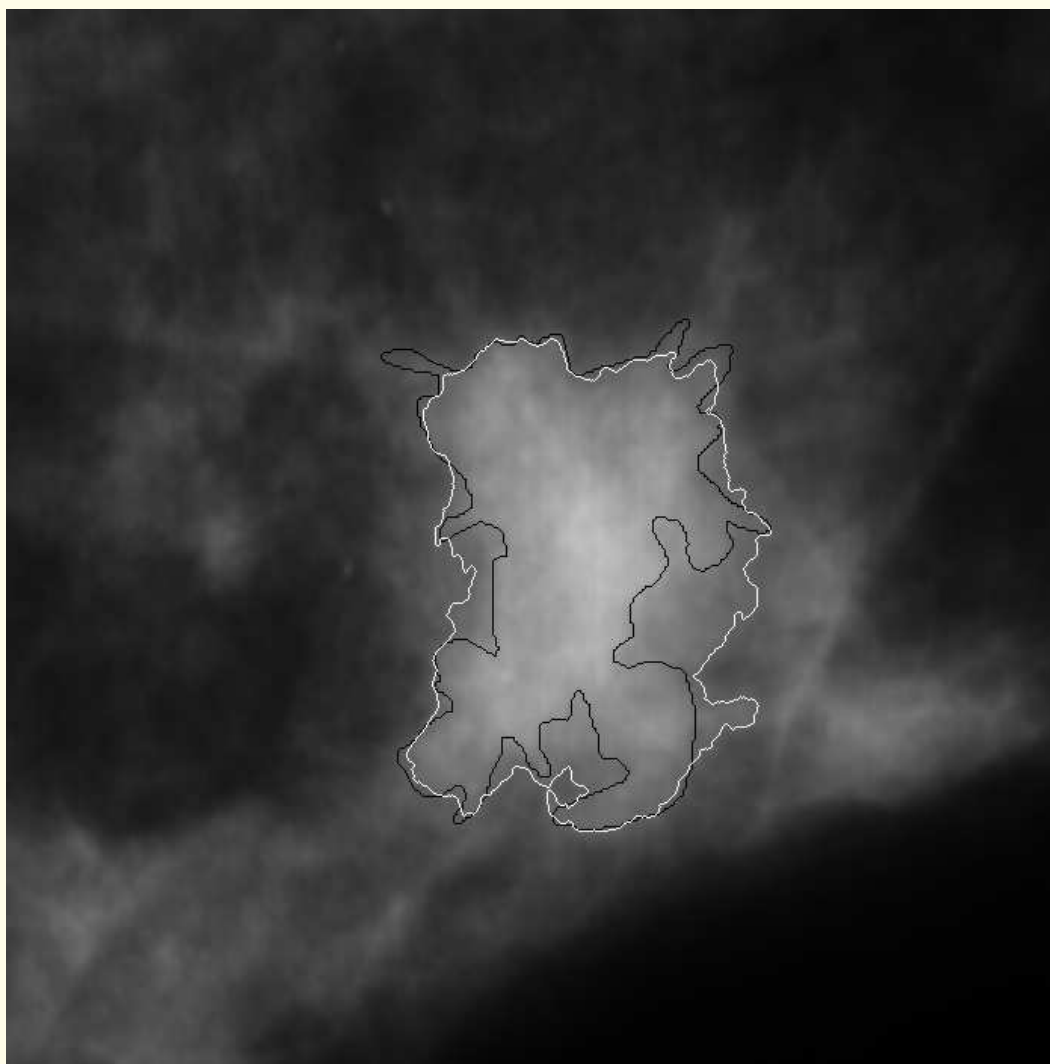


Figure 5.83 (b)

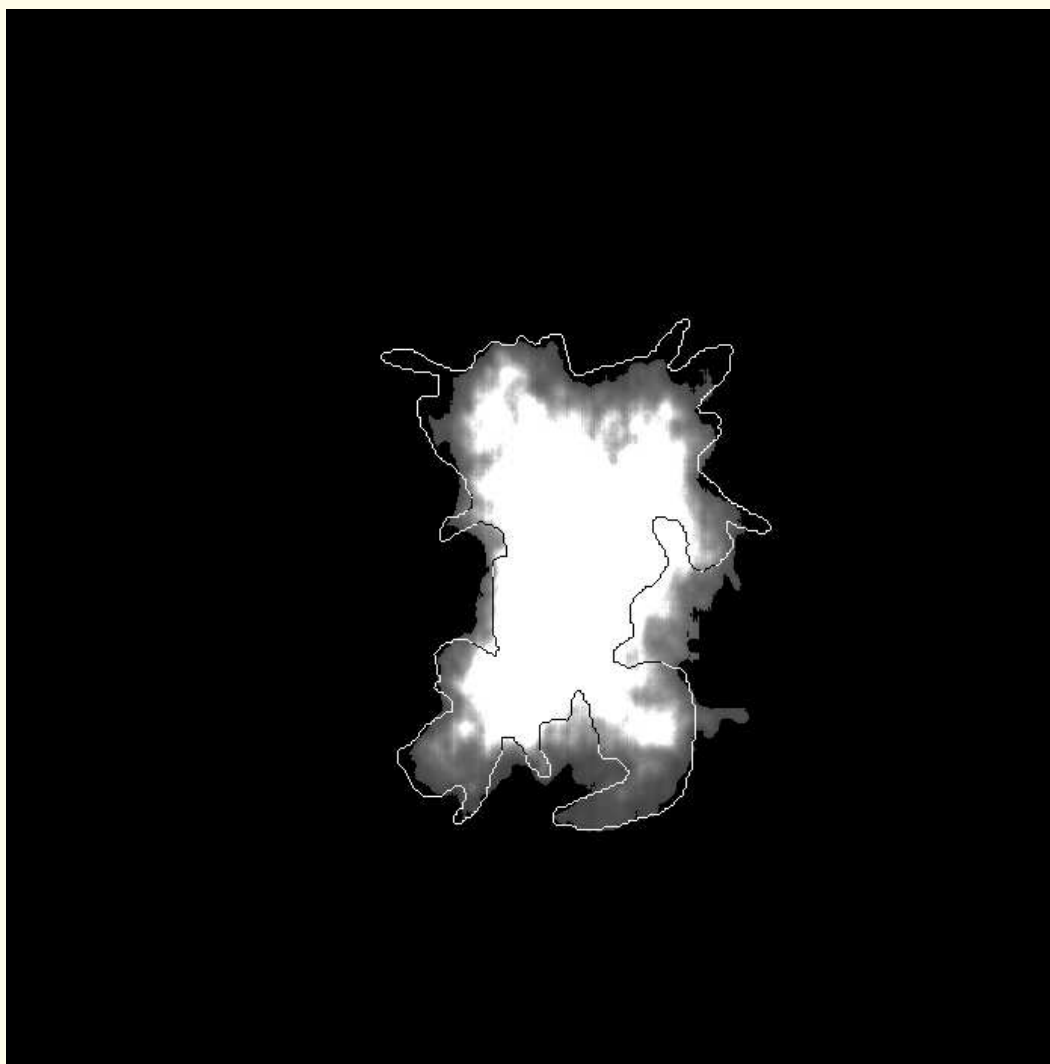
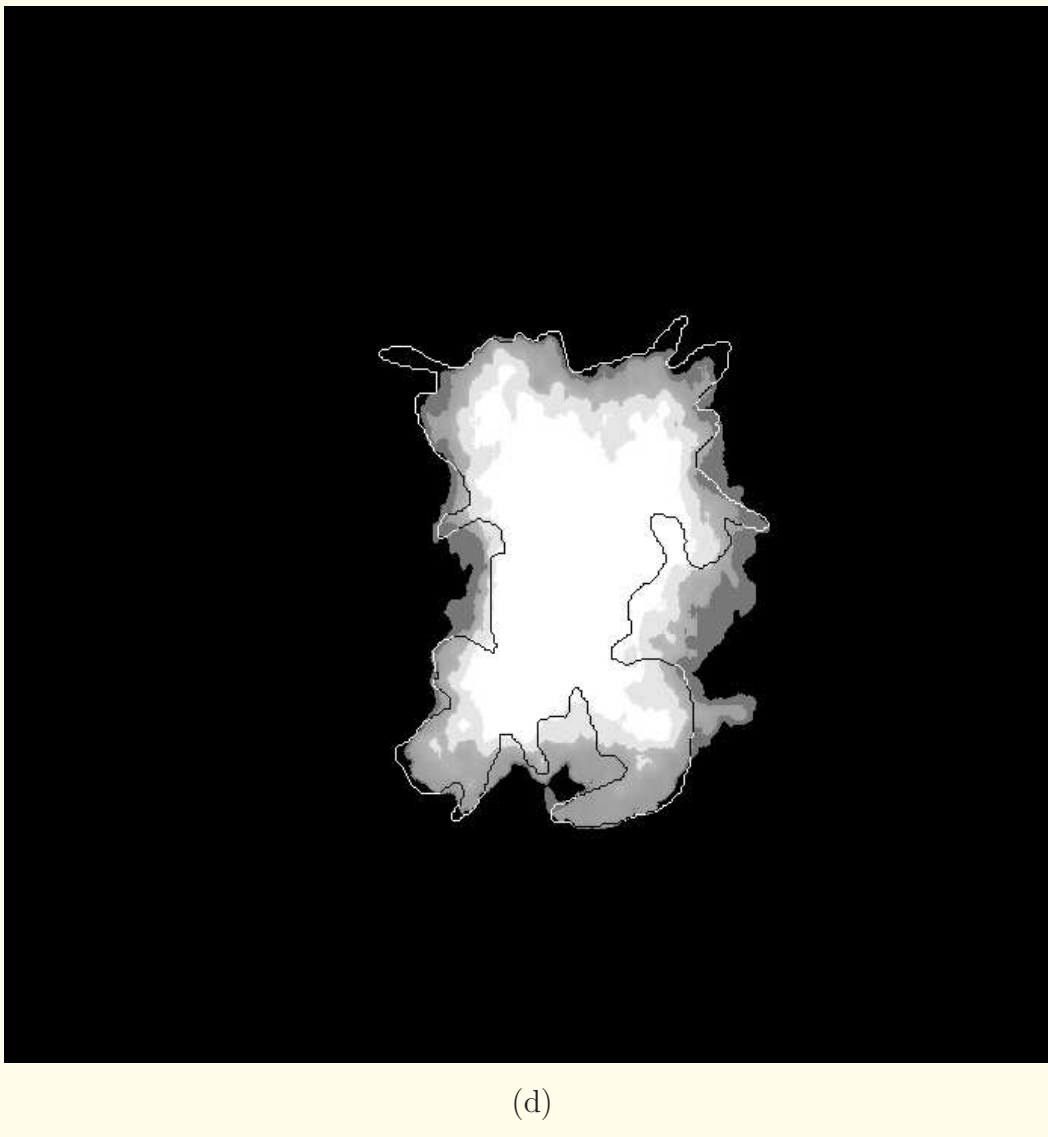


Figure 5.83 (c)



(d)

Figure 5.83: (a) A  $700 \times 700$ -pixel portion of a mammogram with a spiculated malignant tumor. Pixel size =  $62.5 \mu\text{m}$ . (b) Contour extracted (white line) by fuzzy-set-based preprocessing and region growing. The black line represents the boundary drawn by a radiologist (shown for comparison). (c) Result of fuzzy region growing. The contour drawn by the radiologist is superimposed for comparison. (d) Result of the fusion of the contour in (b) and the region in (c) with  $C_r = 1.0$ ,  $C_c = 0.9$ . The contour drawn by the radiologist is superimposed for comparison. Reproduced with permission from D. Guliato, R.M. Rangayyan, W.A. Carnielli, J.A. Zuffo, and J.E.L. Desautels, “Fuzzy fusion operators to combine results of complementary medical image segmentation techniques”, *Journal of Electronic Imaging*, 12(3): 379 – 389, 2003. © SPIE and IS&T



## Evaluation of the results of fusion using a measure of fuzziness:

In order to evaluate the results of the fusion operator, Guliato et al. compared the degree of agreement between the reference contour given by an expert radiologist and each segmentation result:

contour segmentation, region-growing segmentation,

and the result of fusion.

The reference contour and a segmentation result were aggregated using the fusion operator.

The fusion operator yields a fuzzy set that represents the certainty and uncertainty identified during the aggregation procedure.



The maximal certainty occurs when  $\Gamma(p) = 0$  or  $\Gamma(p) = 1$ , where  $\Gamma$  is the membership degree of the pixel  $p$ .

The maximal uncertainty occurs when  $\Gamma(p) = 0.5$ .

In the former case, the information sources agree completely with respect to the pixel  $p$ ;

in the latter, the information sources present maximal conflict with respect to the pixel  $p$ .

Intermediate values of the membership degree represent intermediate degrees of agreement among the sources.



If the uncertainty presented by the fusion result can be quantified, the result could be used to evaluate the degree of agreement among two different information sources.

In order to quantify the uncertainty, Guliato et al. proposed a *measure of fuzziness*:

$$f : \mathcal{F}(X) \rightarrow \mathcal{R}^+, \quad (5.89)$$

where  $\mathcal{F}(X)$  denotes the set of all fuzzy subsets of  $X$ .

For each fuzzy set  $A$  of  $X$ , this function assigns a nonnegative real number  $f(A)$  that characterizes the degree of fuzziness of  $A$ .



The function  $f$  must satisfy the following three requirements:

- $f(A) = 0$  if, and only if,  $A$  is a crisp set;
- $f(A)$  assumes its maximal value if, and only if,  $A$  is maximally fuzzy, that is, all of the elements of  $A$  are equal to 0.5; and
- if set  $A$  is undoubtedly sharper than set  $B$ , then  $f(A) \leq f(B)$ .



Guliato et al. chose to measure fuzziness in terms of the distinctions between a set and its complement, observing that

it is the lack of distinction between a set and its complement that distinguishes a fuzzy set from a crisp set.

The implementation of this concept depends on the definition of the fuzzy complement;

the standard complement is defined as

$$\bar{A}(x) = 1 - A(x), \text{ for all } x \in X.$$



Choosing the Hamming distance, the local distinction between a given set  $A$  and its complement  $\bar{A}$  is measured by

$$| A(x) - \{1 - A(x)\} | = | 2A(x) - 1 |, \quad (5.90)$$

and the lack of local distinction is given by

$$1 - | 2A(x) - 1 |. \quad (5.91)$$



The measure of fuzziness,  $f(A)$ , is then obtained by adding the local measurements:

$$f(A) = \sum_{x \in X} [1 - |2A(x) - 1|]. \quad (5.92)$$

The range of the function  $f$  is  $[0, |X|]$ :

$f(A) = 0$  if, and only if,  $A$  is a crisp set;

$f(A) = |X|$  when  $A(x) = 0.5$  for all  $x \in X$ .



For each mammogram, the reference contour drawn by the expert radiologist was combined, using the fusion operator, with each of the results obtained by contour detection, fuzzy region growing, and fusion, denoted by  $RS_c$ ,  $RS_r$ , and  $RF_r$ .

The fusion operator was applied with both the reliability measures equal to unity, that is,  $C_r = C_c = 1.0$ , for the two information sources being combined in each case.

When the result of contour detection was combined with the contour drawn by the radiologist, the former was converted into a region because the fusion method is designed to accept a contour and a region as the inputs.



For the results shown in Figure 5.83:

$$f(RS_c) = 14,774, f(RS_r) = 14,245, \text{ and } f(RF_r) = 9,710.$$

The aggregation or fusion of the two segmentation results presents lower uncertainty than either, yielding a better result as expected.



Table 5.4: Measures of Fuzziness for the Results of Segmentation and Fusion for 14 Mammograms.

| Mammogram   | $C_r, C_c$ | $f(RS_c)$ | $f(RS_r)$ | $f(RF_r)$ | Is the result<br>of fusion better? |
|-------------|------------|-----------|-----------|-----------|------------------------------------|
| spic-s-1    | 1.0, 1.0   | 14,774    | 14,245    | 9,711     | Yes                                |
| circ-fb-010 | 1.0, 1.0   | 8,096     | 9,223     | 7,905     | Yes                                |
| spx111m     | 1.0, 1.0   | 5,130     | 9,204     | 4,680     | Yes                                |
| spic-fh0    | 1.0, 0.6   | 28,938    | 23,489    | 21,612    | Yes                                |
| circ-x-1    | 1.0, 0.8   | 6,877     | 2,990     | 3,862     | No                                 |
| spic-fh2    | 0.8, 1.0   | 45,581    | 38,634    | 34,969    | Yes                                |
| circ-fb-005 | 1.0, 1.0   | 26,176    | 34,296    | 25,084    | Yes                                |
| circ-fb-012 | 1.0, 0.9   | 16,170    | 15,477    | 12,693    | Yes                                |
| spic-db-145 | 1.0, 0.9   | 8,306     | 7,938     | 7,658     | Yes                                |
| circ-fb-025 | 1.0, 0.6   | 56,060    | 44,277    | 49,093    | No                                 |
| spic-fb-195 | 1.0, 1.0   | 11,423    | 12,511    | 10,458    | Yes                                |
| spic-s-112  | 1.0, 0.6   | 31,413    | 17,784    | 12,838    | Yes                                |
| spic-s-401  | 1.0, 0.6   | 13,225    | 11,117    | 11,195    | No                                 |
| circ-fb-069 | 1.0, 1.0   | 46,835    | 53,321    | 38,832    | Yes                                |

Reproduced with permission from D. Guliato, R.M. Rangayyan, W.A. Carnielli, J.A. Zuffo, and J.E.L. Desautels, “Fuzzy fusion operators to combine results of complementary medical image segmentation techniques”, Journal of Electronic Imaging, 12(3): 379 – 389, 2003. © SPIE and IS&T.



## 5.12 Remarks

We have explored several methods to detect the edges of objects or to segment ROIs.

We have also studied methods to detect objects of known characteristics, and methods to improve initial estimates of edges, contours, or regions.

After ROIs have been detected and extracted from a given image, they may be analyzed further in terms of representation, feature extraction, pattern classification, and image understanding.



Approaches for characterization of regions:

- External characteristics:
  - boundary or contour morphology,
  - boundary roughness,
  - boundary complexity.

It is desirable that boundary descriptors are invariant to translation, scaling, and rotation.



- Internal characteristics:
  - gray level,
  - color,
  - texture,
  - statistics of pixel population.
- Description of (dis)similarity:
  - distance measures,
  - correlation coefficient.



- Relational description:
  - placement rules,
  - string, tree, and web grammar,
  - structural description,
  - syntactic analysis.







# 6

## Analysis of Shape

Several human organs possess readily identifiable shapes: shapes of the heart, brain, kidneys, and bones are well known; in normal cases, do not deviate much from an “average” shape.

Disease processes can affect the structure of organs, and cause deviation from their expected or average shapes.



Even abnormal entities, such as masses and calcifications in the breast, tend to demonstrate differences in shape between benign and malignant conditions.

Most benign masses in the breast appear as well-circumscribed areas on mammograms, with smooth boundaries that are circular or oval;

some benign masses may be macrolobulated.

Malignant (cancerous) tumors are typically ill-defined on mammograms, and possess a rough or stellate (star-like) shape with strands or spicules appearing to radiate from a central mass;

some malignant masses may be microlobulated.



Shape is a key feature in discriminating between normal and abnormal cells in Pap-smear tests.

However, biological entities demonstrate wide ranges of manifestation, with significant overlap between their characteristics for various categories.

Imaging geometry, 3D-to-2D projection, and the superimposition of multiple objects commonly affect the shapes of objects as perceived on biomedical images.



## 6.1 Representation of Shapes and Contours

The most general form of representation of a contour in discretized space:

$(x, y)$  coordinates of the pixels along the contour.

A contour with  $N$  points could be represented by the series of coordinates  $\{x(n), y(n)\}, n = 0, 1, 2, \dots, N - 1$ .

There is no gray level associated with the pixels along a contour.

A contour may be depicted as a binary or bilevel image.



### 6.1.1 *Signatures of contours*

The dimensionality of representation of a contour may be reduced from two to one by converting from a coordinate-based representation to distances from each contour point to a reference point or location.

Convenient reference: centroid or center of mass of contour:

$$\bar{x} = \frac{1}{N} \sum_{n=0}^{N-1} x(n), \text{ and } \bar{y} = \frac{1}{N} \sum_{n=0}^{N-1} y(n). \quad (6.1)$$



The signature of the contour is then defined as

$$d(n) = \sqrt{[x(n) - \bar{x}]^2 + [y(n) - \bar{y}]^2}, \quad (6.2)$$

$n = 0, 1, 2, \dots, N - 1$ ; see Figure 6.1.

Centroids of regions that are concave or have holes could lie outside the regions.



A radial-distance signature may also be derived by computing the distance from the centroid to the contour point(s) intersected for angles of the radial line spanning the range  $(0^\circ, 360^\circ)$ .

However, for irregular contours, such a signature may be multivalued for some angles:

a radial line may intersect the contour more than once.

Going around a contour more than once generates the same signature:

the signature signal is periodic with the period equal to  $N$ , the number of pixels on the contour.

The signature of a contour provides general information on the nature of the contour, such as its smoothness or roughness.

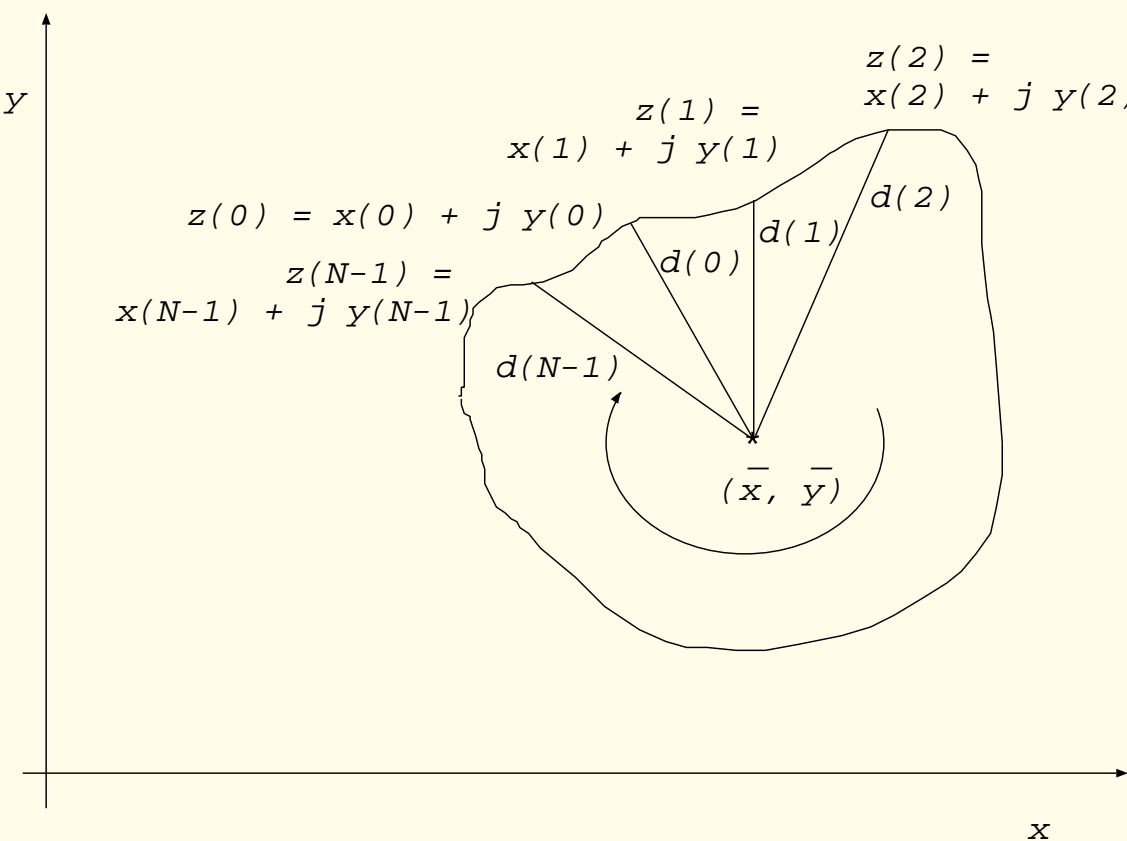
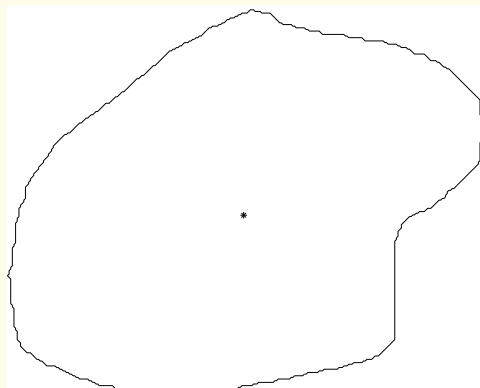
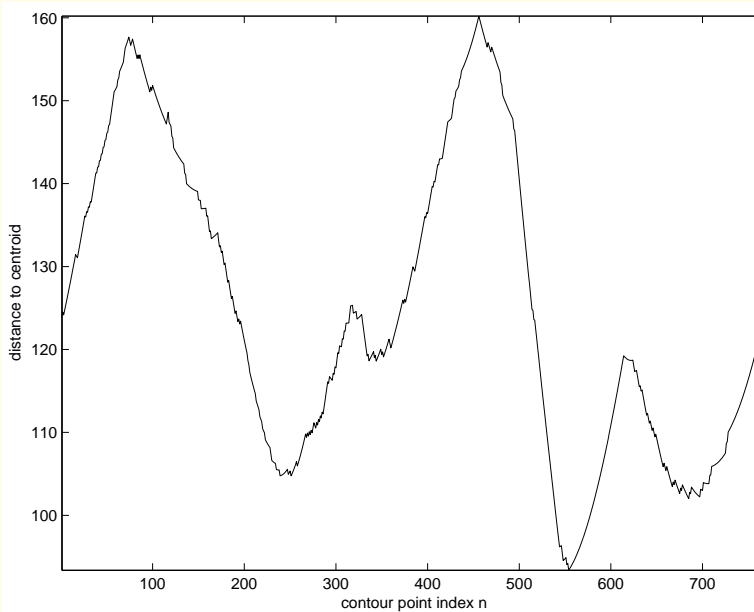


Figure 6.1: A contour represented by its boundary points  $z(n)$  and distances  $d(n)$  to its centroid.

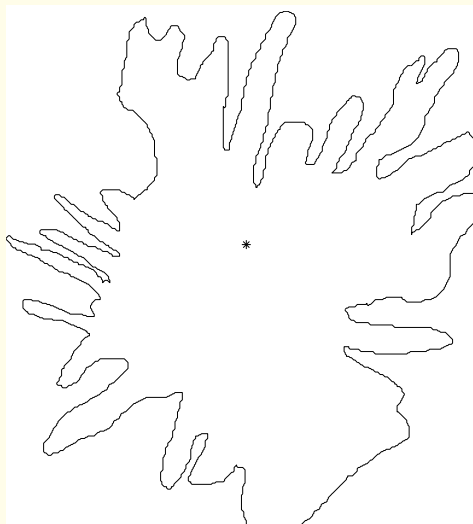


(a)

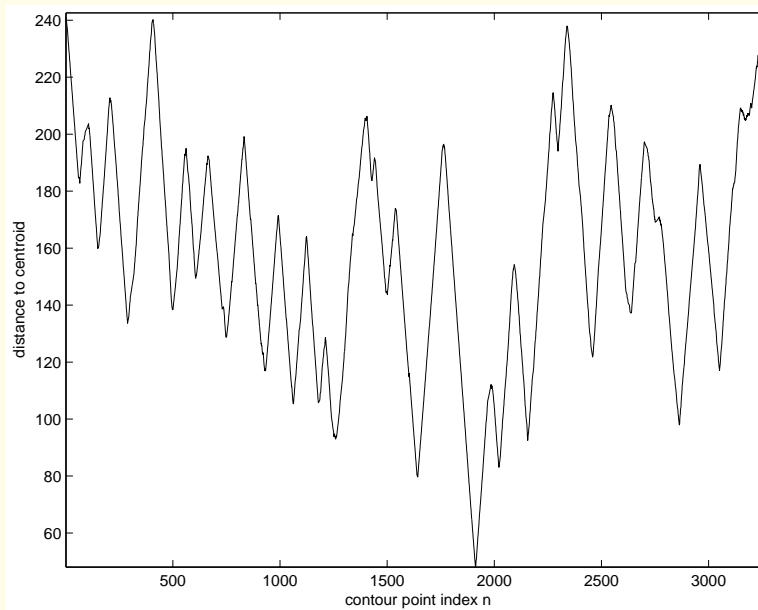


(b)

Figure 6.2: (a) Contour of a benign breast mass;  $N = 768$ . The '\*' mark represents the centroid of the contour. (b) Signature  $d(n)$  as defined in Equation 6.2.



(a)



(b)

Figure 6.3: (a) Contour of a malignant breast tumor;  $N = 3,281$ . The '\*' mark represents the centroid of the contour. (b) Signature  $d(n)$  as defined in Equation 6.2.



### 6.1.2 *Chain coding*

An efficient representation of a contour may be achieved by specifying the  $(x, y)$  coordinates of an arbitrary starting point on the contour, the direction of traversal (clockwise or counter-clockwise), and a code to indicate the manner of movement to reach the next contour point on a discrete grid.



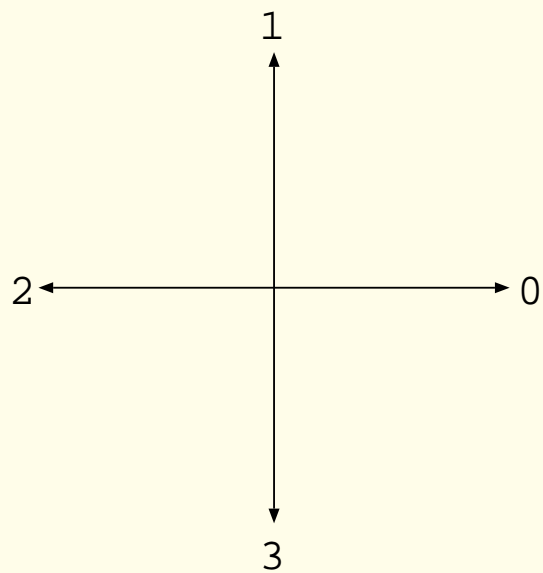
Coarse representation using only four possible movements:

to the point at the left of, right of,

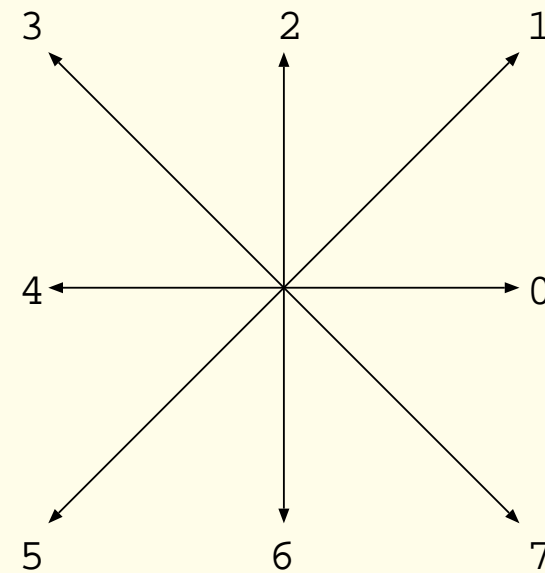
above, or below the current point (Figure 6.4 (a)).

Finer representation using eight possible movements:

including diagonal movements (Figure 6.4 (b)).



(a)



(b)

Figure 6.4: Chain code with (a) four directional codes and (b) eight directional codes.



The sequence of codes required to traverse through all the points along the contour is known as the chain code, or the Freeman chain code.

Chain code facilitates more compact representation of a contour than direct specification of  $(x, y)$  coordinates of all points.

Except the initial point, the representation of each point on the contour requires only two or three bits, depending upon the type of code used.



Chain coding provides the following advantages:

- The code is invariant to shift or translation because the starting point is kept out of the code.
- To a certain extent, the chain code is invariant to size (scaling).

Contours of different sizes may be generated from the same code by using different sampling grids (step sizes).

A contour may also be enlarged by a factor of  $n$  by repeating each code element  $n$  times and maintaining the same sampling grid.

A contour may be shrunk to half of the original size by reducing pairs of code elements to single numbers, with approximation of unequal pairs by their averages reduced to integers.



- The chain code may be normalized for rotation by taking the first difference of the code (and adding 4 or 8 to negative differences, depending upon the code used).
- With reference to the 8-symbol code, the rotation of a given contour by  $n \times 90^\circ$  in the counter-clockwise direction may be achieved by adding a value of  $2n$  to each code element, followed by integer division by 8.

The addition of an odd number rotates the contour by the corresponding multiple of  $45^\circ$ ; however, the rotation of a contour by angles other than integral multiples of  $90^\circ$  on a discrete grid is subject to approximation.



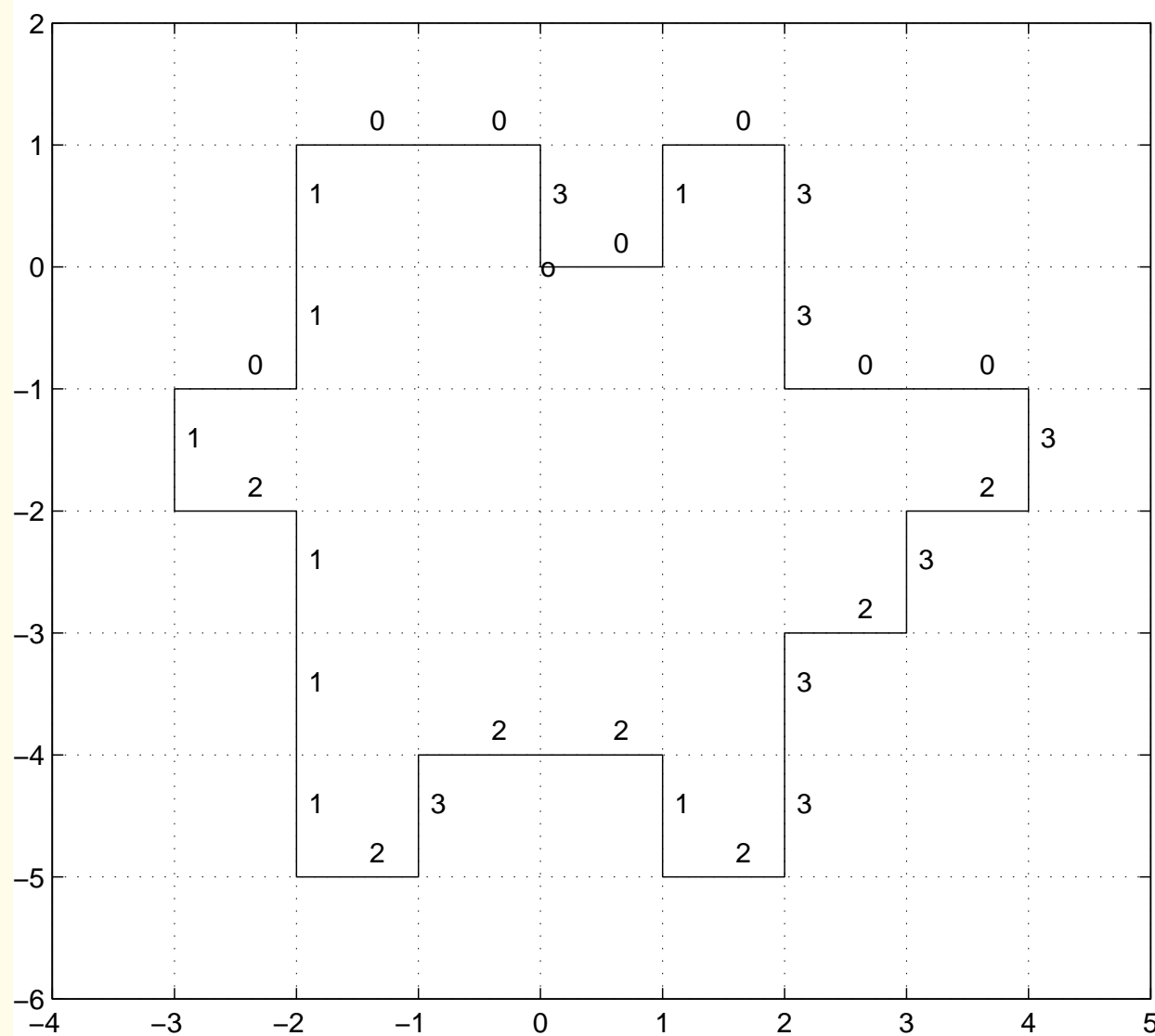
- In the case of the 8-symbol code, the length of a contour is given by the number of even codes plus  $\sqrt{2}$  times the number of odd codes, multiplied by the grid sampling interval.
- The chain code may also be used to achieve reduction, check for closure, check for multiple loops, and determine the area of a closed loop.



**Examples:** Figure 6.5 shows a contour represented using the chain codes with four and eight symbols.

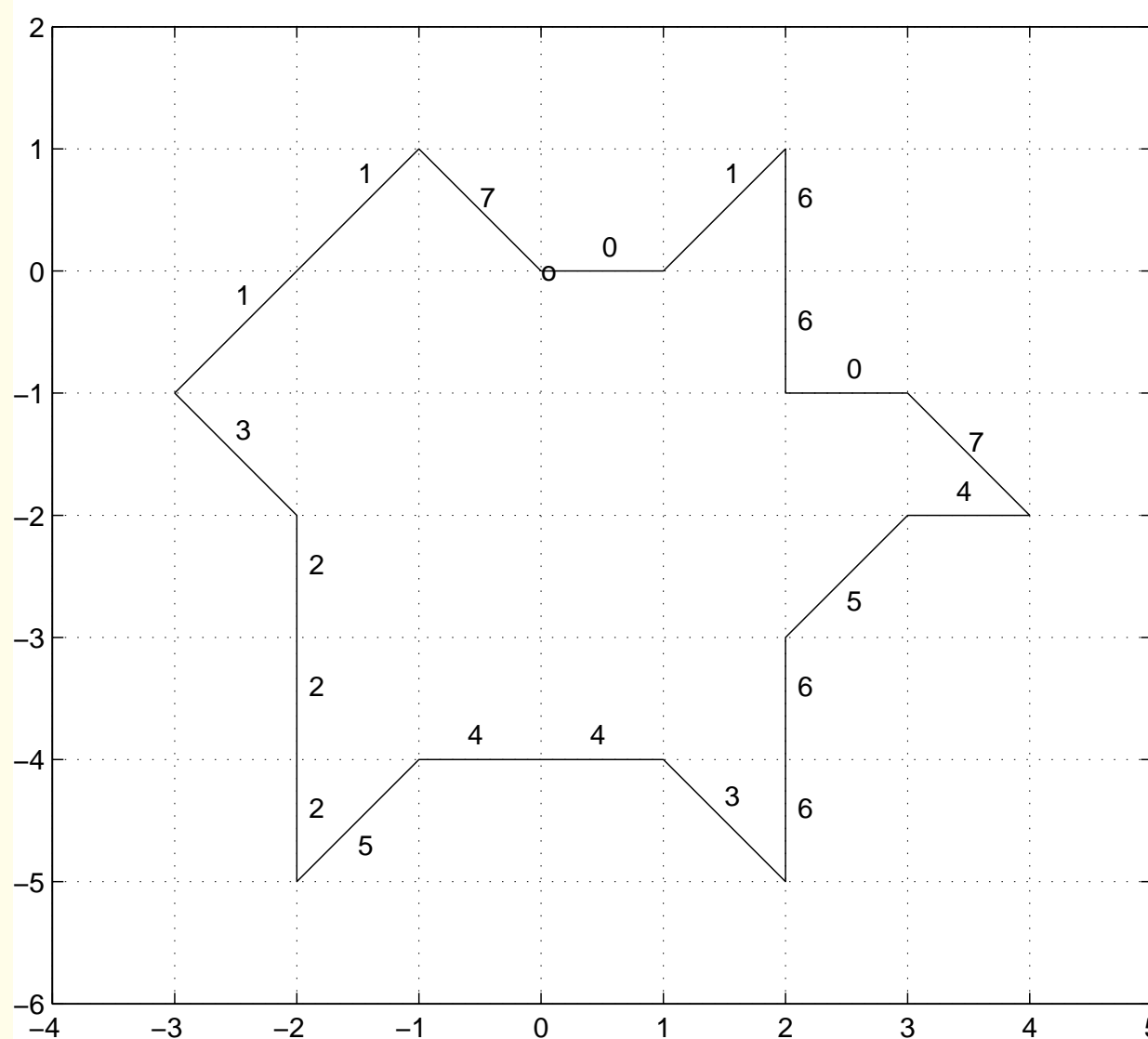
The use of a discrete grid with large spacings leads to the loss of fine detail in the contour.

This feature may be used advantageously to filter out minor irregularities due to noise, artifacts due to drawing by hand, etc.



Chain code: [0 1 0 3 3 0 0 3 2 3 2 3 3 2 1 2 2 3 2 1 1 1 2 1 0 1 1 0 0 3]

Figure 6.5 (a)



Chain code: [0 1 6 6 0 7 4 5 6 6 3 4 4 5 2 2 2 3 1 1 7 ]

(b)

Figure 6.5: A closed contour represented using the chain code (a) using four directional codes as in Figure 6.4 (a), and (b) with eight directional codes as in Figure 6.4 (b). The 'o' mark represents the starting point of the contour, which is traversed in the clockwise direction to derive the code.



### 6.1.3 Segmentation of contours

The segmentation of a contour into a set of piecewise-continuous curves is a useful step before analysis and modeling.

Segmentation may be performed by locating the points of inflection on the contour.

Consider a function  $f(x)$ ; let  $f'(x)$ ,  $f''(x)$ , and  $f'''(x)$  represent the first, second, and third derivatives of  $f(x)$ .

A point of inflection of the function or curve  $f(x)$  is defined as a point where  $f''(x)$  changes its sign.

Derivation of  $f''(x)$  requires  $f(x)$  and  $f'(x)$  to be continuous and differentiable.



The following conditions apply at a point of inflection:

$$f''(x) = 0,$$

$$f'(x) \neq 0,$$

$$f'(x) f''(x) = 0, \text{ and}$$

$$f'(x) f'''(x) \neq 0. \quad (6.3)$$



Let  $\mathbf{C} = \{(x(n), y(n)), n = 0, 1, 2, \dots, N - 1\}$ , represent, in vector form, the  $(x, y)$  coordinates of the  $N$  points on the given contour.

The points of inflection on the contour are obtained by solving

$$\mathbf{C}' \times \mathbf{C}'' = 0 ,$$
$$\mathbf{C}' \times \mathbf{C}''' \neq 0 , \quad (6.4)$$

where  $\mathbf{C}'$ ,  $\mathbf{C}''$ , and  $\mathbf{C}'''$  are the first, second, and third derivatives of  $\mathbf{C}$ , respectively, and  $\times$  represents the vector cross product.



Solving Equation 6.4 is equivalent to solving the system of equations

$$\begin{aligned}x''(n) y'(n) - x'(n) y''(n) &= 0 , \\x'(n) y'''(n) - x'''(n) y'(n) &\neq 0 ,\end{aligned}\tag{6.5}$$

where  $x'(n)$ ,  $y'(n)$ ,  $x''(n)$ ,  $y''(n)$ ,  $x'''(n)$ , and  $y'''(n)$  are the first, second, and third derivatives of  $x(n)$  and  $y(n)$ , respectively.



Segments of contours of breast masses between successive points of inflection were modeled as parabolas by Menut et al.

Difficulty lies in segmentation because the contours of masses are, in general, not smooth.

False or irrelevant points of inflection could appear on relatively straight parts of a contour when  $x''(n)$  and  $y''(n)$  close to zero.



Smoothed derivatives at each contour point could be estimated by considering the cumulative sum of weighted differences of a certain number of pairs of points on either side of the point  $x(n)$ :

$$x'(n) = \sum_{i=1}^m \frac{[x(n+i) - x(n-i)]}{i}. \quad (6.6)$$

$m$ : number of pairs of points used to compute  $x'(n)$ ;  
same for  $y'(n)$ .



Menut et al. and Rangayyan et al. varied the value of  $m$  from 3 to 60 to compute derivatives that resulted in varying numbers of inflection points for a given contour.

The number of inflection points detected as a function of the number of differences used was analyzed to determine the optimal number of differences that would provide the most appropriate inflection points:

value of  $m$  at the first straight segment on the function selected.

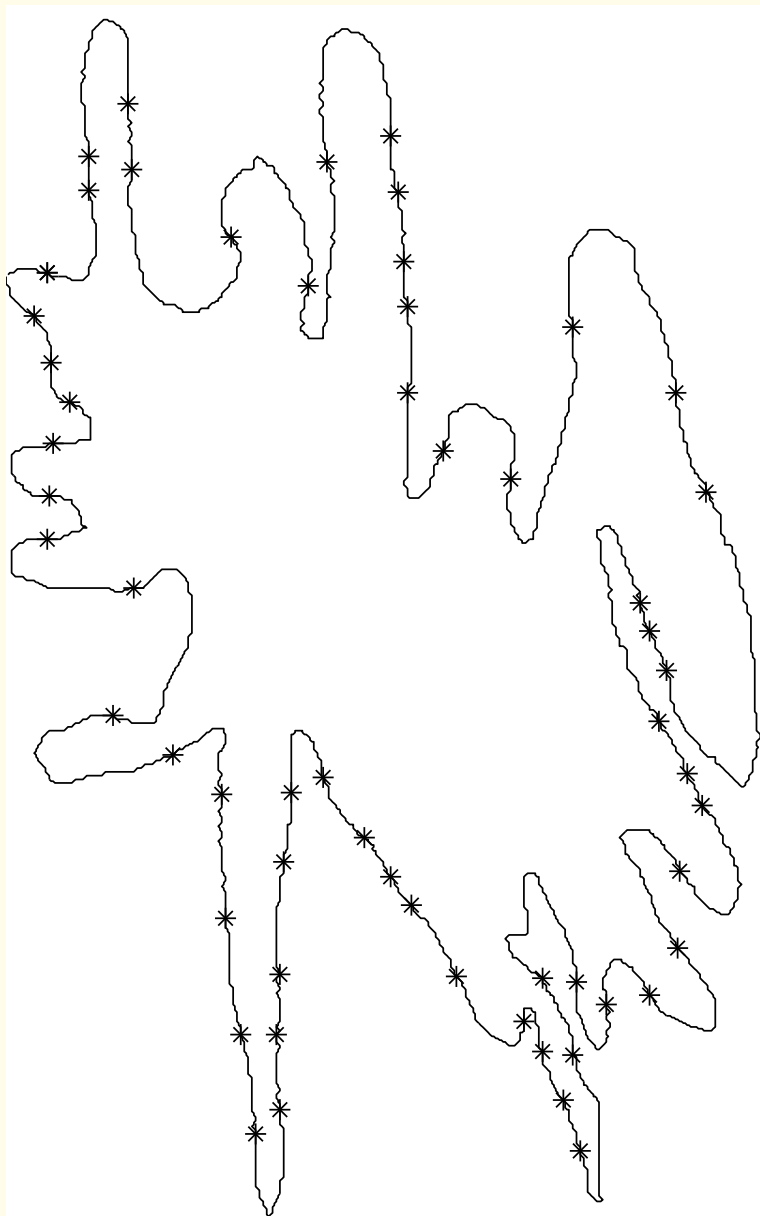


Figure 6.6: Contour of a spiculated malignant tumor with the points of inflection indicated by '\*'. Number of points of inflection = 58. See also Figure 6.8.

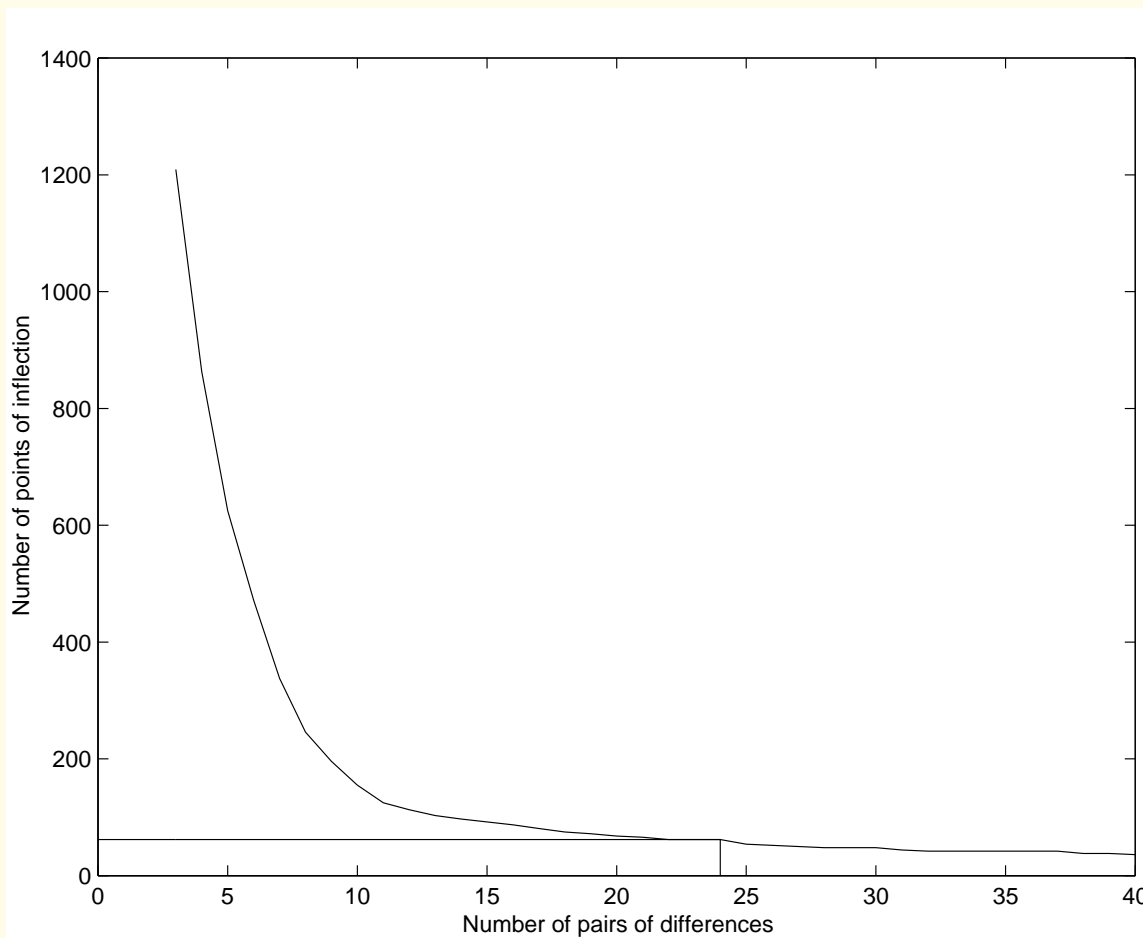


Figure 6.7: Number of inflection points detected as a function of the number of differences used to estimate the derivative for the contour in Figure 6.6. The horizontal and vertical lines indicate the optimal number of differences used to compute the derivative at each contour point and the corresponding number of points of inflection that were located on the contour.

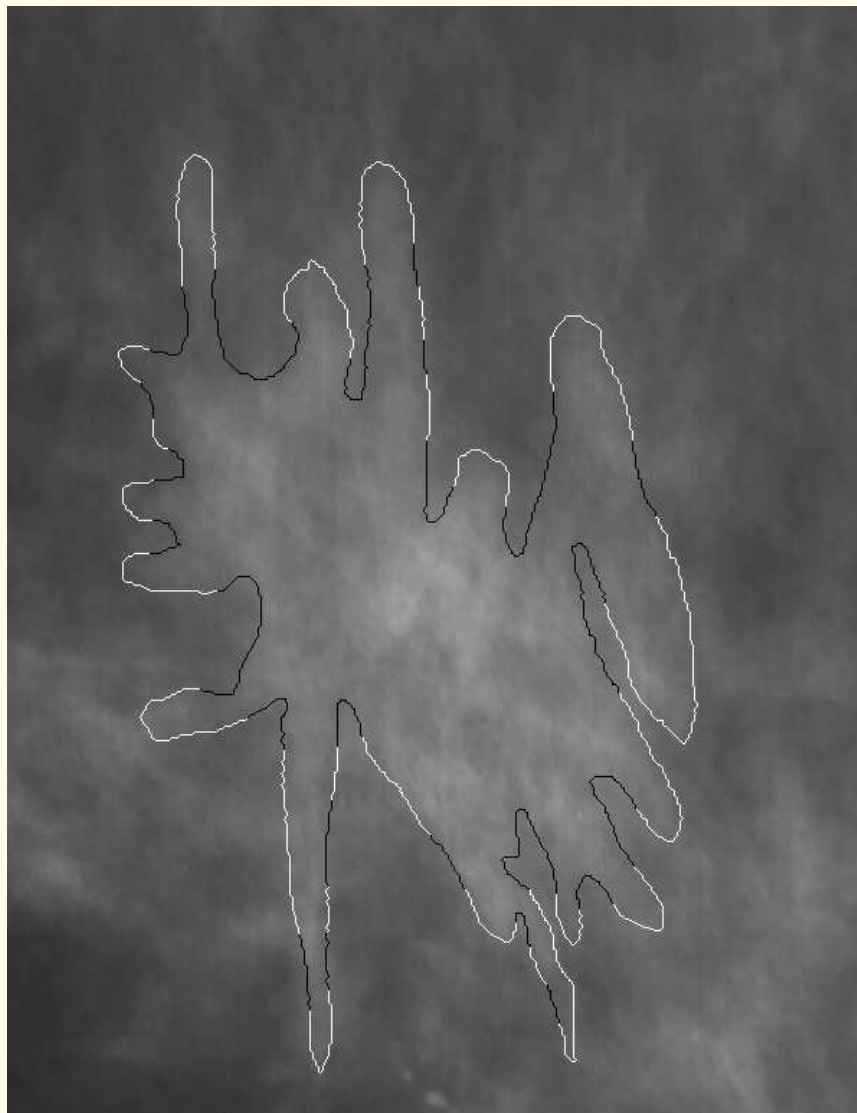


Figure 6.8: Concave and convex parts of the contour of a spiculated malignant tumor, separated by the points of inflection. See also Figure 6.6. The concave parts are shown in black and the convex parts in white. The image size is  $770 \times 600$  pixels or  $37.2 \times 47.7$  mm with a pixel size of  $62 \mu\text{m}$ . Shape factors  $f_{cc} = 0.47$ ,  $SI = 0.62$ ,  $cf = 0.94$ . Reproduced with permission from R.M. Rangayyan, N.R. Mudigonda, and J.E.L. Desautels, “Boundary modeling and shape analysis methods for classification of mammographic masses”, *Medical and Biological Engineering and Computing*, 38: 487 – 496, 2000. © IFMBE.

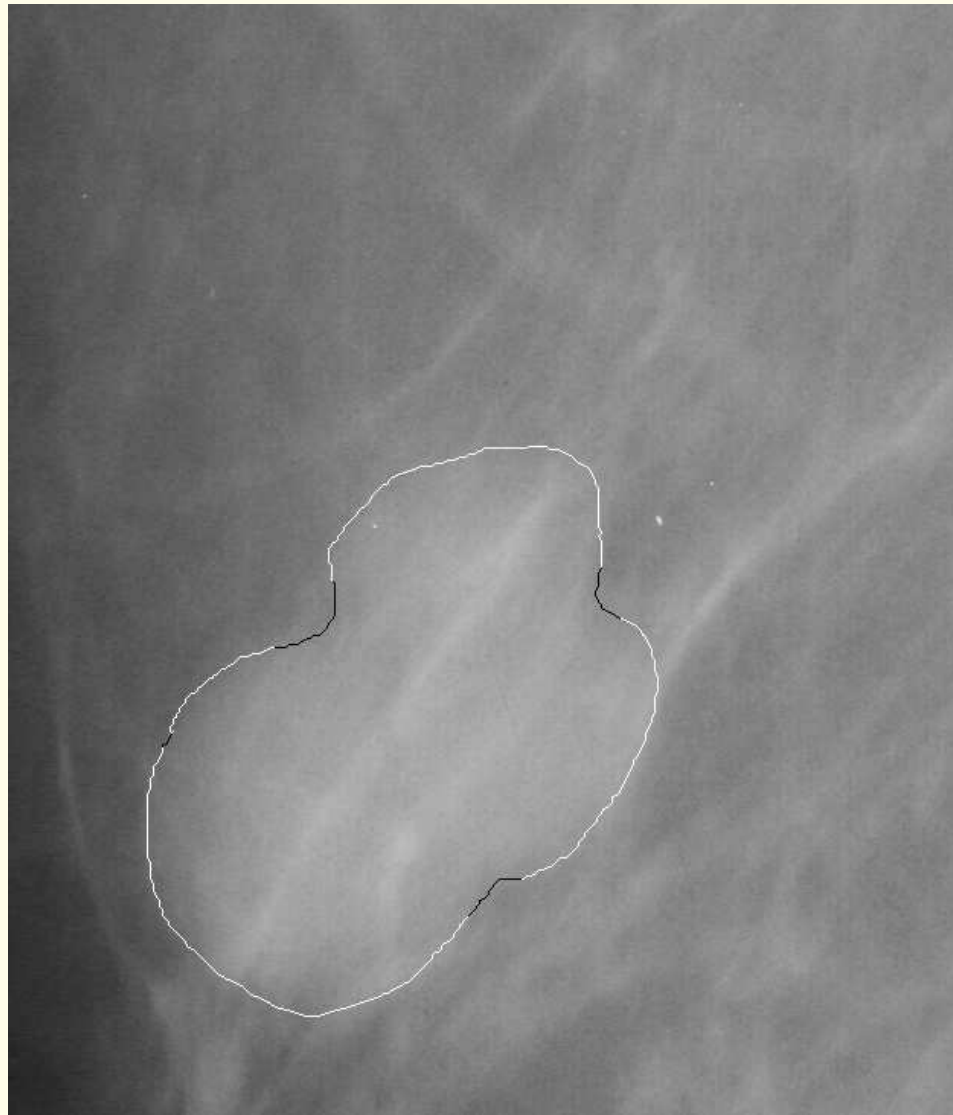


Figure 6.9: Concave and convex parts of the contour of a circumscribed benign mass, separated by the points of inflection. The concave parts are shown in black and the convex parts in white. The image size is  $730 \times 630$  pixels or  $31.5 \times 36.5 \text{ mm}$  with a pixel size of  $50 \mu\text{m}$ . Shape factors  $f_{cc} = 0.16$ ,  $SI = 0.22$ ,  $cf = 0.30$ . Reproduced with permission from R.M. Rangayyan, N.R. Mudigonda, and J.E.L. Desautels, “Boundary modeling and shape analysis methods for classification of mammographic masses”, *Medical and Biological Engineering and Computing*, 38: 487 – 496, 2000. © IFMBE.



### 6.1.4 *Polygonal modeling of contours*

Pavlidis and Horowitz and Pavlidis and Ali proposed methods for segmentation and approximation of curves and shapes by polygons for computer recognition of handwritten numerals, cell outlines, and ECG signals.

Ventura and Chen presented an algorithm for segmenting and polygonal modeling of 2D curves in which the number of segments is to be prespecified for initiating the process, in relation to the complexity of the shape.

Rangayyan et al.: polygon formed by the points of inflection detected on the original contour used as the initial input to the polygonal modeling procedure.



Irregular contour  $\mathbf{C}$  specified by the set of its  $(x, y)$  coordinates:

The contour is divided into a set of piecewise-continuous curved parts by locating the points of inflection.

Each segmented curved part is represented by a pair of linear segments based on its arc-to-chord deviation.

The procedure is iterated subject to predefined boundary conditions so as to minimize the error between the true length of the contour and the cumulative length computed from the polygonal segments.



Given contour:  $\mathbf{C} = \{x(n), y(n)\}, n = 0, 1, 2, \dots, N - 1$ .

Let  $SC_{mk}, SC_{mk} \in \mathbf{C}, m = 1, 2, \dots, M$ , be

$M$  curved parts, each containing a set of contour points,

at the start of the  $k^{th}$  iteration, such that

$$SC_{1k} \cup SC_{2k} \cup \dots \cup SC_{Mk} \equiv \mathbf{C}.$$



1. In each curved part represented by  $SC_{mk}$ , the arc-to-chord distance is computed for all the points, and the point on the curve with the maximum arc-to-chord deviation ( $d_{\max}$ ) is located.
2. If  $d_{\max} \geq 0.25 \text{ mm}$  (5 pixels with a pixel size of  $50 \mu\text{m}$ ), the curved part is segmented at the point of maximum deviation to approximate the same with a pair of linear segments, irrespective of the length of the resulting linear segments.

If  $0.1 \text{ mm} \leq d_{\max} < 0.25 \text{ mm}$ ,

the curved part is segmented at the point of maximum deviation subject to the condition that the resulting linear segments satisfy a minimum-length criterion (1 mm).

If  $d_{\max} < 0.1 \text{ mm}$ , the curved part  $SC_{mk}$  is considered to be almost linear and is not segmented any further.



3. After performing Steps 1 and 2 on all the curved parts of the contour available in the current  $k^{th}$  iteration, the resulting vector of the polygon's vertices is updated.
4. If the number of polygonal segments following the  $k^{th}$  iteration equals that of the previous iteration, the algorithm is considered to have converged and the polygonalization process is terminated.

Otherwise, the procedure (Steps 1 to 3) is repeated until the algorithm converges.

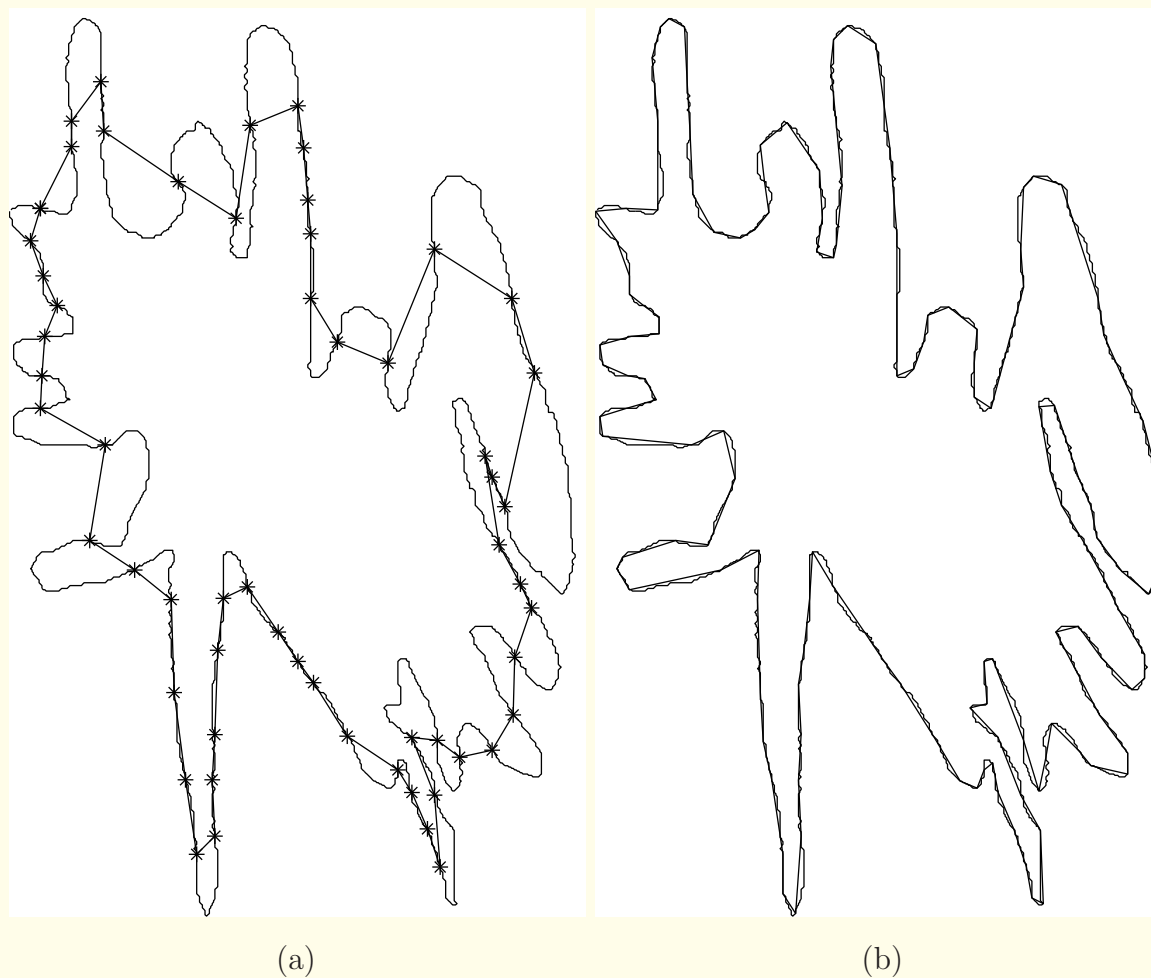


Figure 6.10: Polygonal modeling of the contour of a spiculated malignant tumor. (a) Points of inflection (indicated by ‘\*’) and the initial polygonal approximation (straight-line segments); number of sides = 58. (b) Final model after four iterations; number of sides = 146. See also Figure 6.8. Reproduced with permission from R.M. Rangayyan, N.R. Mudigonda, and J.E.L. Desautels, “Boundary modeling and shape analysis methods for classification of mammographic masses”, *Medical and Biological Engineering and Computing*, 38: 487 – 496, 2000. © IFMBE.

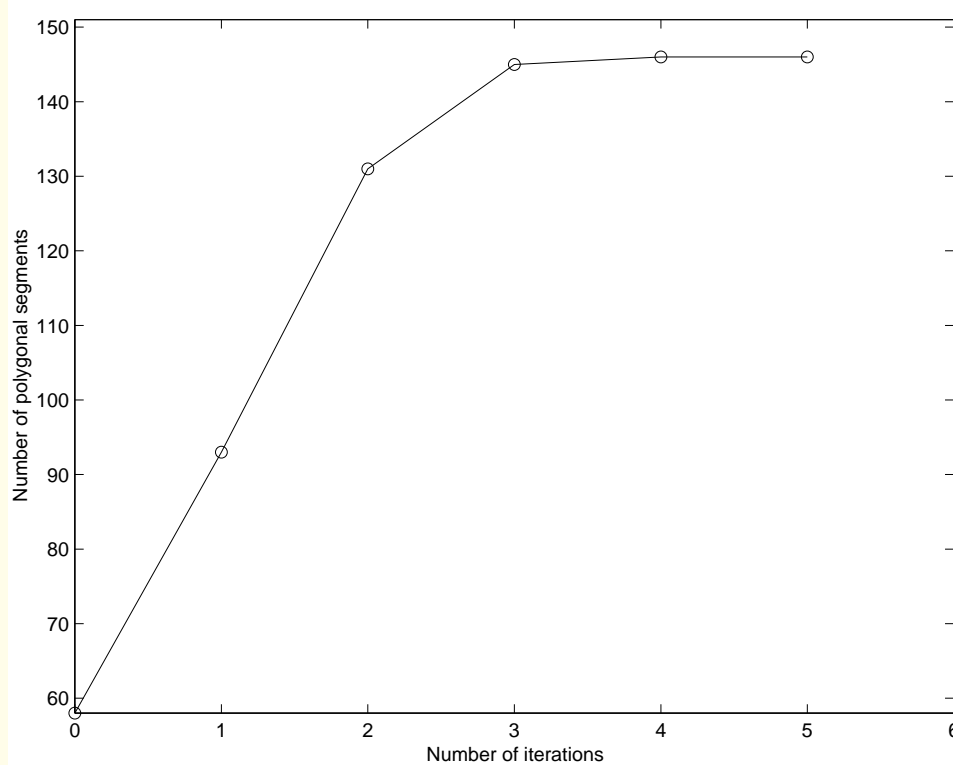


Figure 6.11: Convergence plot of the iterative polygonal modeling procedure for the contour of the spiculated malignant tumor in Figure 6.10. Reproduced with permission from R.M. Rangayyan, N.R. Mudigonda, and J.E.L. Desautels, “Boundary modeling and shape analysis methods for classification of mammographic masses”, *Medical and Biological Engineering and Computing*, 38: 487 – 496, 2000. © IFMBE.

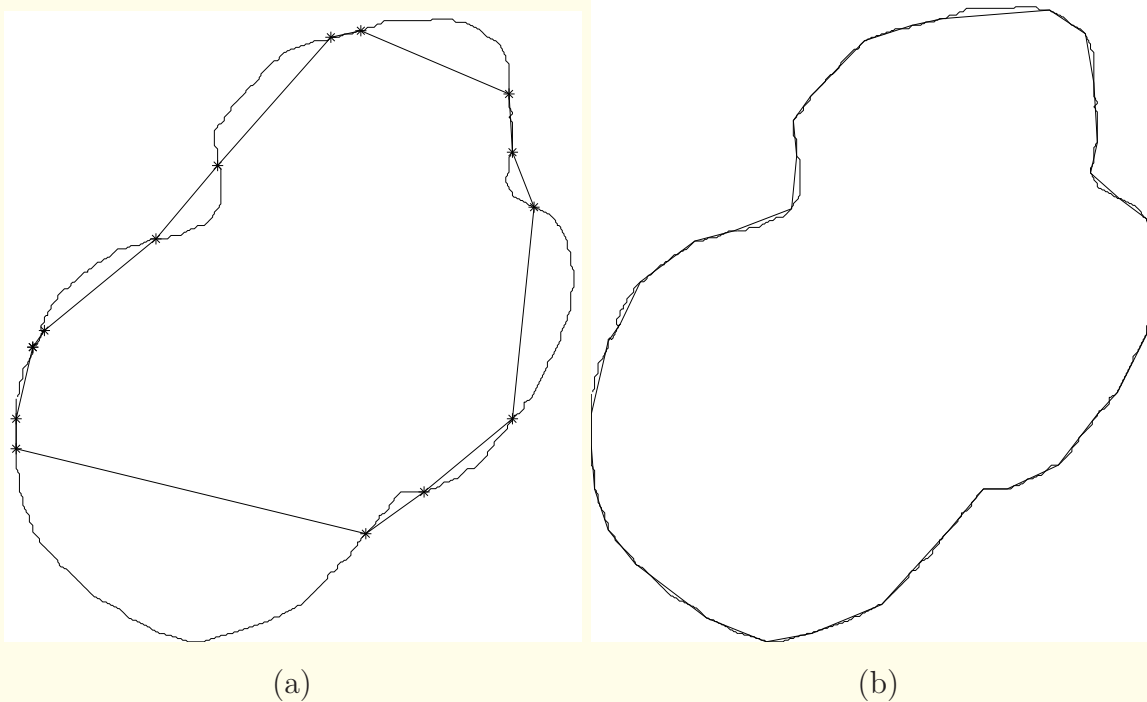


Figure 6.12: Polygonal modeling of the contour of a circumscribed benign mass. (a) Points of inflection (indicated by '\*') and the initial polygonal approximation (straight-line segments); initial number of sides = 14. (b) Final model; number of sides = 36, number of iterations = 4. See also Figure 6.9. Reproduced with permission from R.M. Rangayyan, N.R. Mudigonda, and J.E.L. Desautels, “Boundary modeling and shape analysis methods for classification of mammographic masses”, *Medical and Biological Engineering and Computing*, 38: 487 – 496, 2000. © IFMBE.



### 6.1.5 *Parabolic modeling of contours*

Menut et al.: modeling of segments of contours of breast masses between successive points of inflection as parabolas.

Consider a segment of a contour represented in the continuous 2D space by the points  $[x(s), y(s)]$  over the interval  $S_1 \leq s \leq S_2$ ,

where  $s$  indicates distance along the contour,

and  $S_1$  and  $S_2$  are the end-points of the segment.



Consider the approximation of the curve by a parabola.

Regardless of the position and orientation of the given curve, consider the simplest representation of a parabola as

$$Y = A X^2 \text{ in the coordinate space } (X, Y).$$

$A$  controls the narrowness of the parabola:

the larger the value of  $A$ , the narrower is the parabola.



Allowing for a rotation of  $\theta$  and a shift of  $(c, d)$  between the  $(x, y)$  and  $(X, Y)$  spaces, we have

$$\begin{aligned} x(s) &= X(s) \cos \theta - Y(s) \sin \theta + c, \\ y(s) &= X(s) \sin \theta + Y(s) \cos \theta + d. \end{aligned} \quad (6.7)$$



$$X(s) = [x(s) - c] \cos \theta + [y(s) - d] \sin \theta,$$

$$Y(s) = -[x(s) - c] \sin \theta + [y(s) - d] \cos \theta; \quad (6.8)$$

$$X(s) = s,$$

$$Y(s) = A s^2. \quad (6.9)$$



Taking the derivatives of Equation 6.9 with respect to  $s$ , we get

$$X'(s) = 1,$$

$$Y'(s) = 2As; \quad (6.10)$$

$$X''(s) = 0,$$

$$Y''(s) = 2A. \quad (6.11)$$



Taking the derivatives of Equation 6.8 with respect to  $s$ , we get

$$\begin{aligned} X''(s) &= x''(s) \cos \theta + y''(s) \sin \theta, \\ Y''(s) &= -x''(s) \sin \theta + y''(s) \cos \theta. \end{aligned} \quad (6.12)$$



Combining Equations 6.11 and 6.12, we get

$$X''(s) = 0 = x''(s) \cos \theta + y''(s) \sin \theta, \quad (6.13)$$

which, upon multiplication with  $\sin \theta$ , yields

$$x''(s) \sin \theta \cos \theta + y''(s) \sin \theta \sin \theta = 0. \quad (6.14)$$



Similarly, we also get

$$Y''(s) = 2A = -x''(s) \sin \theta + y''(s) \cos \theta, \quad (6.15)$$

which, upon multiplication with  $\cos \theta$ , yields

$$2A \cos \theta = -x''(s) \sin \theta \cos \theta + y''(s) \cos \theta \cos \theta. \quad (6.16)$$



Combining Equations 6.14 and 6.16 we get

$$2A \cos \theta = y''(s). \quad (6.17)$$

The equations above indicate that  $y''(s)$  and  $x''(s)$  are constants with values related to  $A$  and  $\theta$ .

The values of the two derivatives may be computed from the given curve over all available points, and averaged to obtain the corresponding (constant) values.

Equations 6.14 and 6.17 may be solved to obtain  $\theta$  and  $A$ .



Malignant tumors, with narrow spicules or microlobulations, should have several parabolic segments with large  $A$ .

Benign masses, being oval or macrolobulated, should have a small number of parabolic segments with small  $A$ .

The same reasons should also lead to larger standard deviation of  $A$  for malignant tumors than for benign masses.

In addition to  $A$ , Menut et al. proposed to use the width of the projection of each parabola on to the  $X$  axis:

smaller widths for malignant tumors than for benign masses.

Classification accuracy of 76% obtained with 54 contours.



### 6.1.6 *Thinning and skeletonization*

Objects that are linear or oblong, or

structures that have branching (anostomotic) patterns

may be effectively characterized by their skeletons.

The skeleton of an object or region is obtained by its

medial-axis transform or via a thinning algorithm.



The medial-axis transformation proposed by Blum is as follows:

First, the given image needs to be binarized so as to include only the patterns of interest.

Let the set of pixels in the binary pattern be denoted as  $B$ ,

let  $C$  be the set of contour pixels of  $B$ , and

let  $c_i$  be an arbitrary contour point in  $C$ .



For each point  $b$  in  $B$ , a point  $c_i$  is found such that the

distance between the point  $b$  and  $c_i$ , represented as  $d(b, c_i)$ ,

is at its minimum.

If a second point  $c_k$  is found in  $C$  such that  $d(b, c_k) = d(b, c_i)$ ,

then  $b$  is a part of the skeleton of  $B$ ;

otherwise,  $b$  is not a part of the skeleton.



A simple algorithm for thinning is as follows:

Assume that the image has been binarized, with the pixels inside the ROIs being labeled as 1 and the background pixels as 0.

A contour point is defined as any pixel having the value 1 and at least one 8-connected neighbor valued 0.

Let the 8-connected neighboring pixels of the pixel  $p_1$  being processed be indexed as

$$\begin{bmatrix} p_9 & p_2 & p_3 \\ p_8 & p_1 & p_4 \\ p_7 & p_6 & p_5 \end{bmatrix}. \quad (6.18)$$



1. Flag a contour point  $p_1$  for deletion if the following are true:

- (a)  $2 \leq N(p_1) \leq 6$ ;
- (b)  $S(p_1) = 1$ ;
- (c)  $p_2 \times p_4 \times p_6 = 0$ ;
- (d)  $p_4 \times p_6 \times p_8 = 0$ ;

where  $N(p_1)$  is the number of nonzero neighbors of  $p_1$ ,

$S(p_1)$  is the number of  $0 - 1$  transitions in the sequence

$p_2, p_3, \dots, p_9, p_2$ .

2. Delete all flagged pixels.

3. Do Step 1 replacing conditions (c) and (d) with

- (c')  $p_2 \times p_4 \times p_8 = 0$ ;
- (d')  $p_2 \times p_6 \times p_8 = 0$ .

4. Delete all flagged pixels.

5. Iterate Steps 1 – 4 until no further pixels are deleted.



This algorithm does not remove end points,  
does not break connectivity,  
and does not cause excessive erosion of the region.

**Example:** Figure 6.13 shows a pattern of blood vessels in a section of a ligament, perfused with black ink.

The skeleton represents the general orientational pattern and overall shape of the blood vessels in the original image.

However, information regarding the variation in the thickness (diameter) of the blood vessels is lost in skeletonization.

Eng et al. studied the effect of injury and healing on the microvascular structure of ligaments by analyzing the statistics of the volume and directional distribution of blood vessels.

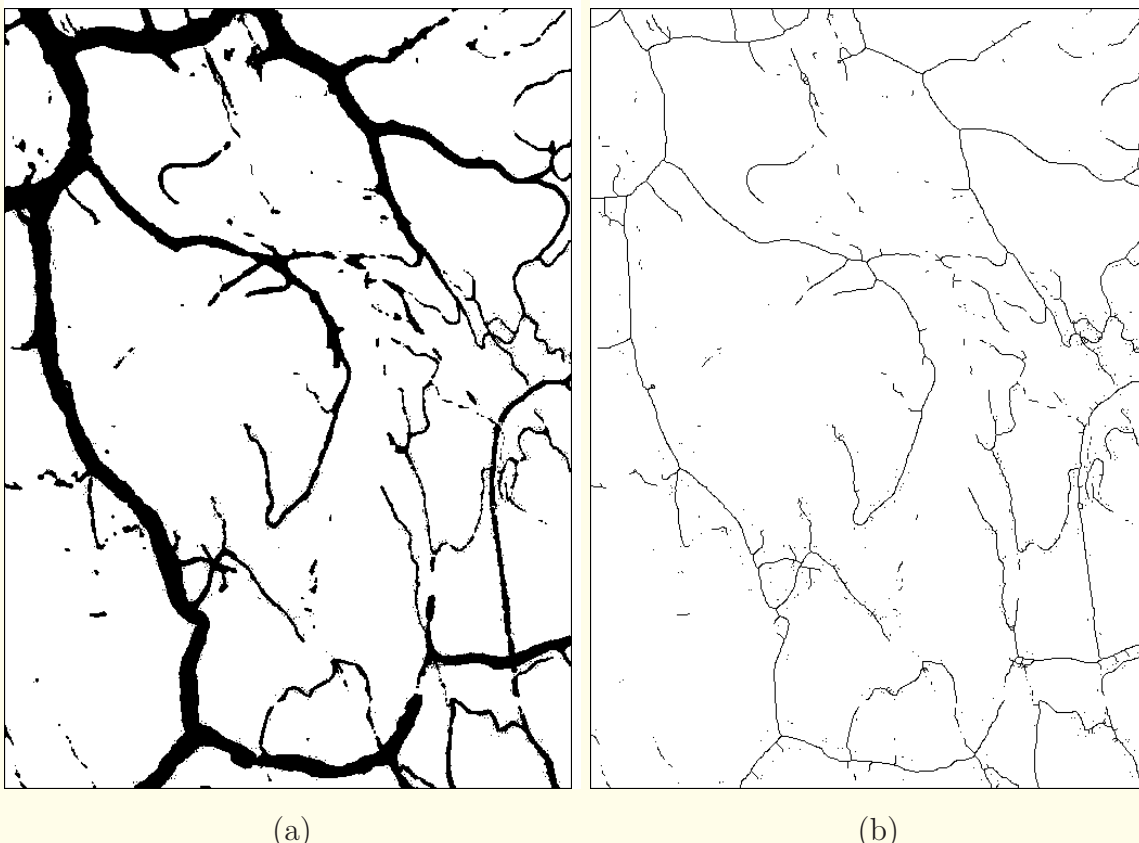


Figure 6.13: (a) Binarized image of blood vessels in a ligament perfused with black ink. Image courtesy of R.C. Bray and M.R. Doschak, University of Calgary. (b) Skeleton of the image in (a) after 15 iterations of the algorithm described in Section 6.1.6.



## 6.2 Shape Factors

It is often desirable to encode the nature or form of a contour using a small number of measures, commonly referred to as *shape factors*.

The nature of the contour to be encapsulated in the measures may vary from one application to another.



Regardless of the application, a few basic properties are essential for efficient representation:

- invariance to shift in spatial position,
- invariance to rotation, and
- invariance to scaling (enlargement or reduction).

Invariance to reflection may also be desirable in some applications.

Shape factors that meet the criteria listed above can effectively and efficiently represent contours for pattern classification.



Basic method:

fit an ellipse or a rectangle to the given (closed) contour.

The ratio of the major axis of the ellipse to its minor axis

or the ratio of the larger side to the smaller side of the

bounding rectangle is known as *eccentricity* or *elongation*

and represents its deviation from a circle.



### 6.2.1 Compactness

Compactness is a simple and popular measure of the efficiency of a contour to contain a given area:

$$Co = \frac{P^2}{A}, \quad (6.19)$$

$P$  and  $A$  are the contour perimeter and area enclosed.

The smaller the area contained by a contour of a given length, the larger will be the value of compactness.



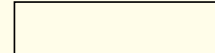
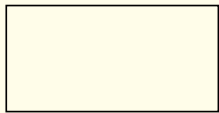
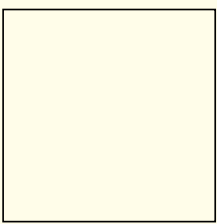
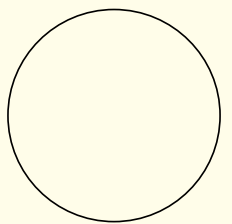
Compactness, as defined in Equation 6.19, has a lower bound of  $4\pi$  for a circle (except for the trivial case of zero for  $P = 0$ ), but no upper bound.

Compactness is invariant to shift, scaling, rotation, and reflection.

To restrict and normalize the range of the parameter to  $[0, 1]$ , as well as to obtain increasing values with increase in complexity:

$$cf = 1 - \frac{4\pi A}{P^2}. \quad (6.20)$$

$cf$  has a lower bound of zero for a circle, and increases with the complexity of the contour to a maximum value of unity.



(a)

(b)

(c)

(d)

(e)

$$Co = 12.57$$

$$16.0$$

$$18.0$$

$$25.0$$

$$41.62$$

$$cf = 0$$

$$0.21$$

$$0.30$$

$$0.50$$

$$0.70$$

Figure 6.14: Examples of contours with their values of compactness  $Co$  and  $cf$ , as defined in Equations 6.19 and 6.20. (a) Circle. (b) Square. (c) Rectangle with sides equal to 1.0 and 0.5 units. (d) Rectangle with sides equal to 1.0 and 0.25 units. (e) Right-angled triangle of height 1.0 and base 0.25 units.

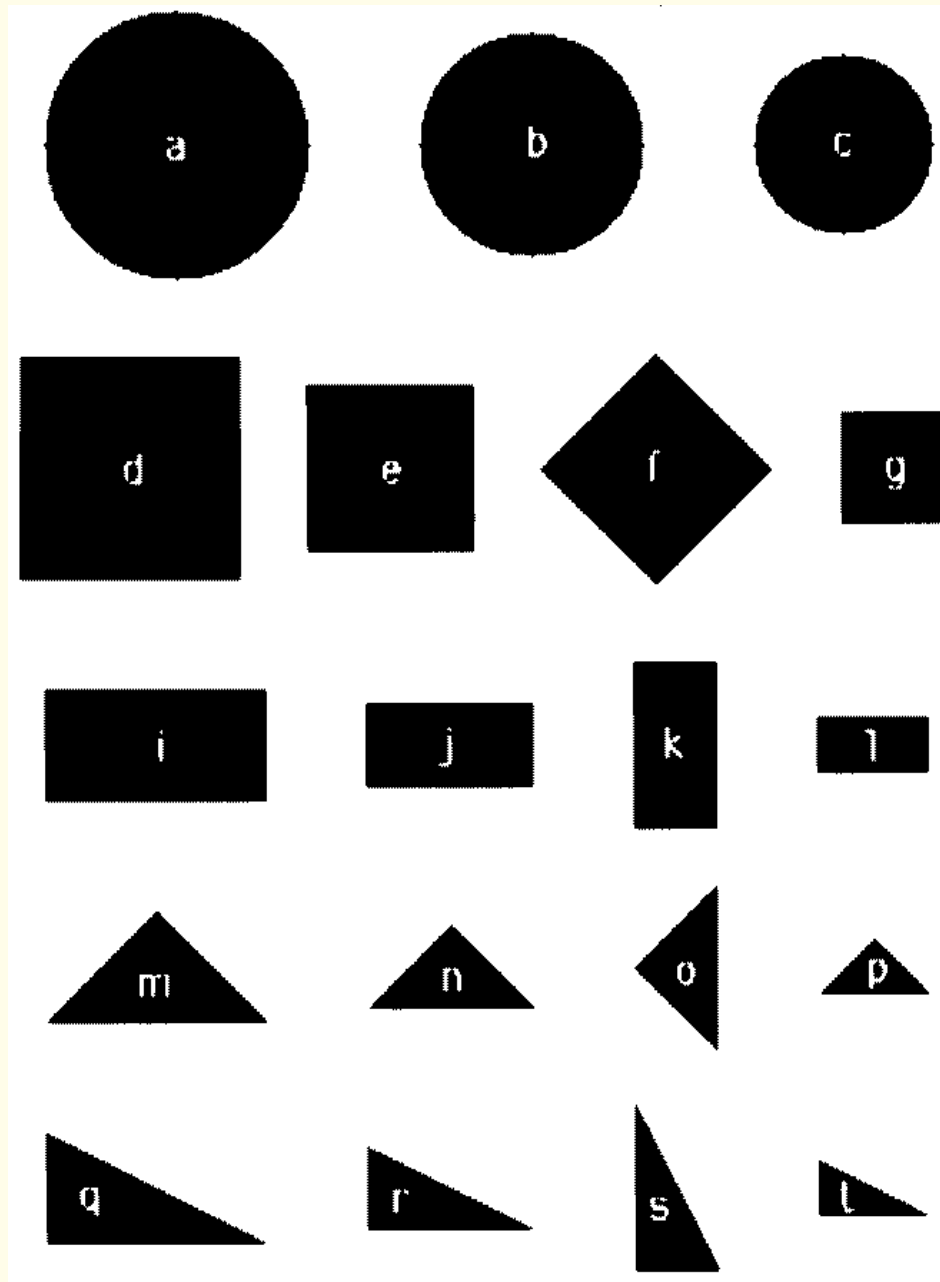


Figure 6.15: A set of simple geometric shapes, including scaling and rotation, created on a discrete grid, to test shape factors. Reproduced with permission from L. Shen, R.M. Rangayyan, and J.E.L. Desautels, “Application of shape analysis to mammographic calcifications”, *IEEE Transactions on Medical Imaging*, 13(2): 263 – 274, 1994. © IEEE.



Table 6.1: Shape Factors for the Shapes in Figure 6.15.

| Shape                             | $Co$  | $cf$   | $F_1 = F'_1$ | $F_2$   | $F'_2$  | $F_3$  | $F'_3$ | $mf$   | $ff$   |
|-----------------------------------|-------|--------|--------------|---------|---------|--------|--------|--------|--------|
| Large circle (a)                  | 14.08 | 0.1078 | 0.0056       | 0.4105  | 0.0042  | 2.0271 | 0.0067 | 0.0011 | 0.0358 |
| Medium circle (b)                 | 14.13 | 0.1105 | 0.0066       | 0.1731  | 0.0037  | 1.9285 | 0.0078 | 0.0012 | 0.0380 |
| Small circle (c)                  | 14.29 | 0.1205 | 0.0085       | 0.1771  | 0.0048  | 1.9334 | 0.0100 | 0.0015 | 0.0432 |
| Large square (d)                  | 15.77 | 0.2034 | 0.1083       | 0.5183  | 0.0870  | 1.9987 | 0.1288 | 0.0205 | 0.1416 |
| Medium square (e)                 | 15.70 | 0.1997 | 0.1081       | 0.5122  | 0.0865  | 2.0126 | 0.1287 | 0.0207 | 0.1389 |
| Rotated square (f)                | 16.00 | 0.2146 | 0.1101       | 0.5326  | 0.0893  | 1.9987 | 0.1309 | 0.0208 | 0.1434 |
| Small square (g)                  | 15.56 | 0.1926 | 0.1078       | 0.4943  | 0.0853  | 2.0495 | 0.1290 | 0.0212 | 0.1362 |
| Large rectangle (i)               | 17.60 | 0.2858 | 0.2491       | -0.3313 | -0.1724 | 1.5385 | 0.2775 | 0.0283 | 0.1494 |
| Medium rectangle (j)              | 17.47 | 0.2807 | 0.2483       | -0.3267 | -0.1710 | 1.5429 | 0.2767 | 0.0284 | 0.1483 |
| Rotated rectangle (k)             | 17.47 | 0.2807 | 0.2483       | -0.3267 | -0.1710 | 1.5429 | 0.2767 | 0.0284 | 0.1483 |
| Small rectangle (l)               | 17.23 | 0.2707 | 0.2468       | -0.3165 | -0.1682 | 1.5583 | 0.2758 | 0.0290 | 0.1420 |
| Large isosceles triangle (m)      | 22.41 | 0.4392 | 0.3119       | 0.0737  | 0.1308  | 2.3108 | 0.3846 | 0.0727 | 0.2248 |
| Medium isosceles triangle (n)     | 22.13 | 0.4322 | 0.3051       | 0.2027  | 0.1792  | 2.2647 | 0.3743 | 0.0692 | 0.2233 |
| Rotated isosceles triangle (o)    | 22.13 | 0.4322 | 0.3051       | 0.2027  | 0.1792  | 2.2647 | 0.3743 | 0.0692 | 0.2238 |
| Small isosceles triangle (p)      | 21.61 | 0.4185 | 0.3014       | 0.1518  | 0.1608  | 2.2880 | 0.3707 | 0.0693 | 0.2198 |
| Large right-angled triangle (q)   | 27.68 | 0.5459 | 0.3739       | 0.0475  | 0.1355  | 1.9292 | 0.4407 | 0.0668 | 0.2217 |
| Medium right-angled triangle (r)  | 27.18 | 0.5377 | 0.3707       | 0.0534  | 0.1396  | 1.9433 | 0.4377 | 0.0670 | 0.2221 |
| Rotated right-angled triangle (s) | 26.99 | 0.5345 | 0.3752       | 0.0022  | 0.0487  | 1.8033 | 0.4347 | 0.0596 | 0.2216 |
| Small right-angled triangle (t)   | 26.26 | 0.5215 | 0.3644       | 0.0646  | 0.1462  | 1.9750 | 0.4319 | 0.0676 | 0.2180 |

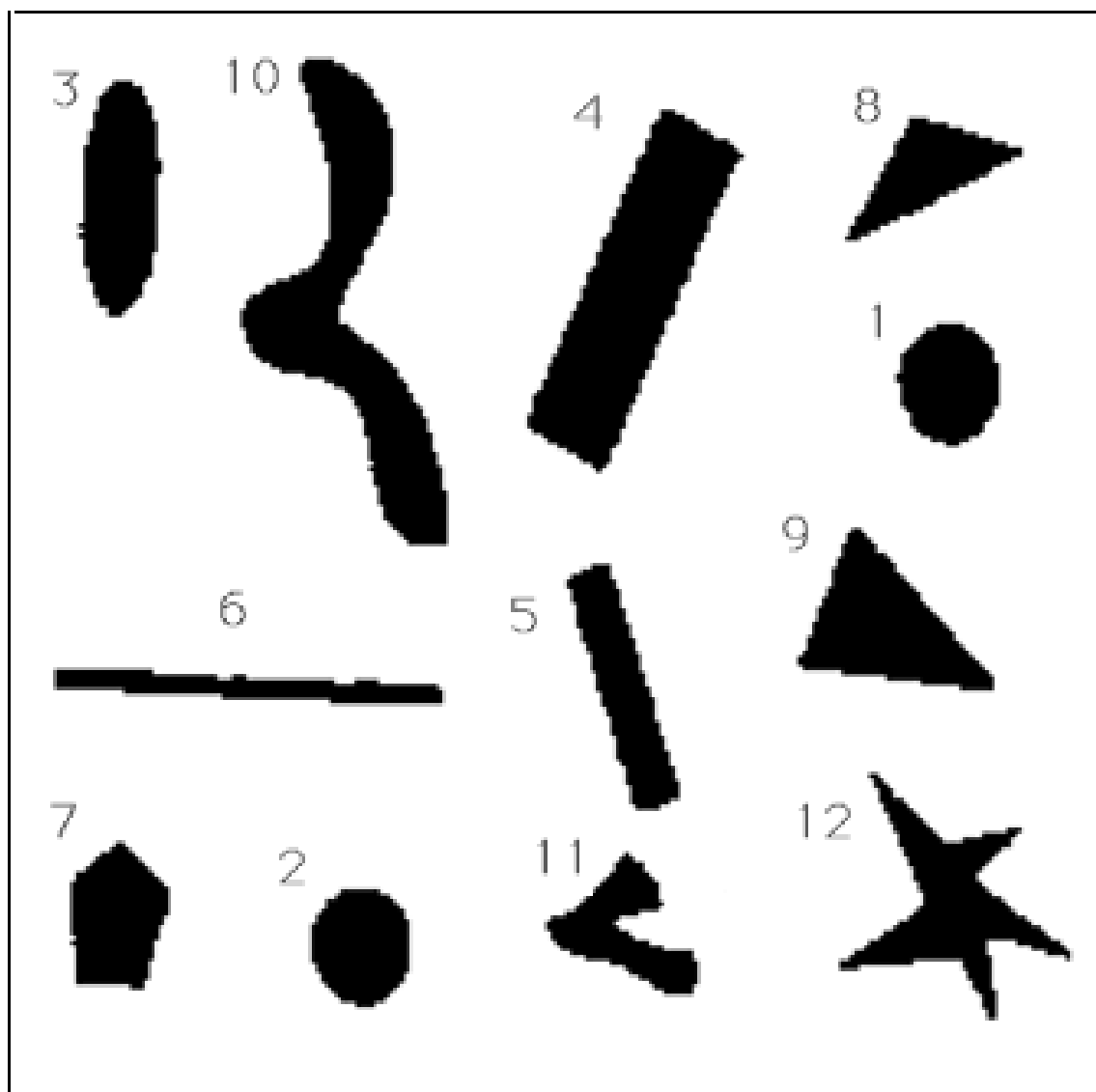


Figure 6.16: A set of objects of varying shape complexity. The objects were prepared by cutting construction paper. The contours of the objects include imperfections and artifacts. Reproduced with permission from L. Shen, R.M. Rangayyan, and J.E.L. Desautels, “Application of shape analysis to mammographic calcifications”, *IEEE Transactions on Medical Imaging*, 13(2): 263 – 274, 1994. © IEEE.

Table 6.2: Shape Factors for the Objects in Figure 6.16 Arranged in Increasing Order of  $ff$ .

| Shape | $cf$ | $mf$  | $ff$ | Type      |
|-------|------|-------|------|-----------|
| 1     | 0.13 | 0.022 | 0.14 | Circle    |
| 2     | 0.11 | 0.019 | 0.14 | Circle    |
| 3     | 0.35 | 0.047 | 0.14 | Ellipse   |
| 4     | 0.55 | 0.047 | 0.17 | Rectangle |
| 5     | 0.62 | 0.060 | 0.18 | Rectangle |
| 6     | 0.83 | 0.084 | 0.18 | Rectangle |
| 7     | 0.22 | 0.038 | 0.19 | Pentagon  |
| 8     | 0.50 | 0.063 | 0.24 | Triangle  |
| 9     | 0.44 | 0.063 | 0.25 | Triangle  |
| 10    | 0.75 | 0.090 | 0.30 | Other     |
| 11    | 0.63 | 0.106 | 0.36 | Other     |
| 12    | 0.81 | 0.077 | 0.42 | Other     |



## 6.2.2 Moments

Statistical moments of PDFs and other data distributions have been utilized as pattern features in a number of applications;

the same concepts have been extended to the analysis of images and contours.

Given a 2D continuous image  $f(x, y)$ , the regular moments  $m_{pq}$  of order  $(p + q)$  are defined as:

$$m_{pq} = \int_{-\infty}^{+\infty} \int_{-\infty}^{+\infty} x^p y^q f(x, y) dx dy, \quad (6.21)$$

for  $p, q = 0, 1, 2, \dots$



A uniqueness theorem states that if  $f(x, y)$  is piecewise continuous and has nonzero values only in a finite part of the  $(x, y)$  plane, then moments of all orders exist,

and the moment sequence  $m_{pq}, p, q = 0, 1, 2, \dots$ , is uniquely determined by  $f(x, y)$ .

Conversely, the sequence  $m_{pq}$  uniquely determines  $f(x, y)$ .



The central moments are defined with respect to the centroid of the image as

$$\mu_{pq} = \int_{-\infty}^{+\infty} \int_{-\infty}^{+\infty} (x - \bar{x})^p (y - \bar{y})^q f(x, y) dx dy, \quad (6.22)$$

$$\bar{x} = \frac{m_{10}}{m_{00}}, \quad \bar{y} = \frac{m_{01}}{m_{00}}. \quad (6.23)$$



The gray levels of the pixels provide weights for the moments as defined above.

If moments are to be computed for a contour, only the contour pixels would be used with weights equal to unity;

the internal pixels would have weights of zero.

For an  $M \times N$  digital image, the integrals are replaced by summations:

$$\mu_{pq} = \sum_{m=0}^{M-1} \sum_{n=0}^{N-1} (m - \bar{x})^p (n - \bar{y})^q f(m, n). \quad (6.24)$$



The central moments have the following relationships:

$$\mu_{00} = m_{00} = \mu, \quad (6.25)$$

$$\mu_{10} = \mu_{01} = 0, \quad (6.26)$$

$$\mu_{20} = m_{20} - \mu \bar{x}^2, \quad (6.27)$$

$$\mu_{11} = m_{11} - \mu \bar{x} \bar{y}, \quad (6.28)$$

$$\mu_{02} = m_{02} - \mu \bar{y}^2, \quad (6.29)$$

$$\mu_{30} = m_{30} - 3m_{20}\bar{x} + 2\mu \bar{x}^3, \quad (6.30)$$

$$\mu_{21} = m_{21} - m_{20}\bar{y} - 2m_{11}\bar{x} + 2\mu \bar{x}^2 \bar{y}, \quad (6.31)$$

$$\mu_{12} = m_{12} - m_{02}\bar{x} - 2m_{11}\bar{y} + 2\mu \bar{x} \bar{y}^2, \quad (6.32)$$

$$\mu_{03} = m_{03} - 3m_{02}\bar{y} + 2\mu \bar{y}^3. \quad (6.33)$$



Normalization with respect to size is achieved by

dividing each of the moments by  $\mu_{00}^{\gamma}$ ,

where  $\gamma = \frac{p+q}{2} + 1$ ,

to obtain the normalized moments as

$$\nu_{pq} = \frac{\mu_{pq}}{\mu_{00}^{\gamma}}. \quad (6.34)$$



Hu defined a set of seven shape factors that are functions of the second-order and third-order central moments as follows:

$$M_1 = \nu_{20} + \nu_{02}, \quad (6.35)$$

$$M_2 = (\nu_{20} - \nu_{02})^2 + 4\nu_{11}^2, \quad (6.36)$$

$$M_3 = (\nu_{30} - 3\nu_{12})^2 + (3\nu_{21} - \nu_{03})^2, \quad (6.37)$$

$$M_4 = (\nu_{30} + \nu_{12})^2 + (\nu_{21} + \nu_{03})^2, \quad (6.38)$$



$$\begin{aligned}
 M_5 = & (\nu_{30} - 3\nu_{12})(\nu_{30} + \nu_{12})[(\nu_{30} + \nu_{12})^2 - 3(\nu_{21} + \nu_{03})^2] \\
 & +(3\nu_{21} - \nu_{03})(\nu_{21} + \nu_{03})[3(\nu_{30} + \nu_{12})^2 - (\nu_{21} + \nu_{03})^2], \quad (6.39)
 \end{aligned}$$

$$\begin{aligned}
 M_6 = & (\nu_{20} - \nu_{02})[(\nu_{30} + \nu_{12})^2 - (\nu_{21} + \nu_{03})^2] \\
 & +4\nu_{11}(\nu_{30} + \nu_{12})(\nu_{21} + \nu_{03}), \quad (6.40)
 \end{aligned}$$

$$\begin{aligned}
 M_7 = & (3\nu_{21} - \nu_{03})(\nu_{30} + \nu_{12})[(\nu_{30} + \nu_{12})^2 - 3(\nu_{21} + \nu_{03})^2] \\
 & -(\nu_{30} - 3\nu_{12})(\nu_{21} + \nu_{03})[3(\nu_{30} + \nu_{12})^2 - (\nu_{21} + \nu_{03})^2]. \quad (6.41)
 \end{aligned}$$

$M_1$  through  $M_7$  are invariant to shift, scaling, and rotation, and are useful for pattern analysis.



## Moments of distances to the centroid:

When an ROI is represented using only its contour, an alternative definition of moments is based upon a sequence that represents the Euclidean distances between the centroid of the region and all of the points along the contour, shown as  $d(n)$  in Figure 6.1.

The distances from the center of a circle to its contour points are all equal to the radius of the circle: variance of the values = 0.

For rough shapes, the distances will vary considerably.

The variance and higher-order moments of the distance values could be expected to provide indicators of shape complexity.



The  $p^{th}$  moment of the sequence  $d(n)$  is defined as

$$m_p = \frac{1}{N} \sum_{n=0}^{N-1} [d(n)]^p, \quad (6.42)$$

and the  $p^{th}$  central moment is defined as

$$M_p = \frac{1}{N} \sum_{n=0}^{N-1} [d(n) - m_1]^p. \quad (6.43)$$



The corresponding normalized moments are defined as

$$\overline{m_p} = \frac{m_p}{(M_2)^{p/2}} = \frac{\frac{1}{N} \sum_{n=0}^{N-1} [d(n)]^p}{\left\{ \frac{1}{N} \sum_{n=0}^{N-1} [d(n) - m_1]^2 \right\}^{p/2}}, \quad (6.44)$$

$$\overline{M_p} = \frac{M_p}{(M_2)^{p/2}} = \frac{\frac{1}{N} \sum_{n=0}^{N-1} [d(n) - m_1]^p}{\left\{ \frac{1}{N} \sum_{n=0}^{N-1} [d(n) - m_1]^2 \right\}^{p/2}}. \quad (6.45)$$

Gupta and Srinath showed that the normalized moments  $\overline{m_p}$  and  $\overline{M_p}$  are invariant to translation, rotation, and scaling.

This set of moments (in an infinite series) reversibly represents the shape of a contour.



Moments of any arbitrarily large order can be derived from a contour and used as features for shape classification.

High-order moments are sensitive to noise:

the resulting classifier will be less tolerant to noise.

Gupta and Srinath selected four normalized low-order moments to form a set of shape features as follows:



$$F_1 = \frac{(M_2)^{1/2}}{m_1} = \frac{\left\{ \frac{1}{N} \sum_{n=0}^{N-1} [d(n) - m_1]^2 \right\}^{1/2}}{m_1}, \quad (6.46)$$

$$F_2 = \frac{M_3}{(M_2)^{3/2}} = \frac{\frac{1}{N} \sum_{n=0}^{N-1} [d(n) - m_1]^3}{\left\{ \frac{1}{N} \sum_{n=0}^{N-1} [d(n) - m_1]^2 \right\}^{3/2}}, \quad (6.47)$$

$$F_3 = \frac{M_4}{(M_2)^2} = \frac{\frac{1}{N} \sum_{n=0}^{N-1} [d(n) - m_1]^4}{\left\{ \frac{1}{N} \sum_{n=0}^{N-1} [d(n) - m_1]^2 \right\}^2}. \quad (6.48)$$



A study by Shen et al. showed that the variations in  $F_2$  and  $F_3$  for differing shape complexity are small

and do not show a simple progression.

$F_2$  was observed to vary significantly for the same (geometric) shape with scaling and rotation.

$F_2$  and  $F_3$  were modified by Shen et al. as follows:



$$F_2' = \frac{M_3^{1/3}}{m_1} = \frac{\left\{ \frac{1}{N} \sum_{n=0}^{N-1} [d(n) - m_1]^3 \right\}^{1/3}}{m_1}, \quad (6.49)$$

$$F_3' = \frac{M_4^{1/4}}{m_1} = \frac{\left\{ \frac{1}{N} \sum_{n=0}^{N-1} [d(n) - m_1]^4 \right\}^{1/4}}{m_1}. \quad (6.50)$$



Compared with the feature set proposed by Gupta and Srinath, the set  $\{F_1, F'_2, F'_3\}$  has the following properties:

- All of the three features are directly comparable.
- $F'_3$  describes the roughness of a contour better than  $F_3$ . In general, the larger the value of  $F'_3$ , the rougher is the contour.



Although  $F'_2$  was observed by Shen et al. to have better invariance with respect to size and rotation for a given geometric shape, it showed no better variation than  $F'_2$  across the shape categories tested.

$$mf = F'_3 - F'_1$$

was shown to be a good indicator of shape roughness because the fourth-order term in  $F'_3$  will be much larger than the second-order term in  $F'_1$  as the contour becomes rougher.



$m\bar{f}$  provides the desired invariance for a given contour type as well as the desired variation across the various shape categories.

The definition of the features  $F'_1$  and  $F'_3$  makes it possible to perform the subtraction directly.

$m\bar{f}$  is limited to the range  $[0, 1]$ .



### 6.2.3 Chord-length statistics

Methods to characterize 2D closed contours using their chord-length distributions were proposed by You and Jain.

A chord-length measure  $L_k$  is defined as the length of the line segment that links a pair of contour points, normalized by the length of the longest chord.

The complete set of chords for a given object consists of all possible chords drawn from every boundary pixel to every other boundary pixel; see Figure 6.17.

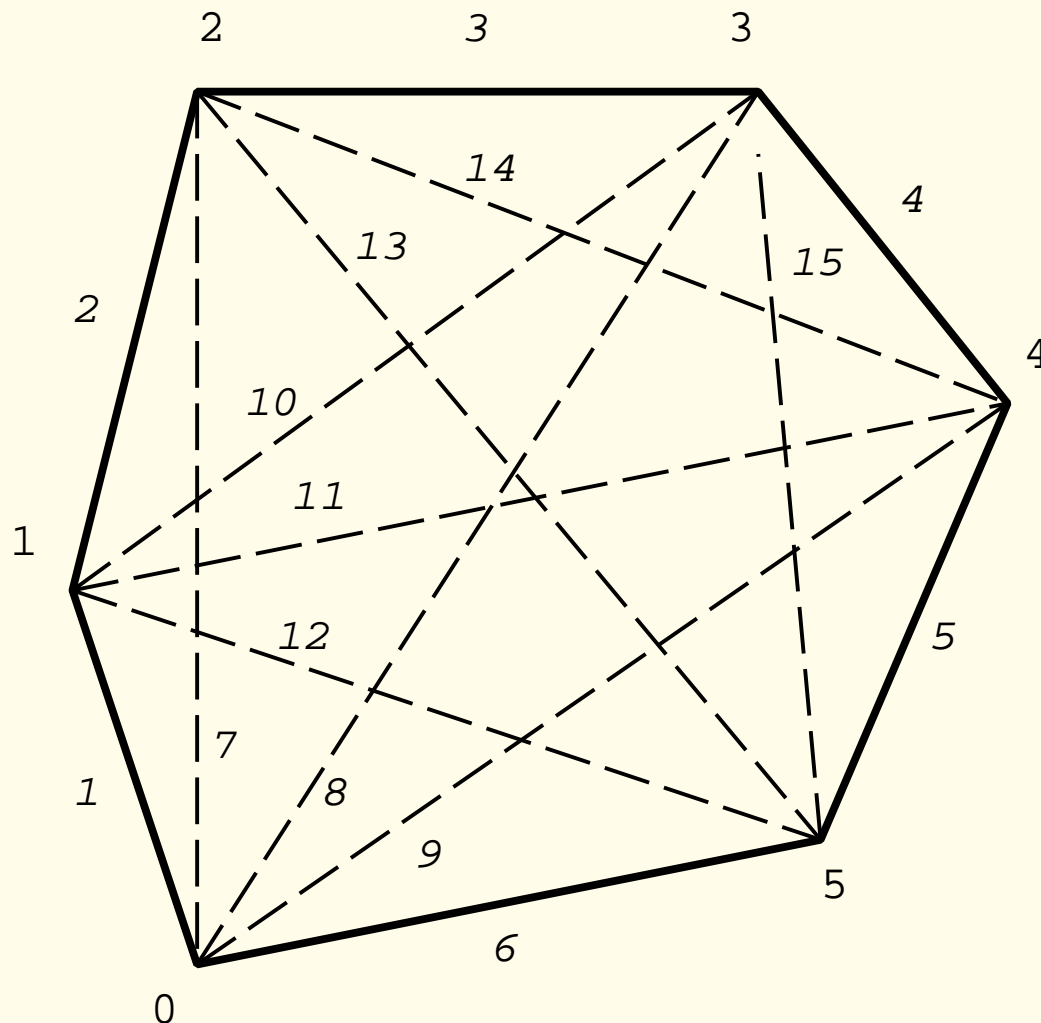


Figure 6.17: The set of all possible chords for a contour with  $N = 6$  boundary points. There exist  $K = N(N - 1)/2 = 15$  unique chords (including the sides of the polygonal contour) in the example. The contour points (0 – 5) are shown in regular font; the chord numbers (1 – 15) are shown in italics.



You and Jain considered the  $K = N(N - 1)/2$  unique chords of the  $N$  boundary points of an object as a sample distribution set,

and computed the Kolmogorov-Smirnov (K-S) statistics of the chord-length distribution for use as shape factors as follows:

$$M_{c1} = \frac{1}{K} \sum_{k=1}^K L_k , \quad (6.51)$$

$$M_{c2}^2 = \frac{1}{K} \sum_{k=1}^K (L_k - M_{c1})^2 , \quad (6.52)$$



$$M_{c3} = \frac{1}{M_{c2}^3} \frac{1}{K} \sum_{k=1}^K (L_k - M_{c1})^3, \quad (6.53)$$

$$M_{c4} = \frac{1}{M_{c2}^4} \frac{1}{K} \sum_{k=1}^K (L_k - M_{c1})^4. \quad (6.54)$$

The measures represent the mean, variance, skewness, and kurtosis of the chord-length distributions.



The chord-length statistics are invariant to translation, scaling, and rotation, and are robust in the presence of noise and distortion in the shape boundary.

Major disadvantage: it is possible for contours of different shapes to have the same chord-length distribution.



### 6.3 Fourier Descriptors

Given a contour with  $N$  points having the coordinates

$$\{x(n), y(n)\}, n = 0, 1, 2, \dots, N - 1,$$

we could form a complex sequence

$$z(n) = x(n) + j y(n), n = 0, 1, 2, \dots, N - 1;$$

see Figure 6.1.

$z(n)$  is a periodic signal with a period of  $N$  samples.

The sequence  $|z(n)|$  may be used as a signature of the contour.



Periodic signals lend themselves to analysis via the Fourier series.

Given a discrete-space sequence  $z(n)$ , we could derive its Fourier series as one period of its DFT  $Z(k)$ , defined as

$$Z(k) = \frac{1}{N} \sum_{n=0}^{N-1} z(n) \exp\left[-j \frac{2\pi}{N} nk\right], \quad (6.55)$$

$$k = -\frac{N}{2}, \dots, -1, 0, 1, 2, \dots, \frac{N}{2} - 1.$$

The frequency index  $k$  could be interpreted as the index of the harmonics of a fundamental frequency.



The contour sample sequence  $z(n)$  is given by the inverse DFT as

$$z(n) = \frac{1}{N} \sum_{k=-\frac{N}{2}}^{\frac{N}{2}-1} Z(k) \exp \left[ j \frac{2\pi}{N} nk \right], \quad (6.56)$$

$$n = 0, 1, 2, \dots, N - 1.$$

The complex coefficients  $Z(k)$  are known as the *Fourier descriptors* of the contour  $z(n)$ .



$Z(k)$  represents a two-sided complex spectrum:

with folding or shifting of the DFT or FFT array,

the frequency index would run as

$$k = -\frac{N}{2}, \dots, -1, 0, 1, 2, \dots, \frac{N}{2} - 1;$$

without folding, as usually provided by FFT algorithms,

the coefficients are provided in the order

$$0, 1, 2, \dots, \frac{N}{2} - 1, -\frac{N}{2}, \dots, -2, -1.$$



Important properties and characteristics of Fourier descriptors:

- The frequency index  $k$  represents the harmonic number or order in a Fourier series representation of the periodic signal  $z(n)$ .

The fundamental frequency ( $k = 1$ ) represents a sinusoid in each of the coordinates  $x$  and  $y$  that exhibits one period while traversing once around the closed contour  $z(n)$ .

- Differing from the spectra of real signals,  $Z(k)$  does not have conjugate symmetry due to the complex nature of  $z(n)$ .
- The zero-frequency (DC) coefficient  $Z(0)$  represents the centroid or center of mass  $(\bar{x}, \bar{y})$ , as

$$Z(0) = \frac{1}{N} \sum_{n=0}^{N-1} z(n) = (\bar{x}, \bar{y}). \quad (6.57)$$



- Each of the fundamental frequency coefficients  $Z(1)$  and  $Z(-1)$  represents a circle.

The set of coefficients  $\{Z(-1), Z(1)\}$  represents an ellipse.

- High-order Fourier descriptors represent fine details or rapid excursions of the contour.
- The rotation of a contour by an angle  $\theta$  may be expressed as  $z_1(n) = z(n) \exp(j\theta)$ , where  $z_1(n)$  represents the rotated contour.

Rotation leads to an additional phase component as

$$Z_1(k) = Z(k) \exp(j\theta).$$



- If  $z(n)$  represents the points along a contour obtained by traversing the contour in the clockwise direction, and  $z_1(n)$  represents the points obtained by traversing in the counter-clockwise direction, we have

$$z_1(n) = z(-n) = z(N - n),$$

$$Z_1(k) = Z(-k).$$



- Shifting or translating  $z(n)$  by  $(x_o, y_o)$  to obtain

$z_1(n) = z(n) + (x_o + j y_o)$  leads to an additional DC component:

$$Z_1(k) = Z(k) + (x_o + j y_o) \delta(k).$$

- Scaling a contour as  $z_1(n) = \alpha z(n)$  leads to a similar scaling of the Fourier descriptors:

$$Z_1(k) = \alpha Z(k).$$

- Shifting the starting point by  $n_o$  samples,

expressed as  $z_1(n) = z(n - n_o)$ ,

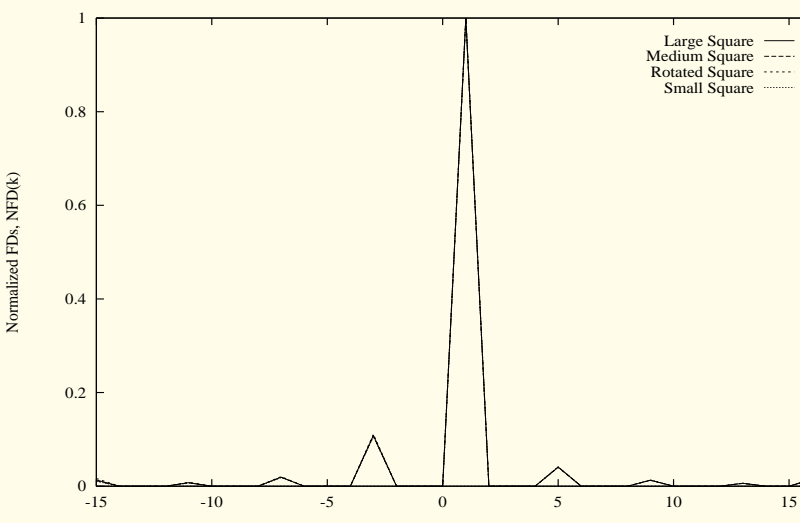
leads to an additional linear-phase component:

$$Z_1(k) = Z(k) \exp[-j \frac{2\pi}{N} n_o k].$$

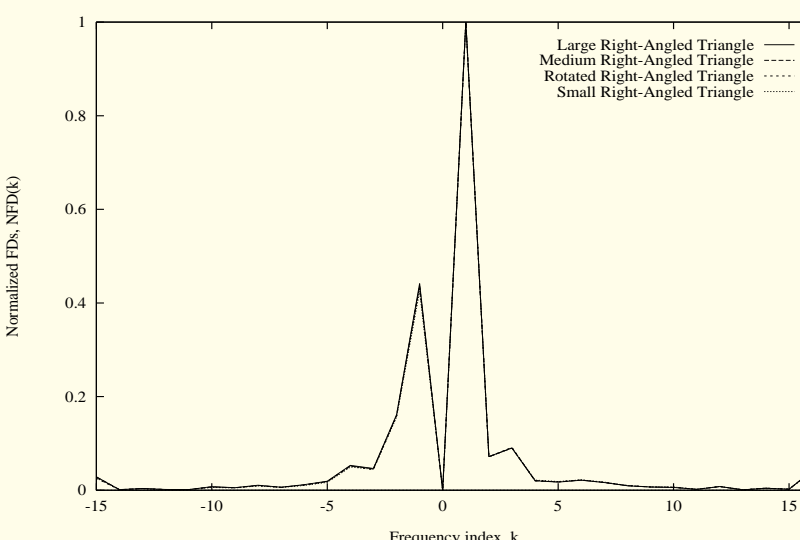


Fourier descriptors may be filtered in a manner similar to the filtering of signals and images in the frequency domain.

The full set or a subset of the coefficients may also be used to represent the contour, and to derive shape factors.

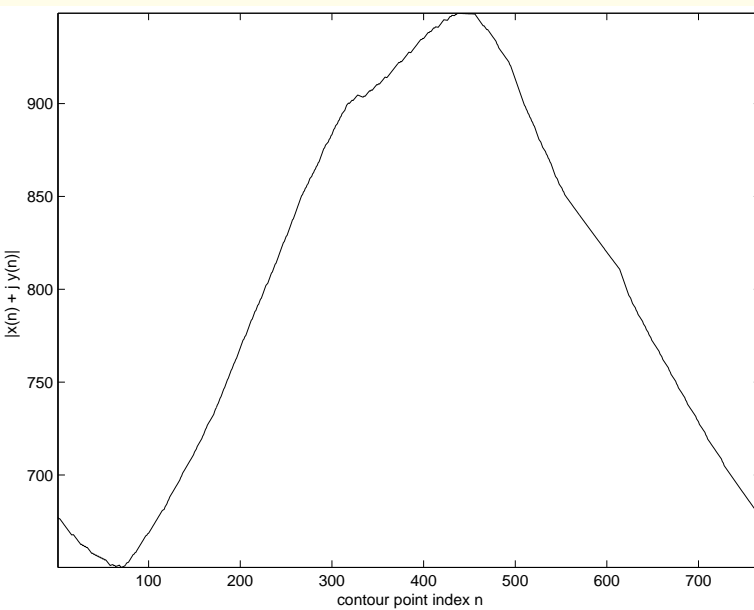


(a)

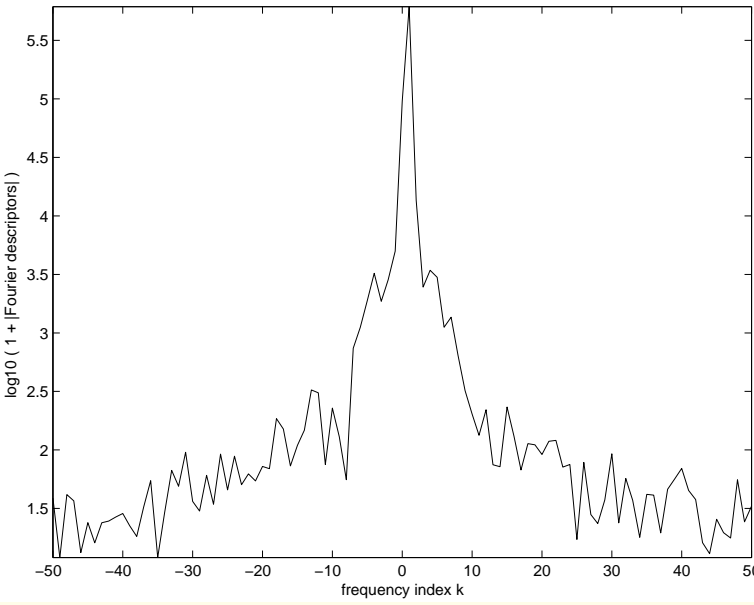


(b)

Figure 6.18: Normalized Fourier descriptors (NFD, up to  $k = \pm 15$ ) for (a) the squares and (b) the right-angled triangles in Figure 6.15. Each figure shows the NFD for four objects; however, due to invariance with respect to scaling and rotation, the functions overlap completely. Reproduced with permission from L. Shen, R.M. Rangayyan, and J.E.L. Desautels, “Application of shape analysis to mammographic calcifications”, *IEEE Transactions on Medical Imaging*, 13(2): 263 – 274, 1994. © IEEE.

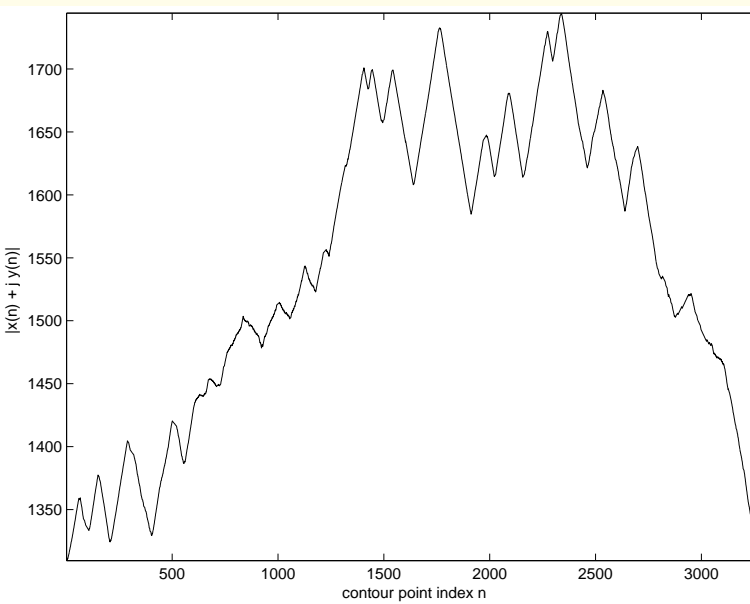


(a)

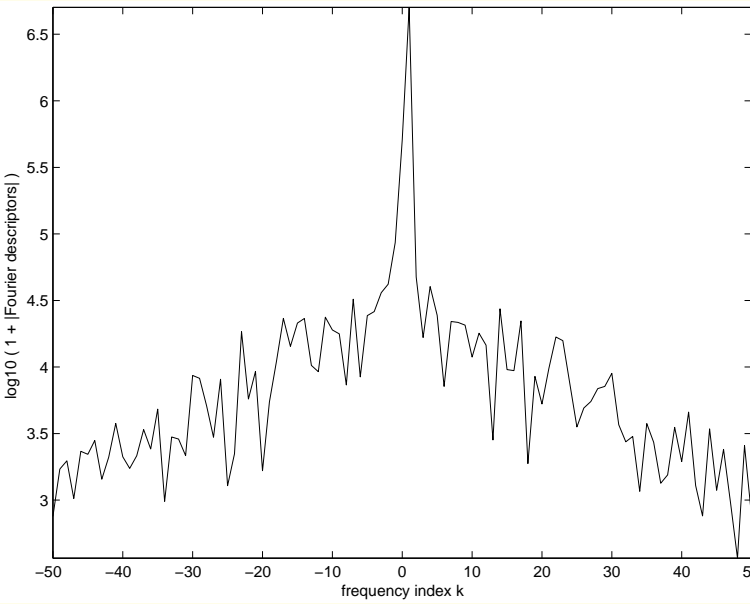


(b)

Figure 6.19: (a) Signature with  $|z(n)|$  of the benign-mass contour in Figure 6.2 (a). (b) Magnitude of the Fourier descriptors, shown only for  $k = [-50, 50]$ .



(a)



(b)

Figure 6.20: (a) Signature with  $|z(n)|$  of the malignant-tumor contour in Figure 6.3 (a). (b) Magnitude of the Fourier descriptors, shown only for  $k = [-50, 50]$ .

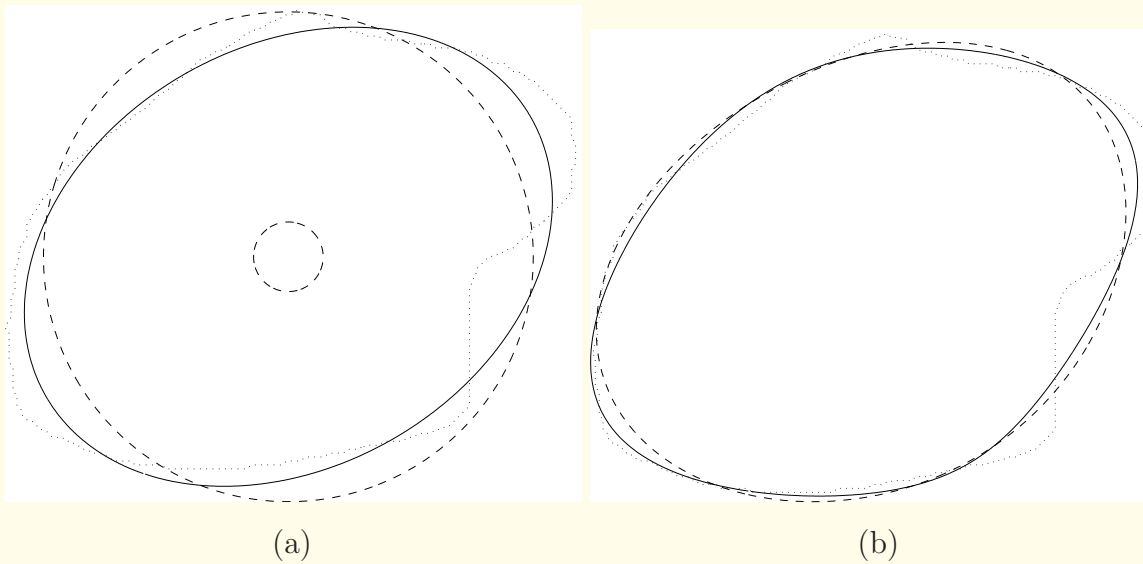
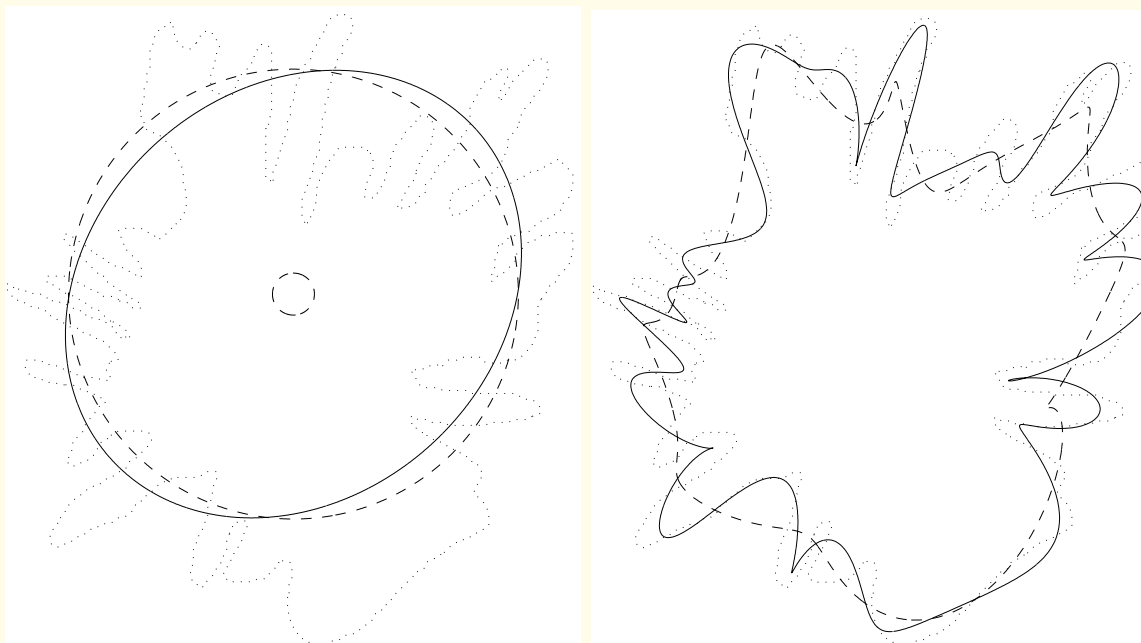


Figure 6.21: Filtering of the benign-mass contour in Figure 6.2 (a) using Fourier descriptors. (a) Using coefficients for  $k = 1$  (smaller circle in dashed line),  $k = -1$  (larger circle in dashed line), and  $k = \{-1, 0, 1\}$  (ellipse in solid line). (b) Using coefficients for  $k = [-2, 2]$  (dashed line) and  $k = [-3, 3]$  (solid line). The original contour is indicated with a dotted line for reference.



(a)

(b)

Figure 6.22: Filtering of the malignant-tumor contour in Figure 6.3 (a) using Fourier descriptors. (a) Using coefficients for  $k = 1$  (smaller circle in dashed line),  $k = -1$  (larger circle in dashed line), and  $k = \{-1, 0, 1\}$  (ellipse in solid line). (b) Using coefficients for  $k = [-10, 10]$  (dashed line) and  $k = [-20, 20]$  (solid line). The original contour is indicated with a dotted line for reference.



## Shape factor based upon Fourier descriptors:

Procedure proposed by Shen et al.:

$Z(0)$  is set equal to zero in order to make the descriptors independent of position.

Each coefficient is divided by  $Z(1)$  in order to normalize for size.

The magnitudes of the Fourier descriptors are independent of position, size, orientation, and starting point of the contour;

note that the orientation and starting point affect only the phase of the Fourier descriptors.



Normalized Fourier descriptors  $Z_o(k)$ :

$$Z_o(k) = \begin{cases} 0, & k = 0; \\ \frac{Z(k)}{Z(1)}, & \text{otherwise.} \end{cases}$$

*Note:* For normalization as above, the points of the contour must be indexed from 0 to  $(N - 1)$  in counter-clockwise order; in the opposite case,  $Z(-1)$  should be used.

Contours with sharp excursions possess more high-frequency energy than smooth contours.

Applying a weighting factor that increases with frequency leads to unbounded values that are sensitive to noise.



Shape factor  $ff$  based upon the normalized Fourier descriptors:

$$ff = 1 - \frac{\sum_{k=-N/2+1}^{N/2} |Z_o(k)| / |k|}{\sum_{k=-N/2+1}^{N/2} |Z_o(k)|}. \quad (6.58)$$

Advantage: limited to the range  $[0, 1]$ ,

not sensitive to noise,

invariant to translation, rotation, starting point, and contour size,

increases as the object shape becomes more complex and rough.



## 6.4 Fractional Concavity

Most benign mass contours are smooth, oval, or have major portions of convex macrolobulations.

Some benign masses may have minor concavities and spicules.

Malignant tumors typically possess both concave and convex segments as well as microlobulations and prominent spicules.

Rangayyan et al. proposed a measure of fractional concavity ( $f_{cc}$ ) of contours to characterize and quantify these properties.



To compute  $f_{cc}$ : after segmentation of the contour, the individual segments between successive inflection points are labeled as concave or convex parts.

A convex part is defined as a segment of the contour that encloses a portion of the mass (inside of the contour);

a concave part is one formed by the presence of a background region within the segment.

Contours may include artifacts and minor modulations that could lead to inefficient representation for pattern classification.

The polygonal modeling procedure was applied to reduce the effect of the artifacts.



The cumulative length of the concave segments was computed using the polygonal model, and normalized by the total length of the contour to obtain  $f_{cc}$ .

$f_{cc}$  is limited to the range  $[0, 1]$ ,

and is independent of rotation, shift, and the size (scaling) of the contour.



## 6.5 Analysis of Spicularity

Invasive carcinomas, due to their nature of infiltration into surrounding tissues, form narrow, stellate distortions or spicules at their boundaries.

Rangayyan et al. proposed a spiculation index ( $SI$ ) to represent the degree of spiculation of a mass contour.

In order to emphasize narrow spicules and microlobulations, a weighting factor was included to enhance the contributions of narrow spicules in the computation of  $SI$ .



For each curved part of a mass contour or the corresponding polygonal model segment, the ratio of its length to the base width can represent the degree of narrowness or spiculation.

A nonlinear weighting function was proposed based upon the segment's length  $S$  and angle of spiculation  $\theta$ , to deliver progressively increasing weighting with increase in the narrowness of spiculation of each segment.

Spicule candidates were identified as portions of the contour delimited by pairs of successive points of inflection.

The polygonal model was used to compute the parameters  $S$  and  $\theta$  for each spicule candidate.



If a spicule includes  $M$  polygonal segments, then there exist  $M - 1$  angles at the points of intersection of the successive segments.

Let  $s_m$ ,  $m = 1, 2, \dots, M$ , be the polygonal segments,

and  $\Theta_n$ ,  $n = 1, 2, \dots, M - 1$ , be the angles subtended.

Then, the segment length ( $S$ ) and the angle of narrowness ( $\theta$ ) of the spicule under consideration are computed as follows:



1. If  $M = 1$ , the portion of the contour delimited by successive points of inflection is relatively straight:

Such parts are merged into the spicules that include them, enhancing the lengths of the corresponding spicules without affecting their angles of spiculation.

The merging process discards the redundant points of inflection lying on relatively straight parts of the contour.

2. If  $M = 2$ , then the length of spicule is  $S = s_1 + s_2$ , and the angle subtended by the linear segments at the point of intersection represents the angle of narrowness ( $\theta$ ) of the spicule.



3. If  $M > 2$ , then the length of the spicule is  $S = \sum_{m=1}^M s_m$ .

To estimate the angle of narrowness, an adaptive threshold is applied by using the mean of the set of angles

$\Theta_n$ ,  $n = 1, 2, \dots, M - 1$ , as the threshold ( $\Theta_{th}$ ) for rejecting insignificant angles ( $\approx 180^\circ$ ).

Mean of angles  $\leq \Theta_{th}$  = estimate of angle of spicule.

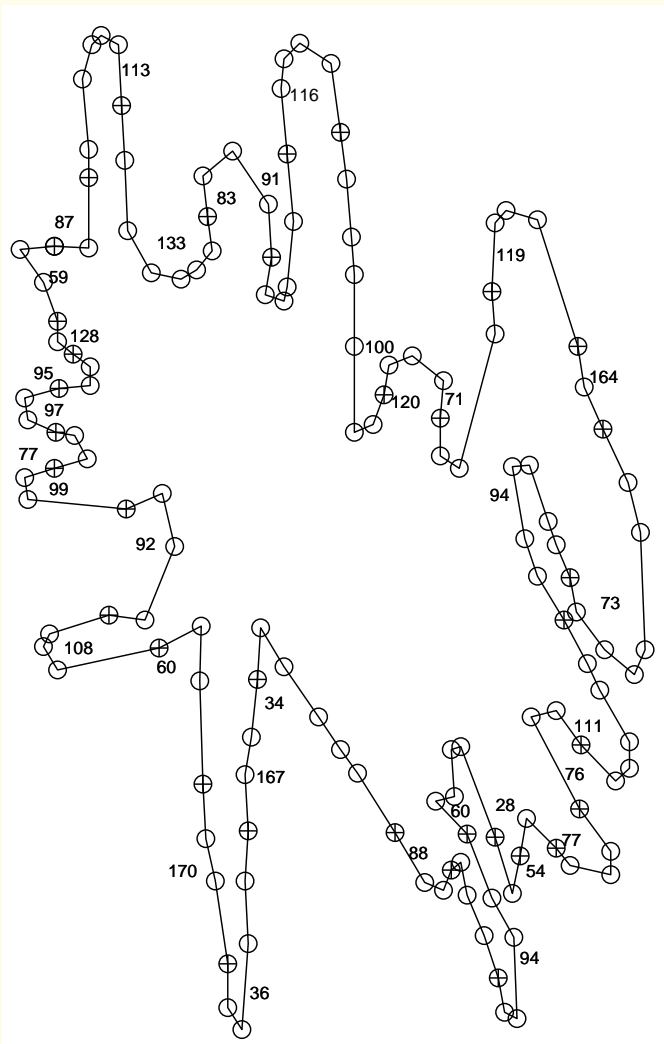
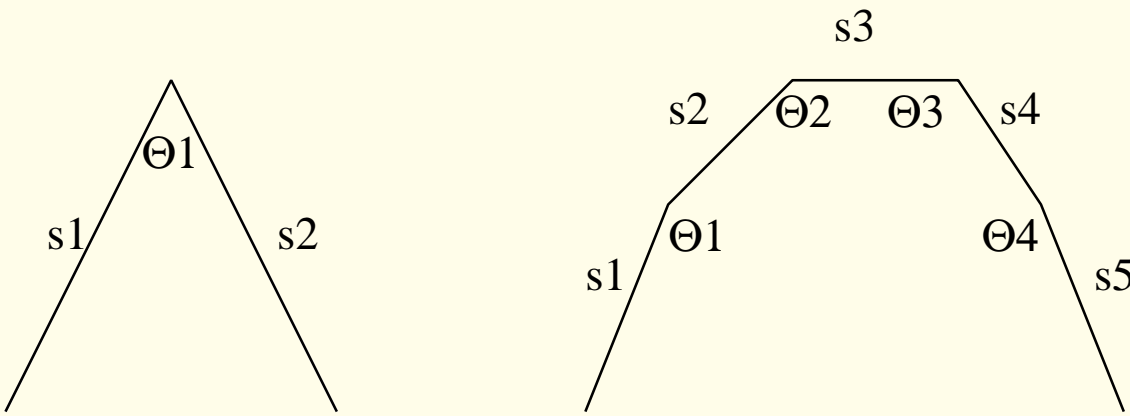


Figure 6.23: The polygonal model used in the procedure to compute  $SI$  for the spiculated malignant tumor shown in Figure 6.8 (with the corresponding polygonal model in Figure 6.10). The ' $\oplus$ ' marks correspond to the points of inflection retained to represent the starting and the ending points of spicule candidates, and the ' $\circ$ ' marks indicate the points of intersection of linear segments within the spicules in the corresponding complete polygonal model. The numbers inside or beside each spicule candidate are the angles in degrees computed for the derivation of  $SI$ . Reproduced with permission from R.M. Rangayyan, N.R. Mudigonda, and J.E.L. Desautels, "Boundary modeling and shape analysis methods for classification of mammographic masses", *Medical and Biological Engineering and Computing*, 38: 487 – 496, 2000. © IFMBE.



$$M = 2$$

$$\theta = \Theta_1$$

$$S = s_1 + s_2$$

$$M = 5$$

$$\Theta_{th} = (\Theta_1 + \Theta_2 + \Theta_3 + \Theta_4) / 4$$

$$\Theta_2 < \Theta_{th}; \quad \Theta_3 < \Theta_{th}$$

$$\theta = (\Theta_2 + \Theta_3) / 2$$

$$S = s_1 + s_2 + s_3 + s_4 + s_5$$

Figure 6.24: Computation of segment length  $S$  and angle of spiculation  $\theta$  for two examples of spicule candidates with the number of segments  $M = 2$  and  $M = 5$ , respectively.  $\Theta_{th}$  is the threshold computed to reject insignificant angles (that is, angles that are close to  $180^\circ$ ). Reproduced with permission from R.M. Rangayyan, N.R. Mudigonda, and J.E.L. Desautels, “Boundary modeling and shape analysis methods for classification of mammographic masses”, *Medical and Biological Engineering and Computing*, 38: 487 – 496, 2000. © IFMBE.



Let  $S_n$  and  $\theta_n$ ,  $n = 1, 2, \dots, N$ , be the length and angle of  $N$  sets of polygonal model segments corresponding to the  $N$  spicule candidates of a mass contour.

$$SI = \frac{\sum_{n=1}^N (1 + \cos \theta_n) S_n}{\sum_{n=1}^N S_n}. \quad (6.59)$$

The factor  $(1 + \cos \theta_n)$  modulates the length of each segment (possible spicule) according to its narrowness.

Spicules with narrow angles between  $0^\circ$  and  $30^\circ$  get high weighting, as compared to macrolobulations that usually form obtuse angles, and hence get low weighting.



## 6.6 Application: Shape Analysis of Calcifications

Malignant calcifications tend to be numerous, clustered, small, varying in size and shape, angular, irregularly shaped, and branching in orientation.

Calcifications associated with benign conditions are generally larger, more rounded, smaller in number, more diffusely distributed, and more homogeneous in size and shape.

One of the key differences between benign and malignant calcifications lies in the roughness of their shapes.

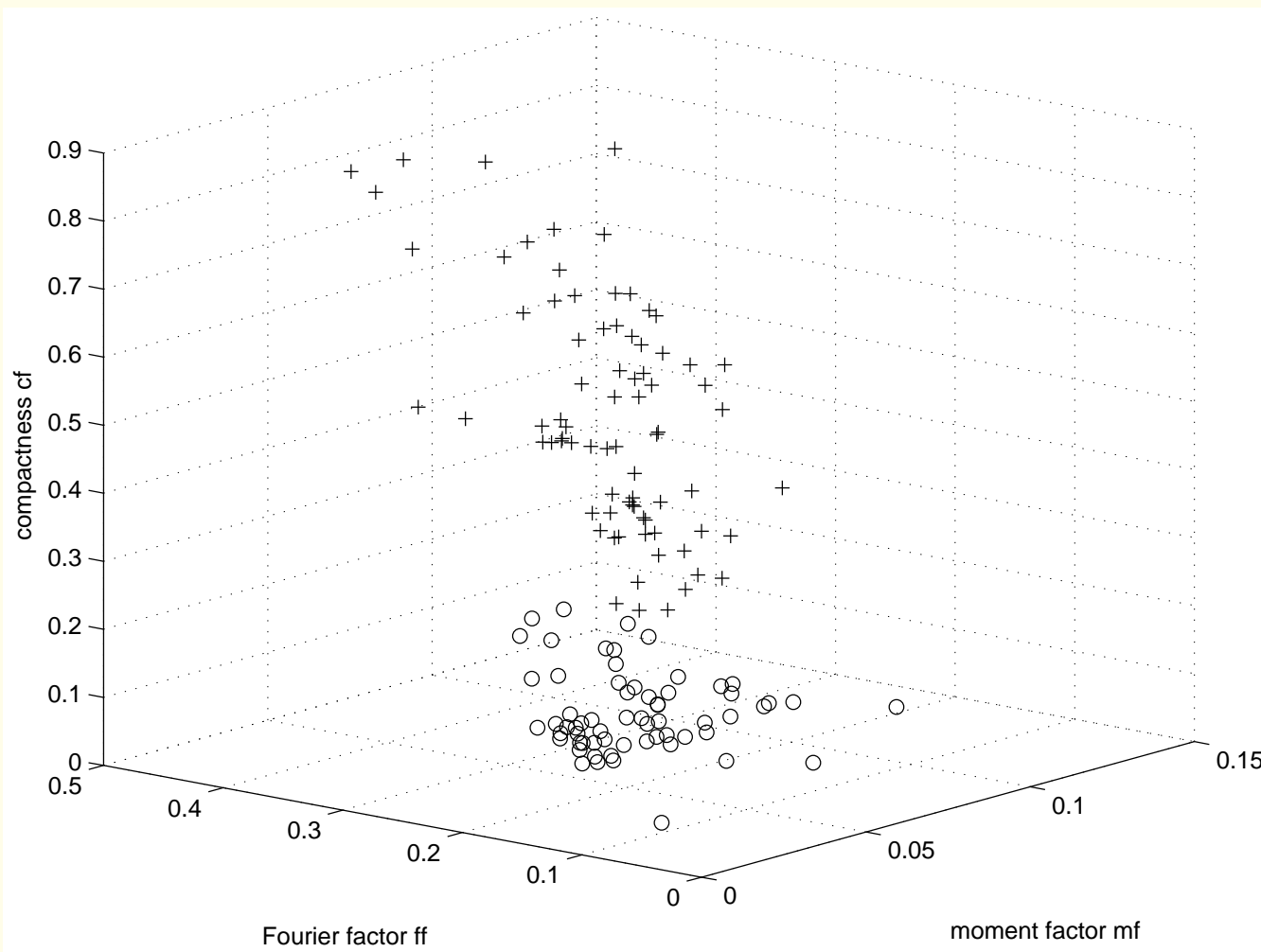


Figure 6.25: Plot of the shape factors ( $mf, ff, cf$ ) of 143 calcifications. The  $+$  symbols represent 79 malignant calcifications, and the  $\circ$  symbols represent 64 benign calcifications.

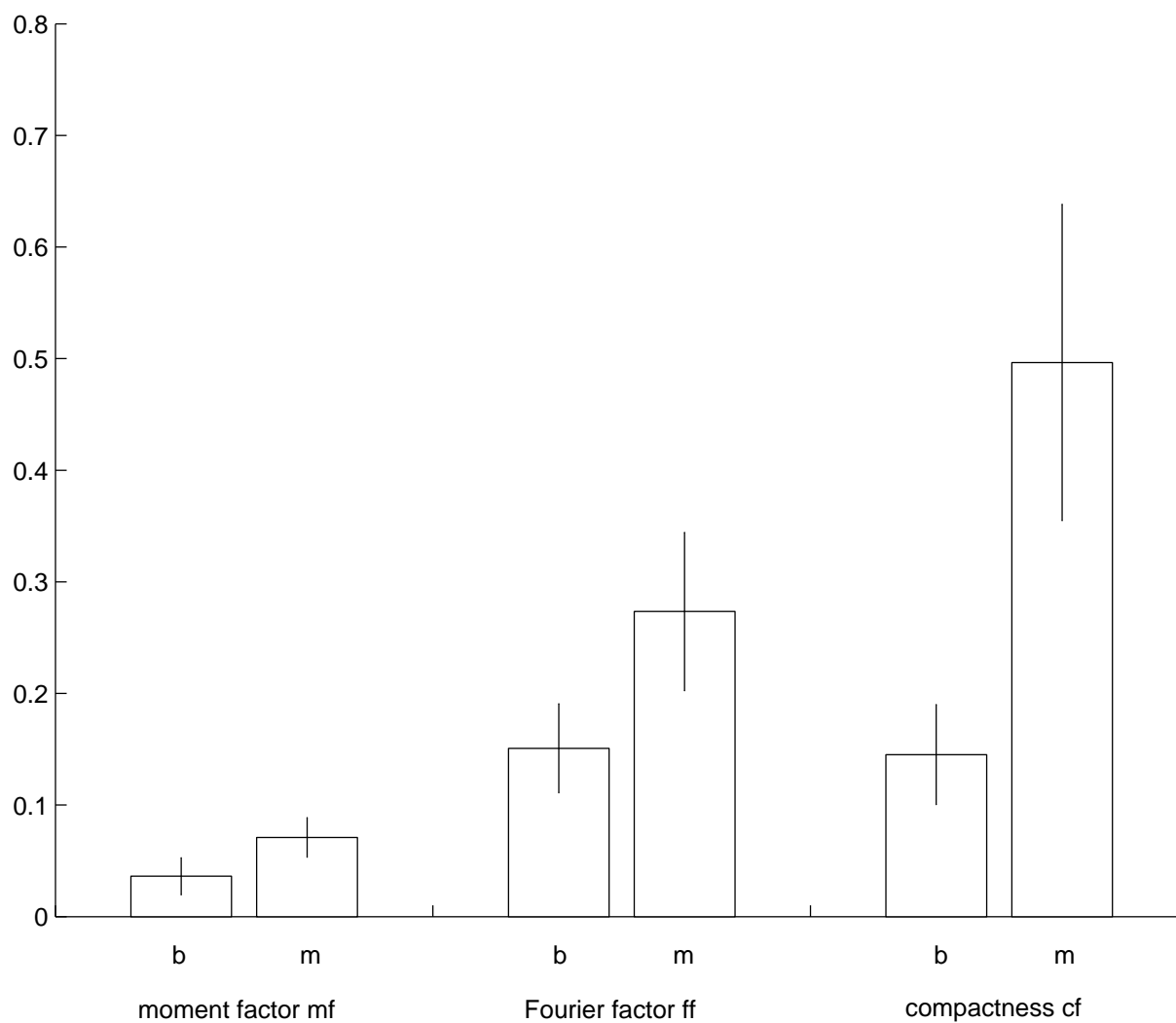


Figure 6.26: Means of the shape factors ( $mf$ ,  $ff$ ,  $cf$ ) of 64 benign calcifications ('b') and 79 malignant calcifications ('m'). The error bars indicate the range of mean plus or minus one standard deviation.



## 6.7 Application: Shape Analysis of Breast Masses and Tumors

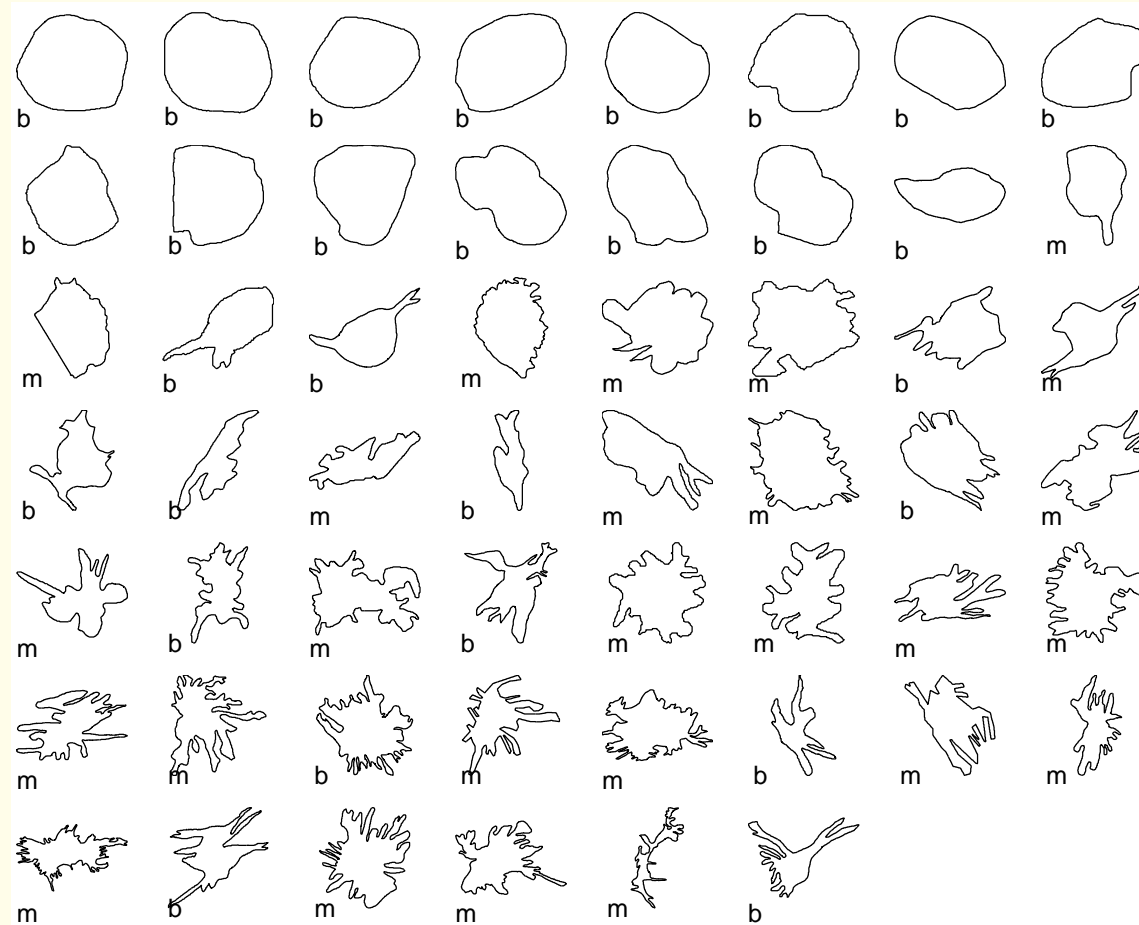


Figure 6.27: Contours of 54 breast masses. ‘b’: benign masses (28). ‘m’: malignant tumors (26). The contours are arranged in order of increasing magnitude of the feature vector ( $cf, f_{cc}, SI$ ). Note that the masses and their contours are of widely differing size, but have been scaled to the same size in the illustration.

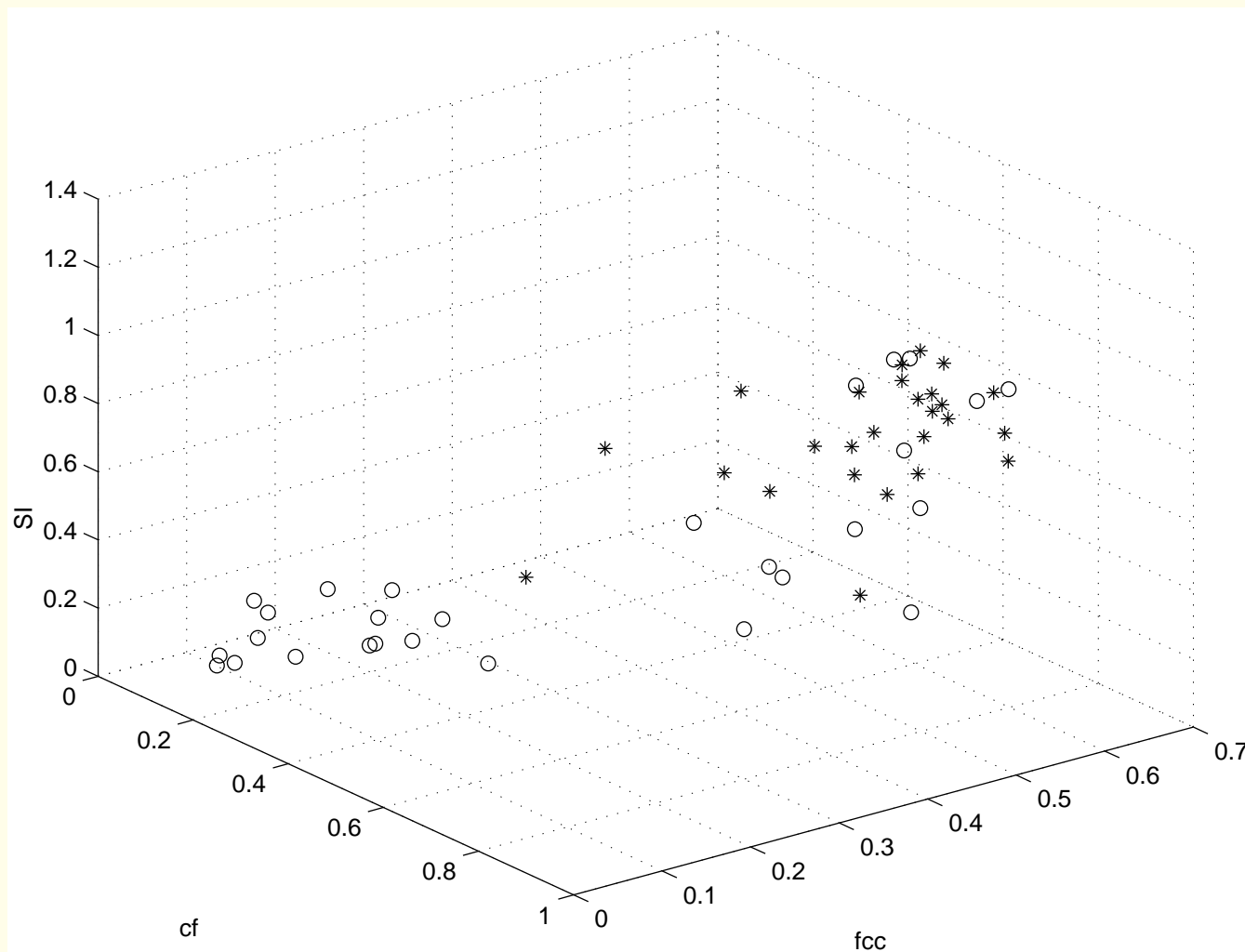


Figure 6.28: Feature-space plot of  $cf$ ,  $fcc$ , and  $SI$ :  $\circ$  for benign masses (28) and \* for malignant tumors (26).  $SI$ : spiculation index,  $fcc$ : fractional concavity, and  $cf$ : modified compactness. See Figure 6.27 for an illustration of the contours.



## 6.8 Remarks

Obtaining contours with good accuracy could be difficult.

It is not a common clinical practice to draw the contours of tumors or organs.

Malignant tumors typically exhibit poor definitions of their margins due to their invasive and metastatic nature:

identification and drawing of their contours is difficult, either manually or by computer methods.



Hand-drawn and computer-detected contours may contain imperfections and artifacts that could corrupt shape factors;

there could be significant variations between the contours drawn by different individuals for the same objects.

It should be recognized that the contour of a 3D entity, such as a tumor, as it appears on a 2D image (for example, a mammogram) depends upon the imaging and projection geometry.



Contours of biological entities often present significant overlap in their characteristics between various categories, such as for benign and malignant diseases.

The inclusion of measures representing other image characteristics, such as texture and gradient, could complement shape factors, and assist in improved analysis of images.